ABSTRACT

Title of Dissertation: BREAKAGE OF SINGLE DROPLETS IN 2-D INERTIAL FLOWS

Author: Derrick I. Ko
Doctor of Philosophy, 2018

Directed by: Professor Richard V. Calabrese
Department of Chemical and Biomolecular Engineering

Droplet break-up research has traditionally focused on droplets in: 1) generally uniform flow fields (constant strain rates or constant turbulence dissipation rates) that are easier to characterize and study, and in 2) highly complex flow fields generated by mixing devices in which the evolution of an entire droplet population with time is of interest. The current work adds to the existing body of knowledge by investigating the effect of short-term high-intensity deformation events on the break-up of single large droplets in both turbulent and inertial laminar flows. This approach consists of two components: high-speed imaging of droplets as they pass through a 2-D slit orifice and CFD simulations of the orifice flow field. The experimental trajectories of the droplets are combined with the CFD-generated flow field to determine the deformation history of the droplet prior to break-up.

In turbulent 2-D orifice flows, droplets and bubbles on the order of the macroscale of turbulence were studied. For these large droplets and bubbles, it was found that the product of strain rate magnitude and un-deformed diameter (essentially the velocity difference across the droplet) was a more suitable velocity scale. A new form of locally-derived, trajectory-dependent Weber number,

consisting of the maximum average strain rate magnitude over an exposure time equal to 0.04 multiplied by the Stokes particle relaxation time, was used to develop a break-up probability model that can be applied to the break-up of both liquid droplets and gas bubbles. The model adds weight to the break-up interpretation of Levich (1962); break-up occurs due to the internal pressure fluctuations overcoming the interfacial stresses of the deformed droplet.

In inertial laminar 2-D orifice flows, the break-up of water droplets in oil was studied at two viscosity ratios. The recommended local Weber number was again based on the maximum average strain rate magnitude over a particular exposure time, but this exposure time was instead 8 multiplied by the oscillation time scale. Using the maximum length achieved by the droplet as the length scale was also found to better represent the potential for break-up. With these modifications, and an associated capillary number-based model for predicting the drop draw ratio, two local Weber number thresholds were defined. First, the threshold for break-up is at We_{local} = 30. Second, the threshold for producing large daughter droplets, termed fracturing in this work, is at We_{local} = 1,000. Between these thresholds, droplets may fracture or undergo a mechanism termed erosion in this work, where a small number of tiny droplets break off from the main body of the droplet. Both of these break-up types are based on an elongative end-pinching mechanism.

BREAKAGE OF SINGLE DROPLETS IN 2-D INERTIAL FLOWS

By

Derrick I. Ko

Dissertation submitted to the Faculty of the Graduate School of the
University of Maryland, College Park in partial fulfillment
of the requirements for the degree of
Doctor of Philosophy
2018

Advisory Committee:

Professor Richard V. Calabrese, Chair

Professor David I. Bigio

Professor Panagiotis Dimitrakopoulos

Professor Kenneth T. Kiger, Dean's Representative

Professor Srinivasa R. Raghavan

Acknowledgments

First and foremost, I would like to thank my adviser, Dr. Richard Calabrese, for his advice and guidance over the last seven years. I have built a reasonably broad base in fluid mechanics with respect to fundamental knowledge, experimentation, numerical simulation, and teaching largely due to his direction. I appreciate his efforts on my behalf.

I would also like to thank my dissertation committee members for their advice, discussion, and help on various aspects of my studies: Dr. Kenneth Kiger for the channel fabrication, Dr. Srinivasa Raghavan for capsule generation and use of his rheometer, Dr. Panagiotis Dimitrakopoulos for capsule dynamics, and Dr. David Bigio for droplet dynamics. In addition, I would like to thank Dr. James Duncan for the loan of the Phantom high-speed camera and Mr. Majid Aroom for help with the flow loop fabrication.

The High-Shear Mixing Research Program has been a great source of motivation and in-depth discussion. I particularly want to acknowledge the financial support of Chevron ETC and the contributions of Dr. Lee Rhyne.

I also want to thank a great number of my fellow graduate students for their help through the course of this project. My current and former labmates—Dr. Justin Walker, Dr. Paul Rueger, Kanan Ghaderzadeh, Jung Kim, Ben Minnick, Daniel Williams, and Ellery Murdock—have been great as both helping hands and as

sounding boards for various ideas. Regarding technical advice from other research groups, I would like to thank:

- Dr. Dana Ehyaei and Kyle Corfman for channel fabrication advice.
- Dr. Naeem Masnadi, Dr. Nate Washuta, and Martin Erinin for help with setting up the Phantom and channel fabrication advice.
- Dr. Chanda Arya, Dr. Ankit Gargava, Dr. Brady Zarket, Kerry DeMella, and Hubert Huang for capsule- and rheometer-related training.
- Aditya Sangli for discussions about droplet break-up.

Finally, I want to express my gratitude for the people who have been supporting me on the home front. Most importantly, my wife, Dr. You-Shin Chen, has been my primary source of inspiration and mental support. Having already travelled a similar path, she has helped me to keep my life and career in perspective. I can't imagine being here without her. The encouragement and support from my mother Christina, father Waito, my brother Justin and sister-in-law Samantha, other family members, and friends has also been of great value.

Table of Contents

List of Figures

List of Tables

Nomenclature

Ca	Capillary number ($Ca = \mu U/\sigma$)
D	diameter [m]
Eo	Eötvös number ($Eo = g\|\rho_c - \rho_d\|D^2/\sigma$)
Fr	Froude number ($Fr = U^2/gL$)
g	gravitational constant [9.81 m/s^2]
H	cross-wise width of channel [12.7 mm]
k	turbulence kinetic energy [m^2/s^2]
L	long axis of deformed droplet [m]
M	Morton number ($M = g\mu_c^4\|\rho_c - \rho_d\|/\rho_c^2\sigma^3$)
P	pressure [Pa]
P	probability of break-up [-]
Q	volumetric flow rate [m^3/s]
Re	Reynolds number ($Re = \rho UD/\mu$)
Re_{ch}	channel Reynolds number ($Re_{ch} = 2\rho_c U_{ch} H/\mu_c$)
t	time [s]
t_{exp}	exposure time [s]
U_{ch}	superficial channel velocity [m/s]
U_{orf}	superficial orifice velocity [m/s]
We	Weber number ($We = \rho U^2 D/\sigma$)
We_{local}	local Weber number($We_{local} = \rho U^2 D/\sigma$)
x	span-wise coordinate [m]
y	cross-wise coordinate [m]
y_{inc}	cross-wise incoming trajectory [m]
z	stream-wise coordinate [m]

$\dot{\gamma}$	magnitude of the strain rate tensor [1/s]
δ	half-width of the orifice [1.5875 mm]
ε	turbulence dissipation rate [m^2/s^3]
λ	viscosity ratio ($\lambda = \mu_d/\mu_c$)
μ	viscosity [Pa-s]

ξ density ratio ($\xi = \rho_d/\rho_c$)

ρ density [kg/m^3]

σ interfacial tension [N/m]

τ stress [N/m^2]

Subscripts

c continuous phase property

crit critical level or threshold

d dispersed phase property

exp exposure

fl fluid particle relaxation time scale

inc incoming property

local dimensionless group defined with a local velocity scale

orf orifice-related property

osc oscillation time scale

St Stokes particle relaxation time scale

x vector component in span-wise direction

y vector component in cross-wise direction

z vector component in stream-wise direction

1. Introduction

Much of the current droplet break-up knowledge, developed to improve industrial mixing processes (Leng & Calabrese, 2004), falls into two broad categories. The first category is the study of single droplets in generally uniform flow fields. These are mainly Stokes flows with constant strain rates (e.g., Taylor, 1934; Grace, 1982) or turbulent flow fields with scalable turbulence dissipation rates (e.g., Kolmogorov, 1949; Hinze, 1955). Break-up of a droplet in these studies can be characterized by a single constant value for its velocity scale. In the second category, the break-up of droplets is studied in more complicated geometries and flows, including mixing devices (e.g., Chen & Middleman, 1967; Calabrese et al., 1986; Berkman & Calabrese, 1988; Rueger & Calabrese, 2013). The flows are typically turbulent and non-uniform, but if the droplets are present for sufficient time, they eventually encounter the turbulent eddy that characterizes break-up and the maximum stable droplet size in that particular device. In both categories of studies, semi-empirical break-up models have been established from physical first principles. These studies provide great insight into the physics of droplet break-up, but one of the important conditions for application of these models is that a droplet or droplet population must be resident in the flow field long enough to experience the critical deformation event that characterizes break-up.

The impact of short-term deformation events on droplet break-up is less well-studied but is of great interest in a number of applications. One such application is to potentially reduce the formation rate of natural gas hydrates within

high-pressure oil pipelines. The break-up of large water droplets in the oil flow as they pass through orifices, pumps, and other constrictions in the pipeline leads to greater interfacial area and thus more rapid formation of gas hydrates. This in turn leads to a greater likelihood of pipeline blockages due to hydrate agglomeration. Another application is the break-up of droplets in high shear mixing devices such as in-line rotor-stator mixers or homogenizers. Droplets experience a significant but limited-duration deformation event as they pass through the stator slots. Unlike in batch devices, droplets in in-line devices may not experience the highest deformation events possible since they pass through the mixing zone only a limited number of times.

The current project aims to improve the state of knowledge by studying the break-up of large single droplets caused by a short-term, high-intensity deformation event in inertial 2-D orifice flows, which includes both turbulent and laminar flows. An acrylic-and-aluminum channel with a 25%-open slit orifice was designed and fabricated. High speed imaging of the droplets in the transparent acrylic test section was conducted to develop droplet trajectories and identify locations and mechanisms of break-up. Relatively simple computational fluid dynamics (CFD) simulations were used to quantify the flow field (mean flow field for turbulent flows) near the orifice. The droplet trajectories were mapped to the computationally-generated flow fields to produce droplet deformation histories (i.e., the specific deformations exerted on the droplet along the droplet's trajectory over time). These histories were analyzed to determine the critical velocity, length, and time scales for characterizing droplet break-up. This ultimately led to the development

of a new form of local Weber number that is based on the trajectory-dependent deformation history of individual droplets.

In addition to the value of investigating short-term deformation events, this work seeks to expand the range of sizes for which break-up of droplets in turbulent flows can be modelled. These analyses could form the basis for developing breakage kernels applicable to early process times (when droplets are relatively large) for population balance modelling. Furthermore, basing the possibility droplet break-up on trajectory-dependent deformation histories was intended to provide a geometry-independent method for quantifying break-up. However, this independence from geometry was not investigated as part of the scope of this work.

1.1. Fundamental Description of Droplet Breakup

In qualitative terms, a droplet is broken when the disruptive stresses acting upon the droplet exceed the cohesive stresses capable of holding it together for a sufficient duration. This simple description belies the complexity of break-up phenomena, however. Understanding break-up phenomena in even relatively simple flows can be complicated by the number and degree of forces involved.

The fundamental physical framework for studying droplet break-up is the conservation of mass and momentum, expressed as the continuity and the Navier-Stokes equations. Equation 1.1-1 and 1.1-2 show the continuity and Navier-Stokes equations for the continuous phase. The velocity u_c and pressure P_c are dependent on fluid density ρ_c, fluid viscosity μ_c, and gravitational acceleration g, where the

subscript *c* denotes a continuous phase property. Equations 1.1-3 and 1.1-4 show the continuity and Naver-Stokes equations for the dispersed phase, with the dispersed phase flow and fluid properties denoted with the *d* subscript. Equations 1.1-5 and 1.1-6 conserve momentum at the interface between the two phases in the surface-normal (subscript *norm*) and surface-tangential (subscript *tan*) directions. The local interface curvature is denoted as $\mathcal{H}$. When solved with the applicable boundary conditions, the Navier-Stokes equations produce a velocity and pressure field as a function of the spatial coordinate *x* and the temporal coordinate *t*.

$$\rho_c \frac{\partial \vec{u}_c}{\partial t} + \rho_c \nabla \cdot \vec{u}_c = 0 \tag{1.1-1}$$

$$\rho_c \frac{\partial \vec{u}_c}{\partial t} + \rho_c \vec{u}_c \cdot \nabla \vec{u}_c = -\nabla P_c + \mu_c \nabla^2 \vec{u}_c + \rho_c \vec{g} \tag{1.1-2}$$

$$\rho_d \frac{\partial \vec{u}_d}{\partial t} + \rho_d \nabla \cdot \vec{u}_d = 0 \tag{1.1-3}$$

$$\rho_d \frac{\partial \vec{u}_d}{\partial t} + \rho_d \vec{u}_d \cdot \nabla \vec{u}_d = -\nabla P_d + \mu_d \nabla^2 \vec{u}_d + \rho_d \vec{g} \tag{1.1-4}$$

$$\left(P_d - \mu_d \Delta_{d,norm}\right) - \left(P_c - \mu_c \Delta_{c,norm}\right) = 2\mathcal{H}\sigma \tag{1.1-5}$$

$$\mu_d \Delta_{d,tan} - \mu_c \Delta_{c,tan} = 0 \tag{1.1-6}$$

For all but the simplest problems, analytical solutions to these equations cannot be constructed because of complexities in the geometry and/or turbulence in the flow field. Despite this, the continuity and Navier-Stokes equations remain important to consider as a mechanistic framework for experimental work and as the basis for CFD simulations. Reduction of these conservation equations to a

dimensionless form leads to a smaller parametric space and can be the basis for further simplification. Equations 1.1-7 to 1.1-12 are possible dimensionless analogues to Equations 1.1-1 to 1.1-6.

$$\frac{\partial \vec{u}_c^*}{\partial t^*} + \nabla^* \cdot \vec{u}_c^* = 0 \tag{1.1-7}$$

$$\frac{\partial \vec{u}_c^*}{\partial t^*} + \vec{u}_c^* \cdot \nabla^* \vec{u}_c^* = -\nabla^* P_c^* + \frac{1}{Re} \nabla^{*2} \vec{u}_c^* + \frac{1}{Fr} \vec{g}^* \tag{1.1-8}$$

$$\frac{\partial \vec{u}_d^*}{\partial t^*} + \nabla^* \cdot \vec{u}_d^* = 0 \tag{1.1-9}$$

$$\frac{\partial \vec{u}_d^*}{\partial t^*} + \vec{u}_d^* \cdot \nabla^* \vec{u}_d^* = -\nabla^* P_d^* + \frac{\lambda}{\xi\, Re} \nabla^{*2} \vec{u}_d^* + \frac{1}{Fr} \vec{g}^* \tag{1.1-10}$$

$$\left(\xi P_d^* - \frac{\lambda}{Re} \Delta_{d,norm}^*\right) - \left(P_c^* - \frac{1}{Re} \Delta_{c,norm}^*\right) = 2 \frac{\mathcal{H}^*}{We} \tag{1.1-11}$$

$$\lambda \Delta_{d,tan}^* - \Delta_{c,tan}^* = 0 \tag{1.1-12}$$

In reducing the dynamical equations to dimensionless form, the five independent dimensionless groups shown in Table 1.1 are formed. These groups represent ratios of the six identified forces governing the two-phase flow behaviour: inertial and viscous forces in the continuous phase, inertial and viscous forces in the dispersed phase, interfacial forces, and gravitational forces. In local droplet break-up studies, the length scale *L* is the un-deformed diameter *D*, while the appropriate choice for the velocity scale *U* depends on the dominant physics of the problem. The choice of *U* is discussed in detail in Sections 4.1 and 5.1 for turbulent and laminar flows, respectively.

Table 1.1. Dimensionless groups from reduction of Navier-Stokes equations.

Name	Definition	Description / Interpretation
Density Ratio	$\xi = \frac{\rho_d}{\rho_c}$	Ratio of inertial forces in the droplet phase to inertial forces in the continuous phase.
Viscosity Ratio	$\lambda = \frac{\mu_d}{\mu_c}$	Ratio of viscous forces in the droplet phase to viscous forces in the continuous phase.
Reynolds Number	$Re = \frac{\rho_c U L}{\mu_c}$	Ratio of inertial forces to viscous forces in the continuous phase.
Froude Number	$Fr = \frac{U^2}{gL}$	Ratio of inertial forces to gravitational forces.
Weber Number	$We = \frac{\rho_c U^2 L}{\sigma}$	Ratio of inertial forces in the continuous phase to interfacial forces.

Despite the reduction of independent parameters, the five dimensionless groups (along with consideration of the geometry of the apparatus) still result in a very large potential design space. To create a manageable and understandable experimental design, it is necessary to establish limits on these groups. Buoyancy typically has a negligible contribution to break-up for small droplets in viscous and strong flows, so Froude number can be neglected. Limitations can also occur for very low or very high Reynolds numbers. For example, droplet breakage experiments conducted in the Stokes flow regime (i.e., negligible inertial forces in both droplet and continuous phases) allows for Reynolds number and density ratio to be neglected. This eliminates the advective term in the dimensionless Navier-Stokes equations (Equations 1.1-8 and 1.1-10). The balance between viscous forces in each fluid and interfacial forces are represented by the two remaining

dimensionless groups, viscosity ratio and capillary number $Ca = We/Re$ (which replaces Weber number for multiphase flow problems in Stokes flows). This forms the basis of the well-known Grace curves (Grace, 1982).

1.2. Project Objectives

The objective of this project was to develop a relationship between flow and/or fluid properties and the thresholds or probability of breakage for relatively large single droplets passing through a 2-D slit orifice in both turbulent and laminar flows. The objective was achieved by synthesizing information from two sources:

- High-speed imaging of droplets passing through and interacting with the orifice provided details of the droplet path and the location of break-up, and
- Simple CFD simulations of the flow field (mean flow field via the Reynolds-Averaged Navier-Stokes (RANS) equations for turbulent flows) provided the details of the flow field in the vicinity of the orifice.

The droplet path from the high-speed imaging was mapped to the simulated flow field to reveal the time-dependent (or position-dependent) conditions experienced by the droplet as it travelled through the orifice. Experiments were performed for the following conditions:

- Oil droplets and air bubbles in turbulent flows of water. The diameters of these fluid particles were on the order of the macroscale of turbulence.
- Water droplets in laminar flows of oil. These laminar flows, having Reynolds numbers significantly greater than 1, had non-negligible inertial components.

Because the flow fields were non-homogeneous, the deformation histories produced from the combination of the experimental imaging and the computationally-developed flow fields were analyzed to discover the appropriate velocity, length, and time scales. These scales were used to develop a new form of local Weber number, which was used to develop break-up thresholds for inertial laminar flows and break-up probabilities in turbulent flows.

1.3. Organization of Dissertation

This dissertation is organized into the following chapters:

- Chapter 1 introduces the motivation and specific goals of this work, along with a fundamental description of droplet break-up with respect to mass and momentum conservation.
- Chapter 2 describes the design and methodology of both the experimental and computational sides of this work. This includes details of the experimental apparatus, fluid properties, operating conditions, image acquisition and analysis procedures, and CFD methodology.

- Chapter 3 focuses on the simulations pertaining to: 1) the design of the channel apparatus, in particular the necessary entry length required to fully-develop both turbulent and laminar flows, and 2) the flow fields near the slit orifice that were combined with the experimental droplet data to provide insight into the local conditions along a droplet's path leading to break-up.
- Chapter 4 presents the experimental data and its analysis with the CFD simulations for the break-up of droplets and bubbles in turbulent 2-D orifice flows. Droplet trajectories, break-up mechanisms, and three approaches to characterizing the probability of break-up are discussed. Comments on the distribution of the daughter droplets are also presented.
- Chapter 5 presents the experimental data and its analysis with the CFD simulations for the break-up of droplets in inertial laminar 2-D orifice flows. Droplet trajectories, break-up mechanisms, and the characterization of break-up are discussed.
- Chapter 6 contains a summary of the work and the important conclusions from each of the three previous chapters. Recommendations for future work are also included.

In addition to information provided in the appendices, this dissertation includes droplet break-up videos in a supplementary PowerPoint file.

2. Experimental and Computational Methodology

As discussed in Section 1.2, physical and computational methods were used together to explore droplet break-up due to flow through a 2-D slit orifice. Sections 2.1 to 2.3 focus on the physical component of work. This includes a description of the channel apparatus and droplet generation device, the fluid properties and operating conditions studied, and details on the imaging and image analysis. The principal output from the physical side of this work are droplet trajectories, locations of break-up, and details of the break-up mechanisms. These are located in Sections 4.2 and 5.2 for turbulent and inertial laminar flows, respectively.

Section 2.4 chapter provides background on CFD methodology. CFD was utilized for two aspects of this work, both of which are the focus of Chapter 3. First, CFD simulations of the inlet geometry and open channel were used to establish the necessary entry length upstream of the orifice to allow the open channel velocity profile to become fully developed in both turbulent and laminar flows. Second, for each flow condition in which droplets were imaged, the flow field near the slit orifice was simulated using the Navier-Stokes equations for laminar flow and the RANS equations for turbulent flow. The critical items gained from the simulations are the detailed deformation fields and their dependence on the channel Reynolds number Re_{ch}. Combining these simulation results with the data gained from the physical studies yielded insight into the critical features of the flow field that lead to breakage.

2.1. Experimental Apparatus and Coordinate Convention

Figure 2.1 illustrates the larger components of the experimental apparatus, consisting of a vertically-oriented channel of rectangular cross-section with a supporting flow loop. The flow travels up the channel, against the direction of gravity. The combined length of the aluminum inlet and upstream sections, determined through CFD simulations of the inlet geometry, was intended to allow both turbulent and laminar flows to fully develop before reaching the test section (see Chapter 3 for details). The test and downstream sections are fabricated from optically-transparent acrylic to allow for imaging of droplets and bubbles within the channel. A Seepex BN10-6L progressive cavity pump provided a volumetric flow rate of between 10 and 130 L/min, resulting in a superficial velocity of between 0.13 and 1.7 m/s in the channel. Comparisons between the GPI flow meter and bucket-fill tests verified that the flow rate is linear with drive frequency. The bucket-fill tests also verified that pump was a constant-volume pump, providing the same flow of water as oil at a given drive frequency.

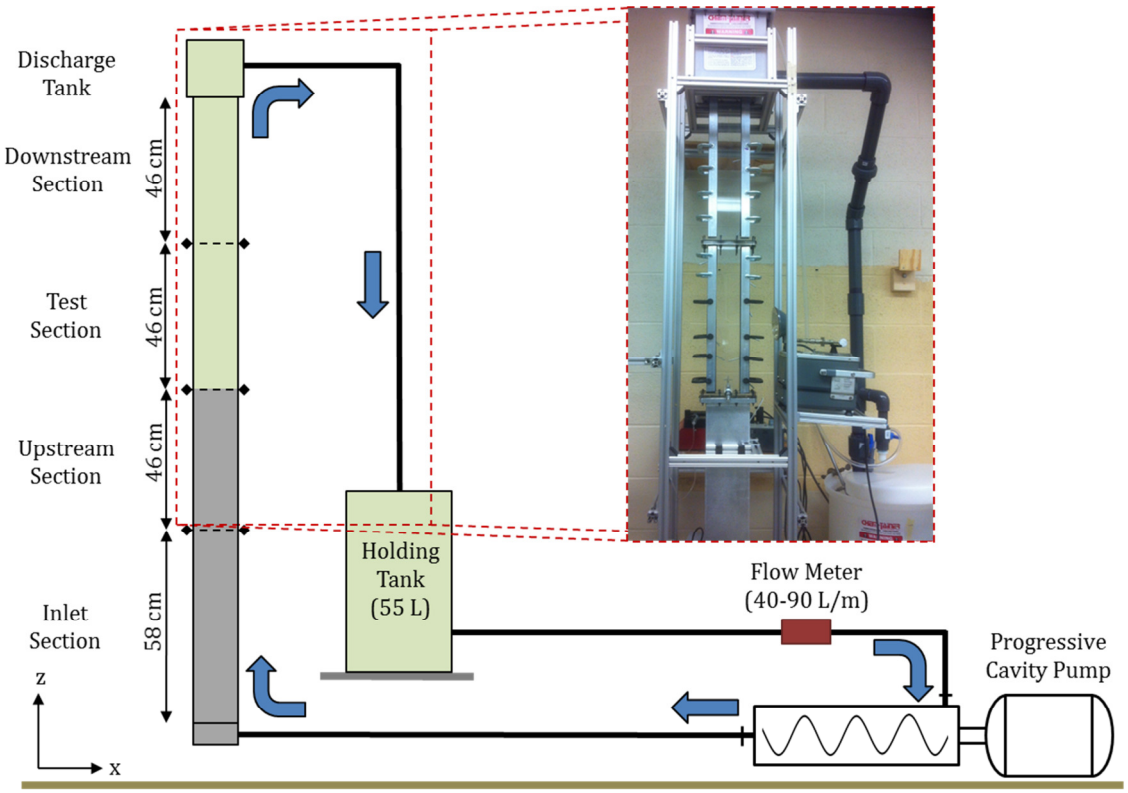

Figure 2.1. General schematic of the flow loop. Inset shows a photograph of apparatus.

The 3-D model of the test section and a sample image from the imaging plane are shown as Figure 2.2(a) and (b), respectively. For most of the current work, the origin is located at the centre of the entrance to the orifice. In the cross-wise (y) direction, the two notable length scales are the width of the channel H (12.7 mm) and the half-width of the orifice (δ = 1.59 mm). The span-wise (x) direction is 102 mm (8 H) in width. The test section is 457 mm in length in the stream-wise (z) direction, with a total channel length of about 2 m (see Figure 2.1). The centred slit orifice has a thickness of 3.18 mm and an opening 3.18 mm x 102 mm in cross-section, with the flow being constricted in the cross-wise (y) direction only. The upstream face of the orifice is located 203 mm from the test section entrance.

Imaging of droplets occurred primarily at the imaging plane at $x = 0$ as shown in Figure 2.2(a).

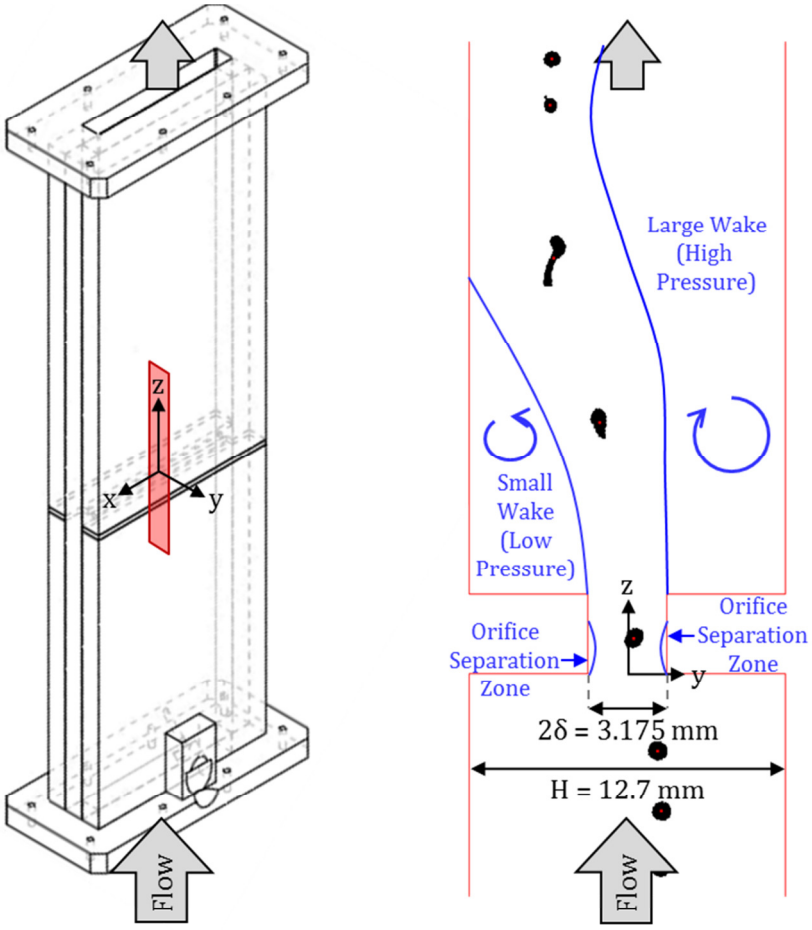

(a) Isometric view of test section

(b) Illustration of imaging plane

Figure 2.2. (a) Isometric view of the test section, with the imaging plane in red. (b) The imaging plane, illustrating important dimensions and flow features. The channel width H and orifice width 2δ are shown. The blue lines illustrate the limits of the separation zones within the orifice and wake zones behind the orifice.

Note that, as shown in Figure 2.2(b), the orifice jet was not symmetric in the flow conditions investigated in this work. Perturbations associated with pump start-up or slight geometric asymmetries in the flow or channel cause the jet to lean

to either side of the channel. To make the analysis and presentation of results consistent, the following coordinate convention was adopted. The origin is at the centre of the orifice entrance. The main flow is in the $+z$ direction, while gravity is in the $-z$ direction. The $+y$ direction is in the direction of the large high pressure wake region, while $-y$ is in the direction of the leaning jet and the small low pressure wake region. Orifice separation zones occur on the inner orifice surfaces on both sides. Refer to Section 3.2 for more details regarding the slit orifice flow field.

At the lowest portion of the acrylic test section is the injection port. Figure 2.3 shows its location as well as its design and an image of the injection port connected to the channel. There are two principal components. The first is a Swagelok straight tube adaptor. The NPT end is attached to the channel at 45°. On the tube adaptor end, a tube with a standard ferrule set is used. Instead of protruding through the nut, the tube is cut flush with the end of the ferrule. The ferrule provides a surface with which to support a soft gas chromatography septum, the second principal component, placed at the end of the ferrule and secured with the nut. This port seals the flow in the channel while allowing a long needle to be inserted through the septum and into the flow for droplet injection. The septum proved to provide adequate sealing for dozens of penetrations without replacement for the needle diameters used in the experiments (33 to 21 gauge).

The needle tips were generally cut and sanded to a 45° angle to make penetration easier and coring of the septum less likely. One of the needles used in the experiments is shown in Figure 2.4(a). The needle was connected to a syringe

and inserted through the septum into the span-wise centre plane ($x = 0$), as illustrated in Figure 2.4(b). The generated droplet sizes depended on the needle size, needle orientation (due to the cut of the tip), the location of the needle tip in the cross-wise (y) direction, local flow around the tube, and interfacial tension. During an experiment, the dispersed phase was dispensed continuously through the needle by a programmable syringe pump (New Era 300 series syringe pump).

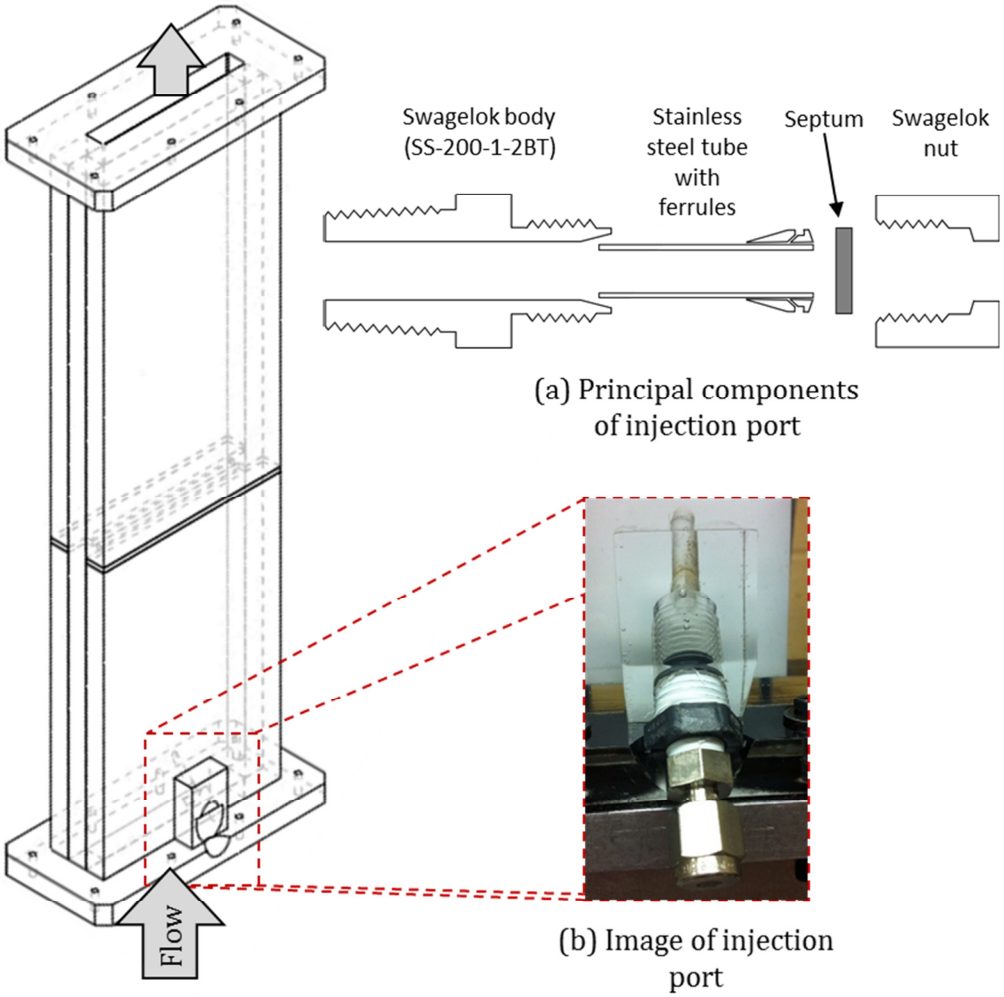

Figure 2.3. Details of the injection port. (a) Principal components. The stainless steel tube with ferrules provides support to the septum. (b) Image of the injection port attached to the test section. There is a PVC adapter between the channel and the Swagelok fitting.

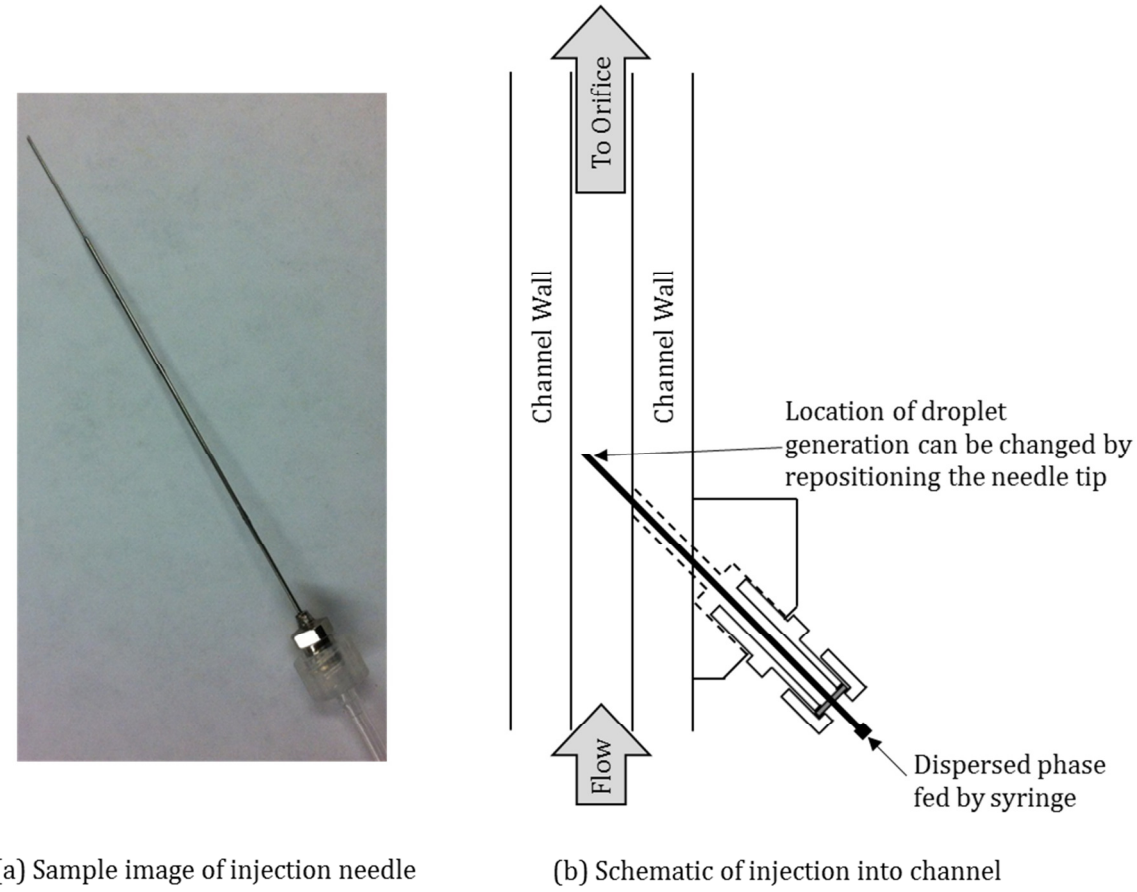

(a) Sample image of injection needle (b) Schematic of injection into channel

Figure 2.4. Injection needle for droplet generation in channel.

2.2. Fluid Properties and Operating Conditions

The physical properties of the fluids used in these experiments are summarized in Table 2.1. The viscosity of two Crystal Oils CO70FG and CO200FG (food-grade mineral oils) used as the continuous phases in the laminar experiments were measured using an AR-2000 thermally-controlled cone-and-plate viscometer. The temperature of the holding tank was held at 23°C with a Thermo/HAAKE Phoenix II circulator. The interfacial tension was measured with the pendant drop method. The procedure and analysis routines found in Rueger (2013), based on the

work of Adamson (1976), were used directly. For each droplet, a series of five images spaced by 1 second were taken, processed, and analyzed; the interfacial tension measurement for the droplet was considered to be the mean of the computed values from the five images. The interfacial tension for air and water as shown in Table 2.1 was based on thirty-seven droplets using water from a variety of sources (water drawn from the holding tanks on two occasions, fresh tap water, de-ionized water, and micro-filtered de-ionized water). The coefficient of variation (i.e., the standard deviation divided by the mean) for these measurements is less than 0.01. The interfacial tension between water and the Crystal Oils was based on eight droplets of each CO70FG and CO200FG. Based on these sixteen droplets, the coefficient of variation is 0.03.

Table 2.1. Material properties for the dispersed phase.

Material	**Density ρ [kg/m^3]**	**Dynamic Viscosity μ [Pa-s]**	**Interfacial Tension with Water σ [N/m]**
Water	998	1.003×10^{-3}	–
Air	1.18	1.85×10^{-5}	0.070
Crystal Oil 70FG [1] (CO70FG)	860	0.0202	0.050
Crystal Oil 200FG [2] (CO200FG)	860	0.0808	0.050

[1] Lot #8857
[2] Lot #11466 blended with a small volume of CO70FG (Lot #8847).

Droplet breakage was investigated for the flow conditions described in Table 2.2. The channel Reynolds number Re_{ch} is defined with the superficial open channel velocity and the hydraulic diameter as the velocity and length scales, respectively. Note that an orifice Reynolds number based on the superficial orifice velocity and

hydraulic diameter of the orifice results is identical to the channel Reynolds number because the superficial velocity is inversely proportional to the hydraulic diameter for the slit orifice geometry.

Table 2.2. Channel operating conditions for turbulent and laminar flows.

Continuous Phase Fluid	**Volumetric Flow Rate Q [m^3/s]**	**Superficial Open Channel Velocity U_{ch} [m/s]**	**Superficial Orifice Velocity U_{orf} [m/s]**	**Channel Reynolds Number Re_{ch} [-]**
CO200FG (Laminar Flow)	5.33×10^{-4}	0.413	1.65	110
	1.14×10^{-3}	0.880	3.52	240
CO70FG (Laminar Flow)	2.84×10^{-4}	0.220	0.88	240
	3.94×10^{-4}	0.305	1.22	330
	5.33×10^{-4}	0.413	1.65	450
	7.17×10^{-4}	0.555	2.22	600
Water (Turbulent Flow)	3.94×10^{-4}	0.305	1.22	7,700
	5.33×10^{-4}	0.413	1.65	10,000
	7.17×10^{-4}	0.555	2.22	14,000
	9.61×10^{-4}	0.745	2.98	19,000

2.3. Image Acquisition and Analysis

Droplet images are the key experimental data for this project. Ideally, an image sequence of a droplet travelling through the orifice would show a substantial amount of the test section, finely resolve droplet shapes, and provide a high temporal resolution to view the transient details of the break-up. However, these desirable image qualities depend on experimental and system parameters that often produce conflicting results. The acquisition of useful images is then often a product

of compromises between the various controlling parameters. These compromises and the general orientation of the cameras and light sources with respect to the test section are discussed in the remainder of this subsection. The details of the image acquisition systems (camera, lens, and lighting) as used in this project are given in the Subsections 2.3.1 and 2.3.2. The image analysis methodology is described in Subsection 2.3.3.

The most obvious compromise is between field of view and resolution. These can be controlled by the camera distance and the magnification of the lens. The field of view must encompass both a short region upstream of the orifice to facilitate measurement of the droplet's un-deformed diameter and a large downstream region to determine the location of any droplet breakage. It is also desirable to achieve a high droplet resolution and thus reduce errors in sizing. This creates a conflict for a given imaging system: improving the field of view decreases the droplet resolution and vice versa. For example, to capture a total field of view of 50.8 mm (4 H) on a 1392x1040 pixel sensor would result in an overall conversion scale of 27 pixels/mm (1392 pixels / 50.8 mm). A 200 μm droplet would be 5.4 pixels in diameter, with a 1 pixel error leading to about 20% error in diameter. On the other hand, if the error in this diameter must be limited to 5%, the spatial resolution must be increased to 100 pixels/mm, resulting in an impractically small 13.9 mm field of view. Note that the latter scenario is also not practical because it would only show 10.4 mm of the cross-wise direction, too little to see across the open channel (H = 12.7 mm). The resolutions of the images in this study were between 30 and 55 μm/pixel.

Another spatial consideration is the perspective error. This is the apparent size difference between two identical objects viewed at different distances. When the camera is close to the plane of focus, small changes in the location of the object around the plane result in relatively large changes in how that droplet is imaged, whereas an object far away would need to be far from the plane of focus to substantially to change the image size. It is therefore desirable to place the camera as far as possible from the apparatus, but this lowers the spatial resolution and the intensity of light that can reach the camera sensor.

The general arrangement of the camera and light source for all experiments is shown in Figure 2.5. The cameras and light sources used are described in following two subsections. The origin is marked at the centre of the orifice entrance. The camera was mounted on a tripod on one side of the apparatus, with the longer side of the sensor aligned with the direction of flow. The camera focused on the imaging plane at the span-wise centre of the channel (see Figure 2.2). The camera was located approximately 0.5 metres from the span-wise centre of the channel, with some variations in the distance for changing the field of view. The backlighting assembly, consisting of the lighting source and potentially a light diffuser, was mounted to the apparatus frame on the opposite side of the channel from the camera, also approximately 0.5 metres from the span-wise centre of the channel. Generally, the droplet interface became more easily defined when the lighting assembly was moved farther from the channel, though this would also have a minor negative impact on the amount of light able to reach the lens.

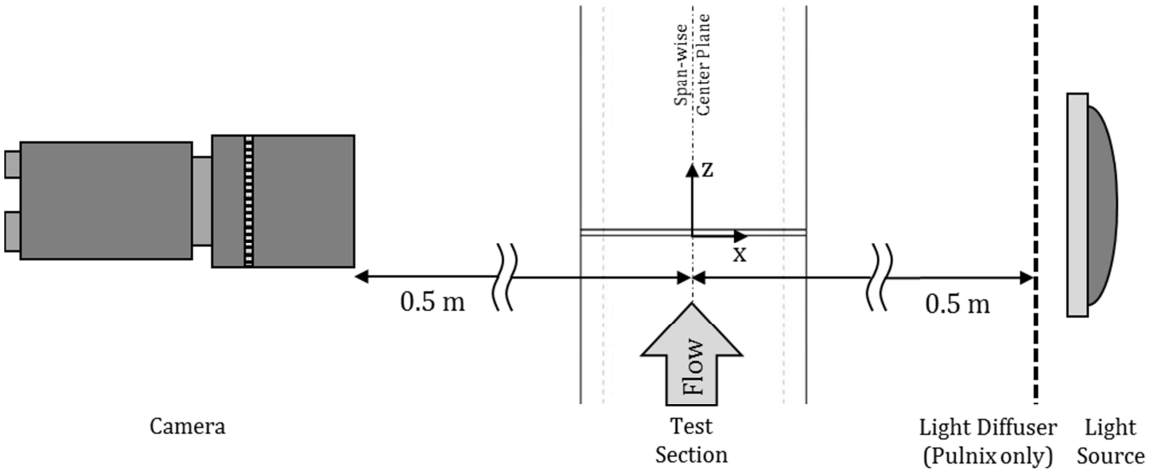

Figure 2.5. Camera and light source orientation with respect to channel test section.

2.3.1. Image Acquisition at Standard Frame Rates

The droplet images in the initial turbulent flow work were acquired using a JAI PULNiX TM-1405GE monochrome digital camera (referred to as the Pulnix camera for the remainder of this dissertation). The camera was connected to the computer through a gigabit Ethernet network card and cable. Configuration and operation of the Pulnix camera is conducted through JAI's Software Development Kit, installed on a standard desktop computer. The Pulnix camera has a maximum frame rate of 29.5 frames per second at the maximum resolution of 1392x1040 pixels. Images were acquired in runs of approximately 10 seconds. The shutter remained open for the entire run, with no delay interval between images. A Nikkor 55 mm lens was attached to the camera via a C-mount adaptor and extension tube.

The droplets and bubbles were backlit with two General Radio (GenRad) 1539-A stroboscopes. These units are equipped with three flash duration settings, of which the medium and fast settings were used in this work. The medium setting

provides 1.2 μs flashes at frequencies of up to 67 flashes per second. The fast setting provides short duration (0.8 μs) flashes at frequencies of up to 420 flashes per second. However, unlike the larger GenRad models, the 1539-A does not have an internal oscillator and must instead be externally triggered. A Sunfounder Uno R3 microcontroller was programmed and calibrated to activate the strobe for a user-specified number of flashes per image frame. To provide uniform background illumination, two layers of white tissue paper were placed in front of the strobes to act as a diffuser.

When the strobe or flash rate of the stroboscopes is greater than the camera frame rate, multiple instances of a droplet can be captured on a single camera frame. This allows for the temporal resolution of the imaging to be improved from the basic camera frame rate, but as the number of flashes per frame (stroboscope flashes per second divided by camera frames per second) increases, the contrast between the moving droplet and the static background decreases. This effect is shown in Figure 2.6. Droplets become very difficult to distinguish at strobes rates greater than 10 flashes per frame. The stroboscopes were programmed to emit 6 and 10 flashes per frame, depending on the needs of the imaging run.

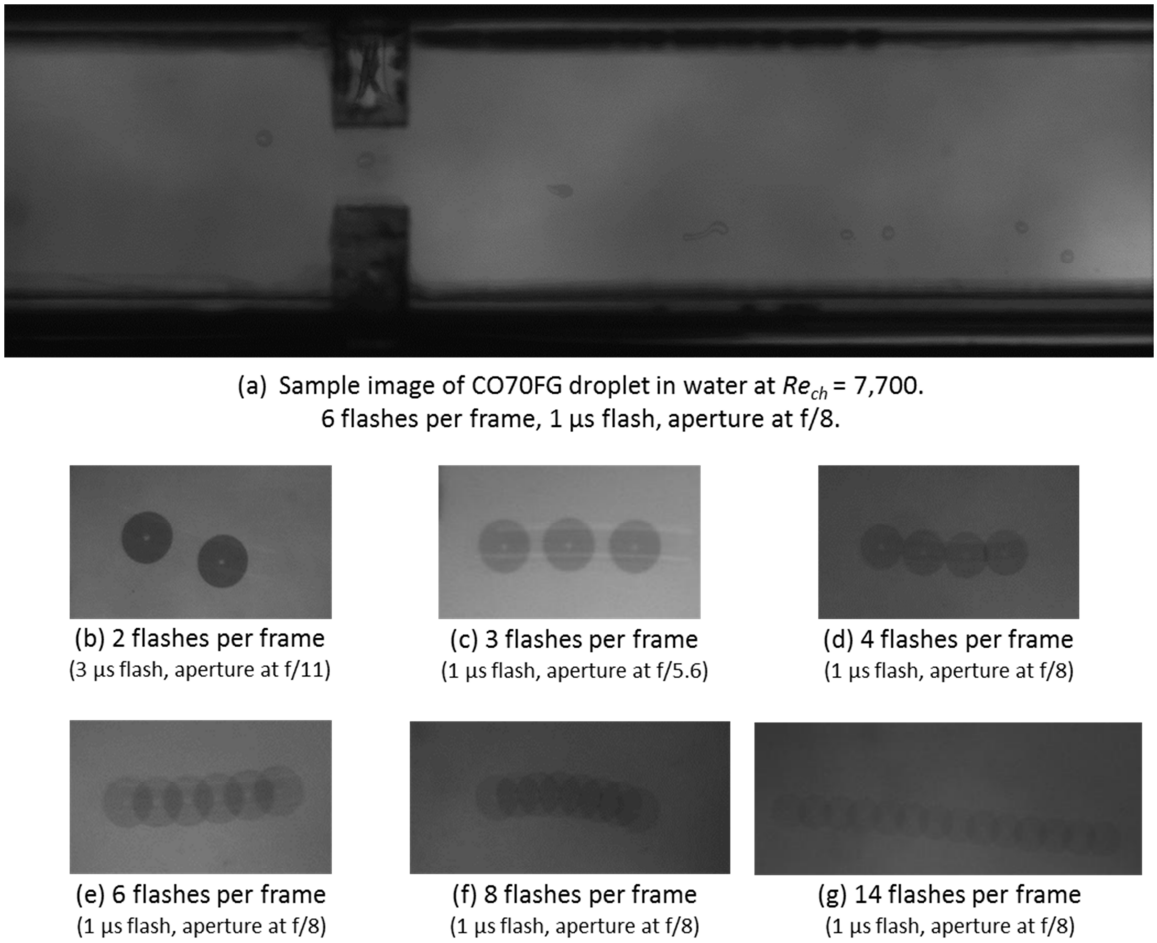

Figure 2.6. Images from Pulnix and strobe system. (a) shows a CO70FG droplet, imaged at a strobe rate of 6 flashes per frame. (b)-(g) each show a single slow-rising air bubble at strobe rates of 2-14 flashes per frame. Note the decreasing contrast with increasing flashes per frame.

2.3.2. High-speed Image Acquisition

The Pulnix system was limited by the maximum strobe flash rate with which droplet contrast could be achieved (10 flashes per frame or, equivalently, 295 flashes per second), but higher imaging rates were needed to resolve droplet trajectories at the higher channel velocities. Two separate tools were used. The droplet trajectories in the turbulent flow experiments were imaged at 1,000–1,400 frames per second with a Vision Research Inc. (VRI) Phantom v640 high-speed camera. This camera was also used to study droplet break-up mechanisms in the laminar flow experiments at 1,800–4,500 frames per second. The Phantom high-speed camera interfaced with a standard desktop computer through the VRI Phantom Camera Control application. The acquired images are stored on the camera's 16 GB internal memory. Second, the droplet trajectories in the laminar flow experiments were studied with a Point Grey (now FLIR) Blackfly-S monochrome camera (BFS-U3-13Y3M), controlled by the Spinview software, at frame rates of 240–600 frames per second. Images are transferred directly to computer storage via USB3 connection. The same Nikkor lens used with the Pulnix imaging system was also used with both the Phantom and Point Grey cameras.

The frame rates of the Phantom and Point Grey cameras exceeded the maximum strobe rate in many cases, so backlighting was provided by a Stocker Yale high-frequency fluorescent illuminator. This unit consists of two 6-watt fluorescent tubes behind a plastic diffuser and an 85 kHz driver. For this work, the diffuser was removed to provide greater illumination. The illuminator was placed such that only

one of the tubes was directly behind the channel; the other tube was essentially unused for the imaging.

2.3.3. Image Processing

To make analysis of the droplet images more tractable, they were first converted to binary images using a set of customized MATLAB scripts. The first step in this process was to subtract the background. At the beginning of and periodically within each imaging session, ten images of the empty flow field (i.e., without any droplets) were acquired. Three new image files were created, containing the average, minimum, and maximum greyscale intensities from the ten background images. The intent of this process was to determine the range of greyscale intensities that could exist on a pixel-by-pixel basis with which to compare images containing droplets.

The additional difficulty encountered in processing the background was the perspective. As shown previously in Figure 2.6(a), the edges of the channel at the closer and farther walls are visible, but these edges are not in the plane of the droplet and are thus not directly useful in any analyses. However, these edge locations were used to calculate the location of the wall in the centre plane.

After the background images were processed, the droplet images were processed as outlined below.

- Each image is compared to the background image set. Individual pixels are considered to be objects when they are outside the range of intensities in the background set. The background image set is also shifted up to 3 pixels in the crosswise direction and 14 pixels in the stream-wise direction such that the number of object pixels is minimized. This accounts for minor drifting in the camera location.
- Pixels deemed to be background pixels in the previous step are removed from the image. A greyscale threshold is used to convert the remaining image to a binary format.
- To eliminate random noise, an erosion process is applied. Each pixel is given a score based on the number of neighbors it has, with a bonus given if a neighbor is completely surrounded. An illustration of the scoring system is shown in Figure 2.7. Pixels with a score of at least 3 are retained. Successive erosion operations are performed until the number of pixels being removed goes to zero.

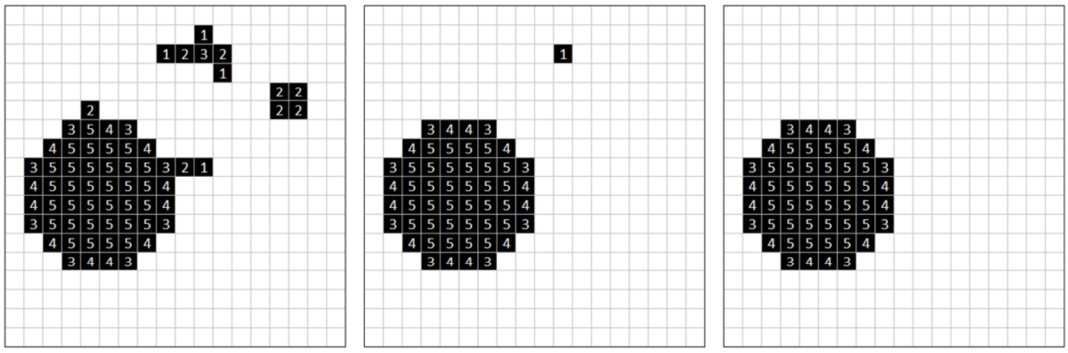

Figure 2.7. Illustration of erosion algorithm. Two erosion operations are performed.

- The remaining pixels are collected into objects using a flood-fill function. Objects with less than 20 pixels are considered to be noise and are eliminated. Objects equal to or larger than 20 pixels are retained in the final image. Their area, equivalent circular diameter, and centroid location are stored for further analysis.

Two important droplet metrics that were acquired from the processed images are the un-deformed diameter D and the incoming trajectory y_{inc}. These metrics were calculated as the averaged circular diameter and y-component of the centroid for five instances of the imaged droplet. Only instances of the droplet imaged at least 6.35 mm (0.5 H) upstream of the orifice were qualified to contribute to the calculation of D and y_{inc}. Droplets closer to the orifice started to deform and migrate toward the orifice opening.

2.4. Computational Methodology

The computational portion of this project was conducted in ANSYS Fluent v16.1. Fluent solves the finite volume form of the relevant transport equations in each cell of the spatially and temporally discretized domain. Due to the immense number of coupled equations (one equation per conserved property per cell), the calculations are conducted sequentially, with iterations required to converge the solution at each time step. The CFD methodology is outlined in the following subsections. For a more detailed discussion on CFD methodology, see Ko (2013) and the ANSYS Fluent Theory Guide (2015).

2.4.1. Governing Transport Equations

Ideally, for both laminar and turbulent flow scenarios, the flow field is governed entirely by the continuity equation, Navier-Stokes equations, and the boundary conditions. For the laminar flow scenarios, this mathematical formulation is sufficient (see Equations 1.1-1 and 1.1-2). However, for turbulent flows, a very fine level of discretization would be needed to resolve all of the turbulent eddies. This technique, named Direct Numerical Simulation (DNS), is currently impractical for many flows of interest. To improve the computational practicality for complicated flows, turbulence at some scales must be modelled instead of simulated.

The most commonly method for simulating turbulent flows is through the Reynolds-Averaged Navier-Stokes (RANS) equations. Reynolds suggested that an instantaneous field variable could be decomposed into a time- or ensemble-averaged component and a fluctuating component. After entering the Reynolds-decomposed pressure and velocity into the continuity and Navier-Stokes equations, the continuity and momentum equations can be averaged to produce the RANS equations as shown in Equations 2.4-1 and 2.4-2. The Reynolds-averaged and fluctuating components are denoted with angle brackets and apostrophes, respectively. The averaging of the equation eliminates many of the terms that included fluctuations, but the terms containing the product of fluctuations remain. These terms are called *Reynolds stresses*.

$$\nabla \cdot \overrightarrow{\langle u \rangle} = 0 \tag{2.4-1}$$

$$\rho \frac{\partial \overrightarrow{\langle u \rangle}}{\partial t} + \rho \overrightarrow{\langle u \rangle} \cdot \nabla \overrightarrow{\langle u \rangle} = -\nabla \langle P \rangle + \mu \nabla^2 \overrightarrow{\langle u \rangle} + \rho \vec{g} - \rho \nabla \cdot \langle u' u' \rangle \tag{2.4-2}$$

While the Reynolds stresses can be treated as conserved quantities (resulting in another six equations per cell), it is more common to use the Boussinesq approximation to model the Reynolds stress terms $-\rho\langle u'u' \rangle$ as a diffusion-like component $\mu_t(\nabla\langle u \rangle + \nabla\langle u \rangle^T)$, where μ_t is a scalar parameter called *eddy viscosity*. This eddy viscosity model presumes that the relationship between the Reynolds stress and the mean gradient of velocity fluctuations is strictly isotropic. In practice, however, the model results in good simulation performance for many general flows.

In this project, the eddy viscosity was calculated from the realizable k-ε equations, an improved form of the standard k-ε equations developed by Launder & Spalding (1974), where k is *turbulence kinetic energy* and ε is *turbulence dissipation rate*. The eddy viscosity is calculated as shown in Equation 2.4-3. The conservation equations for turbulence kinetic energy and turbulence dissipation rate are Equations 2.4-4 and 2.4-5, respectively. The model parameters C_1, C_2, C_μ, σ_k, and σ_ε have default constant or calculated values derived from benchmark scenarios.

$$\mu_t = \rho C_\mu \frac{k^2}{\varepsilon} \tag{2.4-3}$$

$$\rho \frac{\partial k}{\partial t} + \rho \nabla \cdot (ku) = \nabla \cdot \left[\left(\mu + \frac{\mu_t}{\sigma_k} \right) \nabla k \right] + \mu_t \dot{\gamma}^2 - \rho \varepsilon \tag{2.4-4}$$

$$\rho \frac{\partial \varepsilon}{\partial t} + \rho \nabla \cdot (\varepsilon u) = \nabla \cdot \left[\left(\mu + \frac{\mu_t}{\sigma_\varepsilon} \right) \nabla \varepsilon \right] + \rho C_1 \dot{\gamma} \varepsilon - \rho C_2 \frac{\varepsilon^2}{k + \sqrt{\mu \varepsilon / \rho}} \tag{2.4-5}$$

2.4.2. Boundary Conditions

All simulations have constant uniform velocity inlet conditions, with the velocity calculated from the inlet area and the desired volumetric flow rate.

The fluid velocity in wall-adjacent cells is typically modelled with a *wall function*. Wall functions are essentially semi-empirical formulas that predict velocity in wall-adjacent cells based on the local flow conditions and a wall-based coordinate (i.e., distance of the cell from the wall). They do greatly reduce the computational intensity of a simulation because the wall boundary layers do not need to be resolved. However, the accuracy of a wall function is reduced if the simulated flow conditions differ from the conditions for which the wall function was developed. Accuracy is also reduced if the centre of the wall-adjacent cell is either too close to or too far from the wall.

The current project utilizes *enhanced wall treatment*, an option in Fluent that eliminates the limitation on wall adjacent cells being too close to the wall. In addition to having a blended wall function for wall-adjacent cells, the remaining cells in the simulation are classified as either being fully turbulent or viscosity affected based on their wall Reynolds number $Re_{wall} \equiv \rho y_{wall}\sqrt{k}/\mu$, where y_{wall} is the wall-normal distance between the cell centre and the nearest wall. Cells in the fully turbulent region ($Re_{wall} > 200$) utilize the k and ε equations shown in the previous subsection. In the viscosity-affected region ($Re_{wall} < 200$), k and ε are calculated with modified parameters. First, the eddy viscosity is calculated as per

the one-equation model of Wolfshtein (1969). The turbulence diffusion length scale comes from Chen & Patel (1988), and the blending function suggested by Jongen (1988) eliminates the discontinuity in eddy viscosity at Re_{wall} = 200. Second, the turbulence dissipation rate is calculated algebraically as $\varepsilon = k^{1.5}/l_{\varepsilon}$, where l_{ε} is the turbulence dissipation length scale from Chen & Patel (1988).

2.4.3. Discretization and Solution Methods

The following numerical methods were used to discretize and solve the finite volume transport equations.

- Pressure-velocity coupling is a class of techniques that replaces the mass fluxes in the continuity equation with a function of pressure and velocity. This allows pressure to be calculated from the continuity equation. The current project uses the Pressure-Implicit with Splitting of Operators (PISO) algorithm.
- Cell-centre gradients are evaluated using least-squares method. The relationship between the cell-centre gradient of transport property ϕ would ideally be calculated as $\nabla\phi_{cc} \cdot \Delta x_{n,i} = \phi_{n,i} - \phi_{cc}$, where Δx is the vector from the cell centre to the neighbour cell centre and the subscript *n,i* denotes the i^{th} neighbour cell. However, with six neighbours, the system applied to a hexahedral cell is over-constrained, so the cell-centre gradient is calculated to minimize the square of the residuals of the six equations.

- A second-order central differencing scheme is used to calculate pressure at each cell face. It is essentially an average of the two adjacent cell centre pressures plus a correction for the pressure gradients in each cell.
- The advective terms in the momentum, turbulence kinetic energy, and turbulence dissipation rate equations were discretized with the second-order upwind scheme. This scheme evaluates the flux at a face based on the flow field variable and gradient in the upwind cell only.
- The diffusive terms, requiring the gradient of transport property ϕ at the cell face, are represented with second-order central differencing.
- For the transient solver simulations, the second-order implicit temporal discretization scheme was used. The scheme utilizes the flow field at the previous and current time steps to calculate the flow field at the next time step.

2.4.4. Measures for Convergence and Fully-Developed Flow

For the open channel simulations presented in Section 3.1, the steady-state solver was used. For this solver, the residuals are a measure of the degree to which the simulation's flow field has converged. For this project, the steady-state solver flow field was considered to be converged when the residuals reached 10^{-5} for the continuity equation and 10^{-6} for the momentum, turbulence kinetic energy, and the turbulence dissipation rate equations.

Despite being interested in steady-state solutions only, the inlet manifold and slit orifice simulations were solved using the transient solver. The steady-state solver could not resolve the separated and recirculating flows generated at the sharp corners of the inlet and orifice. *Time step convergence* was considered to be achieved when the residuals were less than 10^{-4} for the continuity equation and 10^{-5} for the momentum, turbulence kinetic energy, and turbulence dissipation rate equations. However, it should be noted that these residuals alone are insufficient in for determining whether the flow field has converged.

To determine *flow field convergence* of a steady-state flow, the flow field at different time steps must be compared. To establish when this occurs, it is necessary to calculate the relative difference between flow fields at two different time steps. For each simulation, a variety of interrogation lines for evaluating flow field convergence were created (the locations of these interrogation lines are discussed in the Sections 3.1.1 and 3.2.2). For each cell in the interrogation line, the relative difference was calculated as shown in Equation 2.4-6, where ϕ is the flow field variable of interest. Ideally, a flow field is converged when the relative difference reaches zero for all flow field variables for all cells; in practice, a relative difference of zero cannot be reached in any practical computational time. For this work, the flow field was judged to be converged when the average of these relative differences in stream-wise (z) velocity across the interrogation lines was less than 2%.

$$\Delta\phi_{rel} = \frac{|\phi_2 - \phi_1|}{\phi_1} \times 100\% \quad (2.4\text{-}6)$$

For the inlet manifold simulations presented in Section 3.1.3, the distance from the origin at which fully-developed flow was achieved could be determined only once the flow field had converged. The same types of interrogation lines used to determine flow field convergence were also used to evaluate the progression to fully-developed flow. The flow field was judged to have fully developed when the relative average difference in stream-wise (z) velocity at that position compared to the fully-developed open channel profile (developed in Section 3.1.2) was less than 2%.

2.4.5. Dispersed Phase Modelling

The dispersed phase model (DPM) in Fluent was used at its most basic level to conduct a limited investigation of droplet lateral migration in the turbulent flow experiments (refer to Section 4.2.3 for details). The DPM technique calculates the motion of a chemically-inert spherical particle of given density and diameter caused by the surrounding fluid. The particle itself exerts no physical or dynamic influence on the surrounding continuous phase, so this technique is only suitable for relatively small particles. In addition, the particle is not deformable. These conditions minimize the time required to compute the trajectory but produce a result that should be considered qualitative only when applied to the deformable droplets in the current study.

3. Channel, Inlet, and Orifice Flows

This chapter presents details for the two major computational aspects of this work: (1) the design of the inlet manifold and upstream sections, particularly with regard to the entry length needed to fully develop both turbulent and laminar flows, and (2) simulations of the flow field (laminar flows) or mean flow field (turbulent flows) in the vicinity of the orifice at the operating conditions listed in Table 2.2. These flow fields will be combined with experimental data to develop trajectory-dependent break-up criteria in Chapters 4 and 5. These studies are discussed in Sections 3.1 and 3.2, respectively.

Note that all of these simulations include only the continuous phase. Because the droplets studied in this project were injected one at a time and were significantly smaller than the length scale of the channel, their effect on the flow patterns in the channel and orifice was expected to be negligible.

3.1. Channel Design Simulations

The channel was designed to accommodate a maximum channel Reynolds number Re_{ch} of 1,000 (based on superficial velocity and hydraulic diameter of the open channel) with CO70FG as the continuous phase. This was intended to ensure that the open channel flow was laminar, being well below the limit for laminar flow at Re_{ch} = 2,800 (Hanks & Ruo, 1966). With the 8:1 cross-section of the open channel and an early estimation of the viscosity (μ_c = 0.0242 Pa-s), the design superficial

velocity was 1.1 m/s. For an equivalent flow rate of water, the corresponding channel Reynolds number was 28,000. The primary goal of the channel design simulations was to quantify the entry length needed to fully develop both of these flows (laminar flows of CO70FG at Re_{ch} = 1,000 and turbulent flows of water at Re_{ch} = 28,000) specific to the channel and inlet geometries.

3.1.1. Simulation Geometries and Details

To establish the required entry length, two stages of simulations were needed. First, simulations were conducted for a long open channel with an 8:1 cross-section. Second, simulations were conducted for a variety of inlet geometries to determine the entry length. The open channel simulations were helpful at this second stage to interpret the distance at which fully-developed flow had been reached because the velocity profile at the span-wise centre plane of the 8:1 cross-section could not be modelled as a parallel plate flow. In both stages, the total inlet flow rate for both the turbulent and laminar flow simulations was 1.4 x 10^{-3} m^3/s, corresponding to the 1.1 m/s open channel design velocity.

For the open channel simulations (both turbulent and laminar scenarios), the domain consisted of a simple rectangular channel with a length of 1.14 m long in the stream-wise (z) direction and a cross-section of 12.7 mm x 102 mm. (y and x directions, respectively). Scaled with H = 12.7 mm, the domain is 90 H x 1 H x 8 H. These dimensions are illustrated in Figure 3.1. The origin is located at the centre of the constant velocity inlet boundary. The mesh consisted of approximately 600,000

hexahedral cells. Due to the lack of flow separation, the simulation could be completed with Fluent's steady-state solver.

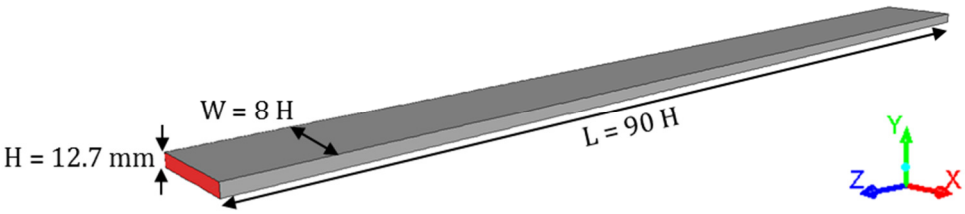

(a) Geometry for open channel simulations

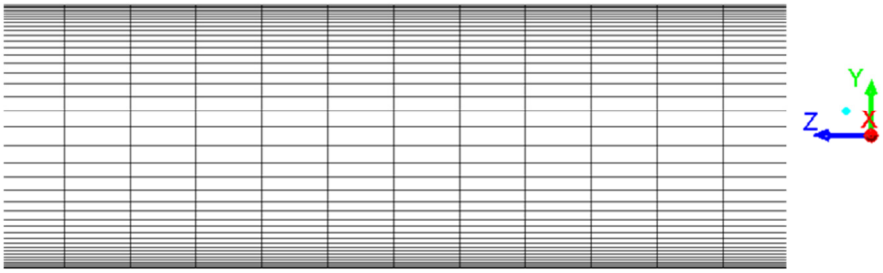

(b) Computational mesh for open channel simulations

Figure 3.1. Geometry and mesh configuration for the open channel simulations. Origin is centre of inlet entrance.

For the inlet manifold simulations, a number of preliminary inlet geometries were simulated to explore the impact of changing the number of inlet tubes and the length and orientation of interior baffles. Having larger tubes to reduce inlet velocity and/or a greater quantity of tubes to provide more even distribution resulted in shorter entry lengths. Baffles also helped to reduce entry lengths. Based on these simulations and some practical concerns regarding attachment of the supply hoses to the inlet section, the inlet manifold geometry illustrated in Figure 3.2 was selected for more detailed analysis. As-built drawings of the inlet are also shown in Appendix A. The flow was supplied through four 22-mm diameter tubes

(nominal 1" diameter tubes). A baffle splits the inlet manifold at the span-wise centre plane and also extended 127 mm (10 *H*) into the channel.

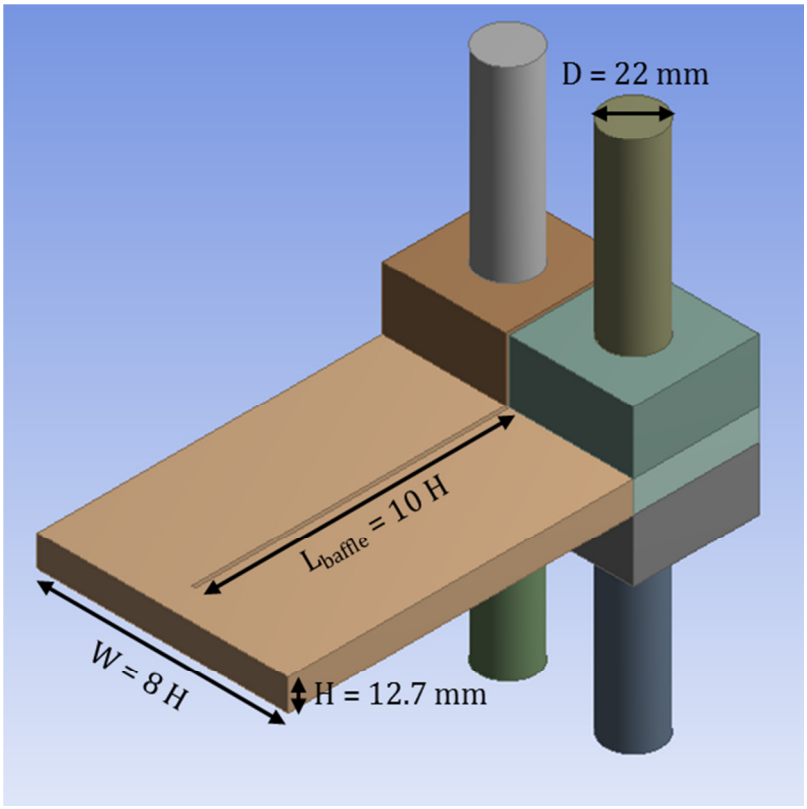

Figure 3.2: Inlet manifold geometry for detailed study.

Figure 3.3 shows the full domain of the entry length simulation in Fluent, which includes both the inlet manifold (see Figure 3.2) in light grey and an open channel with a length of 150 H (1.9 m) in dark grey. The inset shows the origin located at the centre of the channel's cross-section at the interface between the inlet manifold and open channel. The mesh, used for both the turbulent and laminar flow simulations, was comprised of 1.4 million hexahedral cells. Sections of the mesh at the inlet manifold are presented in Figure 3.4.

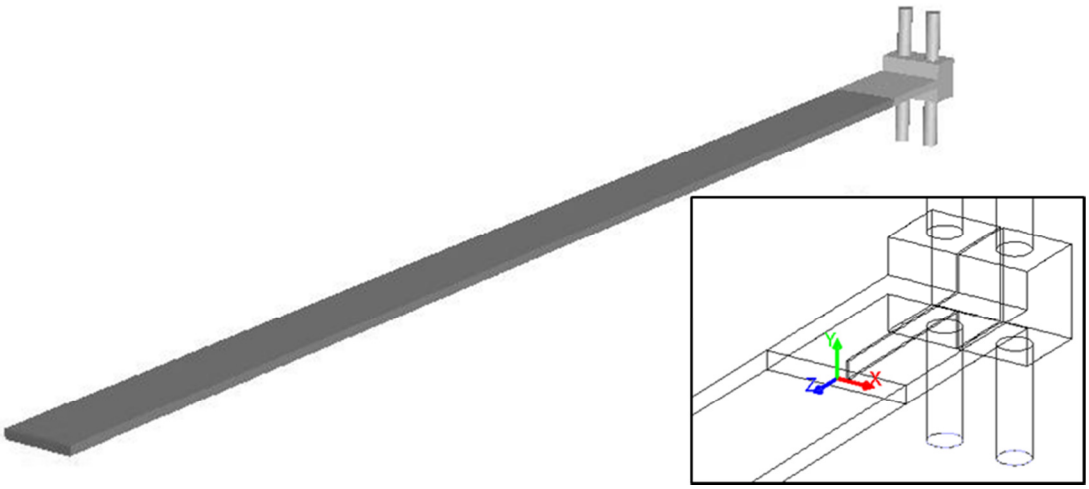

Figure 3.3: Domain for inlet manifold simulations. Inset shows the location of the origin.

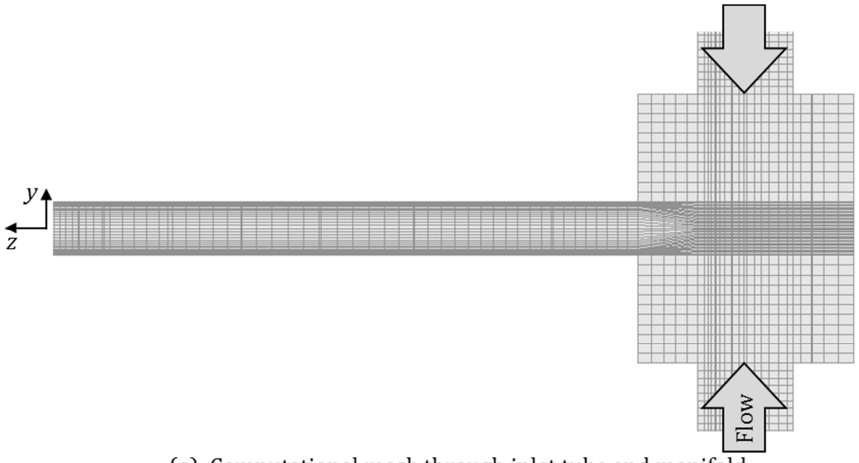

(a) Computational mesh through inlet tube and manifold.

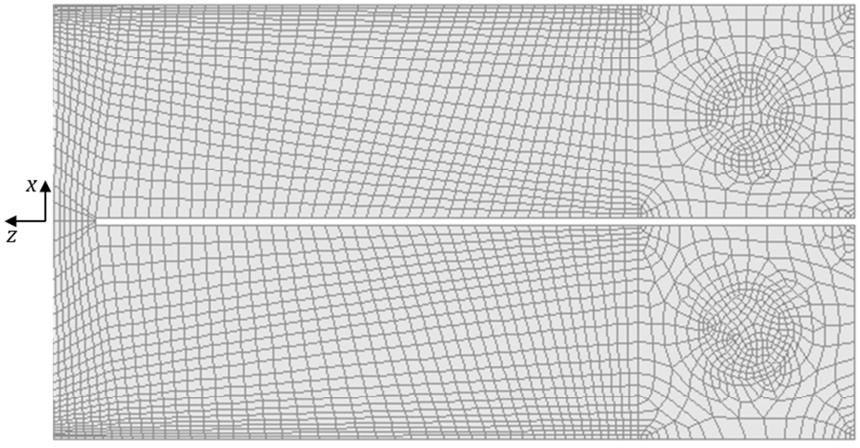

(a) Computational mesh at through span-wise centre plane (x = 0)

Figure 3.4. Computational mesh for the inlet geometry simulations.

The interrogation lines for determining convergence of the flow field and progression to the fully developed flow state (refer to Section 2.4.4 for methodology) for the design simulations are shown in Figure 3.5. These lines are drawn at selected stream-wise (z) positions that are listed with each simulation.

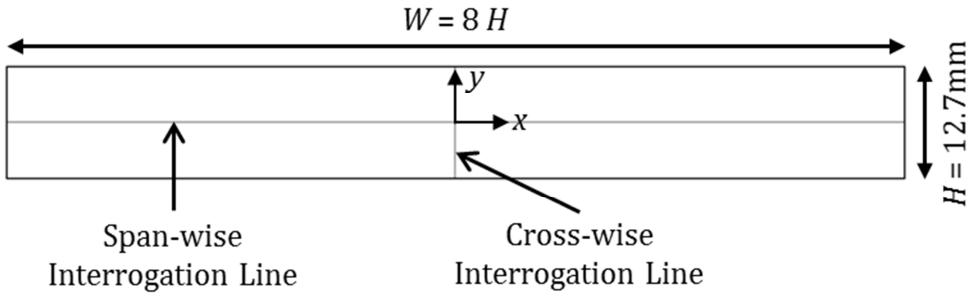

Figure 3.5: Cross-section of open channel, with cross-wise and span-wise interrogation lines in dark grey.

3.1.2. Open Channel Simulation Results

To reach the steady-state solver residual targets discussed in Section 2.4.4, the turbulent and laminar simulations required 600 and 400 iterations, respectively. It was initially assumed that the stream-wise (z) velocity profiles toward the end of the flow domain would be fully developed. To verify this, the interrogation lines shown in Figure 3.5 were drawn at z = 70 H (0.889 m) and z = 80 H (1.02 m). The average relative difference in the stream-wise (z) velocities between these two sets of velocity profiles was 0.2% and 0.1% for the turbulent and laminar flow simulations, well below the 2% threshold for fully-developed flow.

The fully-developed stream-wise (z) velocity profile (taken at z = 80 H) along the cross-wise direction (y) at the span-wise centre plane (x = 0) for the turbulent

flow open channel RANS simulation is shown in Figure 3.6. This velocity profile was symmetric about $y = 0$, so only the positive-y domain is shown. The velocities are normalized by the superficial channel velocity U_{ch} = 1.1 m/s, and the cross-wise coordinate is normalized by the channel width H = 12.7 mm. Note that the average velocity along this line is 1.14 m/s (about 4% higher than the superficial channel velocity U_{ch}.).

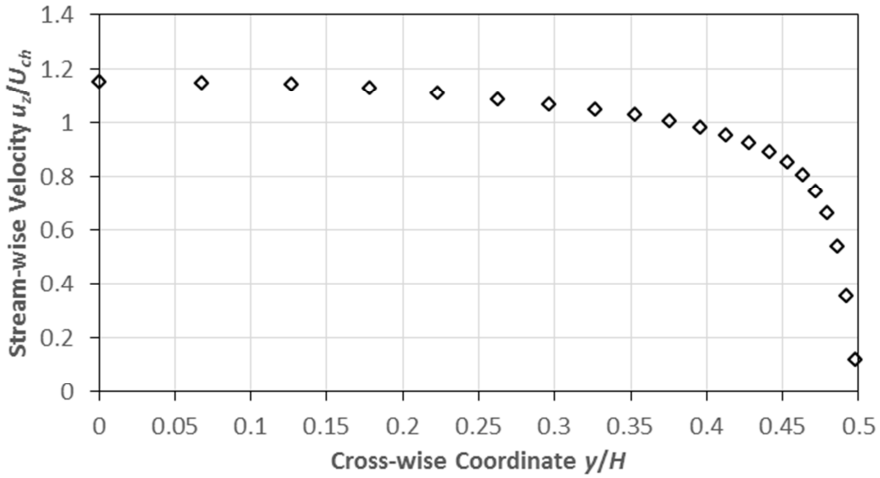

Figure 3.6: Fully-developed stream-wise (z) velocity profile (at $z = 80\ H$) along cross-wise direction y for the turbulent flow open channel RANS simulation.

The fully-developed stream-wise (z) velocity profile (taken at $z = 80\ H$) along the span-wise direction (x) at the cross-wise centre plane ($y = 0$) for the turbulent flow open channel RANS simulation is shown Figure 3.7. This velocity profile was symmetric around $x = 0$.

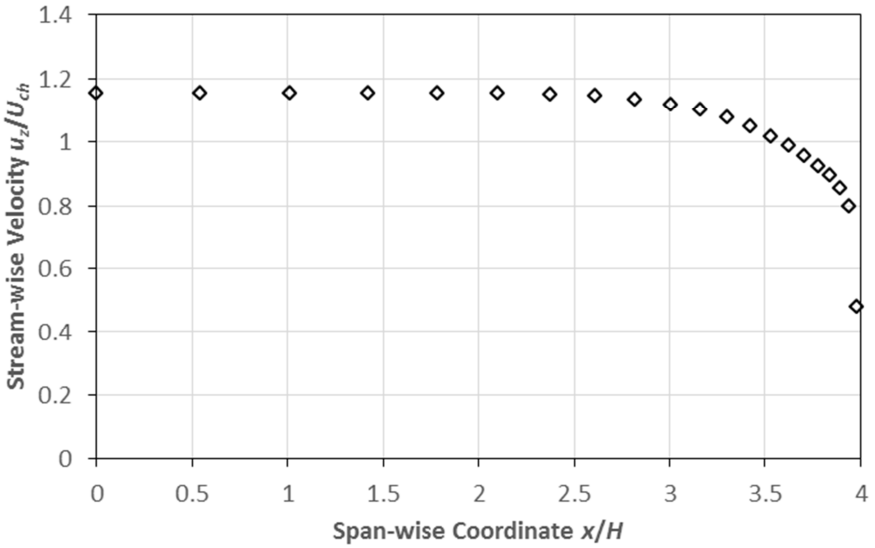

Figure 3.7: Fully-developed stream-wise (z) velocity profile (at z = 80 H) along span-wise direction x for the turbulent flow open channel RANS simulation.

For the laminar flow open channel simulation, the fully-developed stream-wise (z) velocity profile (taken at z = 80 H) along the cross-wise (y) direction at the span-wise centre plane (x = 0) is shown in Figure 3.8. This velocity profile was symmetric around y = 0. The results of the CFD simulation are shown with the open diamond markers. The solid line is the analytically-predicted velocity profile for flow between parallel plates based on the design channel velocity (U_{ch} = 1.1 m/s). The analytical velocity profile was lower than the simulated profile, indicating that the velocities in the centre were increased by the close proximity of the side walls. The simulated velocity profile can instead be modelled using the average velocity along the cross-wise (y) direction at the span-wise centre plane (x = 0) of 1.18 m/s, which is higher than the superficial channel velocity by about 7%.

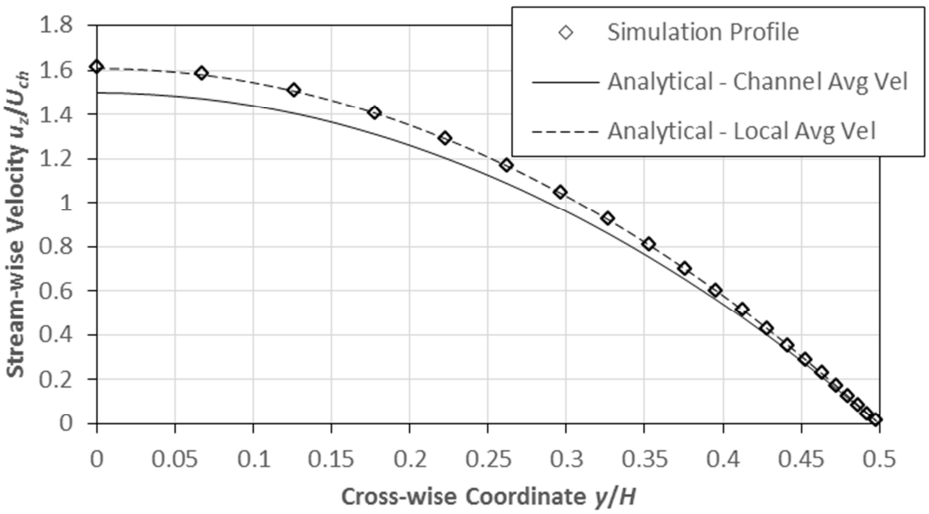

Figure 3.8: Fully-developed stream-wise (z) velocity profile (at z = 80 H) along the cross-wise direction y for the laminar flow open channel scenario. Analytical predictions are based on the channel average (superficial) and local average velocities.

The fully-developed laminar stream-wise (z) velocity profile (taken at z = 80 H) along the cross-wise (y) direction at the span-wise centre plane (x = 0) is shown in Figure 3.9. This velocity profile was symmetric around x = 0.

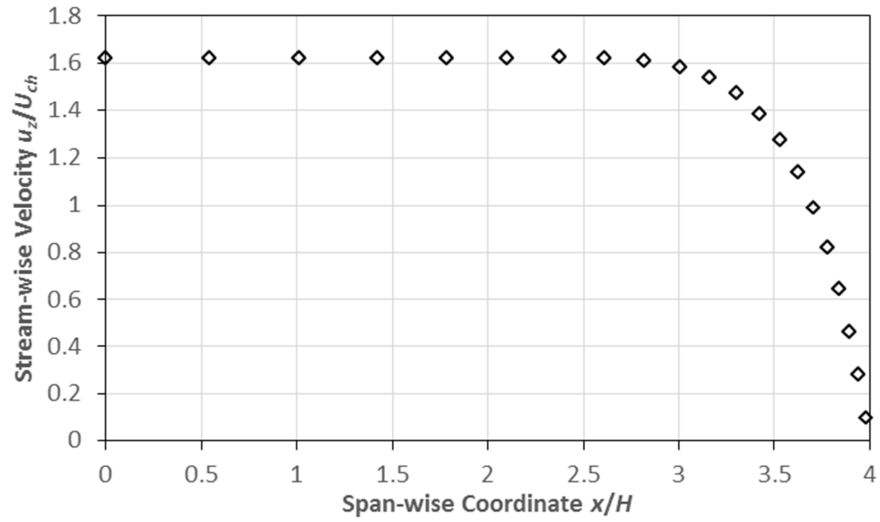

Figure 3.9: Fully-developed stream-wise (z) velocity profile (at z = 80 H) along the span-wise direction x for the laminar flow open channel simulation.

3.1.3. Inlet Manifold Simulation Results

Both turbulent and laminar flows through the inlet manifold were simulated with a 0.0005 second time step, a moderately-refined time step that limits the CFL number ($U\Delta t/\Delta x$, where U is the velocity in the cell, Δt is the time step size, and Δx is the cell size) to less than 0.5 in a majority of each domain. However, the turbulent flow simulation had some problems in reaching the desired time step convergence targets. The cross-wise (y) velocity and turbulence kinetic energy residuals reached plateaus at 1.2×10^{-5} and 1.5×10^{-5}, respectively. A simulation at a lower time step should produce better results, but for the purposes of determining the entry length, the simulation was judged to be adequate. The laminar inlet manifold simulation met the time step targets without any difficulty.

Interrogation lines for determining flow field convergence (see Figure 3.5) were drawn at z = {50 H, 90 H, 130 H} for both turbulent and laminar flow simulations. The average relative difference for the stream-wise (z) velocity profile for these interrogation lines was found to be 0.02% over 1,000 time steps (0.5 seconds) for the turbulent flow simulation and 1.7% over 1,000 time steps for the laminar flow simulation, meeting the 2% flow field convergence target.

To determine the entry length, the interrogation lines shown in Figure 3.5 were drawn every 10 cm. The computed average relative difference between the interrogation line velocity profiles and the fully-developed open channel profiles (developed in Section 3.1.2) are presented in Table 3.1. The criteria for fully-developed flow (relative difference less than 2%, as discussed in Section 2.4.4) was

first met for both flow scenarios at z = 0.90 m = 71 H, so ***the entry length for this device was taken to be 0.90 m***.

Table 3.1. Determination of entry length for the inlet manifold simulations.

Flow Regime	**Average Relative Difference between Velocity Profiles at z and Fully-Developed Open Channel Profiles**			
	z = 0.7 m (63 H)	**z = 0.8 m (63 H)**	**z = 0.9 m (71 H)**	**z = 1.0 m (79 H)**
Turbulent (Re_{ch} = 28,000)	**2.6%**	**2.1%**	1.7%	1.4%
Laminar (Re_{ch} = 1,000)	**3.5%**	1.7%	1.2%	0.9%

3.2. Slit Orifice Flow Field

In high Reynolds number flows through a slit orifice, the non-intuitive flow feature is that the orifice jet does not stay centred within the channel. Any deviation in the symmetry of the jet, whether caused experimentally or numerically, will cause the jet to lean as shown in Figure 3.10. This reduces the size of one of the wake regions but also increases the speed within that wake, leading to a reduction in pressure on that wake region. On the other side of the jet, the wake region becomes enlarged and slower, leading to an increase in pressure. The pressure differential across the jet sustains its asymmetry and is generally known as the Coandă effect (Wille and Fernholz, 1965).

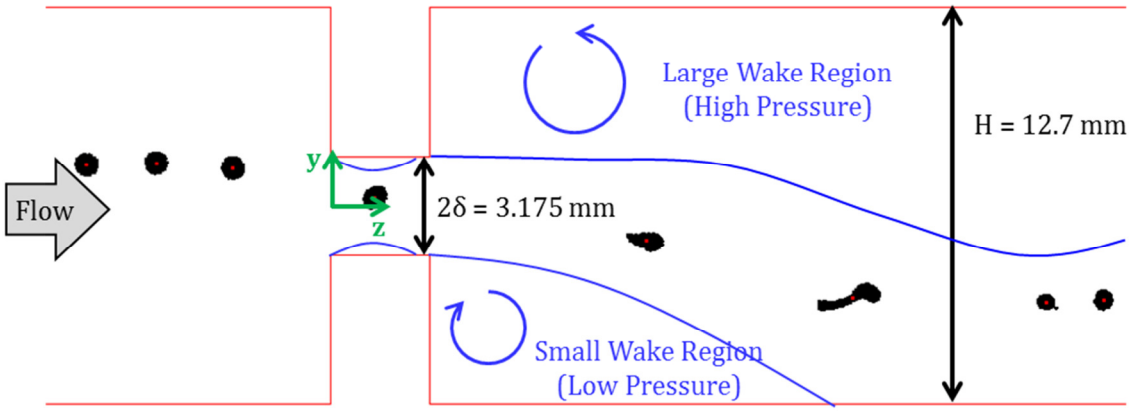

Figure 3.10. Jet leaning due to the Coandă effect. Coordinate convention for the CFD simulations is also shown.

3.2.1. Planar Sudden Expansion and Orifice Flow Literature

Despite the geometric symmetry, flows through planar sudden expansions and planar orifices, illustrated in Figure 3.11, can produce either symmetric or asymmetric flows, depending on the expansion ratio and the Reynolds number. For low Reynolds numbers, the planar jet from a symmetric sudden expansion is symmetric. At higher Reynolds numbers, the jet can lean in either direction, form different numbers of recirculation zones behind the orifice, and exhibit transient behaviour.

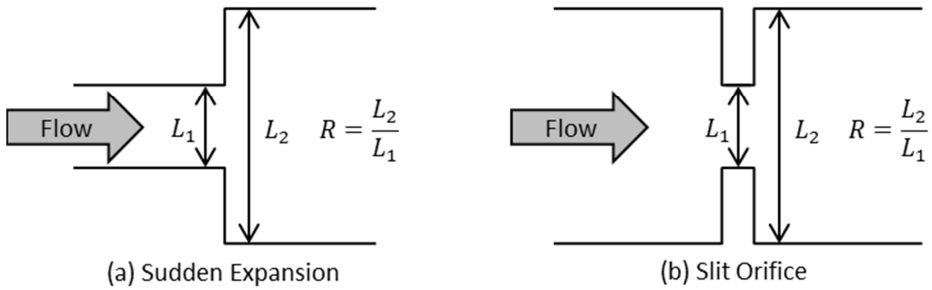

Figure 3.11. Illustration of (a) sudden expansion and (b) slit orifice geometries. The expansion ratio is denoted as R.

For laminar flows, a great deal of experimental data has been acquired. For a 3:1 sudden expansion with an undeveloped inlet velocity profile, Durst *et al.* (1974) showed that the flow became asymmetric at a Reynolds number between 75 and 150 using laser-Doppler anemometry measurements. Cherdron *et al.* (1978) advanced the Durst *et al.* (1974) study by developing a regime plot relating asymmetry to expansion ratio, cross-section ratio, and Reynolds number. Fearn *et al.* (1990) conducted a similar study as Durst *et al.* (1974) study, but with a fully-developed inlet velocity profile. The flow became asymmetric at a Reynolds number of approximately 90. They also observed that the flow preferentially attached to one side of the channel; attachment to the other side could only be achieved if the flow was immediately started at a Reynolds number greater than 125. In addition, their work identified a third recirculation region on the same wall as the small wake region at a Reynolds number of 330. A 2:1 sudden expansion with fully-developed incoming velocity profile was studied by Durst *et al.* (1993), with the flow becoming asymmetric at a Reynolds numbers of about 170.

Numerical methods have also been used to examine laminar sudden expansion and orifice flows. Sobey and Drazin (1986) used bifurcation theory to show a pitchfork bifurcation occurs at some point, with the branches of the pitchfork associated with the two asymmetric flow solutions. At higher Reynolds numbers, they identified eight asymmetric stable solutions and found evidence that another seven unstable solutions may exist. Fearn *et al.* (1990) solved the 2-D Navier-Stokes equations for the 3:1 sudden expansion, with the asymmetric flow solutions occurring first at a Reynolds number of 110 (compared to 90 and 125,

experimentally). They show a similar pitchfork bifurcation as Sobey and Drazin (1986). The linear stability analysis conducted by Shapira *et al.* (1990) for 2:1 and 3:1 expansions identified the critical Reynolds numbers as 290 and 110, respectively. Durst *et al.* (1993) also solved the 2-D equation for the 2:1 sudden expansion; their numerical estimation of the bifurcation point matched the experimental observation well. Battaglia *et al.* (1997) found a critical Reynolds number of approximately 100 from their 2-D simulations of a 3:1 sudden expansion. The 2-D simulations of Drikakis (1997) for expansion ratios from 2:1 to 10:1 resulted in critical Reynolds numbers ranging from 160 to 20 (the critical Reynolds number for a 4:1 expansion ratio was 40). Hawa and Rusak (2001) conducted a variety of numerical analyses to examine the dynamic behaviour of the flow as it approached the critical Reynolds number from either side.

An expansion followed by a contraction can serve to re-stabilize the symmetric condition. Mizushima *et al.* (1996) simulated a number of 2-D 3:1 expansion-contraction systems using a stream function and vorticity formulation. With an aspect ratio (distance to contraction divided by expansion ratio) less than 3, the critical Reynolds number increases, but a second higher critical Reynolds number can also be found where the flow returns to a symmetric condition. A third level aspect-ratio dependent Reynolds numbers, where the flow transitions from the symmetric condition to a periodic condition, were also identified. Mullin *et al.* (2003) conducted a similar study with both computational and experimental methods, but also considered a range out outlet sizes.

Turbulent flow through planar sudden expansions have also been studied, but less extensively. Abbott and Kline (1962) conducted one of the earliest studies, demonstrating that the flow was asymmetric at high Reynolds numbers. De Zilwa *et al.* (2003) demonstrated a good match between experimental measurements and numerical calculations at a Reynolds number of 35,000. Escudier et al. (2002) studied turbulent flow through a sudden expansion of 4:1. The flow was shown to be three-dimensional, and the authors cautioned that good agreement between two-dimensional simulations and experiments does not mean the third dimension is not important. They infer that there are counter-rotating vortices, one in the upper and one in the lower recirculation region.

One of the few articles on turbulent flows through a slit orifice is the work of El Khoury *et al.* (2003). A 25-million cell Direct Numerical Simulation (DNS) was used to simulate a 50% open slit orifice at an open channel Reynolds number of approximately 11,000. The simulation showed that the turbulent orifice flow was similar to the expansion in that the orifice jet leaned to one side. The smaller wake region was somewhat longer than one channel height.

3.2.2. Simulation Geometry and Mesh

The 3-D simulations included the orifice itself and open channel 100 *H* (1.27 m) before and 30 *H* (0.38 m) after the orifice. The simulation geometry is illustrated in Figure 3.12. The additional length was present to minimize boundary condition influences on the flow near the orifice. The inlet boundary condition was a constant,

uniform velocity, and the outlet was at a constant pressure. The main computational mesh was comprised of 1.4 million hexahedral cells. The upstream and downstream regions were relatively coarse, while the central regions near the orifice were the most highly refined. Figure 3.13 shows the density of the computational mesh near the orifice at the centre plane. There are 30 cells across the orifice in both the stream-wise (z) and cross-wise (y) directions.

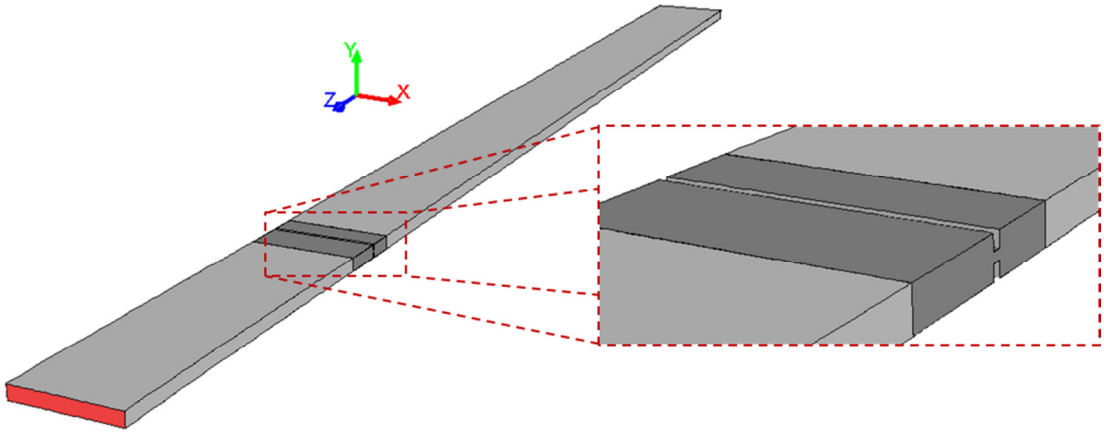

Figure 3.12. Geometry for slit orifice simulations.

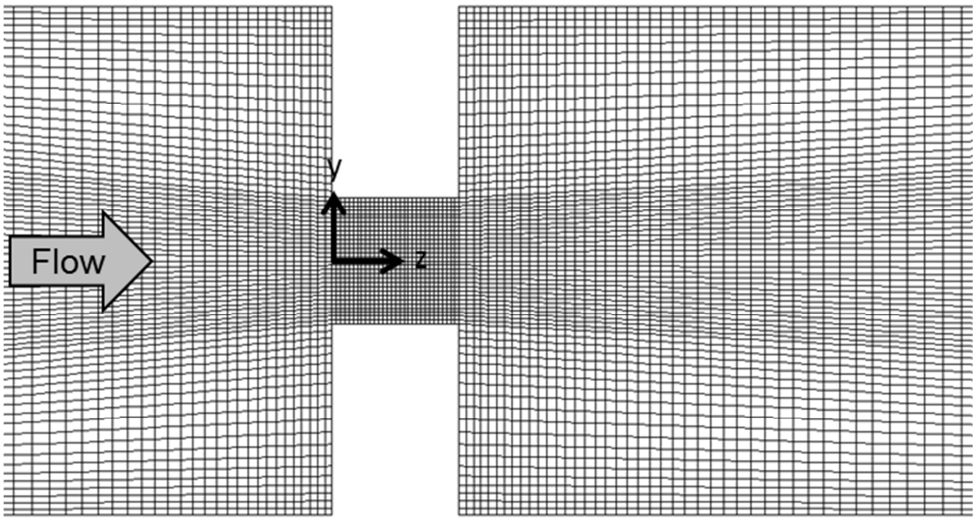

Figure 3.13. Computational mesh at the span-wise centre plane of orifice simulation. The full computational mesh is not shown.

3.2.3. Turbulent Orifice Flow Simulation Results

Each of the turbulent flow conditions in Table 2.2 was simulated using the RANS turbulence model in Fluent. The first three scenarios (Re_{ch} = 7,700 to 14,000) were conducted using the computational mesh discussed in Section 3.2.2. The final scenario (Re_{ch} = 19,000) required additional mesh refinement in the orifice and in the region immediately downstream; the mesh adaption function in Fluent was used to increase the simulation to a total of 3.2 million cells. A time step of 0.0002 seconds was used for all simulations. Flow field convergence was evaluated based on the average relative difference of stream-wise velocity over eighteen cross-wise interrogation lines, spread upstream and downstream of the orifice. Unfortunately, small changes in the jet position occurred over time, leading to high relative differences for cells located at the edge of the jet. To eliminate these influences on the convergence calculation, only velocities greater than 1% of the superficial orifice velocity were included. The average relative difference in stream-wise velocity or each simulation was less than 1%.

The centre plane mean velocity vectors, based on the RANS equations, for each of the four turbulent flow operating scenarios are shown in Figure 3.14. The vector colour is based on the velocity magnitude scaled with either the superficial open channel velocity or the superficial orifice velocity. To improve vector visibility, one quarter of the vectors are displayed for Re_{ch} = 7,700 to 14,000, while one in nine vectors are displayed for Re_{ch} = 19,000. The jet behaviour was as expected, with a lean occurring to one side for all Reynolds numbers. The extent of the small wake

region occurs 1 H (H = 8δ = 12.7 mm) from the downstream surface of the orifice. The similarity in the colours and flow patterns of the vectors indicate that the scaled velocity field is not strongly dependent on channel Reynolds number.

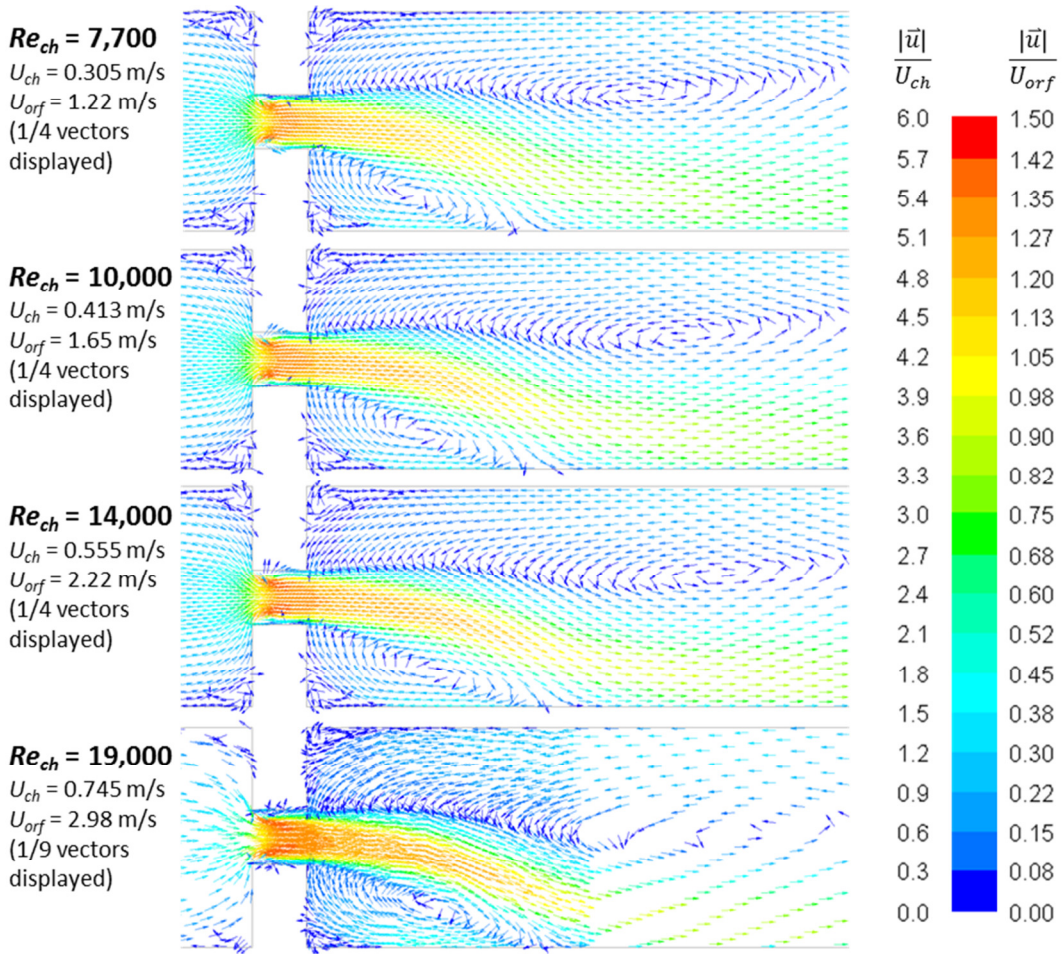

Figure 3.14. Velocity vectors at the centre plane coloured by velocity magnitude for the turbulent flow scenarios.

Figure 3.15 shows experimental evidence supporting the Reynolds-number independence of the turbulent jet. The first two panels show streamlines from FD&C Red #3 dye injected through the injection port at Re_{ch} = 3,400 and 7,100. The last panel shows the capture of bubbles in both wake regions for Re_{ch} = 37,000. These images were taken using the Pulnix camera with the strobe providing a single

flash per frame. Despite the ten-fold change in channel Reynolds number, the extent of the small wake region appears to be very similar. The small wake region is similar in all frames in the image series, indicating that the jet does not display any significant transient behaviour.

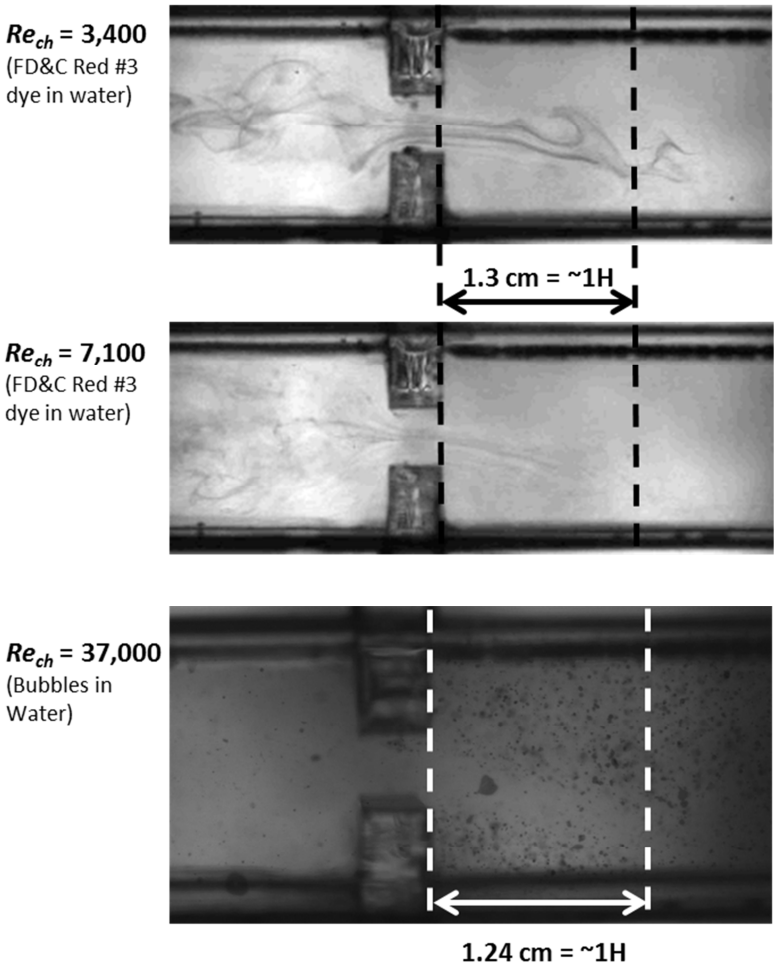

Figure 3.15. Experimental dye and bubble images to illustrate small wake region length as a function of channel Reynolds number Re_{ch}.

Figure 3.16 compares the magnitude of the strain rate tensor (referred to as strain rate magnitude) at the centre plane for the four operating scenarios as contour plots. The limits of the plots are scaled with the channel Reynolds number

Re_{ch}. Values beyond the limits are clipped from view. As with the velocity vectors shown in Figure 3.14, the strain rate magnitude generally scales well with velocity. Only minor differences in the shape and size of the contours are evident.

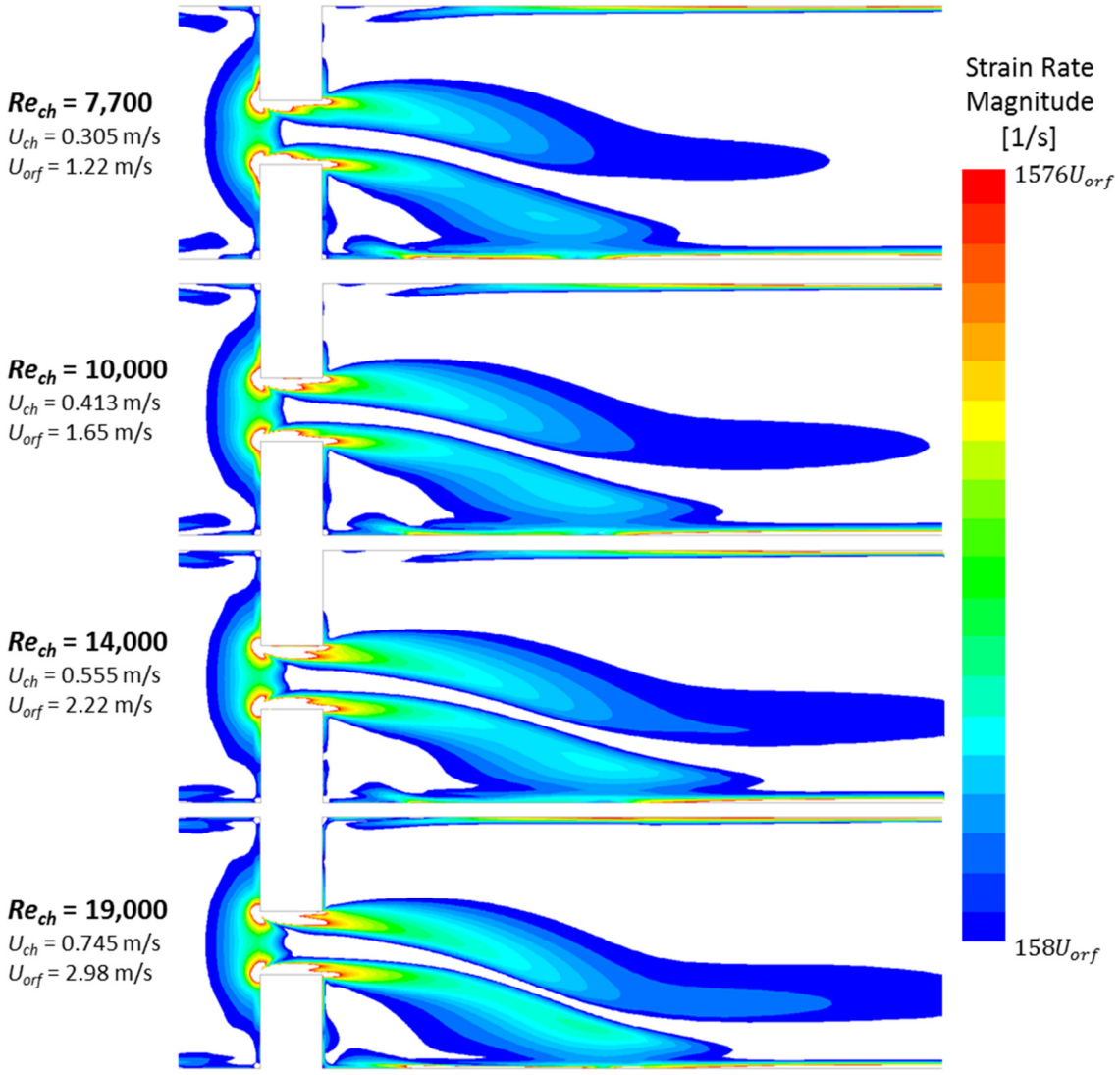

Figure 3.16. Contours of strain rate magnitude at the centre plane for the turbulent flow scenarios. The limits of the colour bar are set to scale with U_{orf} (in m/s) to emphasize the relative similarity of the fields from all four simulations.

Appendix B includes contour comparisons for shear rate, extensional rate, turbulence kinetic energy, and turbulence dissipation rate. Shear and extensional

rates do scale well with the channel Reynolds number. However, the turbulence kinetic energy and turbulence dissipation rate scale only moderately well with the square and cube of velocity, respectively.

3.2.4. Laminar Orifice Flow Simulation Results

3-D laminar flow simulations of the orifice with either CO70FG or CO200FG (20 or 80 cP, respectively) as the continuous phase were conducted with Fluent using a time step of 0.0001 seconds. Four scenarios with CO70FG as the continuous phase (Re_{ch} = 240 to 600) and two scenarios with CO200FG as the continuous phase (Re_{ch} = 110 and 240) were conducted using the computational mesh discussed in Section 3.2.2. The same method for establishing flow field convergence in the turbulent flow scenarios was also used in the laminar flow scenarios, with a maximum average relative difference in stream-wise velocity of 1% being achieved in all simulations except for the CO70FG Re_{ch} = 450 simulation, which reached a minimum of 4%.

The centre plane velocity vectors and strain rate magnitudes for each of the six laminar operating scenarios are shown in Figure 3.17 and Figure 3.18, respectively. Additional results for shear rate and extensional rate are in Appendix B. As with the turbulent flow scenarios, these properties scale well with superficial velocity. However, the length of the small wake region increases slowly with Re_{ch}, resulting in a minor change in the direction of the jet. This agrees qualitatively with

the findings in Battaglia *et al.* (1997), which show increasing wake region length for sudden expansions of other aspect ratios (3:1 and 5:1).

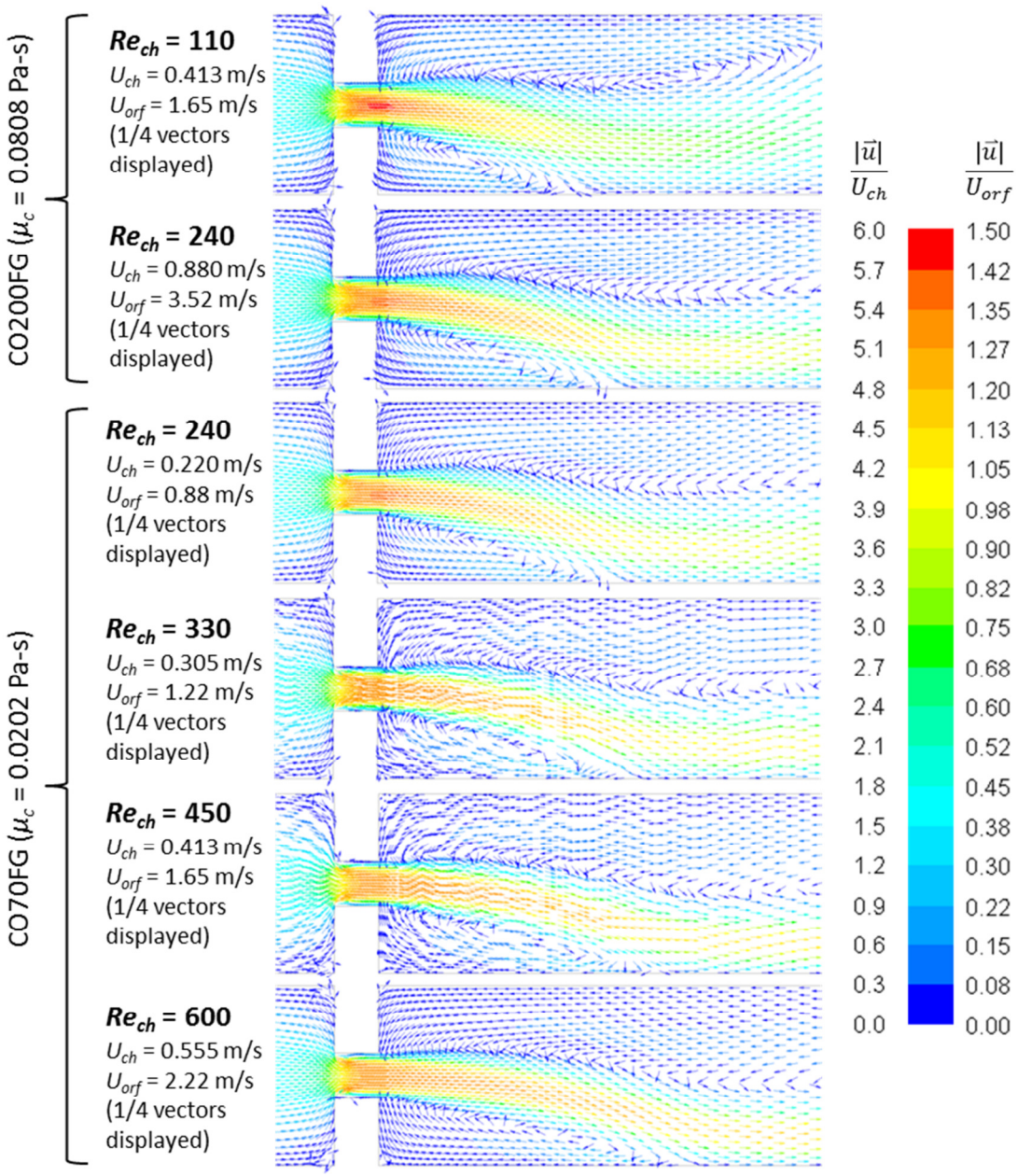

Figure 3.17. Velocity vectors at the centre plane coloured by velocity magnitude for the laminar flow scenarios.

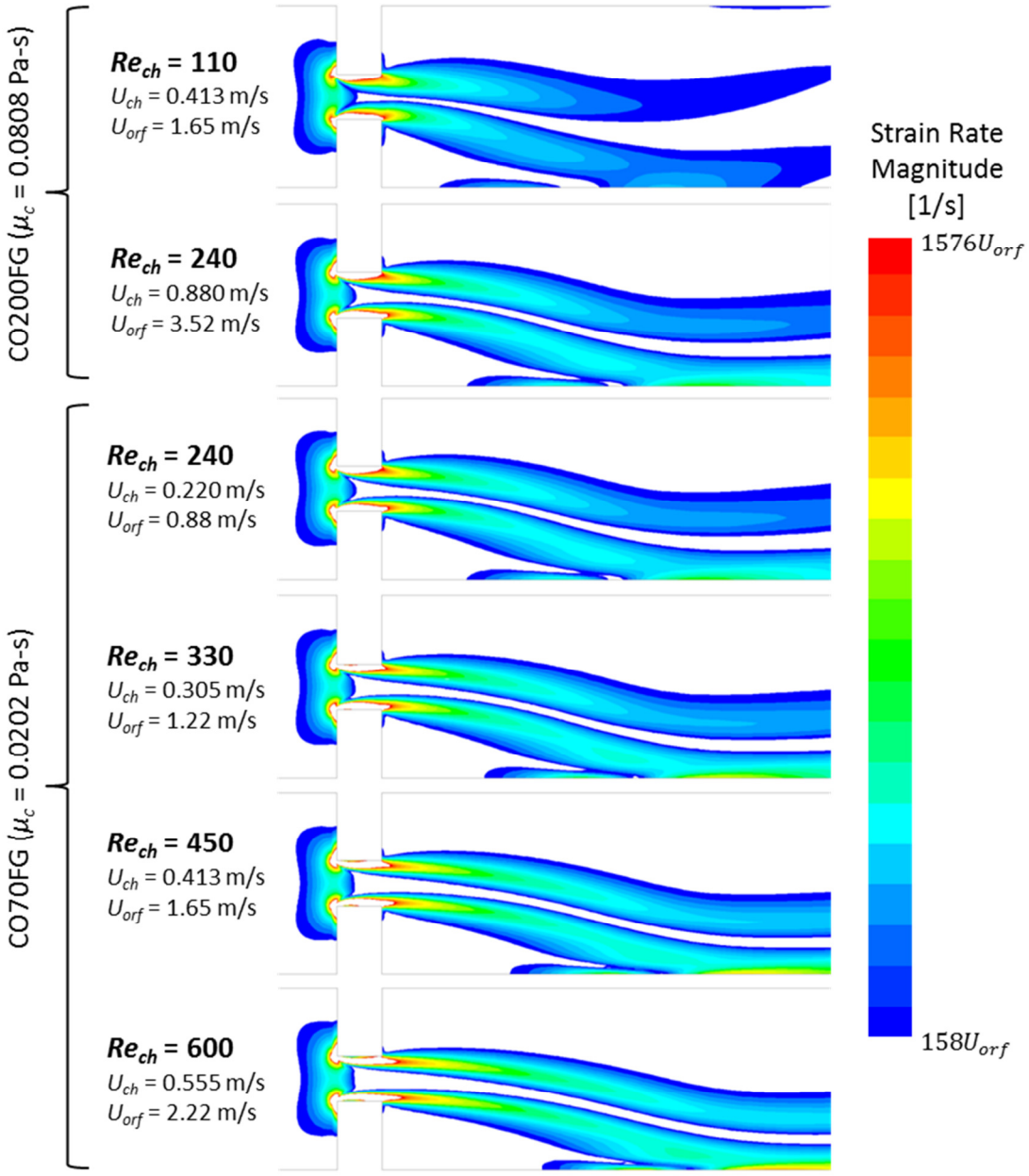

Figure 3.18. Contours of strain rate magnitude at the centre plane for the turbulent flow scenarios. The limits of the colour bar are set to scale with U_{orf} (in m/s) to emphasize the relative similarity of the fields from all four simulations.

Figure 3.19 shows the comparisons between the experimental and computational flow fields. The left panels show Re_{ch} = 110, the lowest flow rate investigated with CO200FG (μ_c = 0.0808 Pa-s). For the experimental flow field, CO70FG with Sudan III dye was injected near the wall on the same side of the channel as the small wake region. The dye line was traced and superimposed over the CFD flow field (red dotted line); it does not define the edge of the region, but it does appear to follow a streamline in the CFD flow field. At Re_{ch} = 600 (μ_c = 0.0202 Pa-s), the dye was more difficult to visualize, so small bubbles were injected into the flow. The right panels show bubbles that are captured in the wake region, indicating that the length of this region is well-predicted computationally.

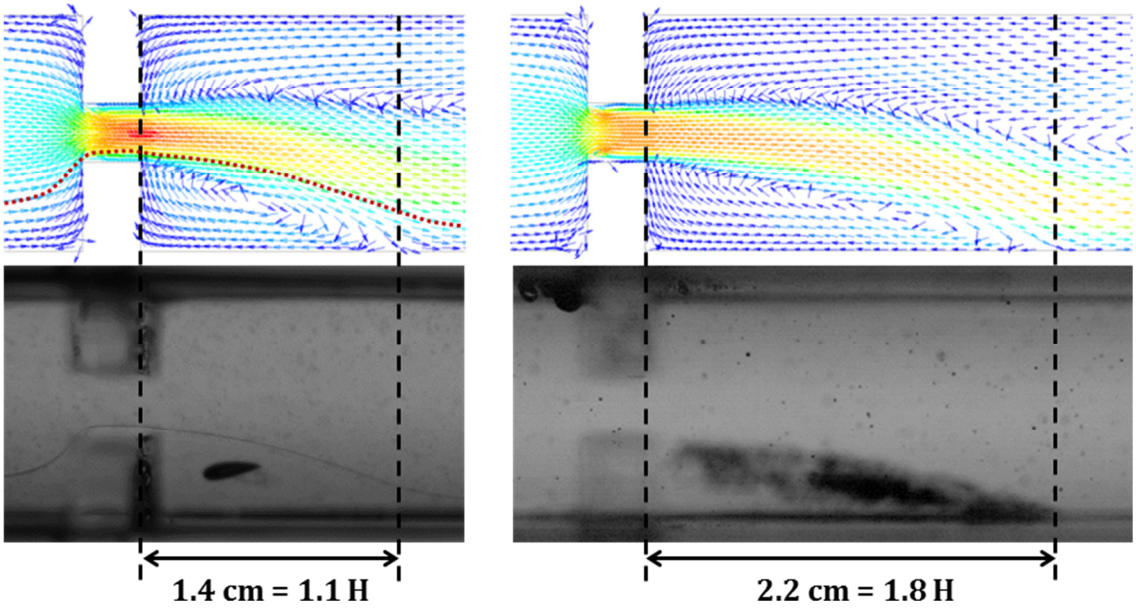

(a) Re_{ch} = 110 (μ_c = 0.0808 Pa-s) (b) Re_{ch} = 600 (μ_c = 0.0202 Pa-s)

Figure 3.19. Comparison between CFD and experimental dye and bubble images, illustrating the match in the small wake region length for both Re_{ch} = 110 (lowest flow rate of CO200FG) and 600 (highest flow rate of CO70FG).

3.3. Key Findings from Channel Design and Slit Orifice Simulations

The key findings from the CFD studies are as follows:

- The average velocity the span-wise centre of the channel was slightly higher than the design superficial channel velocity of 1.1 m/s by about 4% and 7% in turbulent and laminar flows, respectively.
- Based on both turbulent and laminar flow CFD simulations of the inlet manifold, an entry length of 0.90 m is needed to fully-develop the flow prior to reaching the orifice.
- Flow fields near the orifice at Re_{ch} ranging from 110 to 19,000 were generated using CFD simulations. The expected leaning jet was well-simulated.
- The shape of the simulated orifice jet, quantified through measurement of the small wake region behind the orifice, agreed qualitatively with previous literature. For the turbulent operating conditions, the length of the small (low pressure) wake region was constant at approximately 1 H (1.3 cm). For the laminar operating conditions, the small wake region increased slowly from 1.1 H (1.4 cm) at Re_{ch} = 110 to 1.8 H (2.2 cm) at Re_{ch} = 600. Images of dye streamlines in the channel also show a similar shape of the small wake region.

4. Droplet Break-up in Turbulent Flows

This chapter presents the fundamental physics, experimental observations, and various analyses for the droplet break-up experiments in turbulent channel flows. The physics of droplet break-up, including a review of existing literature, are described in Section 4.1. Observations of droplet behaviour are presented in Section 4.2. The development of breakage probability correlations with different Weber number definitions are detailed in Sections 4.3 to 4.5. Comments regarding daughter drop size distributions are provided in Section 4.6. A summary of the conclusions of this work are in Section 4.7.

4.1. Turbulent Break-up Theory and Literature

The basic framework for describing droplet break-up was established by Kolmogorov (1949) and Hinze (1955). They proposed that a droplet should break-up when the disruptive stresses τ_{dis} exceed the cohesive stresses τ_{coh}. For turbulent flows, the disruptive stresses are caused by external dynamic pressure, which is scaled with the inertial scale $\rho_c U_c^2$. For inviscid droplets, the cohesive stresses are the result of interfacial forces scaled with σ/D. The Weber number is defined as the ratio of dynamic pressure to interfacial forces as shown in Equation 4.1-1. The appropriate velocity scale U_c is the characteristic velocity on the length scale of the droplet; this will be discussed in more detail later in this section.

$$We = \frac{\tau_{dis}}{\tau_{coh}} = \frac{\rho_c U_c^2 D}{\sigma} \tag{4.1-1}$$

The appropriate velocity scale U_c is typically taken to be the root-mean-square turbulent velocity fluctuations on the length scale of the droplet size; the definition of this velocity scale thus depends on the size of the droplet relative to the length scales of turbulence. Two length scales to consider are the macro or integral length scale η_M and the Kolmogorov length scale η_K. At the macro length scale, considered to be of order $\eta_M = k^{1.5}/\varepsilon$, the turbulence is anisotropic. The Kolmogorov length scale, calculated as $\eta_K = (\nu^3/\varepsilon)^{1/4}$, represents the size of the smallest turbulent eddies; below this scale, kinetic energy is dissipated to heat by viscosity.

Many practical dispersion operations take place within either the macro scale or the inertial subrange. For droplet break-up at the macro scale of turbulence, the root mean square turbulent velocity is proportional to the macro scale velocities in the system. For example, stirred vessels may use the impeller tip speed. For droplet break-up in the inertial subrange, where droplet diameters are much larger than the Kolmogorov length scale but much smaller than the macroscale ($\eta_K \ll D \ll \eta_M$), Batchelor (1959) related the mean-square velocity fluctuation to energy dissipation rate as $\overline{u'(D)^2} = 2(\varepsilon D)^{2/3}$. With the inertial subrange model, the Weber number is expressed as Equation 4.1-2.

$$We = \frac{\rho_c \varepsilon^{2/3} D^{5/3}}{\sigma} \qquad (\eta_K \ll D \ll \eta_M) \tag{4.1-2}$$

Internal viscous forces can also play a role in stabilizing a droplet against break-up. Hinze (1955) expressed the cohesive stresses as a combination of interfacial and dispersed phase viscous forces. Hinze proposed using the *viscosity group* $N_{Vi} = \mu_d/\sqrt{\rho_d \sigma D}$ to account for viscous contributions to the cohesive stress, but Sleicher (1962) recommended the use an alternate viscosity group $Vi = \mu_d U_d/\sigma$. The internal dynamic pressure is presumed to be proportional to the external dynamic pressure so an appropriate internal velocity scale is $U_d = \sqrt{\tau_{dis}/\rho_d}$ (Hinze, 1955). This yields the viscosity group suggested by Calabrese *et al.* (1986a) and shown in Equation 4.1-3.

$$Vi = \frac{\mu_d U_c}{\sigma}\left(\frac{\rho_c}{\rho_d}\right)^{1/2} \tag{4.1-3}$$

When the disruptive and cohesive stresses are in balance for a particular droplet, the droplet is at its *maximum stable drop size* D_{max}. The corresponding Weber number is the *critical Weber number* We_{crit}. The balance can be written as shown in Equation 4.1-4. In the absence of dispersed phase viscosity effects, the critical Weber number is C_1.

$$We_{crit} = C_1(1 + C_2 Vi) \tag{4.1-4}$$

4.1.1. Levich Stress Balance

Levich (1962) highlighted that the break-up of air bubbles rising in a quiescent fluid was not well-predicted by the Kolmogorov/Hinze interpretation. Experimental observations of free-rising bubbles found that the maximum stable

diameter was around 4 cm. The predicted critical diameter with the Kolmogorov/Hinze interpretation was an order of magnitude smaller. To rectify this, Levich proposed an alternate mechanistic view for bubble break-up. This mechanism and its corresponding Weber number is presented in this section.

Levich considered the disruptive stresses to arise from *internal* dynamic pressure fluctuations (instead of the *external* dynamic pressure fluctuations). This stress was modelled as $\rho_d U_d^2$, where U_d is the internal velocity scale. In general, the fluctuations outside the bubble cause fluctuations inside the bubble, which can be conceptually expressed as $\rho_c U_c^2 \propto \rho_d U_d^2$, where U_c is the external velocity scale. This is essentially the same argument made by Hinze (1955). When the density of the dispersed phase is higher than the density of the continuous phase, this relationship would result in a dispersed phase velocity scale that is a fraction of the external velocity scale. For low- or similar-density dispersed phases, U_d can be scaled with U_c. This disruptive force was assumed to be uniform within the bubble.

The cohesive force was considered to be the interfacial stress associated with a *deformed* bubble (instead of an un-deformed bubble). The deformed bubble was modelled as an oblate spheroid with, consequently, an elliptical cross-section. The critical (i.e., weakest) region for evaluating break-up was the surface with the lowest local curvature $\mathcal{H}_{min}$ because this region would have the lowest capillary pressure. The local curvature can be calculated analytically for an elliptical cross-section; the weakest points are located at the top and bottom of the bubble. Figure 4.1

illustrates the model bubble, with y_{int} and z_{int} as interface coordinates and h and l as the minor and major radii of the deformed bubble.

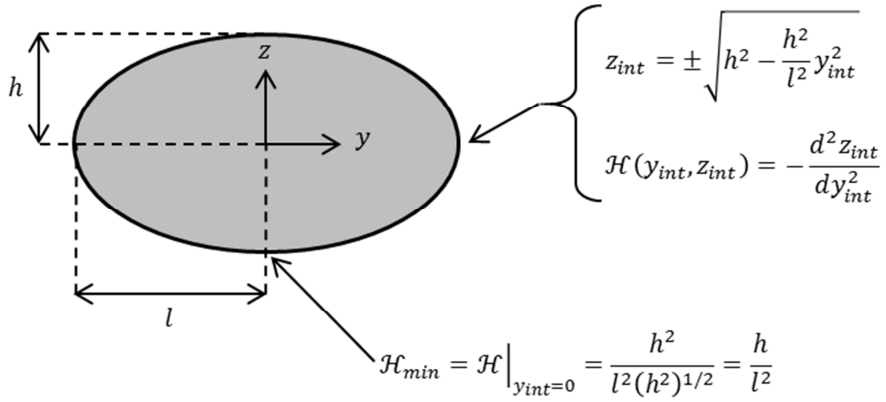

Figure 4.1. Cross-section geometry of the oblate bubble modelled by Levich (1962).

The shape of the bubble (i.e., the minor and major radii h and l) was determined by the macroscale energy balance shown in Equation 4.1-5. The first term represents the energy expended by the continuous phase to deform the bubble by δh (a negative value). The second term represents the increase in surface energy.

$$\Delta P A_c \delta h + \sigma \delta A_c = 0 \tag{4.1-5}$$

The relationship between the cross-sectional area A_c and h was determined through volume conservation. The droplet volume V is proportional to l^2h, or, equivalently, A_ch. This can be re-formulated as A_c being proportional to V/h. Since V is constant, the derivative dA_c/dh can be expressed as $-V/h^2 = -A_c/h$. Setting this equal to $\delta A_c/\delta h$, this can be substituted into Equation 4.1-5 to determine the minor radii as $h = \sigma/\Delta P$. Levich scaled the pressure difference with the external dynamic pressure fluctuations $\rho_c U_c^2$. The resulting expression for cohesive stress for a deformed bubble is shown in Equation 4.1-6.

$$\tau_{coh} = \sigma \mathcal{H}_{min} = \frac{\sigma h}{l^2} = \frac{\sigma h^2}{l^2 h} \propto \frac{\sigma h^2}{D^3} \propto \frac{\sigma^3}{\rho_c^2 U_c^4 D^3} \tag{4.1-6}$$

Levich showed that this interpretation of the disruptive and cohesive stresses allowed for the predicted critical bubble diameter to match the experimentally observed critical bubble diameter. The ratio of disruptive stresses to cohesive stresses based on the interpretation of Levich is shown in Equation 4.1-7. Despite having more complex bubble shapes, Hesketh *et al.* (1987, 1991) utilized the functionally-equivalent Weber number shown in Equation 4.1-8 to study bubble break-up in horizontal pipelines. The Levich interpretation of stresses brought the critical Weber number to order 1 for both bubbles and droplets from their results and the results of previous researchers (Holmes, 1973; Kubie and Gardner, 1977; Karabelas, 1978).

$$We = \frac{\rho_c^2 \rho_d U_c^6 D^3}{96\sigma^3} \tag{4.1-7}$$

$$We = \frac{(\rho_c^2 \rho_d)^{1/3} U_c^2 D}{\sigma}, U_c^2 = (\varepsilon D)^{2/3} \tag{4.1-8}$$

4.1.2. Droplet Break-up in Homogeneous Turbulent Flows

There is a great deal of available literature covering many aspects of droplet break-up. The studies selected for this review focus on critical break-up conditions or probabilities through the imaging or simulation of single droplets exposed to a limited number of deformation events. This means that either the image processing

system must be capable of tracking a number of droplets individually or that the events must occur in a controlled or uniform fashion.

One of the most frequently encountered turbulent break-up models was developed by Coulaloglou and Tavlarides (1977). The local turbulence was assumed to be homogeneous and isotropic, and the modelled droplet sizes were in the inertial subrange. They considered the break-up frequency to be comprised of a break-up time and a break-up fraction. The break-up time was essentially an eddy life time. The breakage fraction was considered be proportional to the fraction of eddies whose mean turbulent kinetic energy exceeded the droplet's surface energy. An exponential expression for breakage fraction assumed the collisions could be modelled using the kinetic theory of gases.

According to Lasheras *et al.* (2002), a weakness common to the model of Coulaloglou and Tavlarides (1977) and others also utilizing a distribution of eddies is that the results often depend on assumptions made regarding the probability of droplet-eddy collisions and on the range of eddy sizes that can affect the droplet. An alternate model proposed by Martinez-Bazan *et al.* (1999a, 1999b) considered the balance between disruptive stresses and cohesive stresses but without the need to evaluate eddy distributions. In their model, they instead postulated that the break-up time should be proportional to the ratio of the droplet diameter to the difference in disruptive and cohesive stresses. In the resulting model, the break-up frequency (taken to be the inverse of break-up time with no additional breakage fraction as in Coulaloglou and Tavlarides) increases with the square root of the stress difference.

Martinez-Bazan *et al.* showed that their model provided improved predictions despite being mechanistically simpler. Eastwood *et al.* (2004) extended this work to viscous drops at low Weber numbers, finding that the break-up time instead scales with the viscous time scale. Rodriguez-Rodriguez *et al.* (2006) used numerical modelling to demonstrate that the break-up time for bubbles decreased with increasing critical Weber number, eventually reaching a constant level.

Andersson and Andersson (2006a, 2006b) imaged large liquid droplets and air bubbles in a reactor with mixing elements designed to produce and dissipate turbulence kinetic energy homogeneously. They view break-up as the result of large deformations and argue that eddies much smaller than the droplet size do not carry enough energy to break droplets. Instead their analysis suggests that eddies up to three times the size of the droplet can be responsible for causing critical levels of deformation. They also show that while air bubbles tend to break unevenly, droplets tend to break more evenly. Bubbles were proposed to break more unevenly because the difference in internal pressure more easily results in flow distribution.

Ravelet *et al.* (2011) studied the dynamics and breakup of rising large diameter (9.3 mm) bubbles. Bubbles were imaged in three planes in a transparent diverging pipe. The turbulent flow of water was directed downward. For break-up to occur, they found that the longest axis of the bubble needed to exceed twice the equivalent spherical diameter. They showed that the critical deformation occurred based on an interaction with a single highly-energetic eddy. Though the bubble

itself did not oscillate as it relaxed, relaxation of the bubble occurred on an oscillation time scale. Ravelet *et al.* argued that, because of the oscillations were highly damped, break-up was not caused by a resonance effect resulting from interaction with many eddies; only a single intense eddy was needed for break-up.

4.1.3. Droplet Break-up in Circular Orifices

One of the earliest studies on break-up in a circular orifice was conducted by Percy and Sleicher (1983). The break-up of a millimetre-sized neutral-density, low viscosity droplets were studied for three different orifice openings ($\beta = d_{orf}/d_{pipe}$ = 0.75, 0.83, and 0.92, with d_{pipe} = 3.81 cm) and three Reynolds numbers (Re = 48,000 to 68,000). The break-up fraction was reported to be linear with drop diameter in the six scenarios examined. It was also interesting in that even a relatively open orifice could effectively break all of these large droplets at high enough velocity.

Galinat *et al.* (2005, 2007) studied the break-up of low-density, low-viscosity liquid droplets in a vertically-oriented 3-cm diameter pipe with three orifice sizes (β = 0.33, 0.50, and 0.66). Through their high-speed imaging, they observed that the break-up occurred at the jet edges or in the turbulent diffusion zone. They also saw an approximately linear relationship between breakage probability and diameter. To collapse their different flow scenarios to a single curve, they related breakage probability to a global Weber number based on the disruptive stress being proportional to the pressure drop across the orifice. The performance of two models were evaluated: a two-parameter breakage probability attributed to

Coulaloglou and Tavlarides (1977) shown in Equation 4.1-10 and a power/exponential model shown in Equation 4.1-11. The power/exponential form was their recommended model based on its fit with their data and that of Percy and Sleicher (1983).

$$\text{One-Parameter Exponential:} \quad P = \exp\left(-\frac{C_1}{We}\right) \tag{4.1-9}$$

$$\text{Two-Parameter Exponential:} \quad P = C_2 \exp\left(-\frac{C_1}{We}\right) \tag{4.1-10}$$

$$\text{Power/Exponential:} \quad P = We^{C_2} \exp\left(-\frac{C_1}{We}\right) \tag{4.1-11}$$

4.1.4. Break-up in Stirred Tanks

Investigating the breakup of liquid droplets in a stirred tank was the goal of a series of works including Maass *et al.* (2007, 2012) and Zaccone *et al.* (2007). Instead of using a stirred tank, a flow cell was built around a stationary Rushton turbine blade, in effect creating a channel similar to the current study. Their Weber number is formulated using the corresponding tip velocity of the impeller being simulated. They show that the exponential model of Coulaloglou and Tavlarides (1977) among others provides a reasonable breakage probability for kerosene droplets with a Weber number of 25. For toluene droplets with similar Weber number, however, the exponential model performed poorly compared to an error function breakage probability model developed by Alopaeus *et al.* (2002).

Solsvik and Jakobsen (2015) conducted single droplet experiments in a baffled tank stirred by a Rushton turbine. Their data showed that, for droplet

diameters less than 2 mm, binary breakage events occurred between 20 and 40% of the time, depending on the dispersed phase material. For larger droplets, the percentage of binary break-up events decreased by about a factor of 2. Size distributions of the daughter droplets were not provided.

4.2. Experimental Observations

This section provides observations from study of the imaged droplets. This includes how the droplets were distributed in size and incoming trajectory, observations on their behaviour as they passed through the orifice, and images of the breakage mechanisms.

4.2.1. Droplet Size and Incoming Trajectory Distribution

Table 4.1 summarizes the quantity of droplets and bubbles imaged for each of the four turbulent flow conditions. Details regarding distribution with respect to diameter and incoming trajectory are provided in Appendix C. The size and incoming trajectory of each droplet was measured at least 0.5 H (6.35 mm) upstream of the orifice to eliminate orifice effects. The droplets included in later analyses had diameters between 200 and 1,200 μm. At a diameter of 200 μm, the droplets had potential image resolution errors of about 15% (based on a typical resolution of 30 μm/px), which was deemed to be adequate for this study. The upper bound on diameter was selected based on consideration of the available data; droplets with diameters greater than 1,200 μm were relatively uncommon and were

thus likely to be poorly-represented in any statistical analyses. Based on the average predicted values of turbulence kinetic energy and turbulence dissipation rate inside the orifice (see Appendix B for flow field data), the macro length scale and Kolmogorov length scale are of order 1 mm and 10 μm, respectively.

Table 4.1. Summary of imaged droplets and bubbles for the turbulent flow experiments.

Channel Reynolds Number Re_{ch}	Oil Droplets Sampled		Air Bubbles Sampled	
	Pulnix	Phantom	Pulnix	Phantom
7,700	510	-	485	-
10,000	348	99	499	86
14,000	348	88	275	67
19,000	348	-	-	-

Because the Phantom data was acquired at much higher temporal resolution than the Pulnix data, the Phantom data was the basis for all observations and analyses requiring the drop trajectories. The Pulnix data was used primarily for the breakage probability contours based on the upstream Weber number discussed in Section 4.4.

4.2.2. Droplet Trajectory Behaviour

To evaluate the behaviour of the droplet trajectories (i.e., the path taken by the droplet as it travels through the orifice), trajectory plots of droplet centroids acquired with the Phantom camera (see Section 2.3) were separated into bins based on their material (CO70FG or air), diameter (three bins), and incoming trajectory (five bins). The bins of dimensionless incoming trajectory $y^*_{inc} = y_{inc}/\delta$ (where δ is

the orifice half-width of 1.59 mm) were evenly-spaced with boundaries at y^*_{inc} = –2.4, –0.8, +0.8, and +2.4, as shown in Figure 4.2.

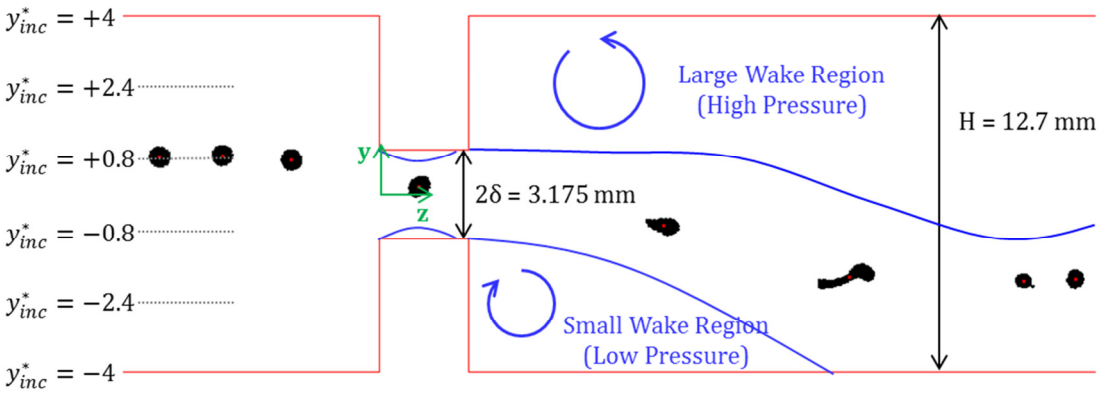

Figure 4.2. Categorization of droplets based on incoming trajectory y^*_{inc}. In this example, the droplet centroid is in the $0.8 < y^*_{inc} < 2.4$ bin.

Figure 4.3 presents an example of the trajectory plots for CO70FG oil droplets. The full set of trajectory plots for both oil droplets and air bubbles is in Appendix D. The blue and red lines represent droplets for channel Reynolds numbers of 10,000 and 14,000, respectively. Solid lines represent unbroken droplets, while dashed lines represent broken droplets. The circle marker denotes where the droplet breaks (or first breaks, in the case of multiple break-up events), travels out of the field of view, or moves out of the focus plane.

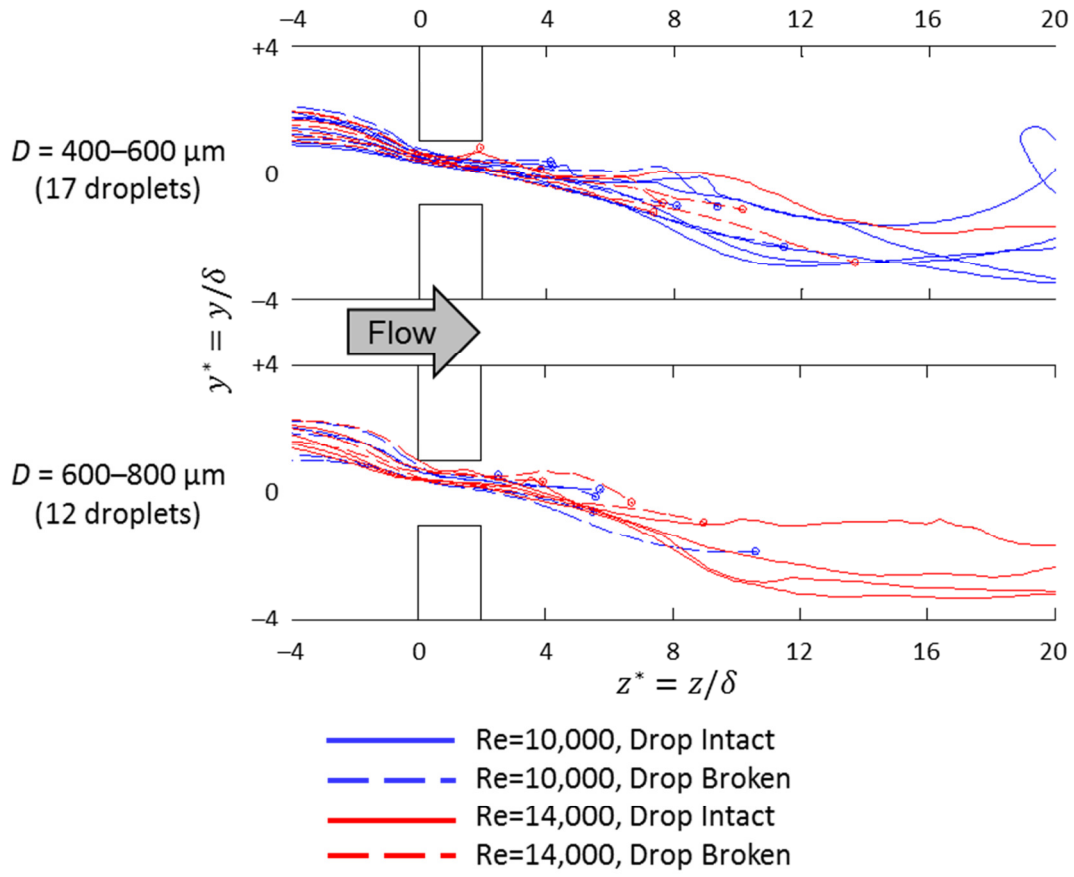

Figure 4.3. Droplet trajectories for CO70FG droplets in turbulent flows of water, originating from $0.8 < y^*_{inc} < 2.4$.

Two interesting observations resulted from a study of these trajectory plots. First, the droplet trajectories do not appear to be dependent on either Reynolds number on droplet diameter. The scatter caused by the fluctuating turbulent motion of the continuous phase masks other effects. Second, droplets predominantly break on interaction with the high strain regions in the orifice and along the edges of the jet. Break-up did not occur in the core of the orifice jet and in the recirculation regions (except when droplets travelled back into the edge of the jet). This agrees with the observations made by Galinat *et al.* (2005) in their study of droplet break-up in a circular orifice.

4.2.3. Lateral Migration of Droplets

One significant variable in the droplet trajectory appeared to be the density of the dispersed phase. A typical example of this is shown in Figure 4.4. The trajectory lines are formatted similarly to Figure 4.3, but the end point markers have been removed and the mean trajectory for each set of trajectories has been added as a bolded black line. The mean trajectory for the air bubbles clearly deviates toward the jet centre more strongly than for the oil droplets. This is because the air bubbles have a lower density and thus mass; for the same diameter (and projected area) and lateral pressure force, the air bubbles accelerate faster than the heavier oil droplets.

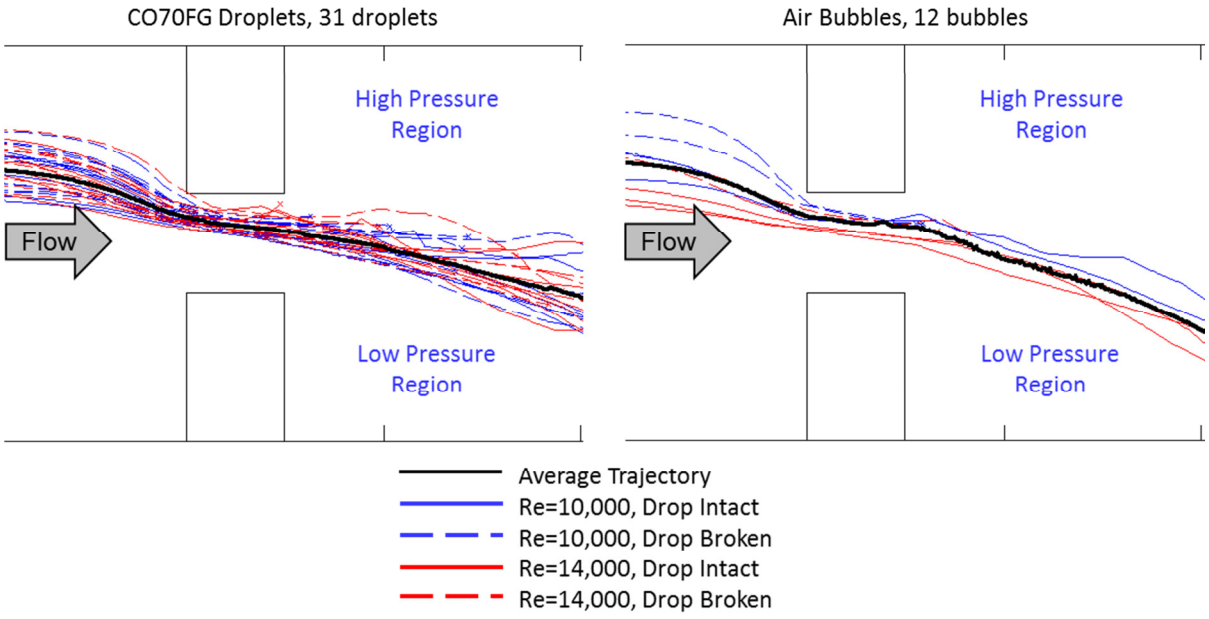

Figure 4.4. Comparison of CO70FG droplet and air bubble trajectories in turbulent flows of water, originating from $0.8 < y^*_{inc} < 2.4$.

The dispersed phase model in Fluent was used to qualitatively verify the presence of the lateral migration. The trajectories for 700 μm diameter spherical

particles for four conditions are shown in Figure 4.5. The top trajectories are based on a particle density of 860 kg/m^3 (the density of CO70FG), while the bottom trajectories are based on a density of 1.2 kg/m^3 (the density of air). The blue and red lines indicate channel Reynolds numbers of 7,700 and 19,000, respectively. The lateral migration of the low-density particle is evident, with the DPM predicting capture of the particle in the low pressure wake region. The most interesting feature is that the degree of lateral migration depends on channel Reynolds number. Particles at both densities actually deviate more strongly at the lower Reynolds number, qualitatively indicating that the pressure does not scale exactly with the square of superficial channel velocity.

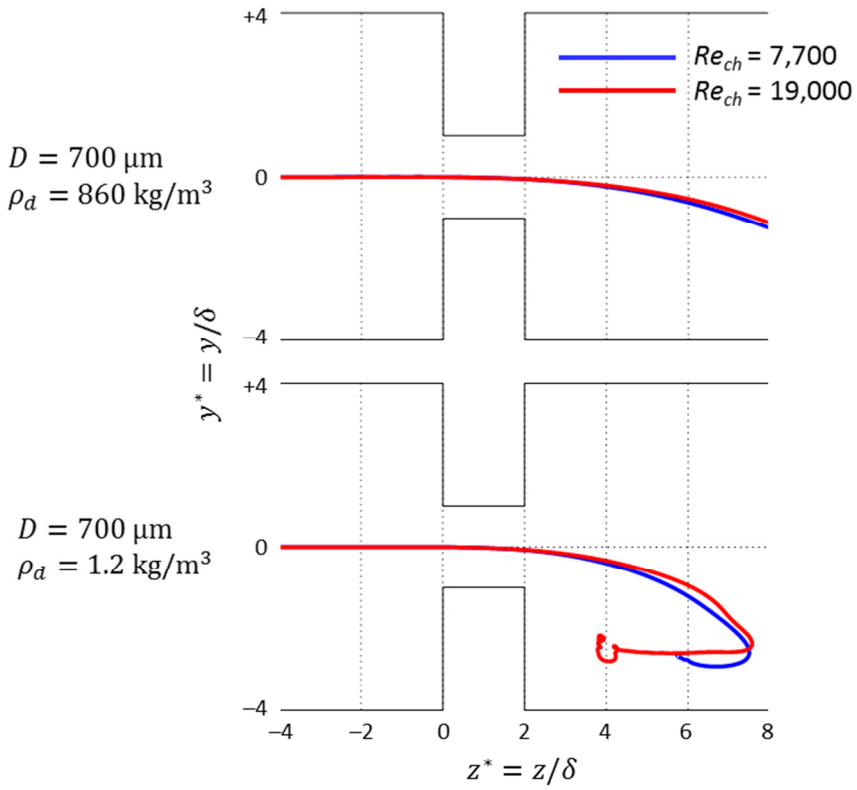

Figure 4.5. Fluent DPM trajectory prediction for solid spherical particles with a diameter of 700 µm and densities of 860 kg/m^3 and 1.2 kg/m^3.

The relative strength of the lateral pressure versus the forward momentum was estimated by considering the pressure across the jet to represent lateral forces and the inertial scale $\rho_c U^2$ of the continuous phase to represent the stream-wise momentum of the particle. To evaluate the pressure difference across the jet, the pressure profiles at a representative stream-wise location z = 0.5 H were plotted as shown in Figure 4.6. If the difference in the wall pressure can be considered representative of the pressure across the jet, the pressure difference was 150 Pa for the 7,700 Reynolds number flows. The inertial scale at this Reynolds number is 93 Pa. The ratio of the pressure difference to the inertial scale is 1.6. For the channel Reynolds number of 19,000, the pressure difference and inertial scales are 830 Pa and 550 Pa, respectively, resulting in a ratio of 1.5. A comparison of the two ratios demonstrates that a particle or droplet in the orifice flow does experience relatively less lateral forces at higher Reynolds numbers.

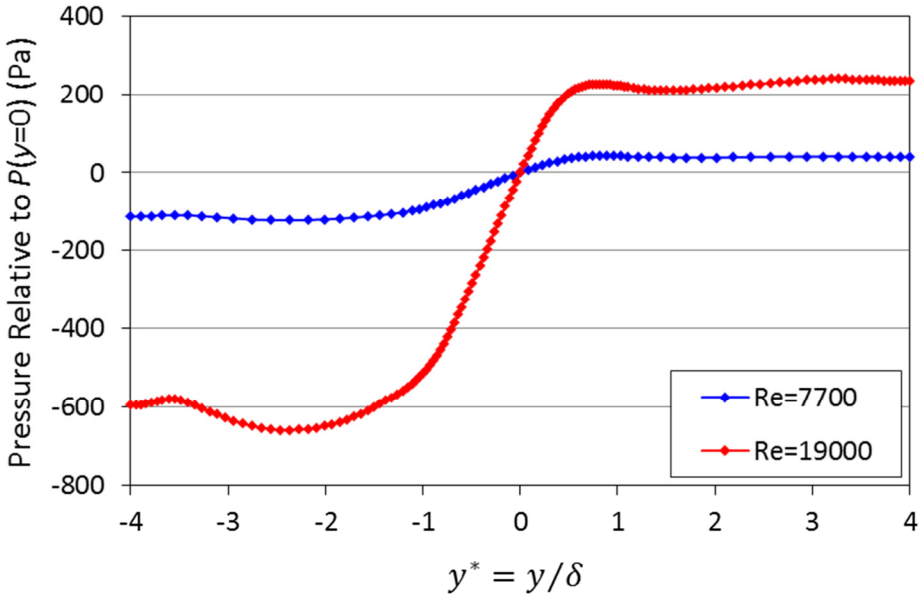

Figure 4.6. Static pressure relative to $P(y = 0)$ versus cross-wise coordinate y^* at z = 0.5 H.

4.2.4. Description of Breakage Events

The combination of the orifice path and the turbulence led to a variety of break-up events. The image sequence for some of these events is presented in this section. See Figure 2.2(b) and Figure 4.2 for the coordinate convention. As a reminder, each image sequence has an arrow pointing to the right for the direction of flow (with gravity to the left) and the notes “high P” and “low P” to mark the high and low pressures sides of the jet, respectively. Video corresponding to each of the figures below is available in the supplementary PowerPoint file.

The simplest break-up events occurred at lower strain rates. Air bubbles also tended to break with simpler mechanisms due to higher interfacial tension and also the lower internal dynamic pressure postulated by Levich (1962). Figure 4.7 shows a binary break-up of a CO70FG oil droplet. The droplet does extend in a minor fashion in the first section of the orifice (where the extensional rates are positive, as shown in Appendix B), but as it exits the orifice, it has a spherical-cap shape. The droplet again extends as it enters and stays within the high shear jet edge. The extended droplet becomes vulnerable to turbulent fluctuations that deform its shape, causing localized curvature that ultimately results in a pinch-off mechanism that is similar to the laminar flow break-up (see Section 5 for more background).

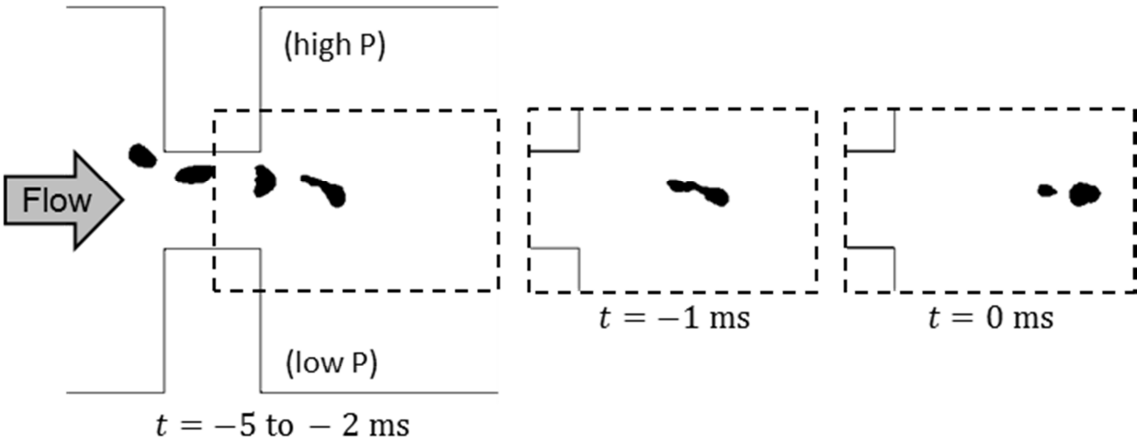

Figure 4.7. Binary break-up of CO70FG droplet (D = 750 μm) due to high deformation rates in jet edge at Re_{ch} = 10,000. Image sequence acquired with Phantom camera (1,000 fps).

Figure 4.8 shows a similar-sized droplet that approaches closer to the leading edge of the orifice and thus passes through the regions of the orifice with greater strain rates. As with the binary break-up, the droplet extends in the orifice but contracts into a spherical cap shape. Because the droplet widens considerably compared to the extended shape at the entrance, one side of the droplet is now much more affected by the core jet velocity. This causes the droplet to fold and tumble in the counter-clockwise direction as it exits the orifice. As with the droplet break-up work of Tjahjadi & Ottino (1991), a daughter droplet forms at any folding points in the shape. However, because of the turbulence, the number of nodes formed (and thus the number of daughters produced) depend on the turbulent eddies that collide with the droplet. A similar break-up event can also occur on the other side of the orifice, though with a clockwise tumbling motion.

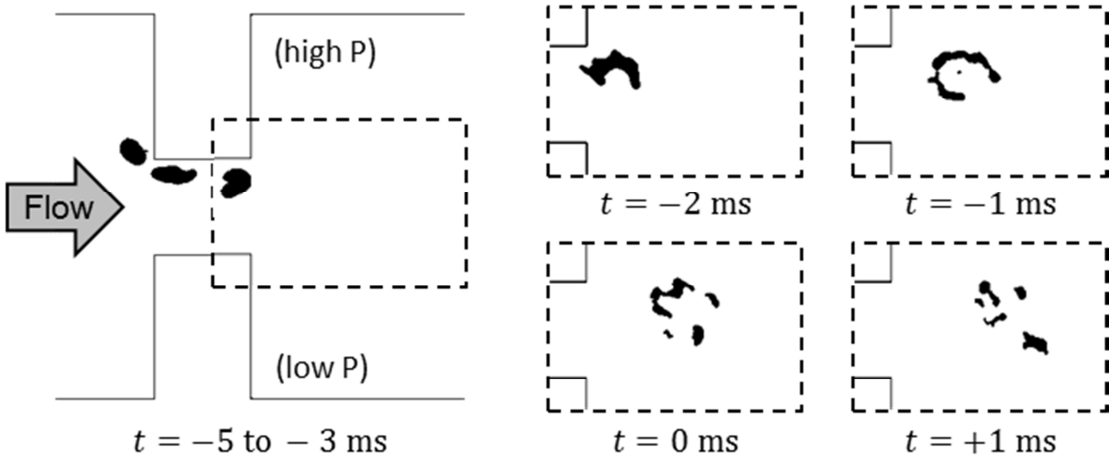

Figure 4.8. Break-up of CO70FG droplet (D = 760 μm) at Re_{ch} = 10,000. The droplet extends significantly in the orifice and becomes folded as it enters the jet edge. Image sequence acquired with Phantom camera (1,000 fps).

Figure 4.9 and Figure 4.10 shows the image sequence for a droplet encountering the jet edge on the low and high pressure sides, respectively. Note that the orifice velocities were on the order of 2–3 m/s. Both droplets slowed down considerably at edges of the jet, undergoing severe deformations before the initial break-up. Unlike the previous two break-up events, the shapes of the droplet prior to break-up in the jet edge vary significantly, indicating that the details of the break-up may be more dependent on local eddies than the mean shear rate. Both droplets experience multiple fractures in the event, with droplet of Figure 4.9 forming 5 daughters and the droplet of Figure 4.10 forming 3 daughters.

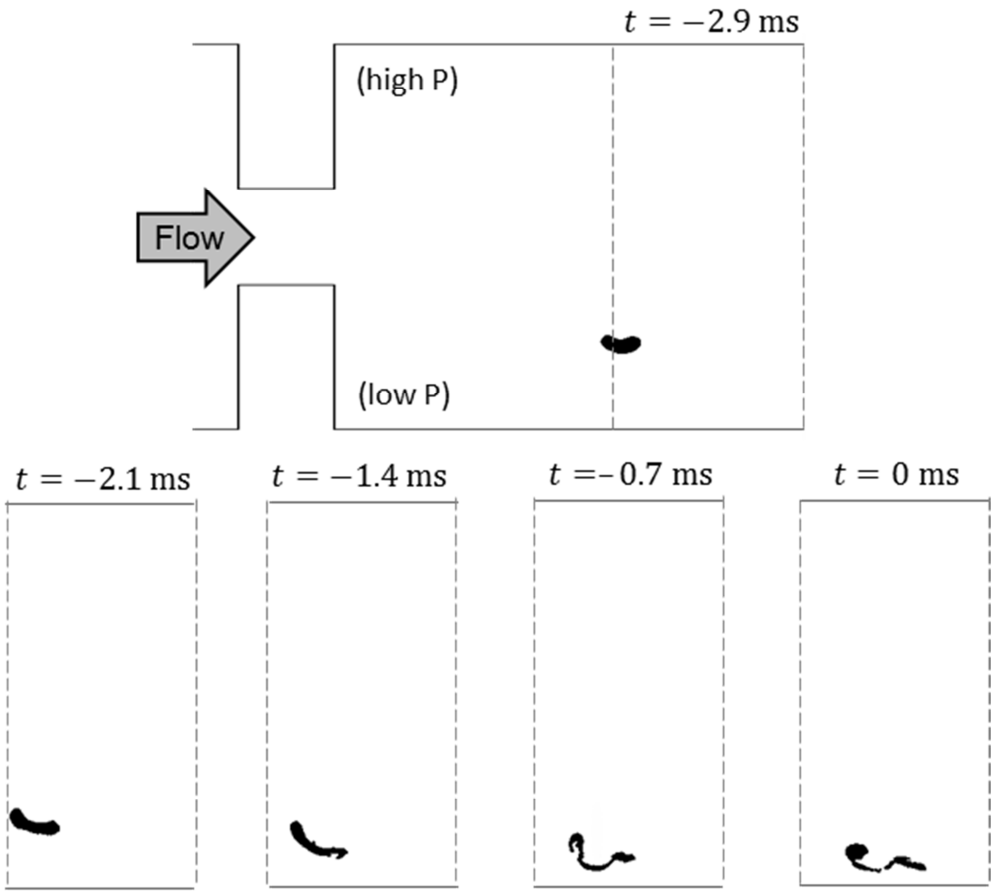

Figure 4.9. Break-up of CO70FG droplet (D = 675 μm) in orifice at Re_{ch} = 14,000 at the jet edge on the low pressure side. The dashed lines mark the region z = 0.75 H to 1.25 H. The time relative to the initial break-up frame is above each image. Image sequence acquired with Phantom camera (1,400 fps).

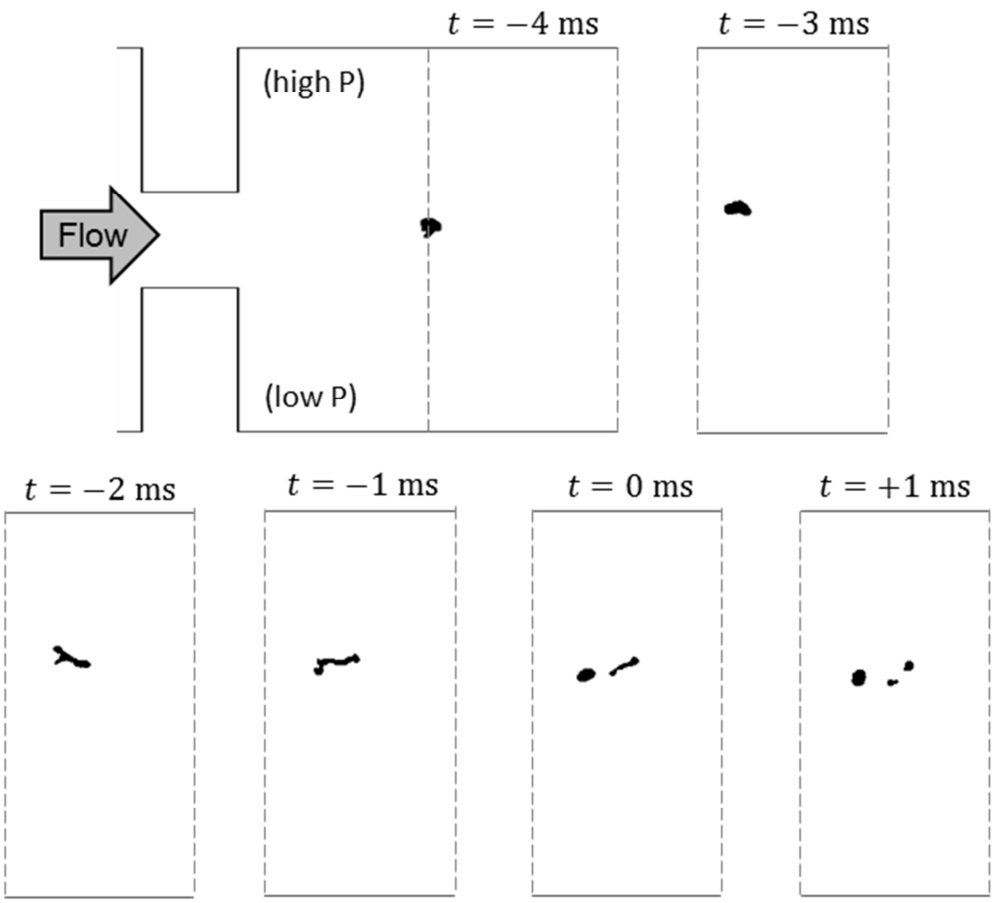

Figure 4.10. Break-up of CO70FG droplet (D = 560 μm) in orifice at Re_{ch} = 10,000 at the jet edge on the high pressure side. The dashed lines mark the region z = 0.5 H to 1 H. The time relative to the initial break-up frame is above each image. Image sequence acquired with Phantom camera (1,000 fps).

Droplets can be caught within the orifice separation zone, resulting in very high gradients across the droplet. This occurrence is more likely when: (i) droplets approach the orifice along the walls, (ii) the droplet material is oil, and (iii) the channel Reynolds number is high. Figure 4.11 is an example of an oil droplet approaching the orifice on the side with the high pressure wake region, but a similar behaviour is observed with the opposite approaching trajectory. The droplet, partially within the separation region, breaks into a spray of fine droplets. Parts of

the droplet can be retained within the separation region for a relatively long period of time. Figure 4.11 also demonstrates one of the challenges of working with the Pulnix and strobe system, namely that the daughter droplets are overlapping past the point of break-up. A video in the supplementary PowerPoint file shows this type of break-up event as captured by the Phantom camera.

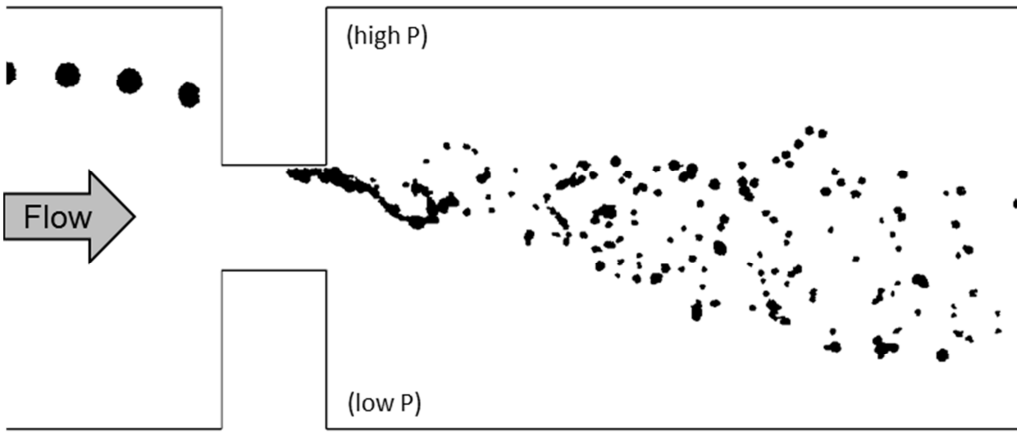

Figure 4.11. Break-up of CO70FG droplet (D = 740 μm) in orifice at Re_{ch} = 10,000. Droplet gets caught in the separation region and fragments into many smaller daughter droplets. Image sequence acquired with Pulnix camera and a strobe rate of 236 fps (8 flashes per frame).

One of the flow characteristics seen in the experimental apparatus but not in the CFD is communication between the high pressure wake region and the separation region within the orifice. Figure 4.12 shows an example of how a droplet can get re-entrained into the orifice, leading to a break-up event similar to that previously described for Figure 4.11.

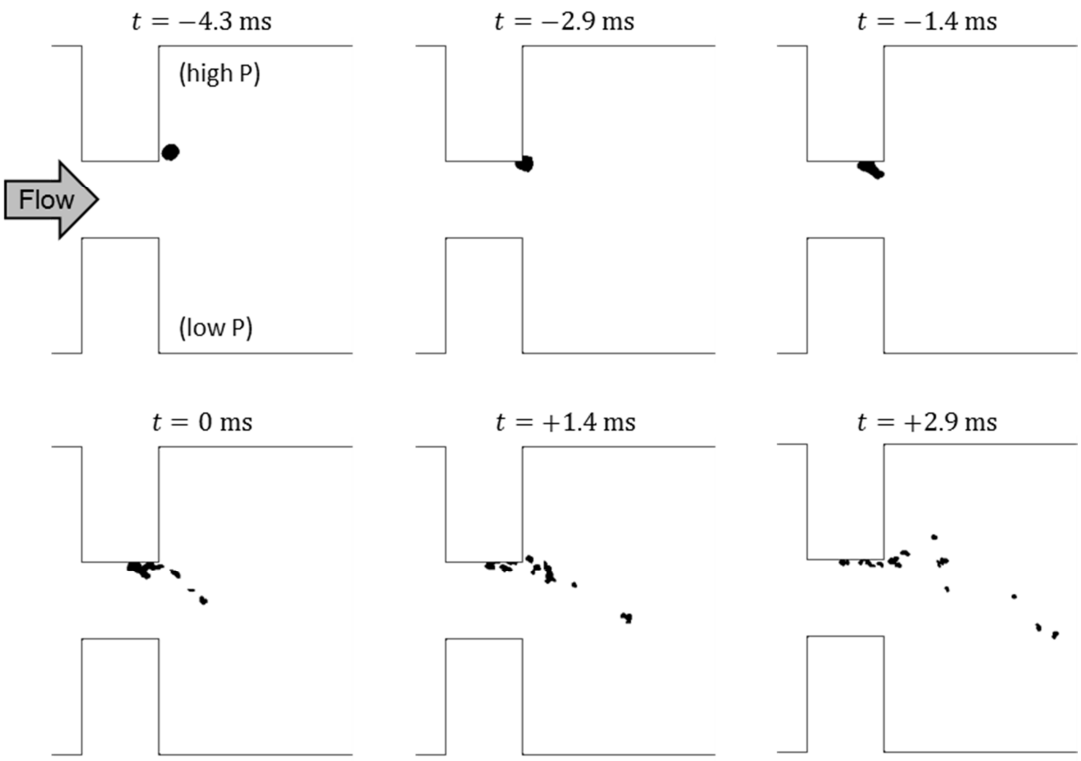

Figure 4.12. Re-entrainment of CO70FG droplet (D = 630 μm) into orifice separation region at Re_{ch} = 14,000. The time relative to the break-up frame is above each frame. Image sequence acquired with Phantom camera (1,400 fps).

Finally, while not a breakage event, coalescence was observed in rare cases. The image series in Figure 4.13 shows the break-up of an air bubble and its subsequent coalescence as it travels in the wake region. The break-up was a typical binary event at the trailing edge of the orifice. The coalescence began about 15 ms after break-up. Both daughters were caught in the low pressure wake region. Coalescence appears to have been initiated by a reduction in speed of the leading daughter, allowing the following daughter to come into contact. The coalesced bubble remained in the low pressure wake region for another 190 ms before experiencing another binary breakage event within the wake region.

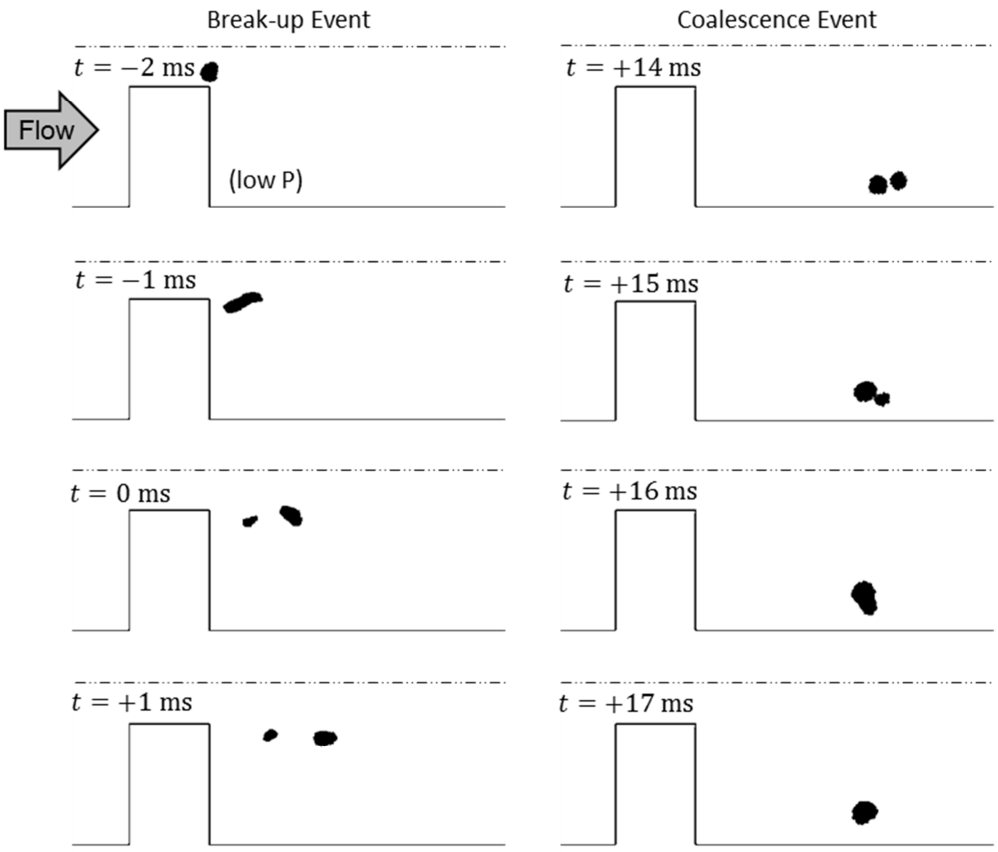

Figure 4.13. Break-up and subsequent coalescence of air bubble (D = 700 μm) at Re_{ch} = 10,000. The dot-dash line marks the centreline of the channel (y = 0). The time relative to the break-up frame is in the upper left corner of each frame. Image sequence acquired with Phantom camera (1,000 fps).

4.3. Droplet Break-up based on Local Conditions

The general expectation is that a droplet can be broken under a range of exposure times. For short exposure times, a greater ratio of disruptive to cohesive stresses would be needed for breakage to occur. A comparatively low ratio of stresses acting over a long period of time may also result in breakage. In other words, the critical ratio of disruptive to cohesive stresses must be a function of a properly-scaled exposure time t^*_{exp}. For an unbroken droplet, the range of Weber

numbers it experiences (over various exposure time scales) should lie entirely below a critical Weber number curve, while broken droplets would have some part of its curve in the unstable region above. This concept is illustrated in Figure 4.14. Ideally, this critical Weber number curve would, like the Grace curves, define break-up exactly; however, due to the random nature of turbulence and the difference between experimental flow field and the simulated mean flow field from the RANS equations, the boundary was expected to be inexact. The results of this approach are presented in Section 4.3.3. A second approach, correlating breakage probabilities to a locally-derived Weber number, was also investigated. This second approach was found to be more successful than the first approach; the methodology and results are presented in Section 4.3.4.

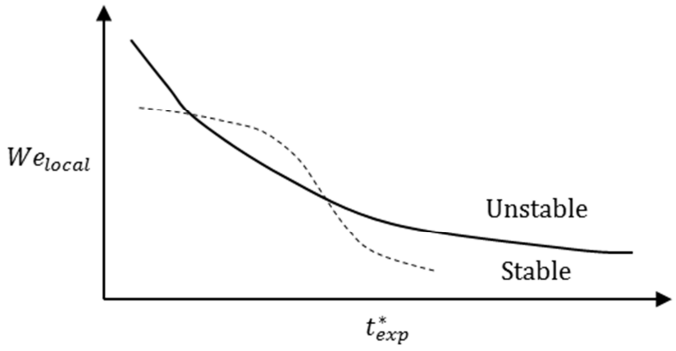

Figure 4.14. Illustration of concept of critical local Weber number as a function of scaled exposure time. Dashed line is a representative path-dependent profile experienced by a droplet that, conceptually, should be broken.

For this study, only the velocity scale was considered as time dependent. The densities, interfacial tension, and droplet diameter (taken to be the un-deformed droplet diameter D) are constant. ***It is assumed that the local Weber number*** $\mathbf{We_{local}}$ ***(defined in Equation 4.3-1) that characterizes break-up for a particular***

exposure time depends on the maximum velocity scale averaged over that exposure time. The velocity scale $U_{t^*_{exp}}$ depends on the droplet trajectory until the point of break-up or exit from the field of view (observed through optical imaging), the local flow field conditions (simulated using CFD) along the trajectory, and the scaled exposure time $t^*_{exp} = t_{exp}/t_{scale}$. Note that for any one droplet trajectory, the maximum averaged velocity scale always decreases with increasing exposure time. The appropriate velocity and time scale t_{scale} are discussed in the following subsections.

$$We_{local,t^*_{exp}} = \frac{(\rho_c^2 \rho_d)^{1/3} D}{\sigma} \left(U_{t^*_{exp}}\right)^2 \tag{4.3-1}$$

It is also assumed that the droplet viscosity does not play a role in the break-up. For air bubbles, this is a reasonable assumption. For oil droplets, this is less certain. Chen and Middleman (1967) correlated the normalized Sauter mean diameter to Weber number only for viscosity groups up to 1.18. Using the superficial velocity through the orifice as the characteristic velocity, the viscosity groups for the four channel Reynolds number scenarios are 0.58, 0.77, 1.1, and 1.4, respectively. This might suggest that, except for the last scenario, the break-up of the droplets will not be substantially affected by droplet viscosity. This conclusion should be considered with caution, however because the response of a droplet to a single short-term event may not align with the behaviour over the large number of events required to produce correlations at equilibrium conditions.

4.3.1. Definition of Time Scale

As in the modelling of other transient processes, the selection of an appropriate time scale was expected to be important in determining break-up conditions. The most basic time scale is the residence time in the orifice $2\delta/U_{orf}$, but it depends only on the channel velocity since geometry is constant. Droplet break-up is observed to depend on more than just a channel velocity; the time scale must also capture the effects of droplet diameter and fluid properties that define the physics of the problem. Interpretation of the data with various time scales may yield physical insights into the relevant breakage mechanisms.

One starting point for this consideration is the equation of motion as applied to a single solid particle. A simplified form is shown as Equation 4.3-2. The particle acceleration is the only term on the left side of the equation. The right hand side of the equation shows fluid drag, buoyancy, and apparent mass (resistance resulting from displacement of the surrounding fluid) terms. Particle properties will be subscripted *d* (same subscript as dispersed phase), while the surrounding fluid will have the subscript *c* (same subscript as continuous phase). $A_{c,p}$, V_p, and C_D are the cross-sectional area, volume, and drag coefficient of the particle. The velocity $\vec{u}_p$ is the velocity of the particle relative to the surrounding fluid. Note that the gravitational vector $\vec{g}$ is defined to be positive in the direction of positive particle relative velocity $\vec{u}_p$.

$$\rho_d V_d \frac{d\vec{u}_p}{dt} = -\frac{1}{2} C_D \rho_c A_{c,p} |\vec{u}_p| \vec{u}_p + (\rho_d - \rho_c) V_d \vec{g} - \frac{1}{2} \rho_c V_d \frac{d\vec{u}_p}{dt} \qquad (4.3\text{-}2)$$

If the velocity, time, and gravity variables are scaled, the drag and apparent mass terms can be combined, as shown in Equation 4.3-3. The velocity scale U_t becomes the terminal velocity shown in Equation 4.3-4. The particle relaxation time t_{scale}, shown in Equation 4.3-5, becomes a function of the terminal velocity.

$$\frac{d\vec{u}_p^*}{dt^*} = -\left|\vec{u}_p^*\right|\vec{u}_p^* + \vec{g}^* \qquad \vec{u}_p^* = \frac{\vec{u}_p^*}{U_t} \qquad t^* = \frac{t}{t_{scale}} \qquad \vec{g}^* = \frac{\vec{g}}{g} \tag{4.3-3}$$

$$U_t^2 = 2\frac{(\rho_d - \rho_c)g}{C_D\rho_c}\frac{V_p}{A_{c,p}} \tag{4.3-4}$$

$$t_{scale} = \frac{U_t}{g}\left(\frac{\rho_d + \rho_c/2}{\rho_d - \rho_c}\right) \tag{4.3-5}$$

The drag coefficient, the ratio of drag force to the inertial scale $\frac{1}{2}\rho_c A_{c,p} u_p^2$, is difficult to quantify without additional experiments or simulations. A particular object's drag coefficient C_D generally varies with Reynolds number and that object's surface roughness. Even for a simple object such as a sphere, the flow pattern evolves with Reynolds number in a complicated manner, caused in large degree by changes in flow separation behaviour. An illustration of a sample drag coefficient curve for a smooth sphere is shown in Figure 4.15, where Re_{sph} is the Reynolds number based on the sphere's terminal velocity and diameter.

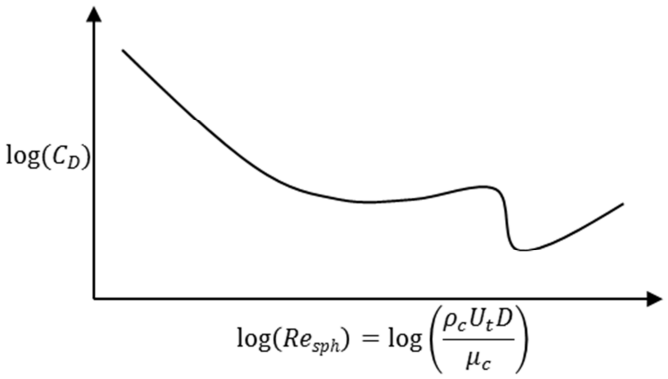

Figure 4.15. Qualitative relationship between drag coefficient and Reynolds number for a smooth sphere. Reproduced from *Welty et al.* (2008).

For a solid sphere in Stokes flow conditions, the terminal velocity can be calculated analytically. The corresponding drag coefficient is $C_D = 24/Re_{sph}$. Substituting this into Equations 4.3-4 and 4.3-5, the Stokes particle relaxation time shown in Equation 4.3-6 is developed (Lumley, 1957; Calabrese, 1975; Calabrese & Middleman, 1979).

$$t_{St} = \frac{D^2(\rho_d + \rho_c/2)}{18\mu_c} \tag{4.3-6}$$

For a fluid particle, the time scale becomes further complicated by the internal circulation and deformation. The time scale could therefore include viscous and interfacial components. Figure 2.5 as presented in Clift *et al.* (1978) is a regime plot relating Reynolds, Eötvös (equivalent to Bond number), and Morton numbers (*Re*, *Eo*, and *M*, respectively) for inviscid fluid particles moving at terminal velocity through a quiescent fluid. Using this velocity in Equation 4.3-5 yields a fluid particle relaxation time, denoted as t_{fl}. To automate calculation of the terminal velocity, the region of the plot necessary for the current work (generally $Eo < 1$) was digitized

and extended assuming continuing linearity between the log(*Re*) and log(*Eo*) for *Eo* < 0.01; this information is presented in Appendix E.

A time scale can also be established from the physics of droplet oscillation. For two inviscid fluids, the frequency of the n^{th} oscillation mode, denoted as Ω_n, is given as Equation 4.3-7 (Lamb, 1932). Higher oscillation modes tend to damp relatively quickly, so the second oscillation mode (the lowest mode) is of primary interest for droplet break-up. The oscillation time scale is then the inverse of the oscillation frequency, as shown in Equation 4.3-8 for the second oscillation mode. Miller & Scriven (1968) provide more information on oscillation frequencies for different fluid conditions.

$$\Omega_n = \sqrt{\frac{8\sigma n(n-1)(n+1)(n+2)}{D^3((n+1)\rho_d + n\rho_c)}} \tag{4.3-7}$$

$$t_{osc} = \frac{1}{\Omega_2} = \sqrt{\frac{D^3(3\rho_d + 2\rho_c)}{192\sigma}} \tag{4.3-8}$$

The eddy life time may also serve as a useful time scale if turbulent eddies are of importance to the break-up mechanisms. The eddy life time is the ratio of turbulence kinetic energy to turbulence dissipation rate as shown in Equation 4.3-9. Turbulence kinetic energy and turbulence dissipation rate typically scale with the square and cube of superficial orifice velocity, respectively. The eddy time is then proportional to the droplet diameter divided by the orifice velocity U_{orf}. It should be noted, however, that the simulation results for turbulence kinetic energy and

turbulence dissipation rate presented in Section 3.2.3 and Appendix B scaled only moderately well with the square and cube of velocity.

$$t_{eddy} = \frac{k}{\varepsilon} \propto \frac{D}{U_{orf}} \tag{4.3-9}$$

Yet another time scale can be formed based on the spring and dashpot break-up models. These models use Hookean spring model with a Newtonian dashpot model as shown in Equation 4.3-10 to represent the contributions of interfacial tension and droplet viscosity to the cohesive stresses (Das, 1996). θ is a dimensionless deformation parameter, where $\theta = 1$ at break up. Assuming $\theta = 0$ at $t = 0$, θ can be integrated and re-arranged to the form showed in Equation 4.3-11. This produces the time scale shown as Equation 4.3-12 within the exponential term representing the delay in deformation caused by the droplet's internal viscosity. However, note that because the CO70FG droplets and air bubbles have orders of magnitude difference in their viscosities, analyses with the spring and dashpot time scale could not collapse the droplet and bubble breakage behaviour into a single model. For that reason, results for this time scale will not be presented in this work.

$$\tau_{dis} = \frac{\sigma}{D}\theta + \mu_d \frac{d\theta}{dt} \tag{4.3-10}$$

$$\theta = \frac{\tau_{dis} D}{\sigma}\left[1 - \exp\left(-\frac{\sigma}{\mu_d D}t\right)\right] \tag{4.3-11}$$

$$t_{s-d} = \frac{\mu_d D}{\sigma} \tag{4.3-12}$$

Each time scale weighs the droplet diameter, dispersed phase properties, and continuous phase properties differently. The definition of the four time scales included in the breakage analyses are summarized in Table 4.2. A sample time scale for a CO70FG droplet and air bubble with D = 700 μm in the Re_{ch} = 10,000 turbulent flow scenario (U_{orf} = 1.65 m/s) is also provided.

Table 4.2. Summary of time scale definitions.

Time Scale	**Time Scale Definition**	**Sample Time Scale D = 700 μm U_{orf} = 1.65 m/s**	
		CO70FG Droplet	**Air Bubble**
Stokes Particle Relaxation Time	$t_{St} = \frac{D^2(\rho_d + \rho_c/2)}{18\mu_c}$	37 ms	14 ms
Fluid Particle Relaxation Time	$t_{fl} = \frac{U_t}{g}\left(\frac{\rho_d + \rho_c/2}{\rho_d - \rho_c}\right)$	17 ms	4.7 ms
Oscillation Time	$t_{osc} = \sqrt{\frac{D^3(3\rho_d + 2\rho_c)}{192\sigma}}$	0.40 ms	0.23 ms
Eddy Time	$t_{eddy} = \frac{D}{U_{orf}}$	0.42 ms	0.42 ms

Part of the goal of the analyses is to determine which of the time scales best suits the data collected, but some comments can be made with respect to their form. The break-up of CO70FG oil droplets and air bubbles is markedly different at equivalent conditions, so the eddy time scale was not expected to produce a good model. The remaining three time scales have different relationships to the droplet

diameter and fluid properties; it is not clear from inspection which will be of greatest advantage for modelling of droplet break-up.

4.3.2. Definition of Velocity Scale

The appropriate velocity scale for the break-up of droplets depends on the regime of flow and the size of the droplet. The current study tests three velocity scales, each based on an aspect of the flow field. Equation 4.3-13 is the most commonly-encountered velocity scale for the break-up of droplets in the inertial subrange. Equation 4.3-14, where $\dot{\gamma}$ is the magnitude of the strain rate tensor and $\dot{\gamma}D$ represents a velocity difference across the droplet, is proposed in the current study as being more relevant for droplets with diameters on the order of the macroscale of turbulence. Using shear rate in place of strain rate magnitude was found to produce similar results and so is not reported. Finally, the square root of turbulence kinetic energy could be used as a velocity scale, as shown in Equation 4.3-15.

$$U_{inertial} \propto (\varepsilon D)^{1/3} \tag{4.3-13}$$

$$U_{macro} \propto \dot{\gamma} D \tag{4.3-14}$$

$$U_{kinetic} \propto \sqrt{k} \tag{4.3-15}$$

Before conducting Weber number calculations, a refined droplet trajectory database was formed. Each basic droplet trajectory was temporally refined into 0.01 ms increments using linear interpolation between the previously-recorded droplet centroids (see Section 2.3.3). For each point in the refined trajectory, the

various flow field variables (velocities, turbulence kinetic energy, turbulence dissipation rate, strain rate magnitude, components of strain rate tensor) were recorded.

To calculate the local Weber number, a purpose-built MATLAB script was developed to conduct the following process:

1) Select the time scale, velocity scale, and scaled exposure time.
2) Load the refined droplet trajectory.
3) For each droplet, calculate the time scale.
4) For each droplet, calculate the dimensional exposure time (the scaled exposure time multiplied by the time scale calculated in Step 3).
5) For each droplet trajectory, average the flow field variable over the dimensional exposure time starting at each point in the trajectory until the point of break-up.
6) For each droplet, take the maximum average of the flow field variable and use it to calculate the maximum local Weber number.

This process produces a single local Weber number for each droplet. This process was repeated for each velocity scale, time scale, and scaled exposure time to form the large Weber number data set used in the analyses presented in Sections 4.3.3 and 4.3.4.

Example: Consider the calculation of the local Weber number based on Stokes particle relaxation time, strain-rate magnitude, and scaled exposure

time t^*_{exp} of 0.01 for an air bubble with D = 843 μm. Its time scale is t_{St} = 19.7 ms (Equation 4.3-5). The exposure time is t_{exp} = 0.197 ms. The temporal resolution of the refined trajectory is 0.01 ms, so 0.197 ms corresponds to 20 points of the trajectory. The local Weber number is thus based on the highest 20-point-average strain rate magnitude experienced by the droplet prior to break-up.

4.3.3. Local Weber Number versus Averaging Time

The investigation into the relationship between Weber number and exposure time was based on the local Weber number versus scaled exposure time curves. The curve for each droplet was overlaid on a single plot to see behavioural trends for the broken and unbroken droplets. Figure 4.16 shows the results for the CO70FG droplets, while Figure 4.17 shows the results for air bubbles. For these example plots, the velocity scale was $\dot{\gamma}D$ and the time scale was the fluid particle relaxation time. Both plots include data at both of the investigated channel Reynolds numbers. Red lines represent droplets or bubbles that have broken due to interaction with the orifice or the jet edge, either breaking or becoming highly deformed before reaching the end of the low pressure wake region. Blue lines represent droplets or bubbles that survived beyond the extent of the low pressure wake region; only about 8% of the droplets and bubbles broke beyond this point.

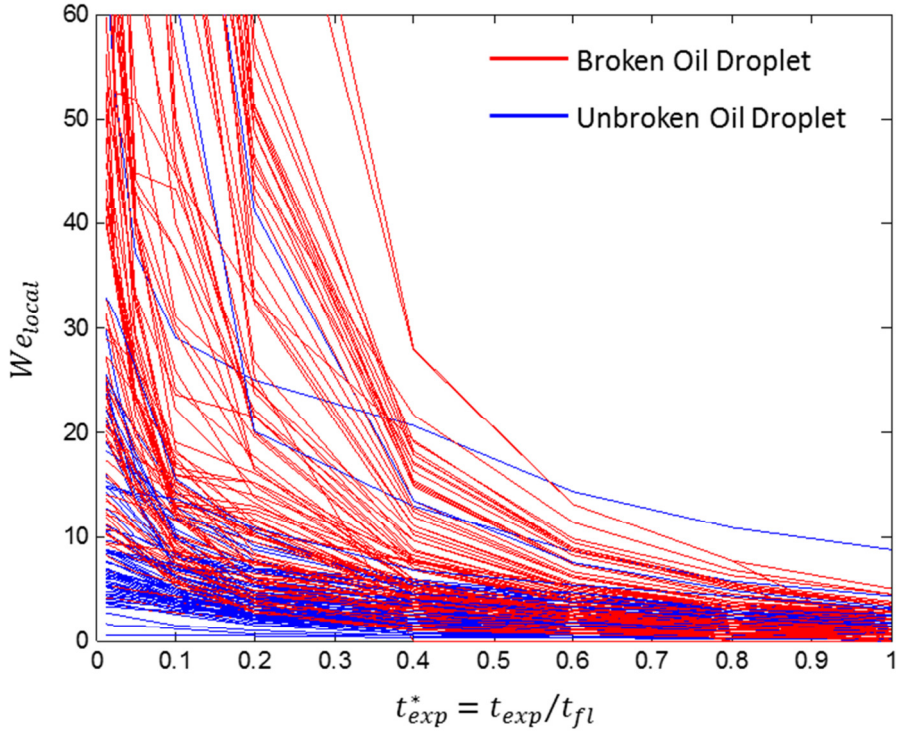

Figure 4.16. Maximum local Weber number along droplet trajectory as a function of scaled exposure time for CO70FG droplets at Re_{ch} = 10,000 and 14,000.

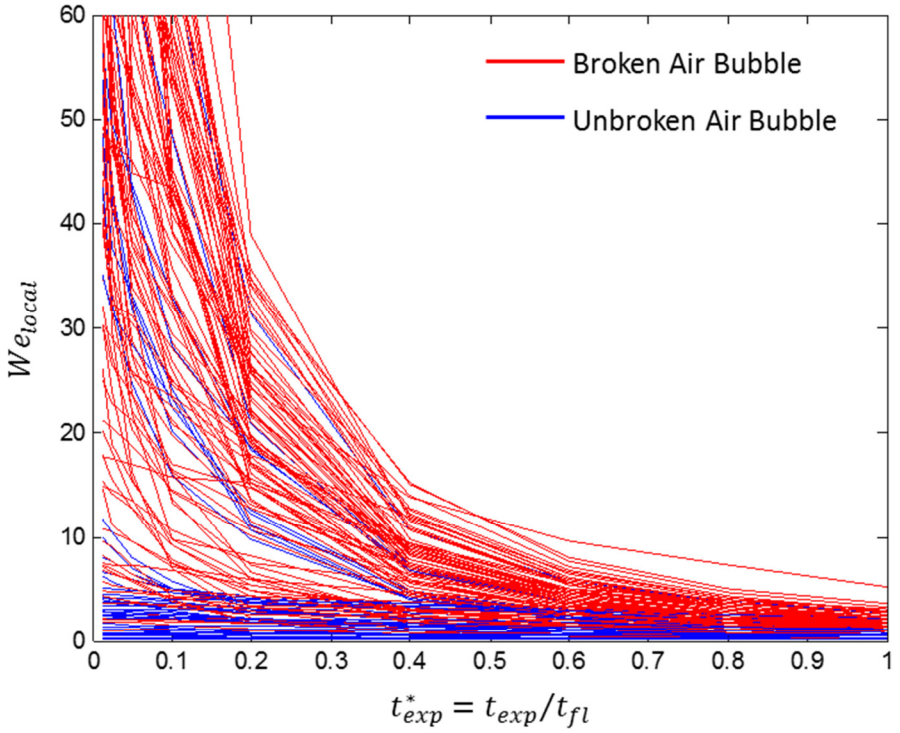

Figure 4.17. Maximum local Weber number along droplet trajectory as a function of dimensionless exposure time for air bubbles at Re_{ch} = 10,000 and 14,000.

Due to turbulence and accumulated errors in the measurements and processing, the red and blue lines are intermixed to moderate degree. While a large portion of the blue lines are below a large portion of the red lines, particularly at the lower time averages, the groupings are not clear enough to define a critical Weber number curve. Other combinations of velocity and time scale were also investigated, but all showed qualitatively similar results and similar degrees of intermixing.

Despite the lack of success with this methodology, two conclusions can be made with these results. First, the blue lines on both oil and air plots are roughly in the same range. This lends support to the dynamical interpretation of Levich (1962) and its importance in droplet break-up. Second, at longer exposure times, the lines are more intermixed. The break-up is thus better characterized by the shorter exposure times.

4.3.4. Breakage Probability versus Local Weber Number

Evaluating breakage probability against local Weber number was an alternate method of identifying which of the time and velocity scales are of greatest importance. A probabilistic approach is necessary since the simple RANS-generated flow field does not provide information on turbulent fluctuations. In other words, the breakage probability represents the likelihood of a droplet encountering a turbulent eddy with the necessary strength to cause break-up.

In this section, ***it is assumed that there is a single characteristic scaled exposure time that best correlates the droplet breakage***. If the appropriate time

and velocity scales are selected, the breakage probability plot should have certain features. First, the behaviour of the plots for both dispersed phase materials should be the same. Second, the probability of break-up at high Weber numbers should approach 1.0. If the characteristic exposure time is too short, the maximum local Weber numbers will depend on sharp spikes in the disruptive stress. These spikes may not be of sufficient duration to actually break the drop, resulting in a large quantity of unbroken droplets with high Weber numbers. Third, the breakage probability at low Weber numbers should approach zero. If too high a characteristic exposure time is selected, unbroken droplets experiencing a subcritical disruptive stress for a long period of time will have a higher Weber number than broken droplets that have experienced supercritical disruptive stress for the correct amount of time. This leads to high breakage probabilities at low Weber numbers.

To evaluate the performance of a particular breakage model—which is dependent on the selected velocity scale, time scale, and scaled exposure time used to calculate each droplet's Weber number—droplets were first categorized into Weber number bins. For each bin, the fraction of broken droplets, taken to be synonymous with the breakage probability, was recorded. A bin was only accepted for the model fitting if it contained at least ten measurements. The data was then fit to the breakage probability versus Weber number models described in Equations 4.1-7 to 4.1-9. The root-mean-square error, weighted with the number of droplets in each bin, was recorded as the metric by which the model fitness was ultimately judged.

In addition to the velocity scale, time scale, and scaled exposure time, the bin structure is a numerical modelling choice that potentially affects the model fitness. With a lower number of bins, each bin has a greater number of points and so should be a better statistical representation. However, this also results in wider bins, making it harder to show sharp changes in breakage probability with Weber number. On the other hand, with a greater quantity of narrow bins, the resolution of the breakage probability curve is potentially better, but the statistics for each bin become worse and the percentage of droplets in discarded bins (bins with less than ten measurements) increases. For this study, thirteen bin structures (9 to 21 bins) were tested for each combination of the physical scales. In all cases, the bins spanned the available range of Weber numbers and had a fixed geometric progression ratio for the nominal bin values. For example, for twelve bins to span a range of nominal bin values from 1 to 100, a geometric progression ratio of 1.468 would be required ($1.468^{12} = 100$). All presented plots are based on nine to fourteen bins; these bin structures yield lower errors than other bin structures while generally utilizing at least 75% of the droplets.

The remainder of this section shows a number of breakage probability plots comparing different time scales, velocity scales, and scaled exposure times. Experimental data for CO70FG oil droplets and air bubbles are indicated with open squares and triangles, respectively. In addition, the three probability models discussed previously—one-parameter exponential, two-parameter, and

power/exponential (Equations 4.1-9 to 4.1-11)—are fitted to the data and presented as green, blue, and red dashed lines.

Figure 4.18 illustrates how selection of the choice of velocity scale affects the breakage probability curves, with CO70FG oil droplets and air bubbles presented separately. The Stokes particle relaxation time was used as the time scale, and the scaled exposure time is 0.04. Note that the lower value of the Weber number defined with turbulence dissipation and rate turbulence kinetic energy is because of the difference in the magnitude of the corresponding velocity scales. All three properties produced similar breakage probability curves for the oil droplets. However, the behaviours of the probability curves for CO70FG and air were substantially different when the velocity scales were based on both turbulence properties. This difference occurred for all combinations of time scale and scaled exposure times. On this basis, the velocity scales based on turbulence dissipation rate and turbulence kinetic energy can be discarded. The remainder of the analysis in this section considers $\dot{\gamma}D$ as the appropriate velocity scale.

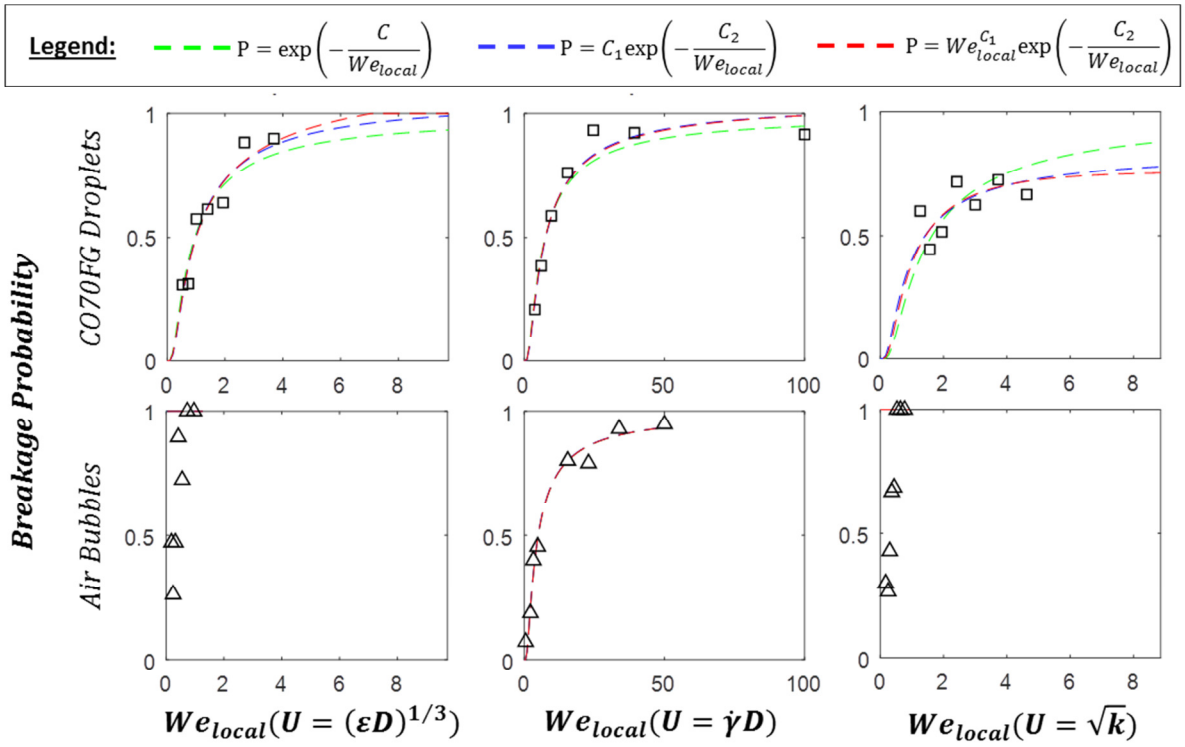

Figure 4.18. Breakage probability versus local Weber number for various time scales. All plots are at a scaled exposure time of t^*_{exp} = 0.04, scaled with the Stokes particle relaxation time.

Figure 4.19 illustrates how the selection of t^*_{exp} influences the breakage probability curve. The velocity and time scales were calculated from strain rate magnitude and the Stokes solid sphere relaxation time, respectively. The lower two exposure times (t^*_{exp} = 0.001 and 0.04), the CO70FG and air curves are qualitatively similar. The lowest exposure time shows one data point at We_{local} = 67 with an abnormally low probability. This suggests that a number of bubbles remain unbroken despite experiencing short-term, high-intensity deformation events. At the highest scaled exposure time (t^*_{exp} = 0.2), the probability curves for CO70FG and air appear to be diverging in their behaviour, indicating that the breakage probability is not well-modelled with the greater exposure times.

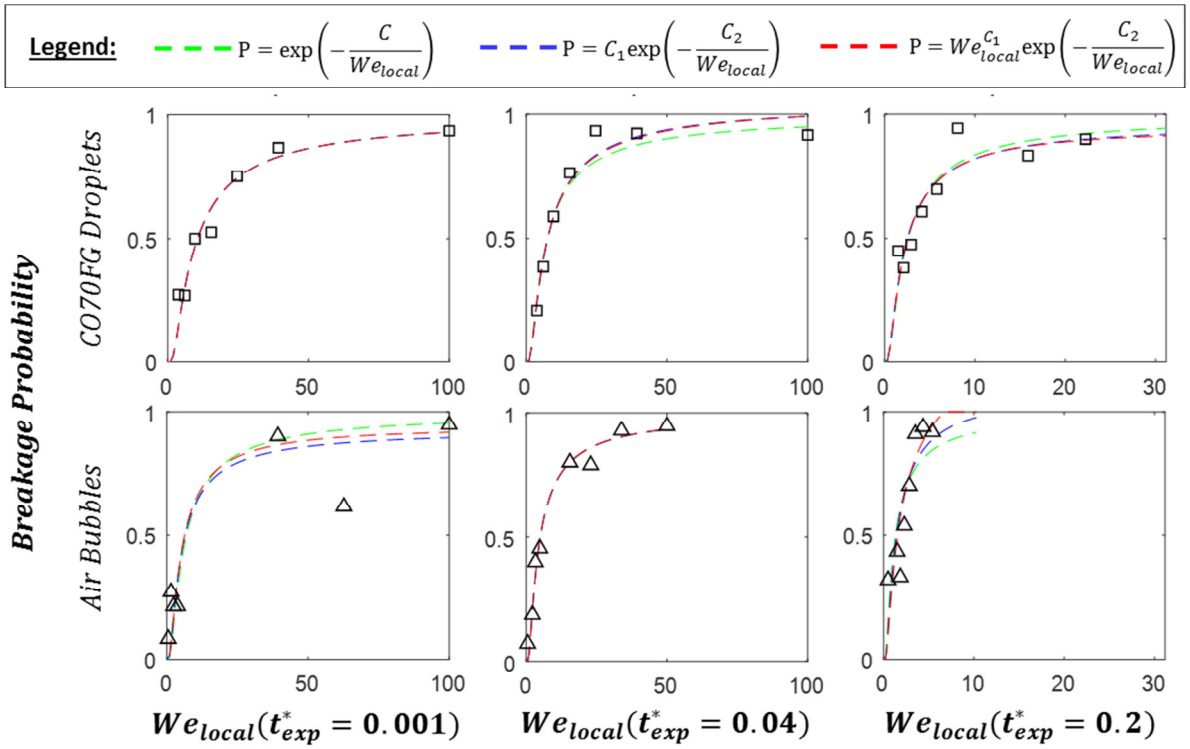

Figure 4.19. Breakage probability versus local Weber number at scaled exposure times of t^*_{exp} = 0.001, 0.04, and 0.2. Local Weber number based on strain rate magnitude. Time scale based on Stokes particle relaxation time.

Figure 4.20 compares breakage probability curves for the four different time scales (see Table 4.2 for a summary of the time scale definitions). The velocity scale is based on the strain rate magnitude. The scaled exposure time was selected to minimize the root-mean-square error (RMSE). Each of the time scales can produce a usable breakage probability model, with Stokes particle relaxation time producing the model with the lowest error. As expected, the eddy time scale breakage model results in the highest error.

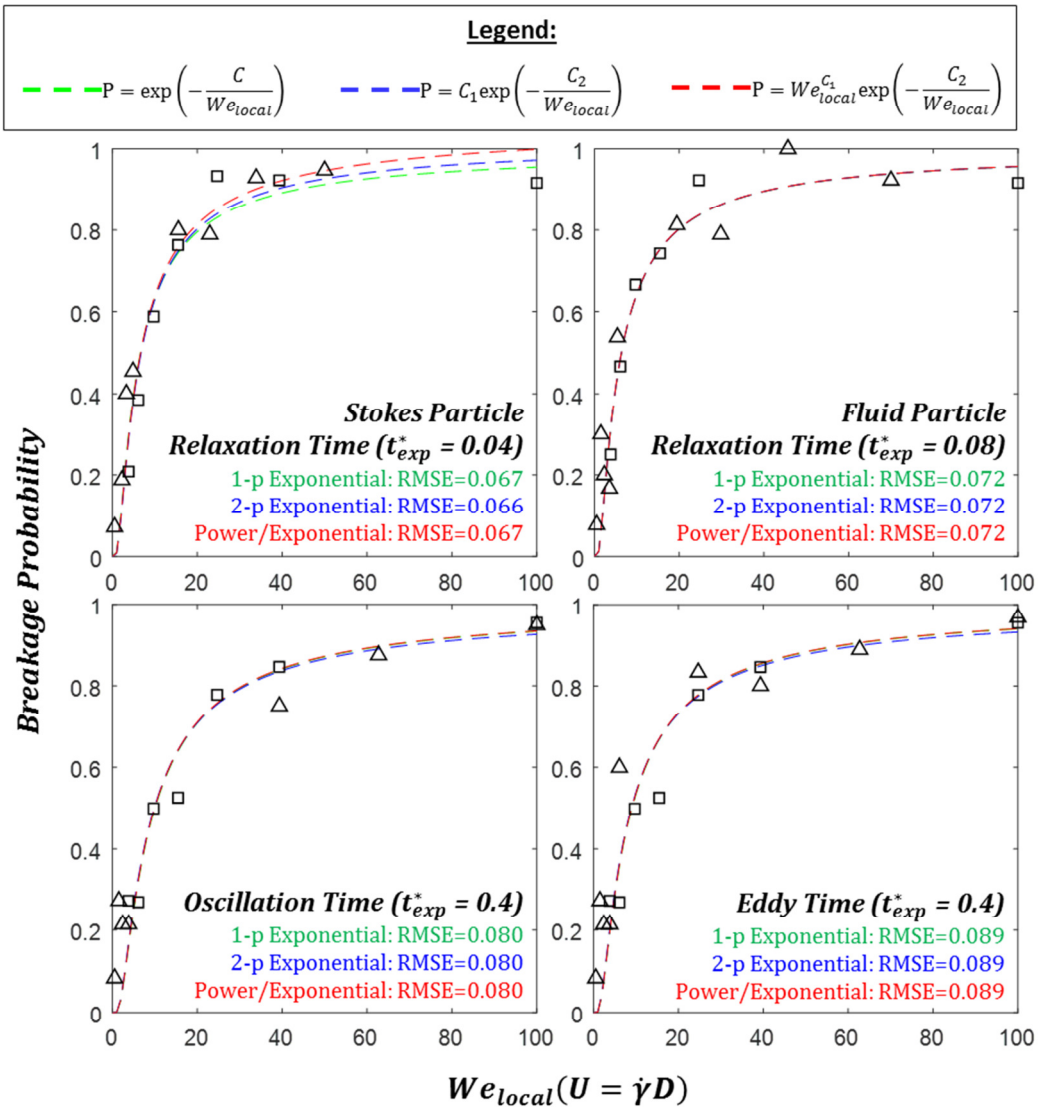

Figure 4.20. Breakage probability versus local Weber number for different time scales. The exposure time is optimized to minimize the RMSE.

While the above analysis has successfully produced breakage probability models and does appear to favour using the Stokes particle relaxation time, it cannot be strongly concluded that this time scale is the most appropriate from a mechanistic standpoint. While the velocity scale could be easily distinguished, the variation in the break-up due to the time scale selection was masked by the variation caused by turbulence. Given that the error associated with each model

were of similar magnitude, choosing the simplest model would be expedient. The recommended model, the 1-parameter exponential model using Stokes particle relaxation time with an exposure time of t^*_{exp} = 0.04, is shown in Equation 4.3-16. It displays a steeper transition to near-100% break-up compared to the oscillation and eddy time models without the complexity of calculating the fluid particle terminal velocity. The models based on the other time scales are also presented in Equations 4.3-17 to 4.3-19.

$$P_{St} = \exp\left(-4.57\frac{\sigma}{(\rho_d\rho_c^2)^{1/3}\dot{\gamma}^2_{t^*_{exp,St}=0.04}D^3}\right), \text{RMSE} = 0.067 \qquad (4.3\text{-}16)$$

$$P_{fl} = \exp\left(-4.40\frac{\sigma}{(\rho_d\rho_c^2)^{1/3}\dot{\gamma}^2_{t^*_{exp,fl}=0.08}D^3}\right), \text{RMSE} = 0.072 \qquad (4.3\text{-}17)$$

$$P_{osc} = \exp\left(-6.91\frac{\sigma}{(\rho_d\rho_c^2)^{1/3}\dot{\gamma}^2_{t^*_{exp,osc}=0.4}D^3}\right), \text{RMSE} = 0.080 \qquad (4.3\text{-}18)$$

$$P_{eddy} = \exp\left(-6.23\frac{\sigma}{(\rho_d\rho_c^2)^{1/3}\dot{\gamma}^2_{t^*_{exp,eddy}=0.4}D^3}\right), \text{RMSE} = 0.089 \qquad (4.3\text{-}19)$$

4.4. Droplet Break-up based on Upstream Conditions

The Weber number based on local flow conditions is useful when detailed deformation field and droplet path information are available, but obtaining this information often requires extensive computational and/or experimental effort. In many cases, this advanced level of information is not available. One simplification that can be applied to this system is to correlate the probability of break-up against

droplet properties upstream of the orifice, where droplet size and trajectory distributions can more easily be measured or estimated.

4.4.1. Definition of Upstream Weber Number

The most complicated variable in the local Weber number defined in Section 4.3.3 is the characteristic strain rate magnitude. In theory, every parameter in the system could have an independent effect on the droplet speed and direction, making calculation of the strain rate magnitude challenging. However, the following observations and data accrued in the current project are of use for defining break-up based on the upstream droplet distributions:

- As shown in Section 3.2.3, the deformation field (in terms of both strain rate magnitude and shear rate) scales well with orifice velocity.
- Droplets approaching the orifice from the channel centre are much less likely to break when compared with droplets that approach the orifice near the channel wall. Qualitatively, this is expected since the strain rate magnitude in the centre region of the orifice is relatively low compared to the strain rate near the orifice surface and corners.
- As noted in Section 4.2, the paths through the orifice and the region immediately beyond do not seem to be strongly affected by droplet diameter or the channel Reynolds number.
- The oil droplets and air bubbles do have differing trajectories through the orifice. Due to the pressure differential across the leaning jet, the droplets

migrate laterally toward the lower pressure side (i.e., the side with the smaller wake region). This effect is moderately dependent on Reynolds number, with greater migration occurring at lower Reynolds number.

These observations suggest that droplet path (and thus the dependence of strain rate on droplet path) is dependent primarily on the incoming trajectory and the droplet material. If this is so, then the locally-derived strain rate can be replaced with a flow-dependent characteristic strain rate if material properties and the incoming trajectory are accounted as additional variables. Figure 4.21 illustrates this concept, with the probability of break-up forming a series of contours dependent on an upstream Weber number We_{upstr} (dependent on diameter and the flow-dependent strain rate) and the dimensionless incoming trajectory $y^*_{inc} = y_{inc}/\delta$, where y_{inc} is the incoming trajectory (-6.35 mm $\leq y_{inc} \leq 6.35$ mm) and $\delta = 3.175$ mm is the half-width of the orifice. The dimensionless incoming trajectory can therefore have values between –4 and 4. The orifice opening is located at $-1 \leq y^*_{inc} \leq 1$. The predicted breakage probability increases with increases in the droplet diameter, the characteristic strain rate, and distance from the channel centre. Some asymmetry is expected due to the lateral migration, resulting in higher break-up probabilities on when y^*_{inc} is negative. The value of the probability reflects differences in local conditions caused by the overall droplet path and turbulence.

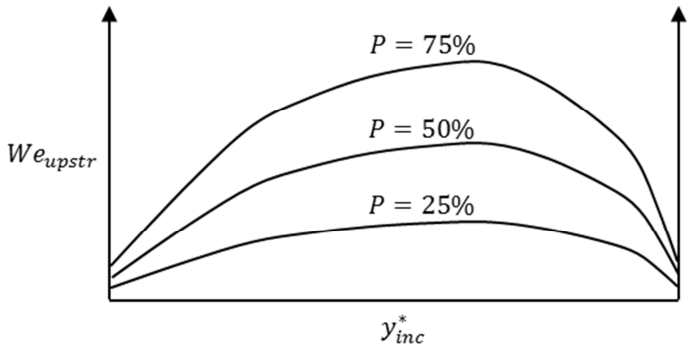

Figure 4.21. Illustration of breakage probability P versus incoming trajectory y^*_{inc} and upstream Weber number We_{upstr} for a particular droplet material.

The form of the upstream Weber number is shown as Equation 4.4-1. Instead of being dependent on a path-dependent strain rate, it depends instead of U_{orf}/δ, which can be interpreted as a characteristic strain rate inside the orifice.

$$We_{upstr} = \frac{(\rho_c^2 \rho_d)^{1/3} D^3}{\sigma} \left(\frac{U_{orf}}{\delta}\right)^2 \tag{4.4-1}$$

4.4.2. Breakage Probability Contour Plots

To determine the breakage probability, both the Phantom and Pulnix data sets were plotted onto We_{upstr} versus y^*_{inc} plots as shown in Figure 4.22 and Figure 4.23 for oil droplets and air bubbles, respectively. Each marker represents one imaged droplet. The colour of the marker reflects the Reynolds number of the channel flow, while the marker type ('X' or 'O') indicates whether that droplet was broken.

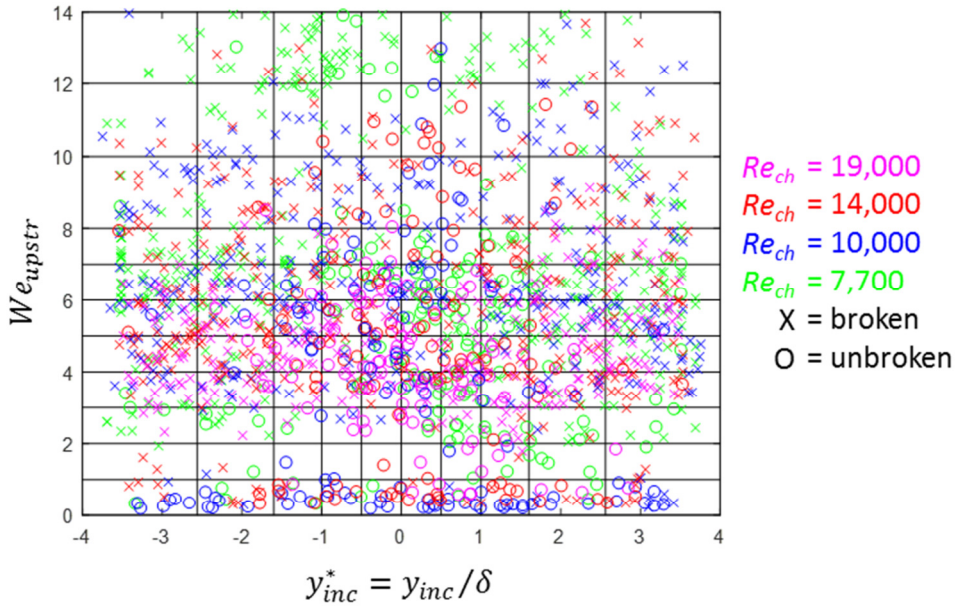

Figure 4.22. Upstream Weber number We_{upstr} versus incoming trajectory y^*_{inc} for CO70FG droplets.

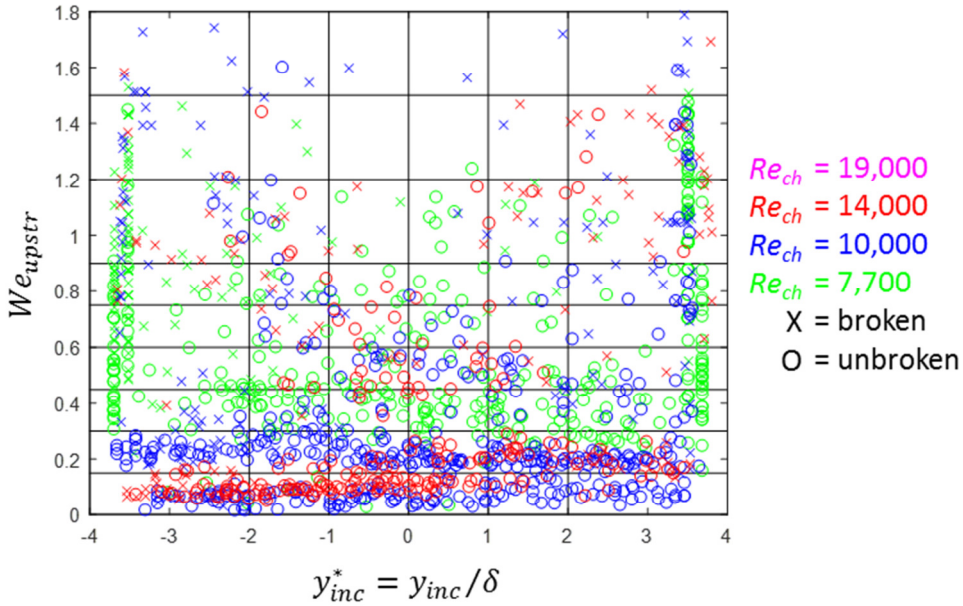

Figure 4.23. Upstream Weber number We_{upstr} versus incoming trajectory y^*_{inc} for air bubbles.

The probability was determined by discretizing the upstream Weber number and the incoming trajectory, resulting in bins each containing a number of broken

and unbroken droplets. The discretization schemes, shown in Figure 4.22 and Figure 4.23, were selected with two priorities in mind: 1) capturing the probability gradients and 2) maintaining at least five droplets in each bin for as much of the domain as possible. The break-up probability for each bin was the number of broken droplets divided by the total number of droplets in the bin. The resulting probabilities are shown in Figure 4.24 for both the oil droplets and air bubbles. Note that a few bins are not coloured; these have total droplet quantities of less than five. To smooth the contours, the probabilities for each y^*_{inc} were fitted to an exponential curve; an example of this is shown in Figure 4.25. In the smoothing process, each bin is weighted evenly.

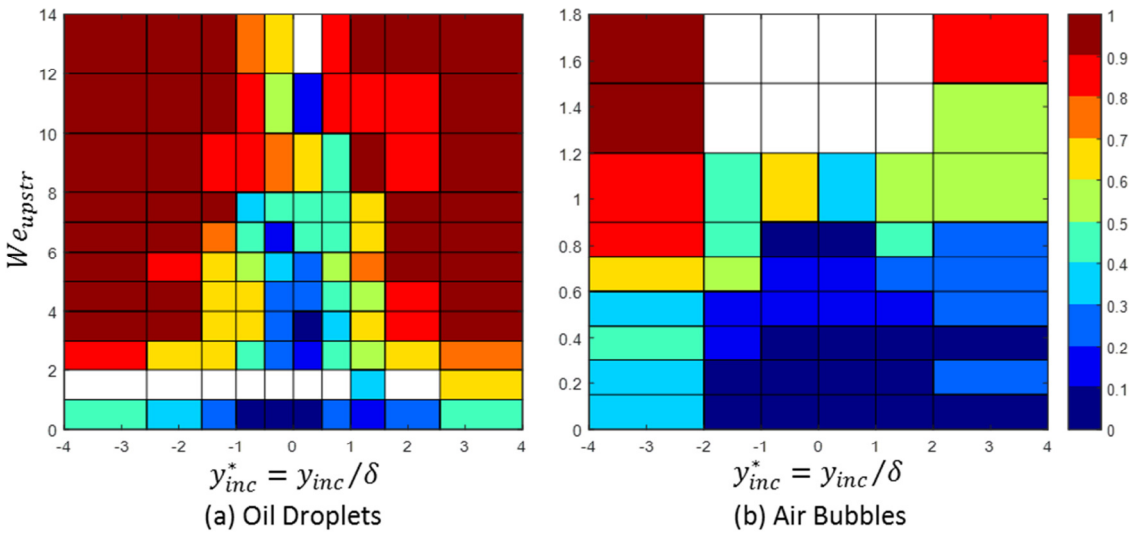

Figure 4.24. Discretized breakage probability for as a function of upstream Weber We_{upstr} number and the incoming trajectory y^*_{inc}.

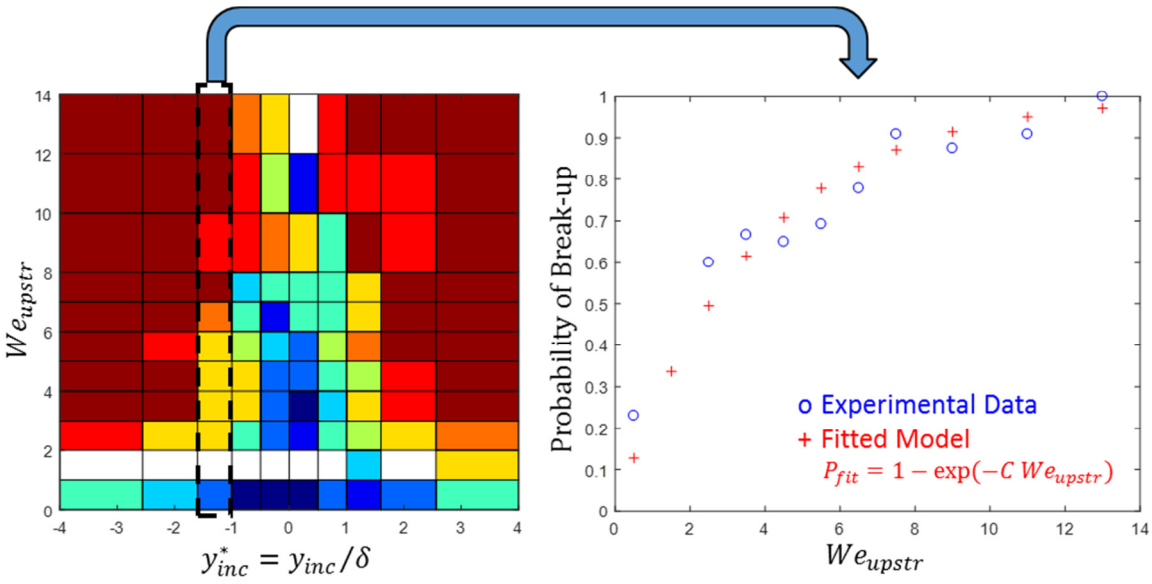

Figure 4.25. Example of contour smoothing routine.

Figure 4.26 and Figure 4.27 are the smoothed contour plots for the break-up of oil droplets and air bubbles, respectively. The probability values are coloured in ten contour levels. Both contour plots show that the breakage is asymmetric; both oil droplets and air bubbles are more likely to break when they approach the orifice from the $y^*_{inc} < 0$ region. This difference is small in the case of oil droplets and extreme in the case of the air bubbles. The asymmetry in the breakage probabilities is caused by the pressure difference across the jet. In addition to stabilizing the lean of the jet, the pressure imposes a lateral force on the droplet, causing migration in the negative y direction. For droplets with $y^*_{inc} > 0$ incoming trajectories, the pressure differential pushes the droplet toward the centre of the jet, away from the high shear regions in and extending from the orifice; this reduces both the duration and the strength of the deformation field experienced by the droplet. On the other hand, when the droplet approaches the orifice with a $y^*_{inc} < 0$ incoming trajectory, the pressure difference pushes or keeps the droplet in the highest shear regions in

and just after the orifice, resulting in a greater probability of break-up. This effect is more pronounced with the air bubbles because of their lower mass.

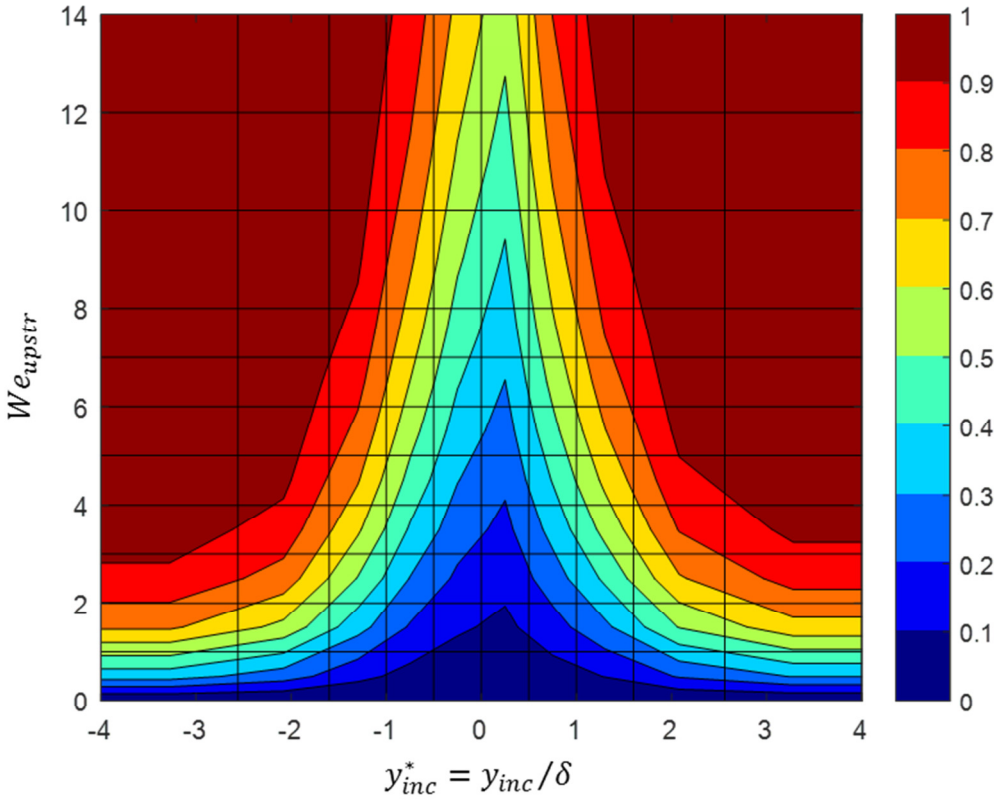

Figure 4.26. Breakage probability as a function of upstream Weber number We_{upstr} and the incoming trajectory y^*_{inc} for CO70FG droplets.

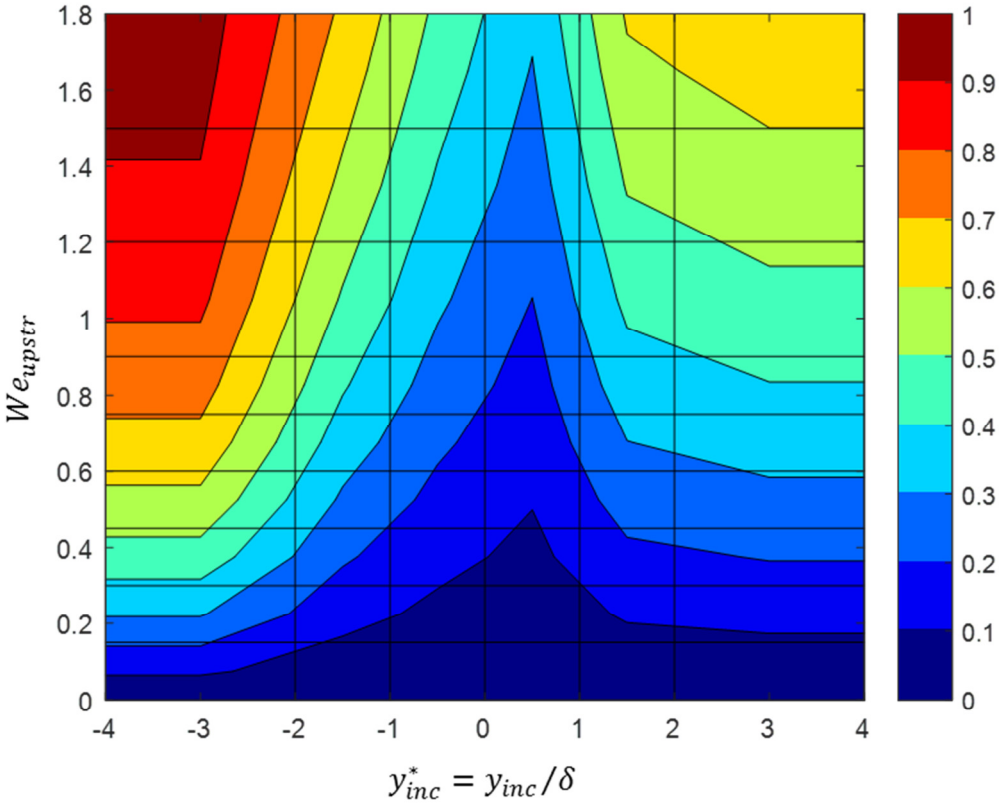

Figure 4.27. Breakage probability as a function of upstream Weber number We_{upstr} and the incoming trajectory y^*_{inc} for air bubbles.

4.4.3. Example of Usage for Breakage Probability Plots

This subsection demonstrates how to use the breakage probability plots by re-applying them to the collected Phantom and Pulnix data sets. As a detailed example, the oil droplet data set at the Re_{ch} = 10,000 will be analyzed using the probability plots. The final results for all scenarios will be presented at the end of the subsection.

Figure 4.28 shows how the analysis would be started. The contour plot is first discretized. The probability value in the centre of each bin is tabulated as the

bin's characteristic probability. The known droplet distribution is organized into the bins; the total quantity in each bin is recorded.

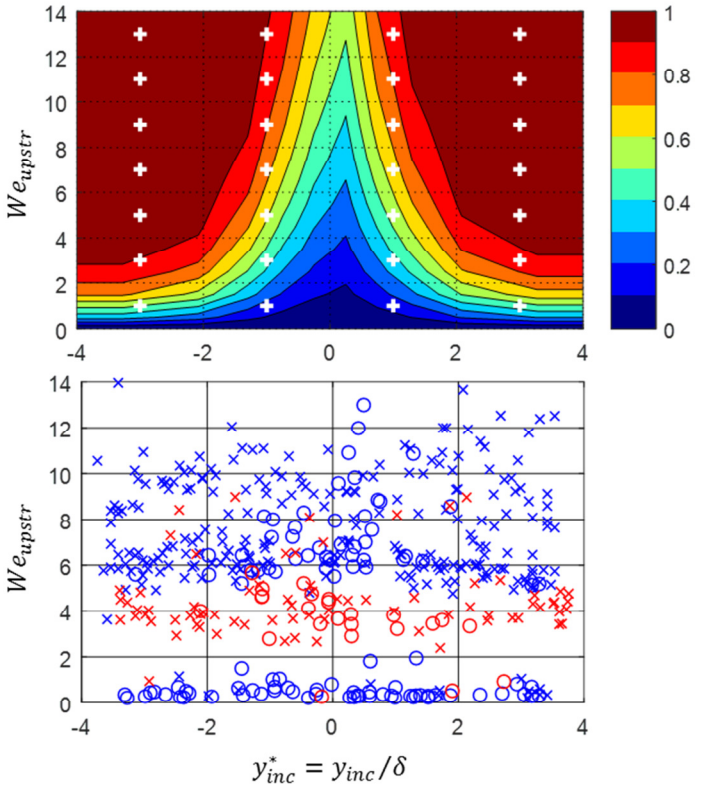

Breakage Probability		y^*_{inc}			
		-3	-1	1	3
We_{upstr}	13	0.95	0.90	0.85	0.95
	11	0.95	0.85	0.80	0.95
	9	0.95	0.80	0.75	0.95
	7	0.95	0.75	0.65	0.95
	5	0.95	0.65	0.55	0.95
	3	0.85	0.45	0.35	0.85
	1	0.50	0.15	0.15	0.45

Droplet Quantity		y^*_{inc}			
		-3	-1	1	3
We_{upstr}	13	1	1	1	4
	11	7	8	13	7
	9	19	21	23	11
	7	22	31	28	15
	5	23	31	20	36
	3	13	13	12	8
	1	13	19	25	14

Figure 4.28. Example for calculating break-up fraction using the probability contour plots. CO70FG droplets in Re_{ch} = 10,000. Upstream droplet size and trajectory are as per the experimental measurements. Red and blue markers correspond to observations from the Phantom and Pulnix data sets, respectively.

The total number of droplets in each bin is multiplied by the corresponding breakage probability to predict the number of broken droplets in that bin. The result is presented in Figure 4.29. For this scenario, the actual droplet break-up is well-predicted by the contour plot.

Actual Drops Broken		y^*_{inc}			
		-3	-1	1	3
We_{upstr}	13	1	1	0	4
	11	7	8	10	7
	9	19	19	17	11
	7	22	20	18	15
	5	22	14	17	34
	3	12	11	4	7
	1	2	2	3	6

Actual Droplets Broken = 313/439
Actual Break-up Fraction = 71%

Predicted Drops Broken		y^*_{inc}			
		-3	-1	1	3
We_{upstr}	13	1.0	0.9	0.9	3.8
	11	6.7	6.8	10.4	6.7
	9	18.1	16.8	17.3	10.5
	7	20.9	23.3	18.2	14.3
	5	21.9	20.2	11.0	34.2
	3	11.1	5.9	4.2	6.8
	1	6.5	2.9	3.8	6.3

Predicted Droplets Broken = 311/439
Predicted Break-up Fraction = 71%

Figure 4.29. Comparison between actual and predicted droplet break-up. CO70FG droplets in Re_{ch} = 10,000. Upstream droplet size and trajectory are as per the experimental measurements.

The results for all seven droplet/flow scenarios are presented in Table 4.3, with the air contour plot discretized in the same manner as the oil contour plot (seven evenly-spaced We_{upstr} bins, four evenly-spaced y^*_{inc} bins). In general, the oil droplet scenarios are well-predicted by the corresponding contour plot. Most of the error was accrued by smaller droplets (lower Weber numbers) at the higher Reynolds number scenarios. These data reside in bins with high probability gradients, so bin refinement can help in these cases. For the break-up of air bubbles, the errors occur due to both smaller droplet sizes and the lateral migration. At lower Reynolds numbers, the lateral migration is stronger than the lateral migration 'average' over the three flow conditions. The actual break-up fraction for droplets approaching on the side of the channel with the high-pressure wake region is consequently lower than the predicted fraction. At higher Reynolds numbers, the opposite is true. This indicates that the breakage probability plot for air bubbles

may benefit from an additional Reynolds number dependence, but the data available is not in sufficient quantity to add another dimension to the analysis.

Table 4.3. Actual versus predicted droplet break-up for all turbulent flow scenarios.

Droplet Material	Re_{ch}	Actual Break-up Fraction	Predicted Break-up Fraction
Crystal Oil 70FG	7,700	71%	78%
	10,000	71%	71%
	14,000	74%	70%
	19,000	69%	66%
Air	7,700	29%	41%
	10,000	27%	22%
	14,000	34%	20%

4.5. Droplet Break-up based on Orifice Conditions

The greatest deformation rates are experienced by the droplet as it passes through the orifice. This does require a higher level of information than the upstream conditions since the trajectory through the orifice must be determined, but measuring and developing this information is still much less intensive than acquiring the detailed local conditions around the droplet for the whole trajectory. The advantage of this approach is that an orifice-based Weber number break-up criterion may be applicable for a wider range of orifice systems, such as orifices of different sizes or multi-orifice plates.

4.5.1. Definition of Orifice Weber Number

In this approach, the orifice-based Weber number is defined by the strain rate magnitude at the intersection of the droplet trajectory within the orifice $y^*_{orf} = y_{orf}/\delta$ and a line located at some depth $z^*_{orf} = z/\delta$ within the orifice. This is shown conceptually in Figure 4.30, where z^*_{orf} is located at an arbitrary location for illustration only.

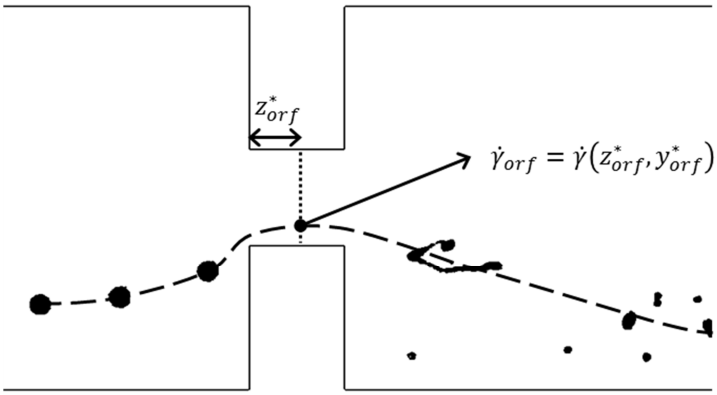

Figure 4.30. The orifice Weber number is based on the strain rate magnitude at the intersection of the droplet trajectory (dashed line) with the dotted line at location z^*_{orf}.

The orifice Weber number is defined in Equation 4.5-1, where $\dot{\gamma}_{orf}$ is the strain rate magnitude at the intersection between z^*_{orf} and the droplet trajectory. An appropriate value of z^*_{orf} was determined through the analysis; this is discussed in the next section. Because the droplet path through the orifice was needed, this analysis is conducted using the Phantom high-speed images only.

$$We_{orf} = \frac{(\rho_c^2 \rho_d)^{1/3} D^3}{\sigma} \left(\dot{\gamma}_{orf}\right)^2 \tag{4.5-1}$$

4.5.2. Breakage Probability Contour Plots

A methodology similar to that employed for the upstream Weber number analysis (see Section 4.4.2) was used for the orifice Weber number analysis. A number of bins for both orifice Weber number and y^*_{orf} were established, and each droplet was placed onto the plot. Figure 4.31 shows the droplets locations based on y^*_{orf} calculated at $z^*_{orf} = 0$. The colour of the marker reflects the channel Reynolds number, while the marker type ('X' or 'O') indicates whether that droplet was broken. The CO70FG oil droplets are moderately-well scattered throughout the We_{orf}-y^*_{orf} domain, with a void in the high-We_{orf}, central y^*_{orf} region due to the low strain rates for trajectories through the centre of the orifice. The air bubbles have a more extreme void, but this is due to the density correction for the Levich stress balance. Despite this, the air bubbles traveling near the corners of the orifice show a wide range of Weber numbers because they often travel much closer to the orifice corners (see Appendix D for droplet trajectories).

These plots were also examined at greater values of z^*_{orf}, ranging from 0.1 to 0.9. With increasing z^*_{orf}, the droplets and bubbles become less scattered because the strain rate magnitude in the central regions drops to zero. The shear is always low in the centre, but the extensional component also becomes low after the top of the orifice separation region has passed. As a result, the droplets in the core region all have near-zero orifice Weber numbers. Only droplets and bubbles travelling closer to the orifice surface can be distinguished by the experienced strain rate magnitude and the droplet diameter. Because of the growing insensitivity of the

orifice Weber number to droplets in the central region, it was considered more useful to base an orifice Weber number on $z^*_{orf} = 0$.

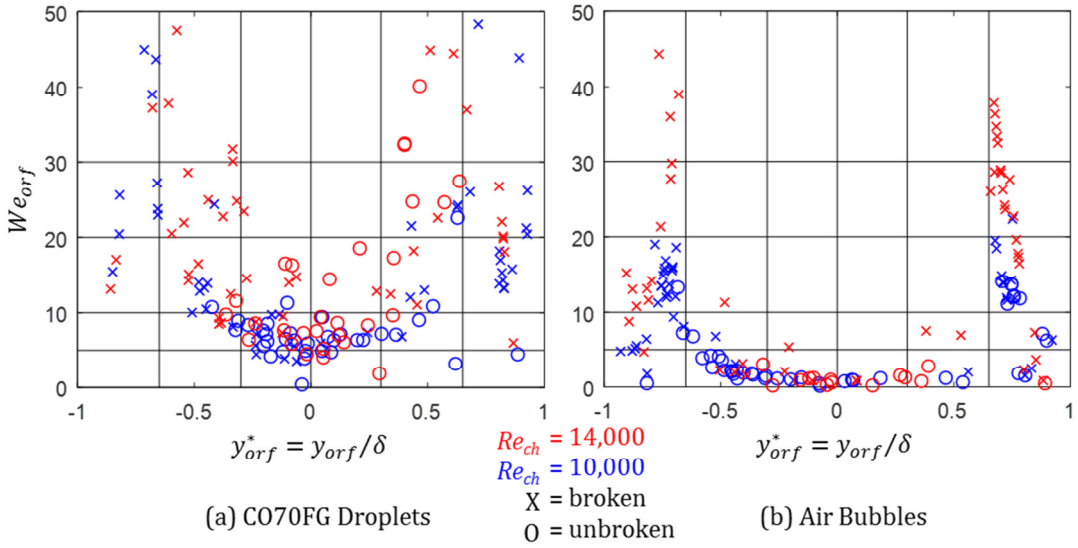

Figure 4.31. Orifice-based Weber number We_{orf}, versus droplet trajectory through $z^*_{orf} = 0$ for both (a) CO70FG droplets and (b) air bubbles. Based on Phantom data only.

Figure 4.32 shows the breakage probability in each bin (analogous to Figure 4.24 for the upstream Weber number). A bin was ignored if it did not contain at least three samples. This plot was smoothed using the same method as with the previous discretized contour plot, but because of the limited number of bins, the smoothing was applied to the nodal data. This provided a slightly greater degree of resolution to the contours.

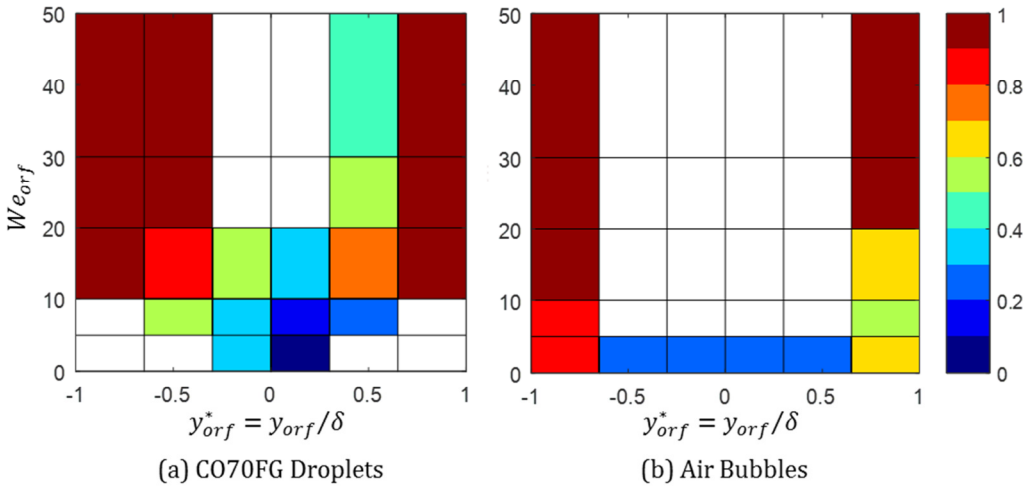

Figure 4.32. Discretized breakage probability as a function of orifice-based Weber number We_{orf} and the trajectory through orifice $y^*_{orf}(z^*_{orf} = 0)$ for both (a) CO70FG droplets and (b) air bubbles.

The final orifice Weber number contour plots are presented as Figure 4.33 for CO70FG droplets and Figure 4.34 for air bubbles. Note that some regions remain blank because of the lack of data. One exception was made for the oil droplet contour plot: the bin centred at roughly $y^*_{orf} = -0.5$ and $We_{orf} = 40$ was considered to be at 100% breakage despite having only two samples. The bin at the immediately lower Weber number was already near 100% breakage, so it is reasonable to assume that at even greater Weber numbers, 100% droplets should also break.

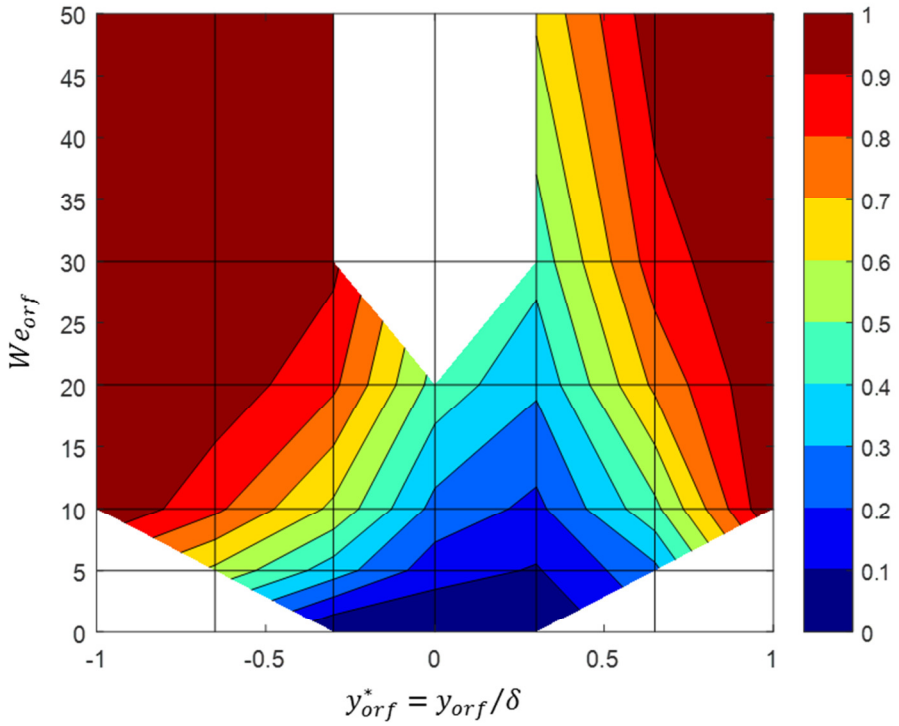

Figure 4.33. Breakage probability as a function of the orifice-based Weber number We_{orf} and the trajectory through orifice $y^*_{orf}(z^*_{orf} = 0)$ for CO70FG droplets.

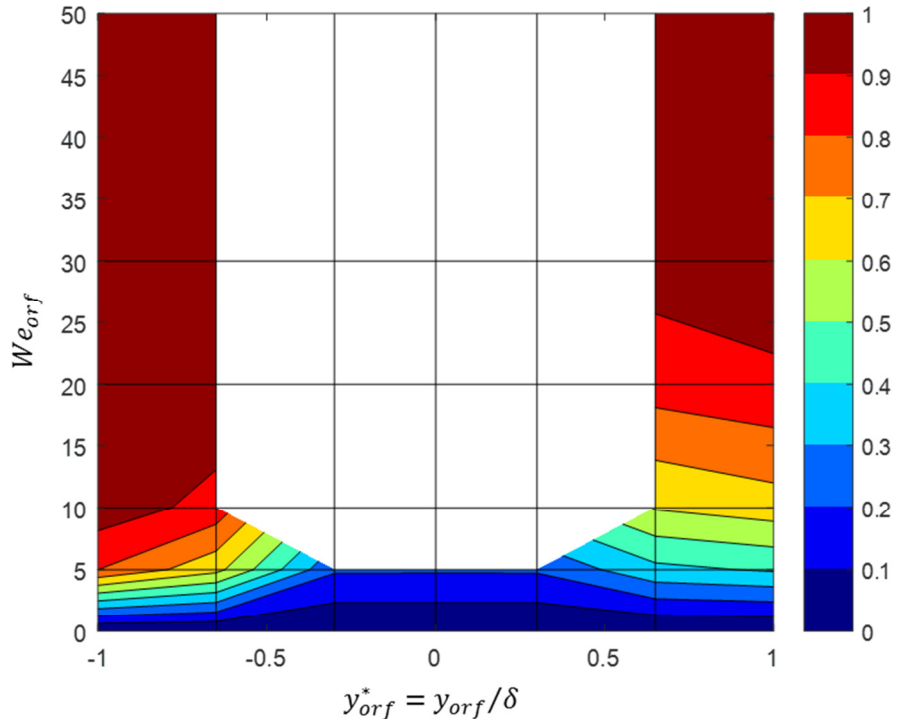

Figure 4.34. Breakage probability as a function of the orifice-based Weber number We_{orf} and the trajectory through orifice $y^*_{orf}(z^*_{orf} = 0)$ for air bubbles.

4.6. Daughter Droplet Distribution

In addition to the threshold at which droplets can break, it is also of interest to understand the number and sizes of daughter droplets produced. The Phantom camera data were used to investigate daughter droplet formation with respect its local Weber number (as recommended in Section 4.3.4) and incoming trajectory.

For the purposes of these analyses, daughter droplets fell into two categories. Droplets in the first category are referred to as *primary daughter droplets*. These are primary daughters were identified and sized through the image processing script outlined in Section 2.3.3. Because of the potential for overlapping in the images, the first four images after the point of break-up were examined. An example image sequence is presented in Figure 4.35. The daughter droplets in the image with the greatest number of daughter droplets were quantified and sized. It was assumed that the volume of these primary daughter droplets scaled with their square-pixel area to the 1.5 power. The volume fraction of the primary daughter droplets was calculated by taking the cubic-pixel volume of each droplet divided by the sum of the cubic-pixels of all droplets.

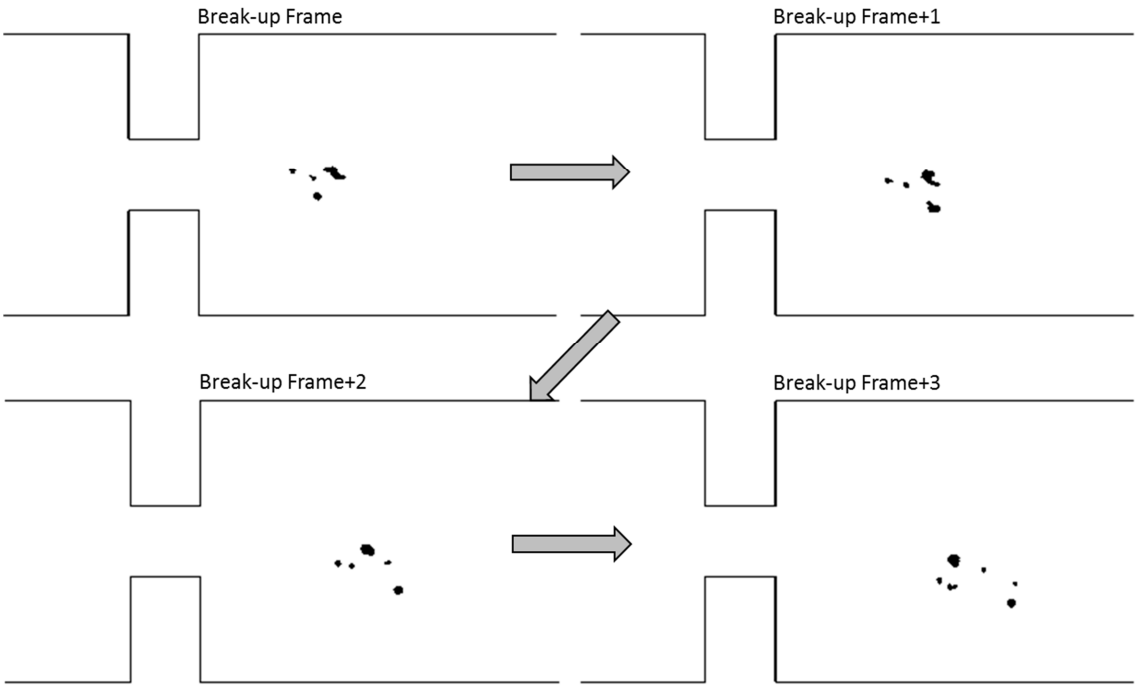

Figure 4.35. Selection of image frame for quantifying and sizing primary daughter droplets. CO70FG droplet in water (D = 630 µm, Re_{ch} = 10,000). In this example, the six primary daughter droplets in the fourth frame were used for further analysis.

Secondary daughter droplets are the second category of droplets. These droplets are smaller than the 20 pixel size threshold used in the image processing script. These droplets were quantified manually by visual inspection from the original image frames. Due to their small size, they were considered to have a negligible volume; only their quantity was recorded.

4.6.1. Number of Primary Daughter Droplets

The results of the preliminary investigation into primary daughter droplet formation are presented in Table 4.4. Each row represents a combination of dispersed phase material and channel Reynolds number. Each column is the

number of primary daughter droplets formed from the break-up of a single droplet. The percentage of droplets for each condition is presented along with the actual sample size in square brackets (the total quantity of droplets imaged with the Phantom camera is presented in Section 4.2.1). For example, 17% (17 of 99) of the CO70FG oil droplets injected into the Re_{ch} = 10,000 flow broke into 2 primary daughter droplets.

Table 4.4. Percentage of droplets forming *N* primary daughter droplets.

Dispersed Phase	Re_{ch}	**Number of Primary Daughter Droplets Formed % of Droplets [# of Droplets]**						
		Not Broken	**2**	**3**	**4**	**5**	**6**	**≥7**
CO70FG	10,000	29% [29]	17% [17]	20% [20]	14% [14]	15% [15]	1.0% [1]	3.0% [3]
	14,000	24% [21]	26% [23]	18% [16]	14% [12]	11% [10]	5.7% [5]	1.1% [1]
Air	10,000	44% [38]	48% [41]	5.8% [5]	2.3% [2]	-	-	-
	14,000	19% [13]	27% [18]	27% [18]	13% [9]	9.0% [6]	-	4.5% [3]

Table 4.4 shows some differences between the break-up of oil droplets and air bubbles. For oil droplets at both Reynolds numbers and air bubbles at Re_{ch} = 14,000, the number of daughter droplets produced were similar. These scenarios produced a wide range of primary daughter droplets, with binary and ternary break-up being nearly equal. A moderate number of break-up events also produced four to five primary daughters. However, the air bubbles at Re_{ch} = 10,000 broke in a very different pattern. Due to a combination of the lower Reynolds number and lower internal stresses (as hypothesized by Levich, 1962), the air bubbles break in a

much simpler manner, with binary break-up being the dominant form. Ternary and greater break-up events were found to be relatively rare.

4.6.2. Analysis of Binary Break-up

Nearly 30% the break-up events were binary, allowing them to be analyzed in more detail. Table 4.5 presents the relationship between the dispersed phase material, the channel Reynolds number, and the volume fraction of the largest droplet produced (the complementary fraction is the volume fraction of the second primary daughter). For example, 33% (6 of 18) of the air bubbles that broke into two primary daughters in the Re_{ch} = 14,000 flow had a larger daughter with a volume fraction of between 0.7 and 0.9, with and a second daughter with a volume fraction of between 0.1 and 0.3.

Table 4.5. Volume fraction of largest droplet for binary break-up.

Dispersed Phase	**Channel Reynolds Number Re_{ch}**	**Volume Fraction of Largest Droplet % of Droplets [# of Droplets]**		
		0.5 – 0.7	**0.7 – 0.9**	**0.9 – 1.0**
CO70FG	10,000	12% [2]	41% [7]	47% [8]
	14,000	26% [6]	48% [11]	26% [6]
Air	10,000	46% [19]	41% [17]	12% [5]
	14,000	22% [4]	33% [6]	44% [8]
Air (Hesketh *et al.*, 1991)	84,000 (pipe flow)	28% [15]	23% [12]	49% [26]
Air (Andersson and Andersson, 2006a)	ε = 8.5 m^2/s^3	~15%	~45%	~40%

For oil droplets at both channel Reynolds numbers and air bubbles at Re_{ch} = 14,000, the break-up is generally uneven, with one droplet having at least a 30% greater diameter than the other (volume fraction > 0.70). The air bubbles at Re_{ch} = 10,000 are again an exception; their breakage produces more similarly-sized daughters.

As a comparison, the data for the break-up of air bubbles in an open horizontal pipeline reported by Hesketh *et al.* (1991) is also shown in Table 4.5. Hesketh *et al.* observed only binary break-up events, with bubbles most often breaking into unequal parts. 49% of the events resulted in droplets with one bubble having twice the diameter of the other (volume fraction > 0.9). The air bubble data at Re_{ch} = 14,000 compares favourably to the results of Hesketh *et al*., despite the differences in Reynolds number and geometry.

The current results are also comparable to the results of Andersson and Andersson (2006a), though their work studied break-up in a different geometry (a reactor with mixing elements). Their turbulence dissipation rate of 8.5 m^2/s^3 is much lower than present in the edges of the slit orifice jet (see Appendix B). They showed mostly binary breakup events for bubbles, so their results are directly comparable to the current work. Andersson and Andersson also showed daughter droplet size distributions for the dodecane-in-water experiments, but these droplets did not always break into two daughters. They are not comparable with Table 4.5 and so are not presented here.

4.6.3. Daughter Distribution versus Local Weber Number

The primary, secondary, and total numbers of droplets are plotted against the local Weber number in Figure 4.36 for CO70FG droplets. Except for the unbroken droplets, each imaged droplet has a marker on all three plots, with the shape and colour of the markers determined by the number of primary daughter droplets formed. There is a greater deal of variation in the number of primary daughters at low Weber numbers compared to high Weber numbers, but this perceived effect may be due to the greater number of points at the low Weber numbers. The variation in production of secondary droplets also appears to be higher at lower Weber numbers.

The corresponding plots for air bubbles are shown in Figure 4.37. The same comments given for oil droplets also apply for air bubbles, though the number of primary and secondary bubbles formed is lower on average.

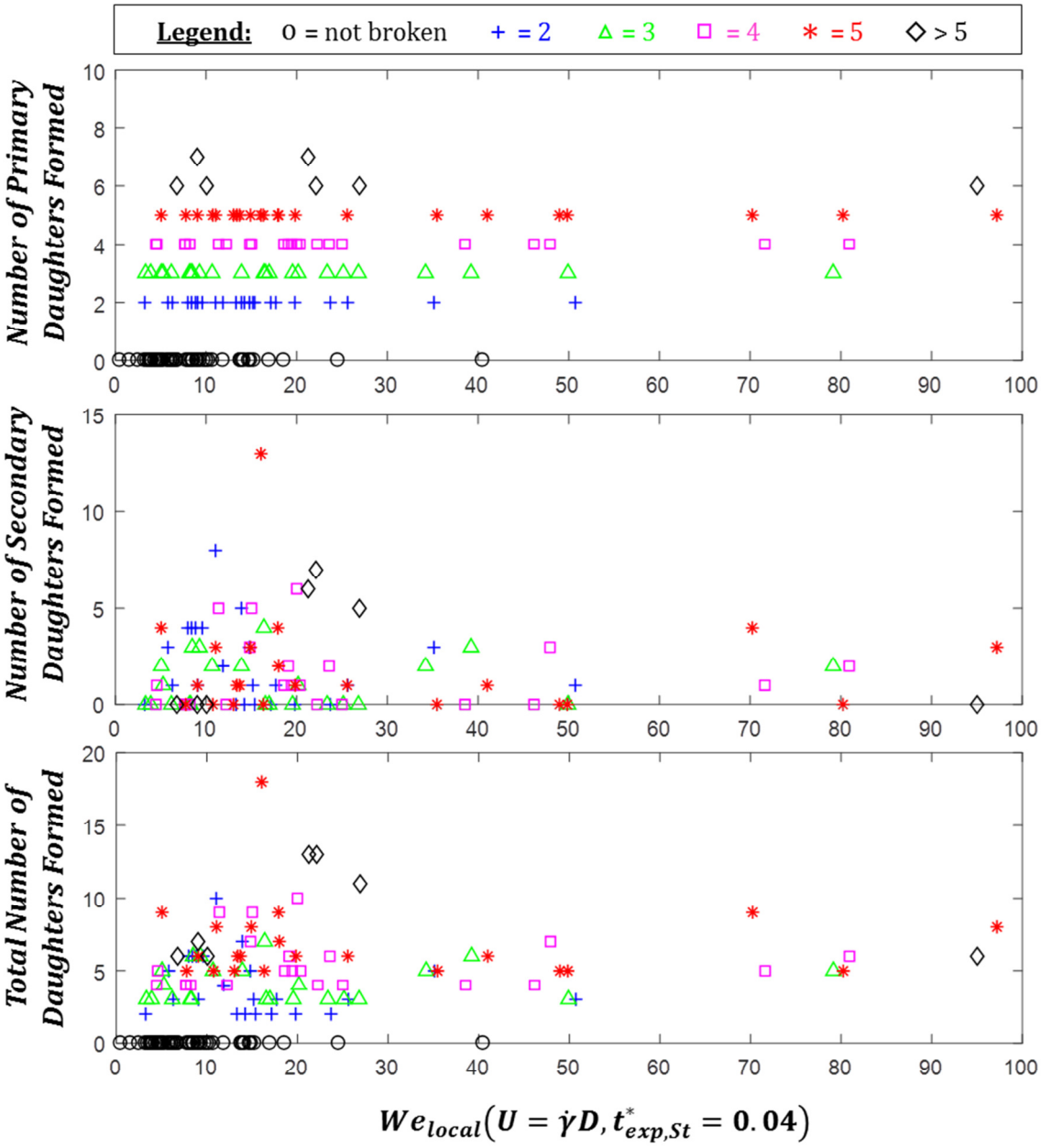

Figure 4.36. Primary, secondary, and total daughter droplet formation as a function of local Weber number for CO70FG droplets.

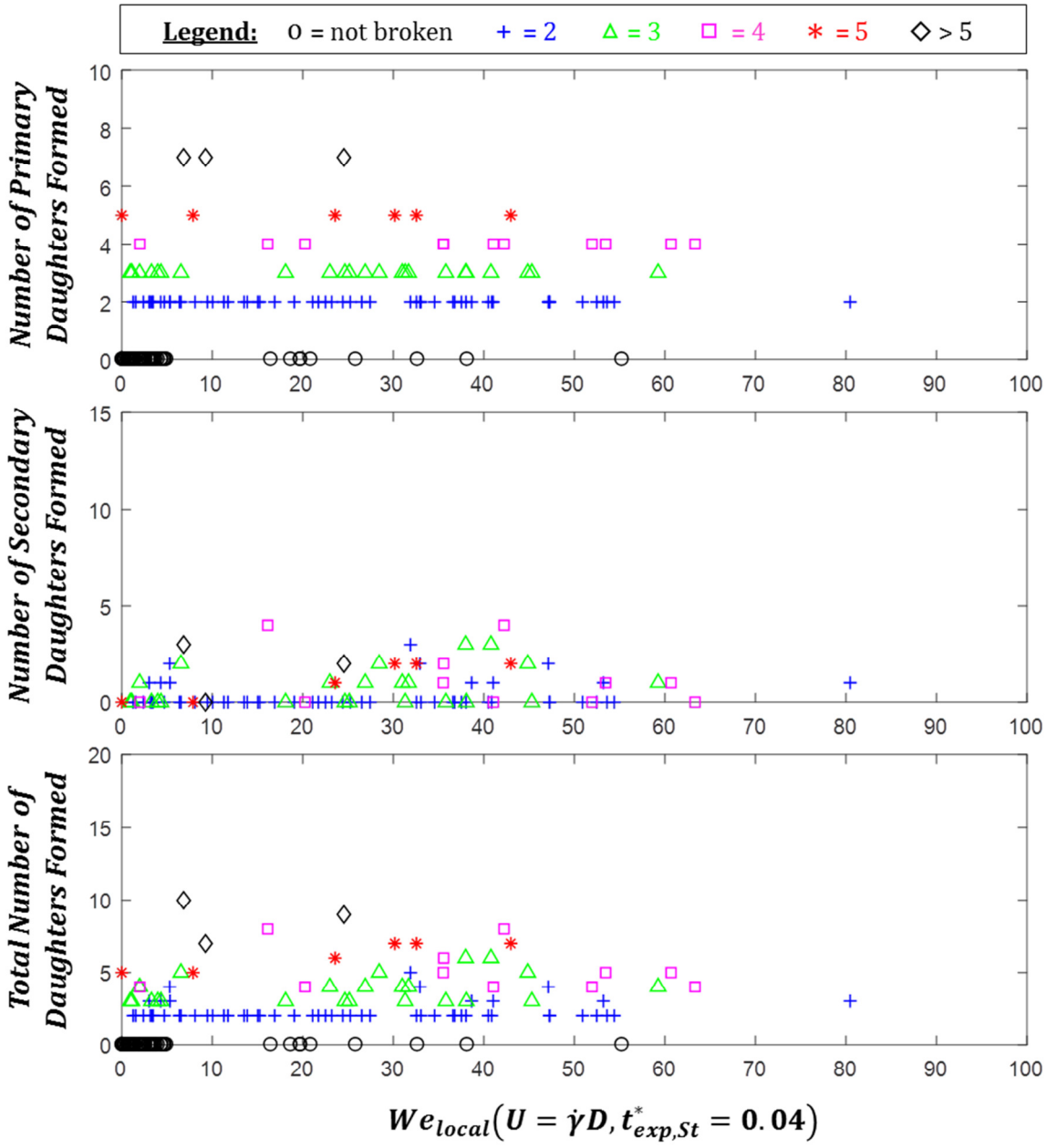

Figure 4.37. Primary, secondary, and total daughter droplet formation as a function of local Weber number for air bubbles.

The volume fraction of the largest daughter droplet versus the local Weber number was also plotted for both CO70FG droplets and air bubbles as shown in Figure 4.38. Unbroken droplets are not plotted, but the markers otherwise follow the same format as for the previous figures. Unfortunately, the markers appear to be randomly scattered. Thus, the local Weber number is not a correlating factor for the size of the largest droplet.

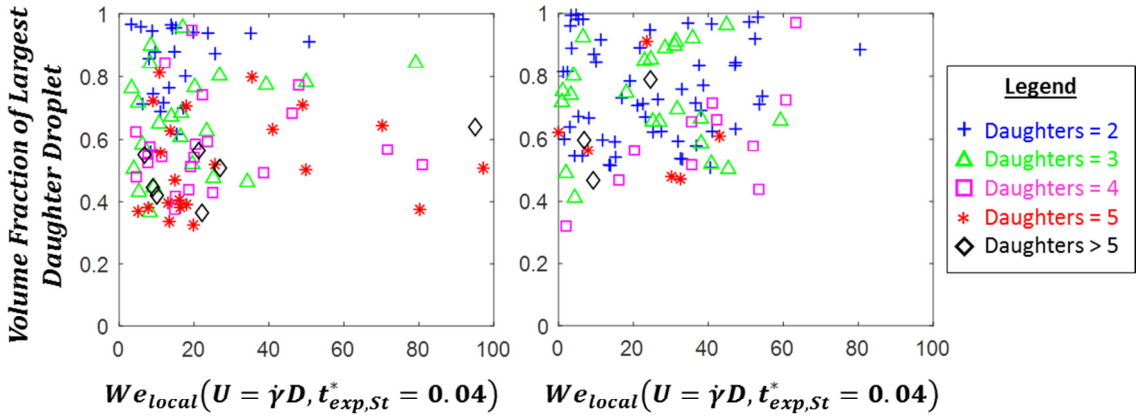

(a) CO70FG Droplets (b) Air Bubbles

Figure 4.38. Volume fraction of largest daughter droplet versus local Weber number for CO70FG droplets and air bubbles.

Figure 4.39 shows the average number of primary, secondary, and total daughter droplets versus local Weber number for both CO70FG droplets and air bubbles. These plots are averages of the data presented in Figure 4.36 and Figure 4.37. Weber number bins without at least five samples are excluded from the plots below. For both CO70FG droplets and air bubbles, the average primary daughter formation appears to be independent of Weber number (3.7 and 2.7 primary daughters for CO70FG and air, respectively). Secondary daughter formation does

show some dependence on Weber number below a value of about 10, but above this value, secondary daughter formation also seems to be constant.

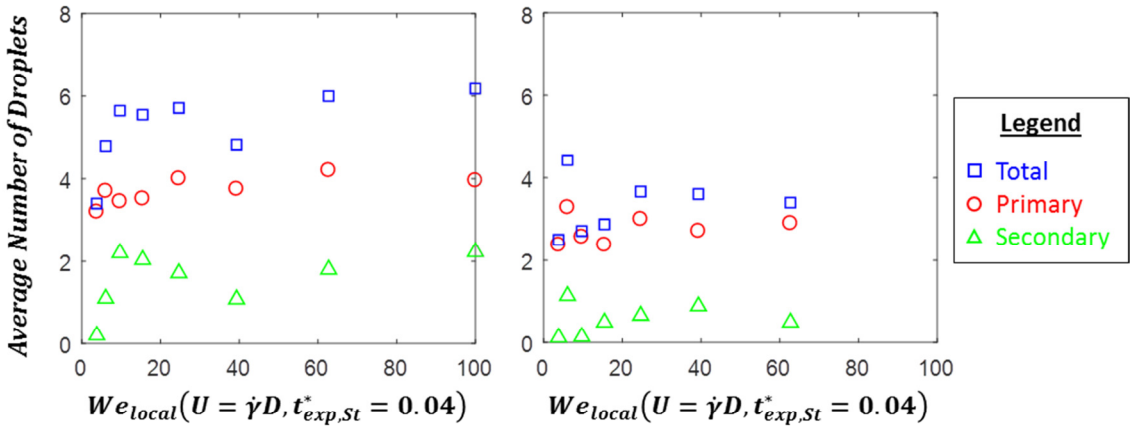

(a) CO70FG Droplets (b) Air Bubbles

Figure 4.39. Average daughter droplet formation as a function of local Weber number.

4.6.4. Daughter Distribution versus Incoming Trajectory

Figure 4.40 shows the primary, secondary, and total numbers of droplets formed against the incoming trajectory for CO70FG droplets and air bubbles. The dashed lines mark the opening of the slit orifice from $-1 \leq y^*_{inc} \leq 1$. The shape and colour of the markers are determined by the number of primary daughter droplets formed. For oil droplets, it appears that greater number of primary and secondary daughters are produced for droplets approaching the orifice closer to the wall. Droplets approaching the centre of the slit orifice did not form many secondary daughters. For air bubbles, the same comments apply, but the number of bubbles formed is generally lower. In particular, secondary daughters are produced primarily by bubbles approaching the orifice right along the wall. Also, the plots

show that the break-up asymmetry caused by the lateral migration results in a difference in the number of daughter droplets formed.

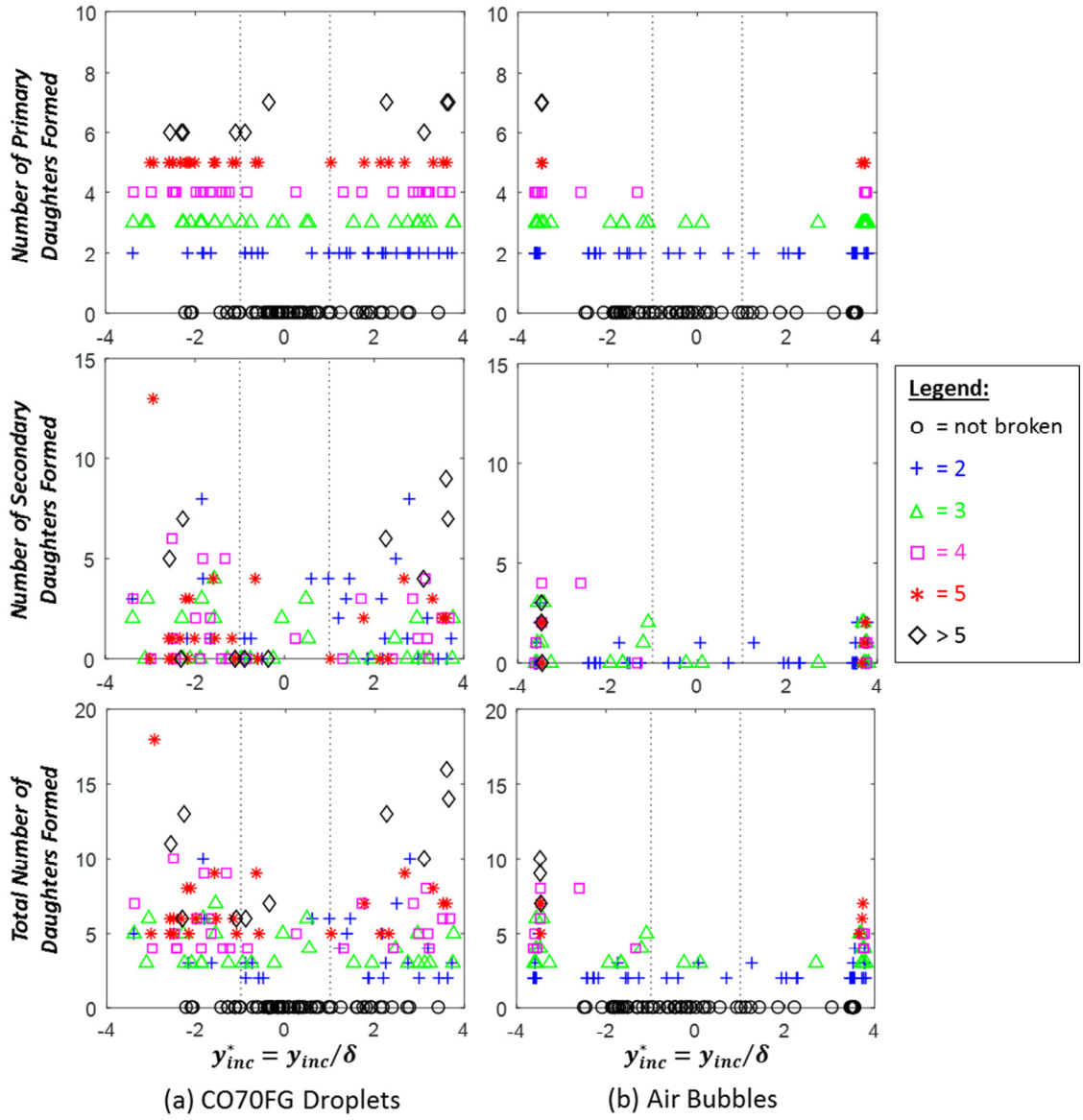

Figure 4.40. Primary, secondary, and total daughter droplet formation as a function of incoming trajectory y^*_{inc} for CO70FG droplets and air bubbles.

Figure 4.41 shows the volume fraction of the largest daughter droplet versus incoming trajectory for both dispersed phase materials. No correlation between the volume fraction of the largest daughter and the incoming trajectory was observed.

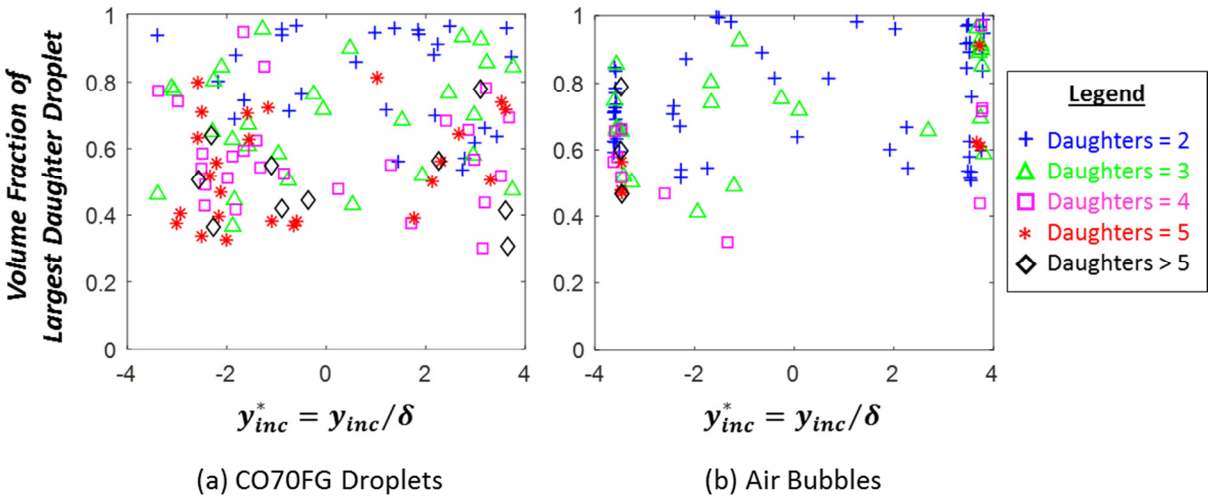

(a) CO70FG Droplets (b) Air Bubbles

Figure 4.41. Volume fraction of largest daughter droplet versus incoming trajectory y^*_{inc} for CO70FG droplets and air bubbles.

The average daughter droplet formation versus incoming trajectory is presented in Figure 4.42. As when comparing the daughter droplet formation against local Weber number, there does not appear to be a significant dependence of average primary daughter formation on incoming trajectory. The average secondary daughter formation does appear to be marginally lower when the droplets approach the orifice opening ($-1 < y^*_{inc} < 1$).

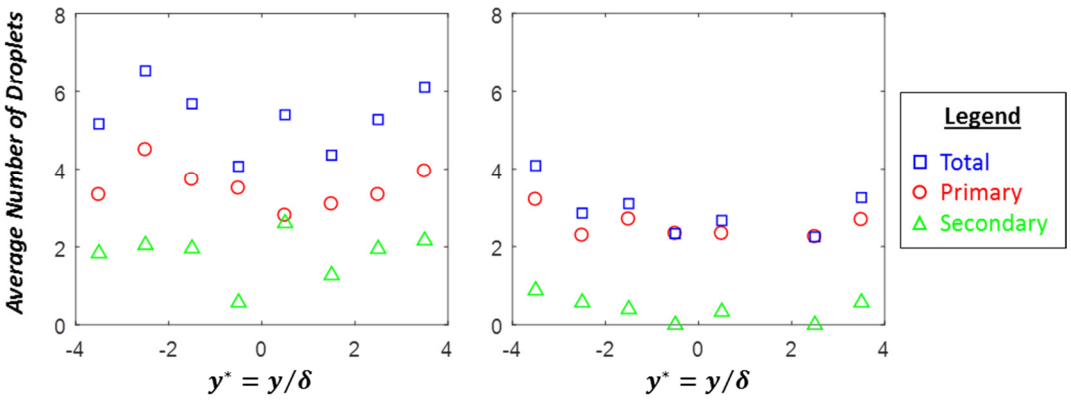

(a) CO70FG Droplets (b) Air Bubbles

Figure 4.42. Average daughter droplet formation as a function of incoming trajectory y^*_{inc}.

4.7. Key Findings for Break-up in Turbulent Flows

The key findings of this study are:

- The random nature of turbulence masks the effect of droplet diameter and channel Reynolds number on the path of droplets through the orifice. The pressure difference that sustains the leaning of the jet also causes lateral migration, particularly for the lower density air bubbles.
- The form of Weber number appropriate to characterizing the break-up of macroscale droplets due a short-term high-intensity deformation event in turbulent flow has been determined (Equation 4.7-1) and incorporated into a break-up probability model as shown below (Equation 4.7-2). ***The break-up of macroscale droplets scales with a macro velocity scale of*** $\dot{\gamma}\mathbf{D}$**.** The $\dot{\gamma}$ to be used here is the maximum average strain rate magnitude over an exposure time of 0.04 multiplied by the Stokes particle relaxation time. Note

that the Levich interpretation of stresses was necessary for the break-up of liquid droplets and gas bubbles to be predicted with the same model.

$$We_{local} = \frac{(\rho_d \rho_c^2)^{1/3} \dot{\gamma}^2_{t^*_{exp,St}=0.04} D^3}{\sigma} \tag{4.7-1}$$

$$P_{St} = \exp\left(-\frac{4.57}{We_{local}}\right), \text{RMSE} = 0.067 \tag{4.7-2}$$

- Contour plots graphically relating the probability of break-up as a function of an upstream Weber number, incoming trajectory, and droplet material have been developed.
- Contour plots graphically relating the probability of break-up as a function of an orifice Weber number, trajectory at the orifice entrance, and droplet material have been developed.
- On average, the production of primary daughter droplets was not influenced by the local Weber number nor the incoming trajectory. However, parent droplets approaching the orifice near the wall would interact more strongly with the orifice, resulting in a wider range of daughter droplet quantities.

5. Droplet Break-up in Inertial Laminar Flows

This section presents the fundamental physics, experimental observations, and various analyses for the droplet break-up experiments in the inertial laminar orifice flows. In these experiments, the break-up of water droplets is monitored in oil flows of two viscosities (0.0202 Pa-s and 0.0808 Pa-s). The physics of droplet break-up in both Stokes and inertial laminar flows is described in Section 5.1. Observations of droplet behaviour, including break-up mechanisms, are presented in Section 5.2. The locally-derived Weber number thresholds for break-up are detailed in Section 5.3. A summary of the conclusions is presented in Section 5.4.

5.1. Laminar Break-up Theory and Literature

The break-up of droplets in laminar flows has been studied primarily in the Stokes flow regime, where the Reynolds number is much less than unity. The consequence of this is that the advective terms in the Navier-Stokes equations (Equations 1.1-1 and 1.1-2) become negligible. With pressure and time scaled with the viscosity term ($\mu_c U/D$ and $\rho_c D^2/\mu_c$, respectively), Reynolds number and density ratio are eliminated from the analysis. These studies most often utilize small, neutrally-buoyant droplets that also eliminate the need to consider gravitational forces. The capillary number Ca (the ratio of disruptive viscous stresses to cohesive interfacial stresses), viscosity ratio λ, and the structure or type of flow continue to be influencing factors in the break-up. Theory and literature

dealing with this category of droplet break-up are presented in Section 5.1.1 and 5.1.2. Reviews of this topic have been written by Rallison (1984) and Stone (1994).

Studies of droplet break-up in non-Stokes (or inertial) laminar flows are less common due to the additional complications caused by the non-linear advective term. None of the dimensionless numbers in Table 1.1 can be eliminated, resulting in a substantially larger parameter space than the corresponding Stokes flow. Studies of droplet break-up in this sub-regime are discussed in Section 5.1.3.

Note that researchers studying laminar flow phenomenon have typically followed the convention of Taylor (1934) and other earlier studies, using the un-deformed radius a as the length scale. This convention is particularly convenient for analytical solutions and numerical studies. This differs but is functionally-equivalent to the turbulent flow break-up convention of using the un-deformed diameter D as the length scale. This dissertation will continue to express the length scale as D. For ease of comparison, references to literature values will be modified appropriately.

5.1.1. Droplet Break-up in Prototypical Stokes Flows

Droplet break-up in Stokes flow was first studied by Taylor (1934), who looked at two prototypical linear flows: simple extensional flow (SEF) and simple shear flows (SSF). It is the work of Grace (presented in 1971 and published formally in 1982) that is considered the fundamental basis for analysis of break-up in these prototype flows. Grace's data for the break-up of small neutrally-buoyant droplets

was combined with the data of Taylor (1934) and Rumscheidt & Mason (1961) to determine the critical capillary numbers Ca_{crit} for droplet break-up for a wide range of viscosity ratios. Is principle, when $Ca > Ca_{crit}$, a droplet has the potential to break if a minimum drop draw ratio and exposure time are also met. A conceptual illustration of the Grace curves is shown in Figure 5.1, including an improvement made to the SEF curve by Bentley & Leal (1986) using a computer-controlled four-roll mill apparatus.

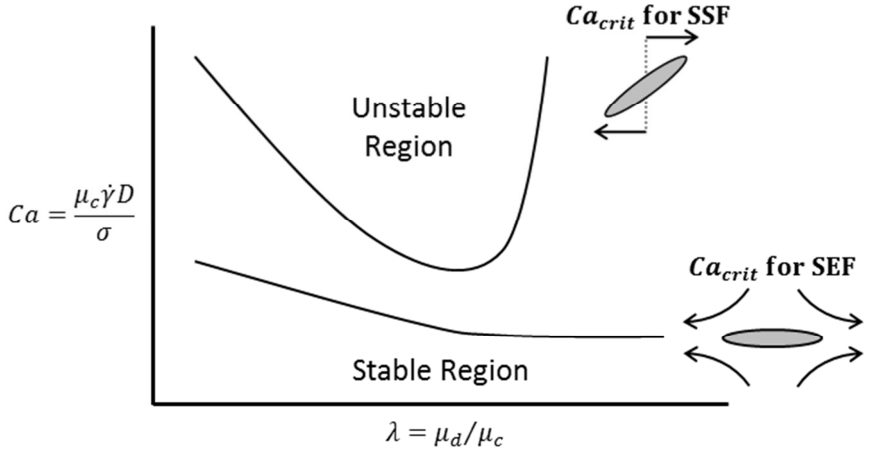

Figure 5.1. Conceptual illustration of the Grace (1982) curves. This illustration includes an improvement to the SEF curve added by Bentley & Leal (1986).

In SEF, a droplet above the corresponding critical capillary curve grows in an unbounded fashion. While Taylor (1934) reported that droplets that broke during extension, Grace (1982), Bentley & Leal (1986), and others have found that the droplet breaks primarily after cessation of the extensional flow if the droplet has reached a minimum degree of extension. The basic shape of the droplet as it retracts is shown in Figure 5.2. As interfacial tension pulls the extreme ends toward its centre, the local curvature of the droplet causes the formation of a neck with high

capillary pressure. This drives flow out of the neck and results in "retractive end-pinching". If the droplet is long enough, successive end-pinching can occur. Stone & Leal (1989a) demonstrated numerically that retractive end-pinching is inhibited when viscosity ratio is high because the flow from the central thread flows more slowly into the end bulbs, slowing the neck formation and thus the end-pinching. However, despite the substantial amount of work in the area of break-up in SEF, the nature of break-up for $Ca > Ca_{crit}$ is not well-understood. Ha & Leal (2001) showed that beyond the critical drop draw ratio, a droplet could achieve a higher deformation and still retract to a spherical droplet. At even greater drop draw ratio, a droplet would again be broken, but this time into a greater number of daughter droplets. The fundamental mechanism behind this intermediate stable region is unknown.

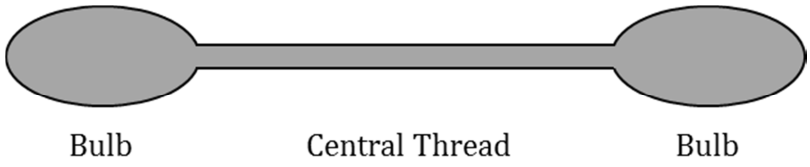

Figure 5.2. Basic shape of droplet for end-pinching mechanisms.

In SSF, an unstable droplet breaks while the shearing flow is still active. The primary mechanism of fracture, "elongative end-pinching", was identified by Marks (1998) in his study of droplet break-up in sudden onset shear flows. The break-up is the result of flow toward the tips of the extended droplet, again resulting in local curvature that drives neck pinching (see Figure 5.2). This mechanism can occur successively if the deformed droplet is long enough.

In both SEF and SSF, break-up via capillary wave instability is possible if the central thread (see Figure 5.2) exists for a sufficient amount of time. Tomotika (1935) used linear stability theory to demonstrate that a cylindrical fluid thread immersed in another fluid could not be indefinitely stable. Rumscheidt & Mason (1962) visualized the central region of an infinitely long fluid thread, showing the break-up of the thread into uniform daughters. Stone *et al.* (1986) also observed capillary wave instability in SEF, but only after an initial retractive end-pinching event. Both Marks (1998) and Zhao (2007) observed capillary wave instability for $Ca > 1.5Ca_{crit}$ and $Ca > 2Ca_{crit}$, respectively, with the discrepancy possibly being caused by differences in apparatus geometry. Zhao (2007) also noted that the details of the capillary wave instability depended on the viscosity ratio, with higher viscosity ratios resulting in both large daughters and satellites.

Tip-streaming is another mechanism of break-up that can occur in these prototype flows, but this typically occurs due to gradients in interfacial tension caused by interfacial agents such as surfactants. Since the fluids in the current work are free of interfacial agents, tip-streaming will not be discussed in this dissertation.

5.1.2. Droplet Break-up in Other Stokes Flow Conditions

Bentley & Leal (1986) and Stone *et al.* (1986) also used their computerized four-roll mill to examine a range of 2-D linear flows between SEF and SSF. The four-roll mill has the versatility to generate a range of linear flows between extensional

and shear flows by changing the ratio of roller speeds. Flows with increasing shear were shown to be increasingly difficult to break. This is illustrated in Figure 5.3.

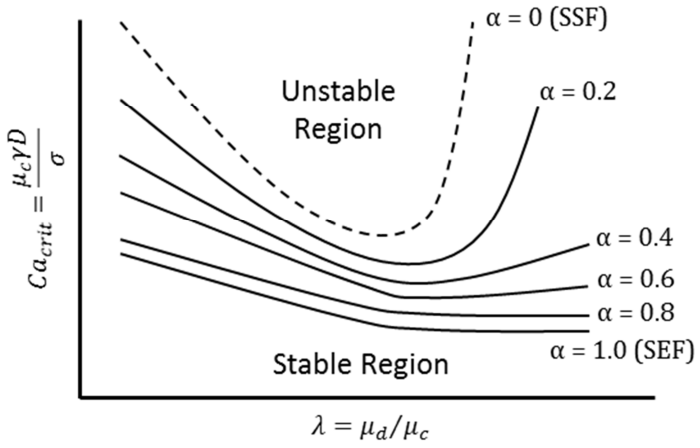

Figure 5.3. Conceptual illustration of the Ca_{crit} curves for droplet break-up in various flows generated by the the four-roll mill of Bentley & Leal (1986).

Stone & Leal (1989b) investigated how the initial shape of a droplet in an extensional flow could be broken for $Ca < Ca_{crit}$. The experiment consisted first of stretching a droplet being at Ca_{crit}. Once the desired degree of stretching had been achieved, the flow was slowed to a sub-critical Ca. It was shown that the sub-critical Ca could still break a droplet provided a certain degree of extension had been reached. Generally, a greater extension was required to break a droplet at lower Ca for the slowed flow.

Stegeman *et al.* (2002) also investigated the effects of the initial droplet shape and simple inhomogeneous flows on the subsequent break-up. The work uses an analytical model that describes the shape of a slender droplet in an axisymmetric extensional flow. An extended droplet shape was shown to reduce Ca_{crit}. In terms of time, they exposed two droplets to a time-dependent strain rate

profile (linear increase from 0 to 1.3 Ca_{crit} then a linear decrease back to zero) of different lengths. Both had an average Ca of 0.65, but with a longer exposure time, one of the droplets was broken.

Confinement is another feature that has also received some study. Vananroye et al. (2006) studied droplet break-up in a counter-rotating parallel plate device. The goal was to understand whether there would be a change in Ca_{crit} with increasing confinement ratio D/H, where H is the distance between the two plates. They found that for viscosity ratios $\lambda = 1$, confinement did not affect Ca_{crit}. However, for $\lambda = 0.30$, Ca_{crit} started to rise at $D/H > 0.3$. Conversely, for $\lambda > 3$ (droplets that would be unbreakable by shear in SSF), Ca_{crit} actually decreases with increasing D/H. At $D/H > 0.7$, the same Ca_{crit} is capable of breaking up droplets of two different viscosities. In all cases, highly confined droplets were more deformed than less confined droplets. Aside from the suggestion that internal flow patterns were different, no detailed explanations for these phenomena were offered by the authors. It is possible that the higher viscosity droplets do not well-distribute their internal flow in response to confinement. This might be exacerbated by the 'sudden onset' flow; instead of successively increasing the shear rate for a stably-deformed droplet, the authors apply successively increasing shear to a relaxed un-deformed droplet. A more highly viscous droplet may not be able to quickly form the internal circulation necessary to stabilize the droplet as it might have under the experimental methodology of Grace (1982), producing a seemingly-contrary result. As evidence of this, the $\lambda = 5$ droplets broke even with relatively low confinements of 0.15. It is

not yet apparent why a less-viscous droplet becomes more deformed yet more stable due to confinement.

A mechanism that does not occur in linear flows is folding. The study of droplet break-up by Tjahjadi & Ottino (1991) in their eccentric rotating cylinder device produces a non-linear, chaotic flow field. While showing primarily capillary wave break-up, they also have experimental images of U-type and V-type folding. For the U-type folding (a shape that was seen in the current work), their image shows a daughter droplet that forms at the fold itself, with subsequent break-up along the arms due to a combination of retractive end-pinching and capillary wave instability.

5.1.3. Droplet Break-up in Inertial Laminar Flows

In comparison to studies in the Stokes flow regime, experimental studies of droplet break-up in inertial laminar flows are relatively poorly studied. However, the study of inertial effects on break-up using numerical means has become increasingly useful with improving computational capabilities.

Brady & Acrivos (1982) observed that many previous works assumed that the inertial effects inside a slender droplet in SEF could be neglected, but the droplet Reynolds number (utilizing droplet density and viscosity) reached unity or greater. Their work extended previously-derived flow equations to account for internal inertia. They discovered that the internal flow field always produced a very weak

stabilizing effect. They recommended neglecting internal inertia on break-up for this reason.

Inertial shear flows have been better explored. The volume-of-fluid (VOF) method was used by Renardy & Cristini (2001a, 2001b) to study the effect of inertial shear flows on droplets ($\lambda = 1$, $\xi = 1$). In general, droplets with higher droplet Reynolds number $Re_{drop} = \rho_c \gamma D^2/\mu_c$ have lower corresponding critical capillary number Ca_{crit}. For $Re_{drop} > 120$, the product of Ca_{crit} and Re_{drop}—essentially a critical Weber number We_{crit}—is a constant with a value of approximately 24 for the single viscosity ratio evaluated. The break-up at lower capillary numbers was attributed to differences in droplet behaviour. In inertial shear flows, the faster flow around the extreme ends of the droplet result in a suction or lift force that leads to the droplet orienting closer to the cross-wise axis when compared to orientation in the corresponding Stokes flow. This results in shear acting over a greater droplet length and, consequently, a lower critical capillary number. The shape of the droplet is affected by these lift forces; in contrast to the evenly-rounded end bulbs imaged by Marks (1998), the VOF model predicts that the lift will cause a moderately sharp tip that 'points' toward the walls. At higher viscosity ratios ($1 \leq \lambda \leq 5$), the VOF simulations of Khismatullin *et al.* (2003) showed that the maximum viscosity ratio (i.e., the viscosity ratio above which droplets cannot be broken) increases with increasing inertial influence.

Using a diffuse interface free energy lattice-Boltzmann technique, Komrakova *et al.* (2014, 2015) simulate the approximately the same range of droplet Reynolds

numbers, but also extended the viscosity ratio to include lower values ($0.1 < \lambda < 2$) and supercritical capillary numbers. This study also showed both elongative end-pinching for $Ca_{crit} < Ca < 2Ca_{crit}$ and capillary wave break-up at $Ca = 2Ca_{crit}$ at $\lambda = 2$, with the capillary wave break-up producing equal-sized daughter droplets. For these conditions at Stokes flow, Zhao (2007) produced bimodal droplets, but since the inertial effect causes an increase in the maximum viscosity ratio that can be broken, it is possible that the threshold for unimodal/bimodal capillary wave break-up also migrates to a higher viscosity ratio.

A summary of the critical capillary numbers as a function of both viscosity ratio and droplet Reynolds number for the inertial shear flow work of Renardy & Cristini (2001a, 2001b), Khismatullin et al. (2003), and Komrakova *et al.* (2015) is presented as Figure 5.4. The VOF and lattice-Boltzmann techniques provide results that are in reasonable agreement. The presence of inertial effects ultimately allows break-up via shear with substantially greater effectiveness than might be expected from the Grace curves.

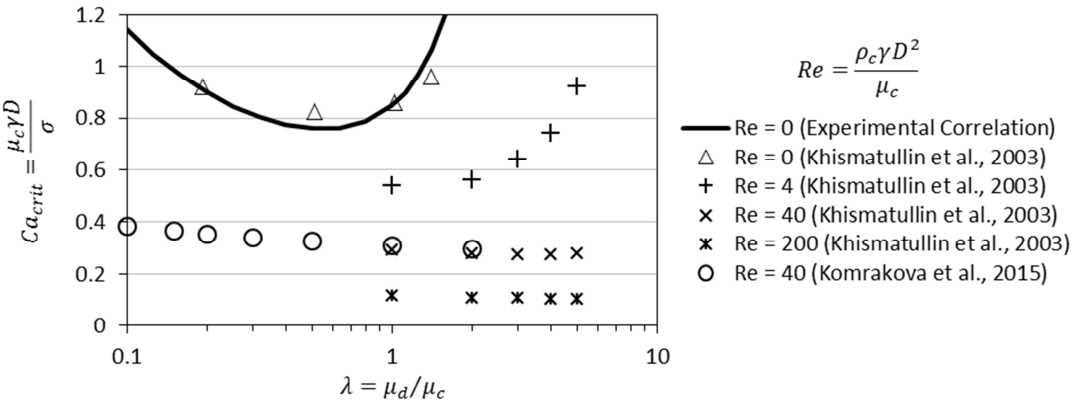

Figure 5.4. Critical capillary number as a function of Reynolds number for inertial shear flows. The solid line is based on a correlation from Marks (1998).

5.2. Experimental Observations

This section provides observations from study of the imaged droplets. This includes how the droplets were distributed in size and incoming trajectory, observations on their behaviour as they passed through the orifice, and images of the breakage mechanisms.

5.2.1. Droplet Size and Incoming Trajectory Distribution

Table 5.1 summarizes the quantity of droplets and bubbles imaged for each of the six inertial laminar flow conditions. Additional details regarding distribution with respect to diameter and incoming trajectory are provided in Appendix C. The size and incoming trajectory of each droplet was measured at least 0.5 H (6.35 mm) upstream of the orifice to eliminate orifice effects. As with the turbulent flow experiments, the droplets included in these analyses were of diameters between 200 and 1200 μm. In addition to the imaged droplets reported in Table 5.1, the Phantom camera was also used to investigate the break-up mechanisms at higher frame rates (1800–4500 fps) than were possible with the Point Grey camera.

Table 5.1. Summary of imaged droplets for the laminar flow experiments acquired with the Point Grey camera at framing rates of 240–580 fps.

Continuous Phase Fluid	Channel Reynolds Number Re_{ch}	Oil Droplets Sampled
CO200FG (μ_c = 0.0808 Pa-s)	110	223
	240	127
CO70FG (μ_c = 0.0202 Pa-s)	240	180
	330	135
	450	191
	660	206

5.2.2. Droplet Trajectory Behaviour

The trajectories of the water droplets in the laminar experiments were visualized in a similar manner to the droplet trajectories in turbulent flows presented in Section 4.2.2. However, unlike the turbulent flow trajectories, the trajectories in the inertial laminar flow tended to be repeatable, leading also to repeatable outcomes. Due to the large amount of data to visualize, only selected trajectories are presented in this section. The full set of trajectories is available in Appendix D. The droplets were separated into 14 bins based on their incoming trajectory ($-3.5 \leq y^*_{inc} \leq 3.5$, in increments of 0.5). This section will discuss the impact of the droplet, flow, and fluid parameters on the droplet trajectories.

Figure 5.5 shows trajectories for droplets with $-3.0 \leq y^*_{inc} \leq -2.5$ for channel Reynolds numbers of 110 and 450. These conditions were chosen because droplets across a wide span of diameters were imaged across this narrow range of

incoming trajectories. The markers indicate the centroid of an imaged unbroken droplet, with the marker colour indicating the diameter of the droplet. The plots indicate that the trajectories within one channel height of the orifice ($z^* \leq 10$), where the strain rates are highest, are not affected by the droplet diameter.

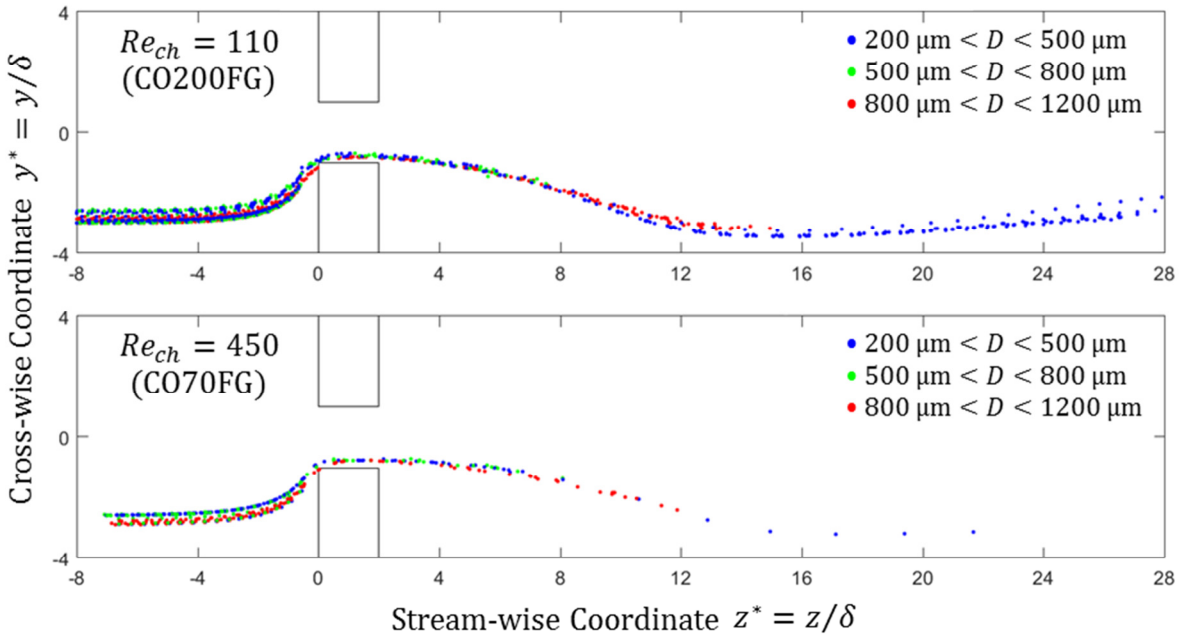

Figure 5.5. Droplet trajectories for water droplets in laminar flows of at Re_{ch} = 112 (μ_c = 0.0808 Pa-s) and Re_{ch} = 450 (μ_c = 0.0202 Pa-s). Incoming trajectories are from $-3.0 < y^*_{inc} < -2.5$. Markers are coloured by droplet diameter.

Figure 5.6 shows droplet trajectories for $1.0 < y^*_{inc} < 1.5$ in a similar fashion to the previous figure, but with different marker colours for each of the six flow conditions. At $z^* < 10$, the trajectories do not appear to be influenced by either channel Reynolds number or continuous phase viscosity. At $z^* > 10$, there are deviations based on both of these parameters. Following the droplets across their associated flow field (see Appendix B for computational flow field results) for CO200FG (black to blue markers) and CO70FG (cyan to green to magenta to red

markers) shows that the trajectories are responding to the changes in the jet shape, with droplets in the stronger jets travelling closer toward the wall at $y^* = -4$. However, this is not strictly a Reynolds number-dependent phenomena since there is a difference in behaviour between the two $Re_{ch} = 240$ scenarios, suggesting that there is a separate inertia- or viscosity-related effect.

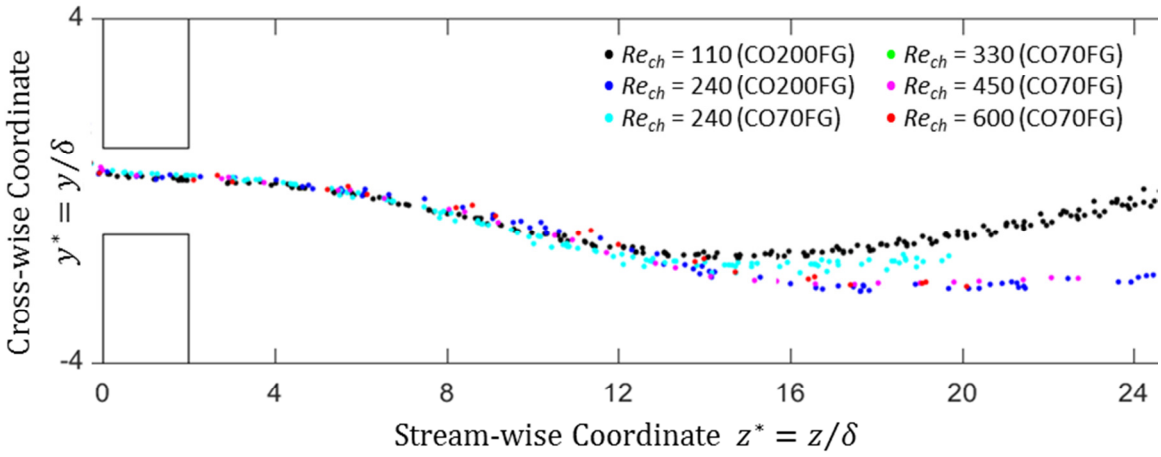

Figure 5.6. Droplet trajectories for water droplets in laminar flows of CO70FG (μ_c = 0.0202 Pa-s) and CO200FG (μ_c = 0.0808 Pa-s). Incoming trajectories are from $1.0 < y^*_{inc} < 1.5$. Markers are coloured by Re_{ch} (see Table 2.2).

The break-up locations of all the droplets imaged in these experiments is presented in Figure 5.7. In the case that multiple break-up events occur for a single parent droplet, only the first is presented. All breakage events occur as the droplet travels in or across the edges of the jet, where the shear rates are highest. Note that water droplets in CO200FG (μ_c = 0.0808 Pa-s) exhibit the widest range of break-up locations. The viscosity of the continuous phase appears to act as a stabilizing factor, allowing the droplet to extend to a greater length before break-up occurs.

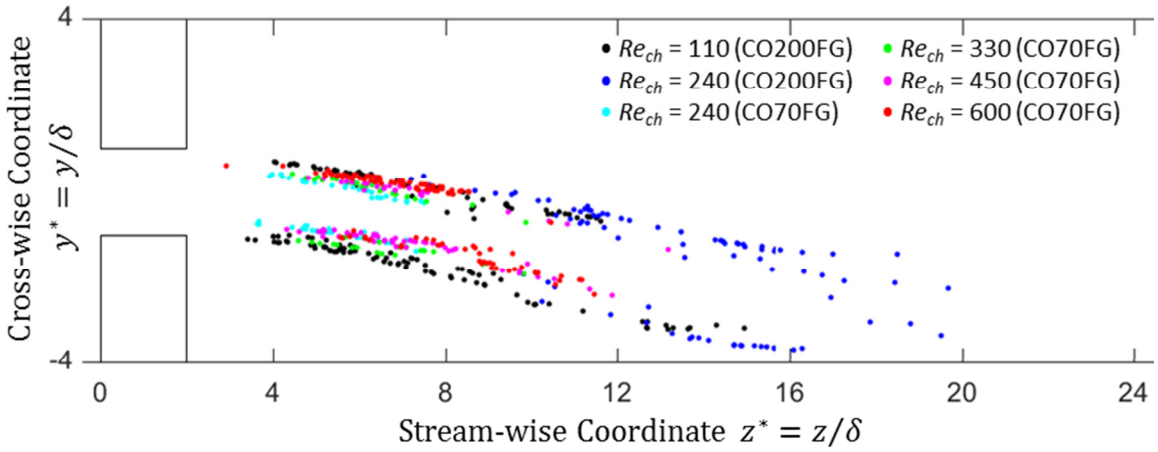

Figure 5.7. Break-up locations for water droplets in laminar flows of CO70FG (μ_c = 0.0202 Pa-s) and CO200FG (μ_c = 0.0808 Pa-s). Markers are coloured by Re_{ch}.

5.2.3. Description of Breakage Events

Each of the figures in this section have a corresponding video in the supplementary PowerPoint file.

Droplets entering the central region of the orifice ($-1 \leq y^*_{inc} \leq 1$) tended to stay within the jet centre. As a result, these droplets deformed little (typically to drop draw ratios less than 1.1) and did not break at all. This indicates that the short-duration exposure to extensional stresses alone was not sufficient to significantly deform or break droplets.

As previously shown in Figure 5.7, droplets break-up at the edges of the orifice jet, where the shear rates are highest. Figure 5.8 shows a typical example of a simple break-up process. The droplet is traveling about 20–30% slower than the surrounding fluid, which drags the droplet into an extended shape within the orifice. This is different than the turbulent flow case (where the droplet was deformed but

not extended in the orifice) because the laminar flows produce a much smaller separation region inside the orifice. Note that the leading end of the droplet also bends toward the centre line; this is likely due to the inertial lift mechanism simulated by both Renardy & Cristini (2003) and Komrakova et al. (2014). As it exits the orifice, it stays within the high-shear jet edge, which continues to stretch the droplet. The rear narrows, and the smaller radius of curvature results in a higher capillary pressure that pushes flow forward. The additional curvature caused by the bend also appears to increase local capillary pressure, resulting in flow out of the bend and subsequent pinch off. The leading daughter is larger than the trailing daughter, and a satellite droplet is often produced.

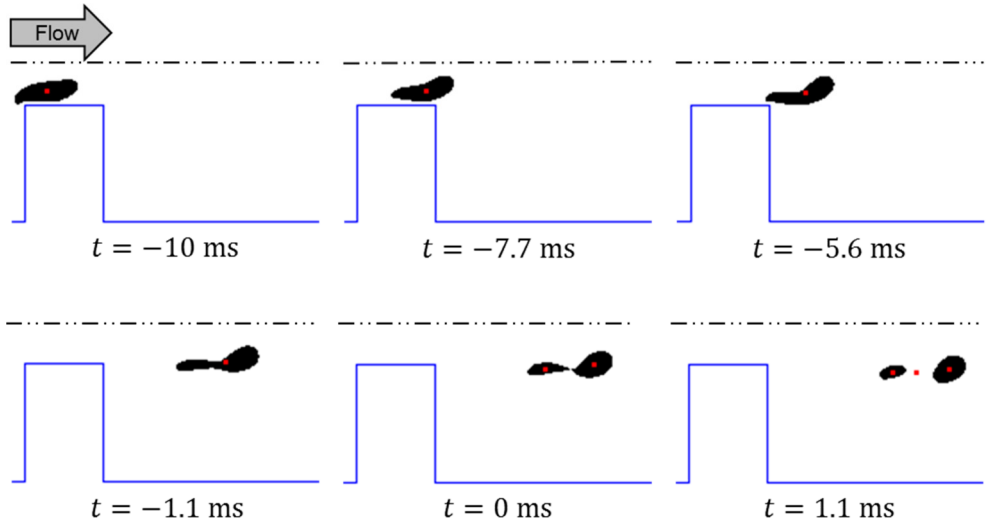

Figure 5.8. Images of a water droplet (D = 1,170 μm) fracturing in the jet edge at Re_{ch} = 240 (μ_c = 0.0202 Pa-s). Time relative to breakup at t = 0 is below each image. The red markers are droplet centroids. The dash-dot-dot line is the channel centre line (y = 0). Image sequence acquired with Phantom camera (1,800 fps).

Figure 5.9 shows how a droplet will behave when experiencing a stronger deformation. The droplet extends quite a bit more strongly and is carried farther

before break-up. As with the droplet in Figure 5.8, the stretched form has a larger leading end that is pointed toward the jet centre and a smaller trailing end. The end bulbs pinch off, and the thread continues to contract, forming new bulbs that pinch off sequentially. This mechanism appears to be the elongative end-pinching first described by Marks (1998) rather than the retractive end-pinching seen in Bentley & Leal (1986). Note that trailing bulb pinches off slightly earlier than the leading bulb in this example, but this was not generally true for all droplets examined.

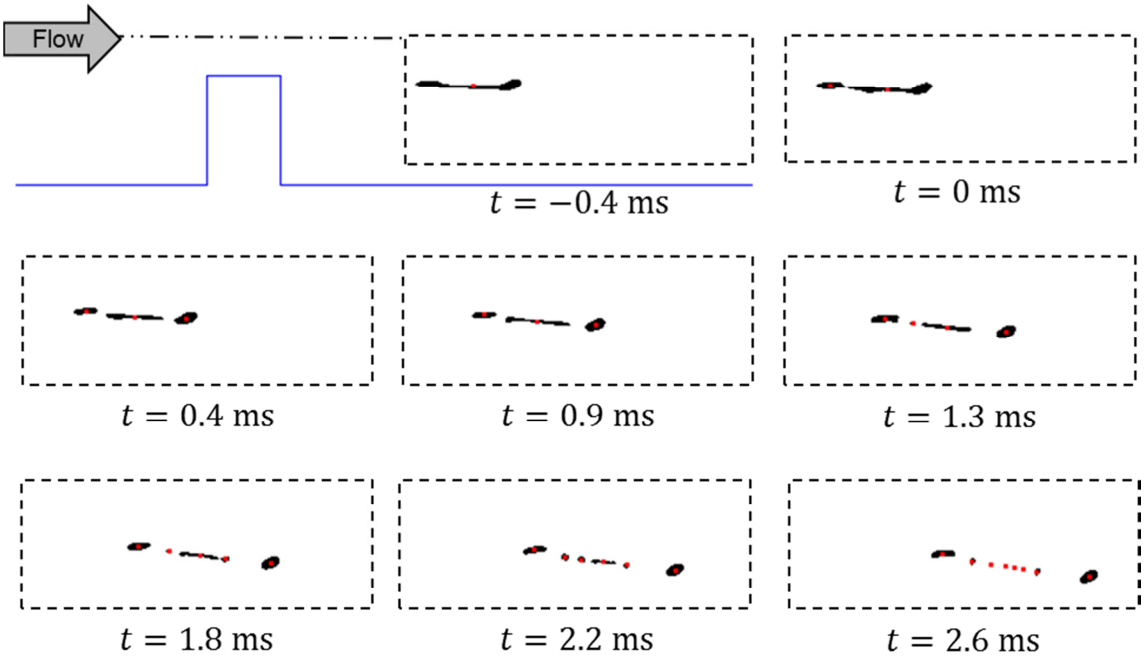

Figure 5.9. Images of a water droplet (D = 690 µm) fracturing in the jet edge at Re_{ch} = 600 (μ_c = 0.0202 Pa-s). Time relative to breakup at t = 0 is below each image. The red markers are droplet centroids. The dash-dot-dot line is the channel centre line (y = 0). Image sequence acquired with Phantom camera (4,510 fps).

For smaller disruptive stresses, break-up can also occur in a similar fashion. However, the cohesive interfacial stresses are relatively stronger, resulting in less deformation. With lower deformation, the trailing end does not tend to form a bulb.

Figure 5.10 shows a typical example. As the rear end narrows, the rear end becomes a sharper, thinner tail without a major bulb at the end. The tail does break up with an end-pinching mechanism, but because the inner fluid more easily flows forward, the tail-end droplets that are formed are relatively small (around 100 μm or smaller). Since these erosion-type events do not result in a significant size reduction for the primary drop, they will be identified separately in the following section.

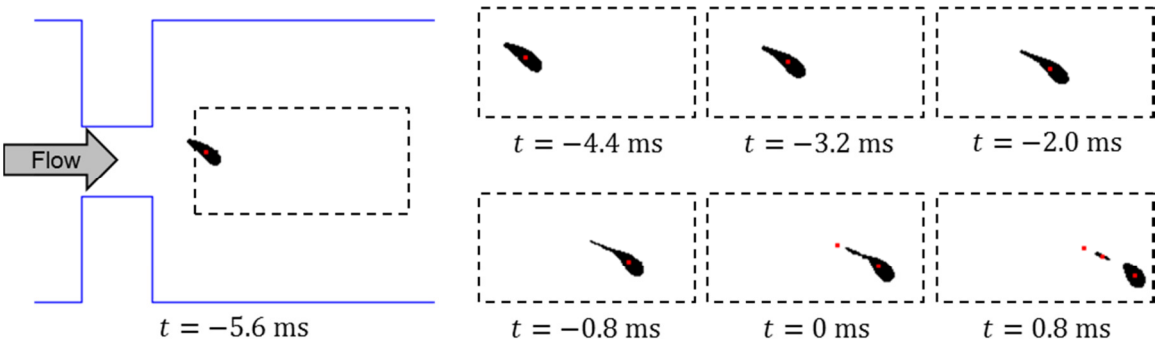

Figure 5.10. Erosion break-up of a water droplet (D = 930 μm) in jet edge at Re_{ch} = 330 (μ_c = 0.0202 Pa-s). Time relative to breakup at t = 0 is below each image. The red markers are droplet centroids. Image sequence acquired with Phantom camera (2,500 fps).

For droplets strongly influenced by the orifice, both fracture and erosion may occur. This is more likely to occur when the Reynolds number is higher. It also occur more frequently for the more viscous CO200FG (μ_c = 0.0808 Pa-s) continuous phase, indicating that the outer flow acts as a stabilizing factor to develop a greater degree of droplet extension prior to break-up. Figure 5.11 shows a droplet that produces five droplets due to tail-end erosion from times t = –5.3 ms to –0.59 ms,

then five daughter droplets through fracturing. Both types of break-up are fundamentally successive end-pinching.

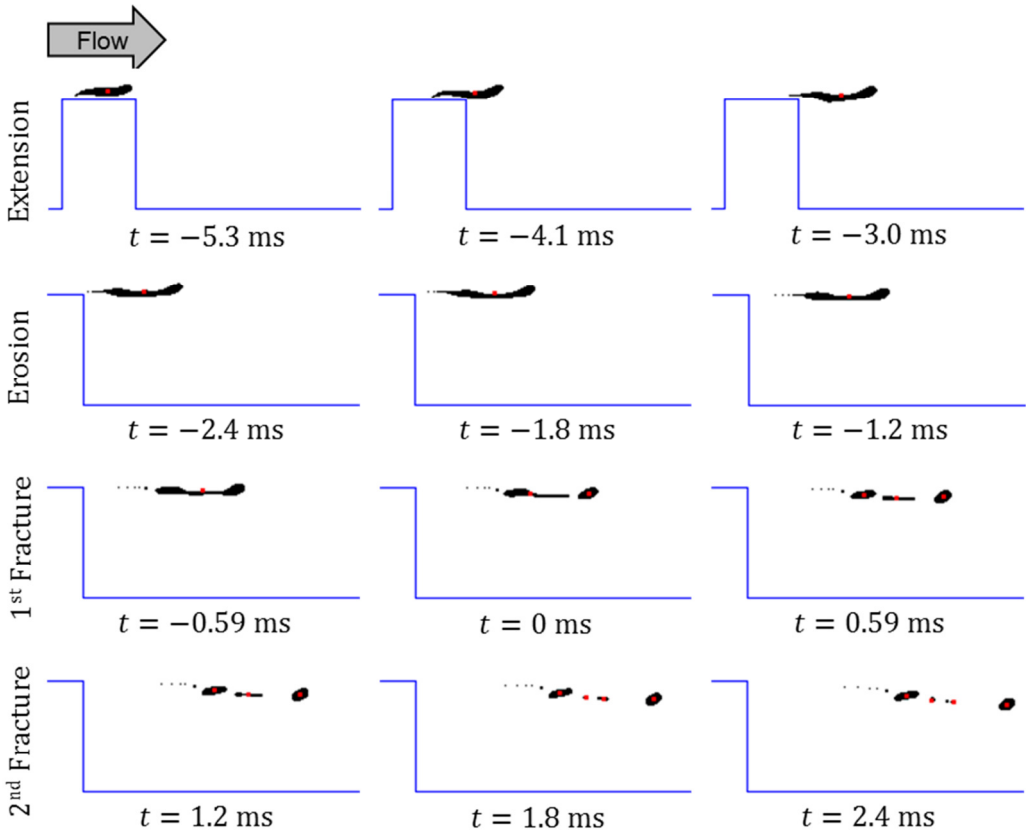

Figure 5.11. Break-up of a water droplet (D = 730 µm, y^*_{inc} = –2.2) by erosion and successive fracturing at Re_{ch} = 450 (μ_c = 0.0202 Pa-s). Time relative to first fracture at t = 0 is below each image. The red markers are droplet centroids for the larger daughter droplets. Image sequence acquired with Phantom camera (3,380 fps).

5.2.4. Bubble Entrainment Behind and Inside Orifice

Because a large volume of air needed to be purged from the system, the initial flows contained a wide range of bubbles that provided an opportunity to witness some interesting flow behaviour. Unlike in the turbulent flows, air in these

laminar flows could be entrained in any of the recirculation regions for long durations. This behaviour was not observed for water droplets in either CO70FG or CO200FG. Note that these phenomena are described only for the reader's interest; investigation of these phenomena is not within the scope of this study.

Despite being significantly less dense than the surrounding oil, it appears that the bubbles can become captured in the recirculating wake regions behind the orifice. Figure 5.12 shows bubble entrainment in the wake from the broad (viewing the x-z plane) and narrow (viewing the y-z plane) of the channel for Re_{ch} = 120 (μ_c = 0.0202 Pa-s). Some bubbles have coalesced and reached nearly-stable equilibrium positions. The lower bubbles in the image, located in the smaller wake region, have a slight back and forth vibration in the stream-wise (z) direction. Two higher bubbles are in the larger wake region, where they are moving in a small circular pattern (left droplet moving clockwise, right droplet moving counter-clockwise).

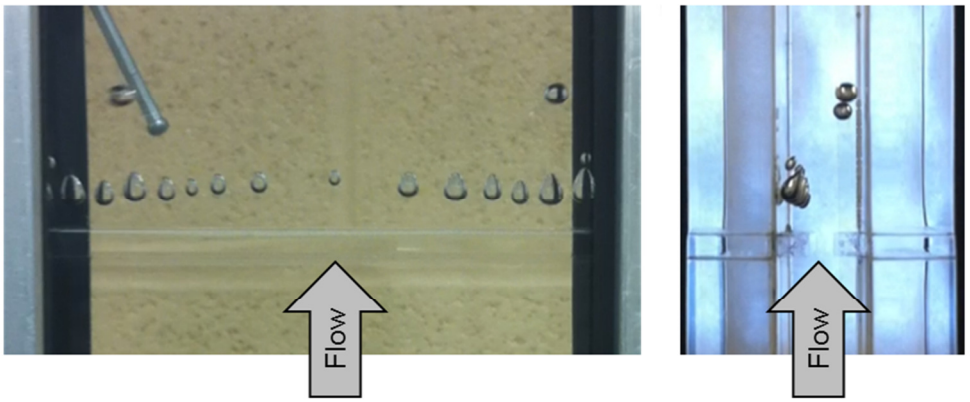

Figure 5.12. Nearly-stable positions of bubbles in the orifice wake regions at Re_{ch} = 120 (μ_c = 0.0202 Pa-s). The broad face of the channel (x-z plane) and the

typical view of the slit orifice (*y*-*z* plane) are shown in the left and right images, respectively. The orifice jet leans to the left in the right image.

A great deal of air can be entrained in both wake regions. Figure 5.13 shows air accumulation in the small wake region to coalesce into a few large cavities. The shape of these cavities was highly unstable. There was a large degree of lateral shifting, with bubbles seemingly being captured along its span and continuously ejected from the extreme ends of the span.

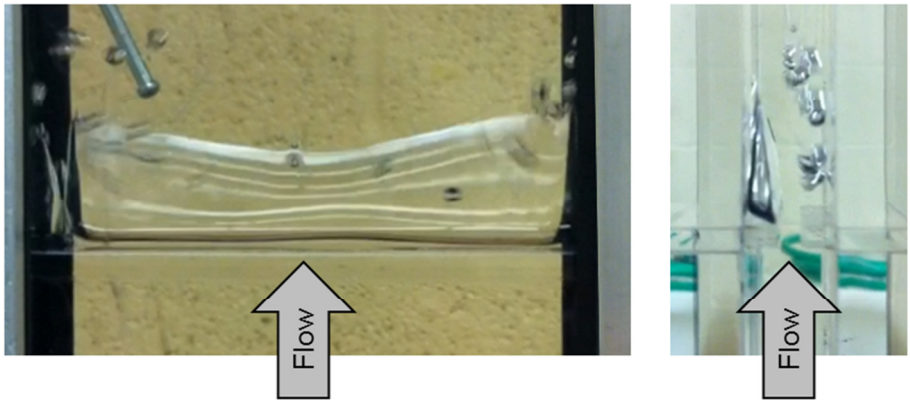

Figure 5.13. Large cavity in small wake region behind orifice at Re_{ch} = 360 (μ_c = 0.0202 Pa-s). The broad face of the channel (*x*-*z* plane) and the typical view of the slit orifice (*y*-*z* plane) are shown in the left and right images, respectively. The orifice jet leans to the left in the right image.

At higher Reynolds number, air is entrained into the separation zone within the orifice itself. Figure 5.14 shows the formation of these dynamically-stable bubbles at Re_{ch} = 1,000 (μ_c = 0.0202 Pa-s). These bubbles are narrow and densely-spaced along the entire span of the orifice; they were not observed to coalesce. They are maintained by the capture of tiny bubbles in the flow, but also eject tiny bubbles at their sharp downstream ends.

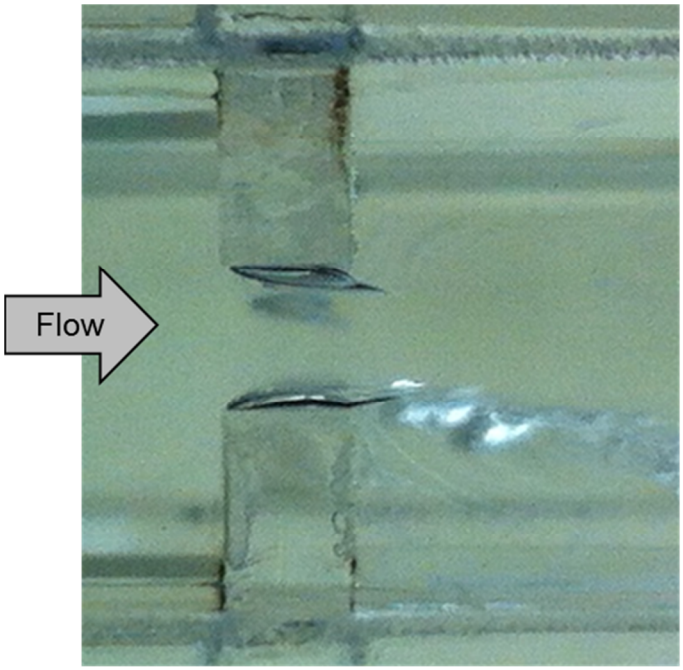

Figure 5.14. Bubbles attached to inner orifice surface at Re_{ch} = 1,000 (μ_c = 0.0202 Pa-s). The orifice jet leans down in this image.

5.3. Droplet Break-up based on Local Conditions

The approach to identifying the break-up criteria was based on the procedure in Section 4.3.4. In that section, the locally-derived Weber number (at an optimal scaled exposure time) was related to a probability of break-up for turbulent flows. However, because the droplet trajectories were found to be repeatable despite the strength and complexity of the flow, sharply-defined thresholds for erosion and fracture in terms of Weber number or other appropriate dimensionless group are desirable. This idealization is illustrated in Figure 5.15, where the thresholds for erosion and fracture ($We_{local,e}$ and $We_{local,f}$, respectively) are dependent on the local Weber number We_{local} (again at an optimal scaled exposure time) but not on other parameters such as the incoming trajectory y^*_{inc}.

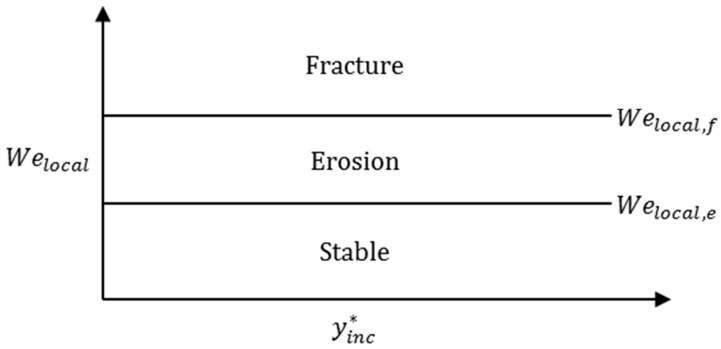

Figure 5.15. Illustration of concept of critical local Weber numbers for inertial laminar flows. The goal is to define thresholds for erosion and fracture breakage in terms of a local Weber number only.

As for the turbulent break-up analyses outlined in Section 4.3.4, only the velocity scale was considered to be time dependent. The form of the Weber number is shown in Equation 5.3-1; it is of the form recommended in Section 4.3.4 but without the Levich density correction since the laminar break-up experiments are for a fixed density ratio. ***It is assumed that the local Weber number*** **We_{local}** ***(defined in Equation 5.3-1) that characterizes break-up depends on the maximum strain rate magnitude averaged over an appropriate scaled exposure time.***

$$We_{local,t^*_{exp}} = \frac{\rho_c D}{\sigma}\left(\dot{\gamma}_{t^*_{exp}} D\right)^2 \tag{5.3-1}$$

The behaviour of We_{local} versus y^*_{inc} was initially studied for a range of exposure times scaled with the Stokes particle relaxation time (Equation 4.3-6). These efforts succeeded in defining thresholds for break-up. Figure 5.16 is the best result of this work (see the following Section 5.3.1 for the metric used in this evaluation); it shows local Weber number with $t^*_{exp} = 0.18$, based on the Stokes

particle relaxation time, versus incoming trajectory for all droplets in the laminar flow experiments. The marker style indicates Re_{ch}, while the colour indicates the break-up type (fracture, erosion, or unbroken). There are 92 droplets with a local Weber number greater than 400; all of these droplets passed close to the orifice surface and broke via the fracture break-up type. In the region $20 < We_{local} < 100$, there are droplets that have remained unbroken and others that have broken by either erosion or fracture. It is thus clear that the local Weber number as defined in Equation 5.3-1 is insufficient to act as a predictor for both break-up and the type of break-up to occur.

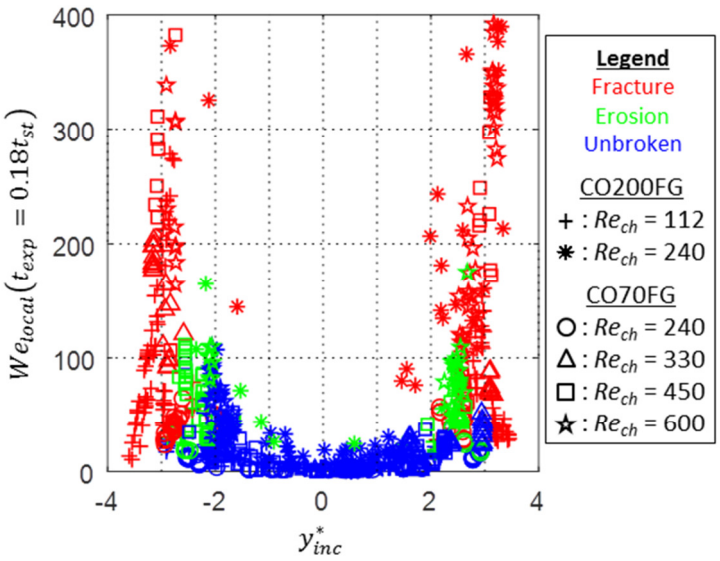

Figure 5.16. Local Weber number (Equation 5.3-1, t^*_{exp} = 0.18) versus incoming trajectory for all droplets in the laminar flow experiments. 92 of the 1062 droplets have We_{local} > 400; break-up of these 92 droplets were by fracture.

The goal of the remaining sections of this chapter will be to define the appropriate scaled exposure time and the corresponding thresholds for erosion and fracture break-up.

5.3.1. Metrics for Evaluating Fitness of Weber Number Models

Since reduced overlapping of the fracture, erosion, and unbroken droplets should characterize a well-performing local Weber number, the fitness of a particular We_{local} definition can be quantified by counting the droplets that have fractured or remained unbroken within the range of We_{local} for which erosion was found. This will be referred to as the penetration number N_{pen}. To reduce the dependence of N_{pen} on outliers, 5% of the data was removed for the calculation of N_{pen} only:

- For the droplets that were observed to fracture, the lowest 5% of the data in terms of Weber number was removed.
- For droplets that were observed to erode, the lowest 2.5% and highest 2.5% of data were removed.
- For the unbroken droplets, the highest 5% of data was removed.

For Figure 5.16, N_{pen} = 274. This means that there were 274 fractured or unbroken droplets with local Weber numbers (based on $t^*_{exp} = 0.18$) in the 'erosion range' of Weber numbers, in this case $17.5 < We_{local} < 112$. This is over a quarter of the data and is one of the best case results; other values of t^*_{exp} result in larger values N_{pen}, indicating that there is more overlapping of the data ranges and thus a poorer definition of local Weber number.

5.3.2. Local Weber Number with Long Axis as Length Scale

Because the initial selection of Weber number and Stokes particle relaxation time did not separate the break-up types as well as desired, other dimensionless groups and time scales were investigated. In the literature for droplet break-up in Stokes and inertial laminar flows, both capillary number and Reynolds number have been used to characterize break-up, while Ohnesorge number is the standard dimensionless group for analyzing the break-up of jets. For the time scales discussed in the turbulent flow break-up section (see Table 4.2), the fluid particle response time and the oscillation time were investigated further. However, after tabulating the N_{pen} for these combinations of dimensionless groups and time scales, none of them produced a positive effect. For these conditions, the fluid particle response time was within 6% of the Stokes particle response time and so resulted in the same N_{pen} values. A local Weber number based on the oscillation time scale ($t^*_{exp} = 8$) produced a similar N_{pen}. Other combinations resulted in substantially higher N_{pen}.

The greatest reduction in N_{pen} was achieved by replacing the length scale in the dimensionless group (previously the un-deformed diameter D) with the maximum length of the long axis L over the course of the droplet trajectory. Figure 5.17 shows the result of this new form of Weber number (with the exposure time still scaled with the Stokes particle relaxation time). For this formulation, N_{pen} is 109. Note that to retain most of the data in the plot, the We_{local} axis is logarithmic. There is a boundary between the unbroken and broken droplets at $We_{local} \cong 100$.

The droplets undergoing erosion and fracture are mixed, but the ratio of the droplets fractured to eroded is greater than 2:1 after $We_{local} \cong 1{,}600$.

Figure 5.18 shows the improvement from switching the time scale to the oscillation time scale, with the optimal $t^*_{exp} = 8$. N_{pen} is reduced to 60. The threshold between unbroken and broken is located at $We_{local} \cong 30$, while the threshold to fracture is at $We_{local} \cong 1{,}000$.

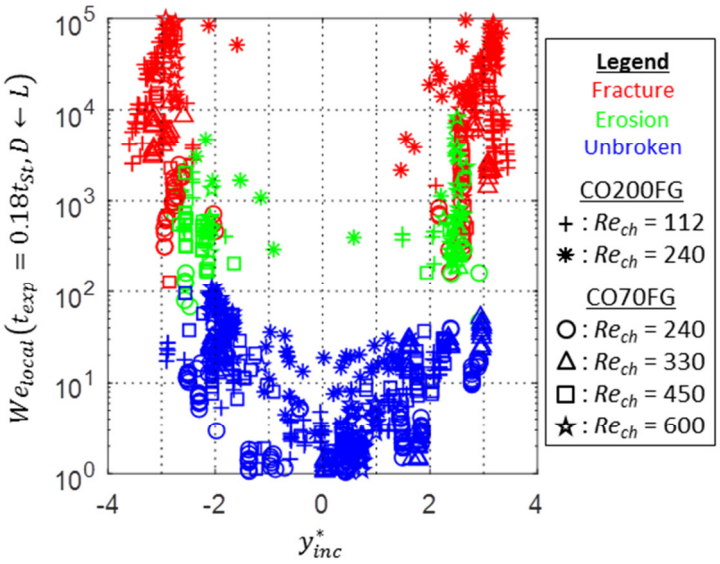

Figure 5.17. Local Weber number (t^*_{exp} = 0.18 based on the Stokes particle relaxation time and the length scale D replaced by droplet long axis L) versus incoming trajectory. N_{pen} = 109.

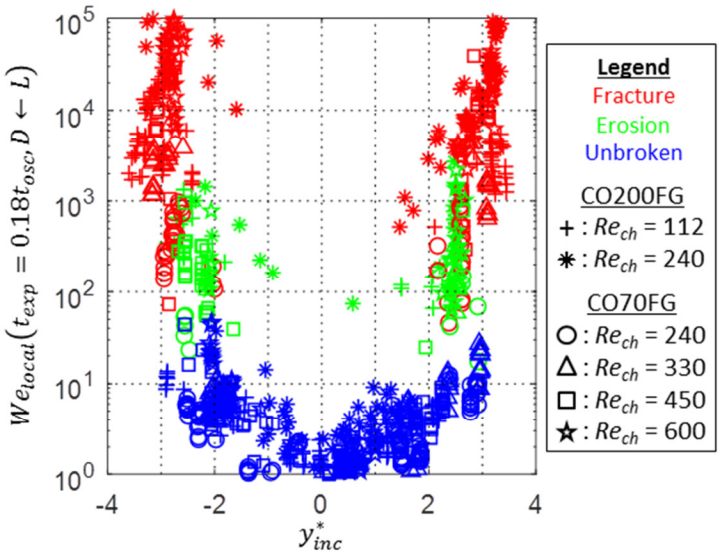

Figure 5.18. Local Weber number (t^*_{exp} = 8 based on the oscillation time scale and the length scale D replaced by droplet long axis L) versus incoming trajectory. N_{pen} = 60.

5.3.3. Modelling Droplet Extended Length

Compared to the turbulent flow model presented in Section 4.3.4, the disadvantage of the recommended Weber number form is that it relies on having the extended length of the droplet. The data produced in this work can be used to provide a prediction of this extended length. Model development attempted to correlate drop draw ratio with Weber number, capillary number, or Reynolds number, but these were all resulted in large errors. The product $Ca_{local}\,\lambda^n$, where n were exponents between 0 and 1, helped to reduce the error, with drop draw ratio best correlating with n = 0.5.

For each of the time scales for which local Weber number thresholds were discussed in Section 5.3.2, a corresponding drop draw ratio model with the capillary

number Ca_{local} utilizing the same maximum average strain rate magnitude value is presented below. Equation 5.3-2 and Figure 5.19 are for the Stokes particle relaxation time scale ($t^*_{exp} = 0.18$), while Equation 5.3-3 and Figure 5.20 are for the oscillation time scale ($t^*_{exp} = 0.8$). Both of the equations are limited such that the drop draw ratio must be a minimum of 1. These correlations must be used with caution since there is a significant amount of variation in the actual data and a lack of clear mechanistic basis.

$$\frac{L}{D} = \max[1.0\ ;\ 34.0(Ca_{local}\lambda^{0.5})^{0.130} - 26.1]\,,\mathrm{RMSE} = 0.97 \qquad (5.3\text{-}2)$$

$$\frac{L}{D} = \max[1.0\ ;\ 35.3(Ca_{local}\lambda^{0.5})^{0.156} - 24.4]\,,\mathrm{RMSE} = 0.85 \qquad (5.3\text{-}3)$$

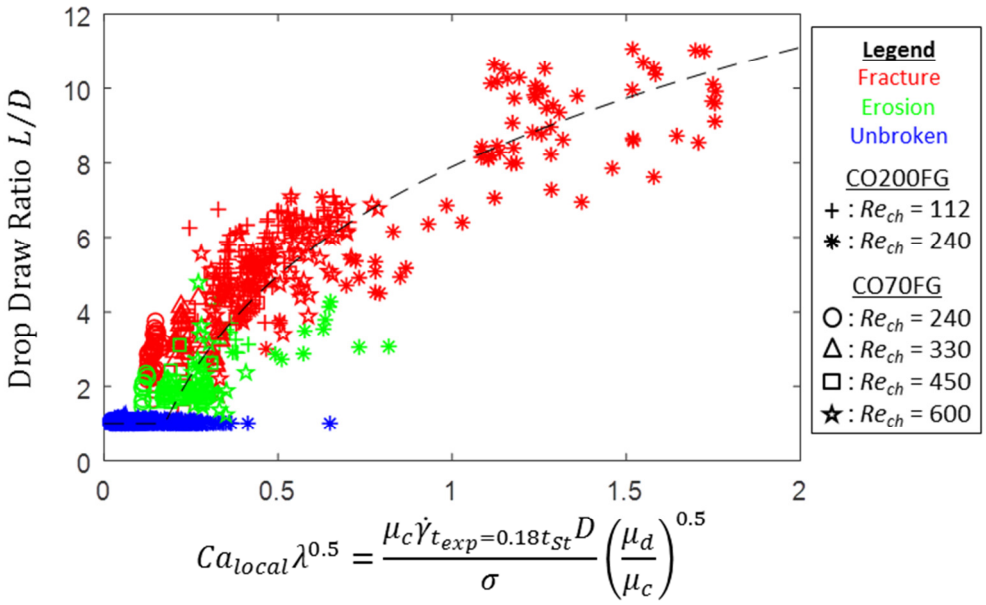

Figure 5.19. Drop draw ratio L/D versus the product $Ca_{local}\,\lambda^{0.5}$ (t^*_{exp} = 0.18 based on the Stokes particle relaxation time scale). The model represented by the dashed line is given in Equation 5.3-2. The RMSE is 0.97.

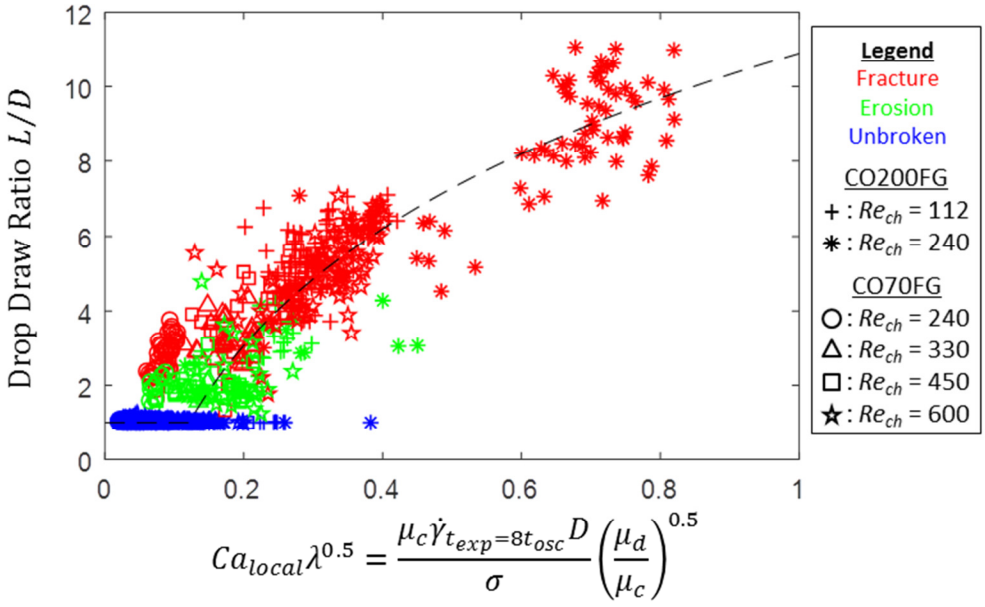

Figure 5.20. Drop draw ratio L/D versus the product $Ca_{local}\,\lambda^{0.5}$ (t^*_{exp} = 8 based on the oscillation time scale). The model represented by the dashed line is given in Equation 5.3-3. The RMSE is 0.85.

5.3.4. Discussion of Break-up in Inertial Laminar Flows

For the break-up of droplets in the inertial laminar 2-D orifice flow, the analyses of the experimental data indicate that there are contributions from inertial, surface, and viscous effects. The extension of the droplet was best fitted to a locally-derived capillary number Ca_{local}, meaning that the deformation is motivated by viscous stresses and opposed by interfacial stresses. Higher deformation was generally achieved for larger droplets, droplets in faster flows, and droplets in the higher viscosity CO200FG flows, all of which is included in the capillary number. Interestingly, however, the best correlation has a partial contribution from the viscosity of the dispersed phase fluid. While the open literature for break-up in inertial shear flows (summarized in Figure 5.4) does not include the viscosity ratios

tested in these experiments, break-up of droplets with low viscosity ratio in Stokes flows require a greater strain rate to succeed since the inner fluid shifts its flow to help stabilize the droplet. The role the dispersed phase viscosity plays in the deformation mechanism cannot be determined from the current experimental analyses, but it is possibly related to inner fluid's inability to re-distribute internal flow in response to very strong changes in the outer flow conditions.

The break-up, on the other hand, was better described by the local Weber number We_{local} as the ratio of inertial to interfacial stresses. The break-up location and the quantity of daughter droplets produced appeared to be consistent for a group of droplets with particular size, incoming trajectory, and channel flow rate. Since pressure is inertia-scaled in inertial flows, the disruptive inertial stresses may originate in pressure acting on the droplet interface. The pressure differences scale with the relative velocity difference across the extended droplet. It is not clear, however, why the cohesive interfacial forces are better represented with the deformed length as the length scale. A cylinder of fluid with short axis length B should ideally have a slightly greater interfacial stresses due to its smaller length scale. One possible interpretation is that the additional bending at each end of the droplet, caused by jet curvature and also inertial lift forces, results in a locally-weaker interfacial stresses. The use of L as the length scale results in a weaker interfacial stress, but this cannot be viewed mechanistically accurate.

The oscillation time scale was shown to produce better separation of droplets with the three break-up types (unbroken, erosion, and fracture) when

compared with the Stokes particle relaxation time. This time scale definition was from the work of Miller & Scriven (1967) on droplet oscillations, but the formulation seems to be similar to work on jet break-up. For example, the form of the oscillation time scale for a liquid droplet in a vacuum is functionally-identical to the form of the time scale for a break-up of an inviscid jet in a non-participating medium (McKinley & Renardy, 2011). This would allow for the time scale to be interpreted as being applicable to a problem in which both fluids are approximately inviscid, including jets or highly extended droplets.

5.4. Key Findings for Break-up in Inertial Laminar Flows

The key findings of the work described in this chapter are:

- Despite the complexity of the flow field and the strong inertial character of the flow, both droplet trajectories and break-up outcomes tend to be repeatable.
- The droplet trajectory is only affected by diameter, channel Reynolds number, and viscosity ratio beginning 1 H (1.3 cm) downstream of the orifice.
- Droplet break-up, whether by erosion or fracture, appears to be related to the elongative end-pinching discovered by Marks (1998). Erosion occurs at moderate local Weber numbers, while fracture occurs at high local Weber numbers.
- The droplet images show bending of the leading end toward the center of the jet; this is an experimental result that supports the idea that aerodynamic lift,

first shown in the simulations of Renardy & Cristini (2001a), becomes a factor in droplet break-up in inertial flows.

- Droplet break-up due a short-term high-intensity deformation event in inertial laminar flow can be characterized using the local Weber number definition in Equation 5.4-1. L is the length of the extended droplet and $\dot{\gamma}$ as the maximum average strain rate magnitude over an exposure time of 8 multiplied by the droplet's oscillation time scale. Based on this definition, a droplet will remain unbroken with We_{local} as high as 30, while generating droplet fracture reliably occurs at We_{local} as low as 1,000. For $30 < We_{local} < 1{,}000$, either erosion or fracture may occur.

$$We_{local} = \frac{\rho_c L^3}{\sigma} \dot{\gamma}^2_{t_{exp}=8t_{osc}} \tag{5.4-1}$$

- The drop draw ratio L/D was correlated to the product of the local capillary number Ca_{local} and the square root of the viscosity ratio λ, as shown in Equation 5.4-2. Ca_{local} is calculated from the same strain rate magnitude definition used in We_{local} but uses the un-deformed diameter D as the length scale. The max function ensures that the resulting drop draw ratio has a minimum value of 1. This model does not have a clear mechanistic basis and does not model much of the variation observed in the experimental imaging, so it must be used with caution.

$$\frac{L}{D} = \max[1.0\ ;\ 35.3(Ca_{local}\lambda^{0.5})^{0.156} - 24.4]\,, \text{RMSE} = 0.85 \tag{5.4-2}$$

- Because of the uncertainty in the drop draw ratio model (Equation 5.4-2), it may be more convenient to define the local Weber number with the un-deformed diameter D as the length scale, as shown in Equation 5.4-3. The recommended $\dot{\gamma}$ is the maximum average strain rate magnitude over 0.18 multiplied by the Stokes particle relaxation time scale. If a droplet has a $We_{local} < 20$, it is predicted to remain unbroken. For $We_{local} > 100$, fracture is expected. In the region between ($20 < We_{local} < 100$), it is possible for any of the three behaviours (fracture, erosion, or unbroken) to occur.

$$We_{local} = \frac{\rho_c D^3}{\sigma} \dot{\gamma}^2_{t_{exp}=0.18t_{St}} \tag{5.4-3}$$

6. Summary, Conclusions, and Recommendations

This chapter presents the key observations and conclusions from each phase of this project. Also presented are recommendations to further understand the influence of short-term deformation events on droplets in inertial flows.

6.1. Summary of Project Objectives and Methodologies

The objective of this project was to develop a capability to predict the occurrence of droplet break-up due to short-term, high intensity deformation events in turbulent and inertial laminar flows. A channel apparatus with 2-D slit orifice, along with an associated flow loop, was built. High-speed imaging of droplets through the slit orifice was used to determine the droplet trajectories. CFD simulations of the flow field were combined with each droplet trajectory to determine the time-dependent deformation history at each point along the trajectory. These trajectory-specific deformation histories allowed for different combinations of velocity, length, and time scales to be investigated with respect to forming characteristic dimensionless groups that could be correlated to break-up or break-up probability. The results of this work include predictive models for break-up and observations of the break-up mechanisms in both turbulent and inertial laminar flows.

6.2. Channel, Inlet, and Orifice Flows

The channel, inlet, and orifice flows were studied primarily using CFD. These flows are described in greater detail in Chapter 3.

- CFD simulations of the open channel indicated that, due to the limited width of the channel, the average velocity the span-wise centre of the channel was slightly higher than the design superficial channel velocity of 1.1 m/s (as would be predicted with flow between infinite parallel plates) by about 4% and 7% in turbulent and laminar flows, respectively.
- CFD was used to establish the entrance length required to fully-develop both turbulent and laminar flows prior to the test section. The physical apparatus was design with the required entry length of 0.90 m.
- Mean flow simulations were conducted for four turbulent and six laminar operating conditions, with the channel Reynolds numbers Re_{ch} ranging from 110 to 19,000. In all cases, the expected leaning jet due to the Coandă effect was well-simulated. Flow field information is presented in Appendix B.
- The shape of the simulated orifice jet, quantified through measurement of the small wake region behind the orifice, agreed qualitatively with previous literature. For the turbulent operating conditions, the length of the small (low pressure) wake region was constant at approximately 1 H (1.3 cm). For the laminar operating conditions, the small wake region increased slowly from 1.1 H (1.4 cm) at Re_{ch} = 110 to 1.8 H (2.2 cm) at Re_{ch} = 600. Images of dye streamlines in the channel also show a similar shape of the small wake

region and, for the turbulent flow, independence of the shape from the channel Reynolds number.

6.3. Droplet Break-up in Turbulent Flows

The break-up of droplets in turbulent flows is discussed in Chapter 4. High-speed imaging was used to track oil droplets and air bubbles of sizes on the order of the macroscale of turbulence. Forms of the Weber number mechanistically appropriate to the turbulent flow and the size of the droplets relative to the size of the turbulent eddies were developed.

- The random nature of turbulence masks the effect of droplet diameter and channel Reynolds number on the path of droplets through the orifice. There is a degree of lateral migration, caused by the pressure difference that sustains the leaning of the jet, which more strongly affects the lower density air bubbles. This results in a greater degree of breakage for droplets approaching the side of the orifice with the small, low pressure wake region because the lateral migration is acting to push the droplets into the jet edge.
- The form of Weber number appropriate to characterizing the break-up of macroscale droplets due a short-term high-intensity deformation event in turbulent flow has been determined. In contrast to the inertial subrange model, where the velocity scale is $(\varepsilon D)^{1/3}$, ***the break-up of macroscale droplets scales with a macro velocity scale of*** $\dot{\gamma}\mathbf{D}$. The $\dot{\gamma}$ to be used here is the maximum average strain rate magnitude over an exposure time of 0.04

multiplied by the Stokes particle relaxation time. The local Weber number, defined in Equation 6.3-1, can be used to calculate the probability of break-up as shown in Equation 6.3-2. Note that the dynamical interpretation of Levich (1962) was critical in developing this equation for use with both liquid droplets and gas bubbles.

$$We_{local} = \frac{(\rho_d \rho_c^2)^{1/3} \dot{\gamma}^2_{t^*_{exp,St}=0.04} D^3}{\sigma} \tag{6.3-1}$$

$$P_{St} = \exp\left(-\frac{4.57}{We_{local}}\right), \text{RMSE} = 0.067 \tag{6.3-2}$$

- Contour plots graphically relating the probability of break-up as a function of an upstream Weber number (based on the superficial channel velocity instead of a local flow quantity), incoming trajectory, and droplet material have been developed. The advantage of this plot is that the three independent variables are based on the droplet condition upstream of the orifice, where the flow is more easily sampled. These plots are presented as Figure 4.26 for breakage of oil droplets and Figure 4.27 for breakage of air bubbles. An example of how to use the contour plots is in Section 4.4.3.
- Contour plots graphically relating the probability of break-up as a function of an orifice Weber number (based on the strain rate magnitude experienced by the droplet at the orifice entrance), trajectory at the orifice entrance, and droplet material have been developed. These plots allow droplet break-up to be predicted in cases where the upstream geometry is not a 4:1 contraction,

such as for multi-orifice plates. These plots are presented as Figure 4.33 for breakage of oil droplets and Figure 4.34 for breakage of air bubbles.

- On average, the production of sizable daughter droplets during the initial breakage event was approximately constant. Oil droplets produce 4 sizable daughters, and air bubbles produce 2.5 sizable daughters. However, there was a greater degree of variation in the production of these daughter droplets when the parent droplet was approaching the orifice closer to the channel wall.

6.4. Droplet Break-up in Inertial Laminar Flows

The break-up of droplets in inertial laminar flows is discussed in Chapter 5. All channel Reynolds numbers are well above unity, so the advective terms of the Navier-Stokes cannot be neglected. The analyses focused on determining the appropriate Weber number form for the break-up of liquid droplets only.

- Despite the complexity of the flow field and the strong inertial character of the flow, droplet trajectories for a specific set of conditions (droplet diameter, incoming trajectory, channel Reynolds number) tend to be repeatable, resulting in deterministic break-up behaviour.
- Close to the orifice, where strain rates are highest, the droplet trajectories are not dependent on droplet diameter or channel Reynolds number. At distances greater than 1 H (1.3 cm) from the leeward side of the orifice, there

are noticeable differences in trajectory based on channel Reynolds number and viscosity ratio.

- As with break-up in turbulent orifice flows, break-up in inertial laminar orifice flows occur in the high shear regions at the edges of the orifice jet.
- The break-up events were categorized as either fracture or erosion, but both seem to fundamentally originate from an elongative end-pinching mechanism. Fracture produces daughter droplets of more comparable size, with the leading end always producing a larger droplet than the trailing end. Erosion refers to a droplet for which the internal flow redistributes quickly enough that the trailing end does not form a significant bulb; this tail produces daughter droplets with diameters of 100 μm or less. The erosion mechanism happens over a specific and moderate range of local Weber numbers, while fracture is typically characterized by high local Weber numbers.
- The leading ends of droplets passing through the orifice were observed to bend toward the center of the jet. This bending is likely due to the aerodynamic lift mechanism first shown in simulations of Renardy & Cristini (2001a).
- The form of Weber number appropriate to characterizing the break-up of droplets due a short-term high-intensity deformation event in inertial laminar flow has been determined. The local Weber number We_{local} is defined in Equation 6.4-1, with L as the length of the extended droplet and $\dot{\gamma}$ as the maximum average strain rate magnitude over an exposure time of 8

multiplied by the droplet's oscillation time scale. Based on this definition, a droplet will remain unbroken with We_{local} as high as 30, while generating droplet fracture reliably occurs at We_{local} as low as 1,000. For $30 < We_{local} < 1{,}000$, either erosion or fracture may occur.

$$We_{local} = \frac{\rho_c L^3}{\sigma} \dot{\gamma}^2_{t_{exp}=8t_{osc}} \tag{6.4-1}$$

- The drop draw ratio L/D was correlated to the product of the local capillary number Ca_{local} and the square root of the viscosity ratio λ as shown in Equation 6.4-2. Ca_{local} is calculated from the same strain rate magnitude definition used in We_{local} but uses the un-deformed diameter D as the length scale. The max function ensures that the resulting drop draw ratio has a minimum value of 1. This model needs to be used with caution because it does not yet have a clear mechanistic basis and does not explain a significant amount of variation measured in the experimental data.

$$\frac{L}{D} = \max[1.0\ ;\ 35.3(Ca_{local}\lambda^{0.5})^{0.156} - 24.4], \text{RMSE} = 0.85 \tag{6.4-2}$$

- Because of the uncertainty in the drop draw ratio model (Equation 6.4-2), it may be more convenient to define the local Weber number with the un-deformed diameter D as the length scale, as shown in Equation 6.4-3. In this case, the recommended $\dot{\gamma}$ is the maximum average strain rate magnitude over 0.18 multiplied by the Stokes particle relaxation time scale. If a droplet has a $We_{local} < 20$, it is predicted to remain unbroken. For $We_{local} > 100$,

fracture is expected. In the region between ($20 < We_{local} < 100$), it is possible for any of the three behaviours (fracture, erosion, or unbroken) to occur.

$$We_{local} = \frac{\rho_c D^3}{\sigma} \dot{\gamma}^2_{t_{exp}=0.18t_{St}} \tag{6.4-3}$$

6.5. Future Work

- The local Weber numbers were derived based only on conditions local to the droplet, with the intent of making this relationship applicable under a broad range of devices. To demonstrate that this is the case, study with additional constrictions geometries and devices is needed.
- The current study treated the droplets as inviscid. This may not be so for oil droplets in the turbulent water flows. A mechanistic model, accounting for both interfacial tension and viscosity effects, could be developed from first principles. Preliminary analysis of the current data, with the interfacial stresses augmented by a viscosity term as shown in Equation 6.5-1, showed some benefit. However, the appropriate form of the combined cohesive stress and the relative importance of each component have not been determined.

$$We'_{local} = \frac{(\rho_c^2 \rho_d)^{1/3} \left(\dot{\gamma}_{t^*_{St}} D\right)^2}{\frac{\sigma}{D} + C_\mu \mu_d \dot{\gamma}_{t^*_{St}}} \tag{6.5-1}$$

- Improvement to the drop draw ratio correlations for laminar flows would improve the usability of the recommended local Weber number definition. In addition to developing a better understanding of the dynamics, there are path-dependent factors, such as the turning angle into the orifice, which may yield an improved model.

Appendix A: Apparatus Drawings

Appendix A contains the as-built assembly and part drawings for the flow channel fabricated for this project. These drawings are in three groups as listed below. Note that the aluminum baffle plate (part 5 of the inlet segment) had a tendency to get stuck in its alignment grooves, possibly due to oxidation of the aluminum in water. It was replaced with a polystyrene baffle plate of the same dimensions.

- Inlet Segment (7 drawings)
- Upstream Segment (3 drawings)
- Test and Downstream Segments (6 drawings)

The inlet and upstream segments were fabricated from sheet aluminum by Excel Machine & Fabrication Inc. in Baltimore, MD, USA. The test and downstream segments were fabricated from transparent cast acrylic by Precision Plastics Inc., in Beltsville, MD, USA.

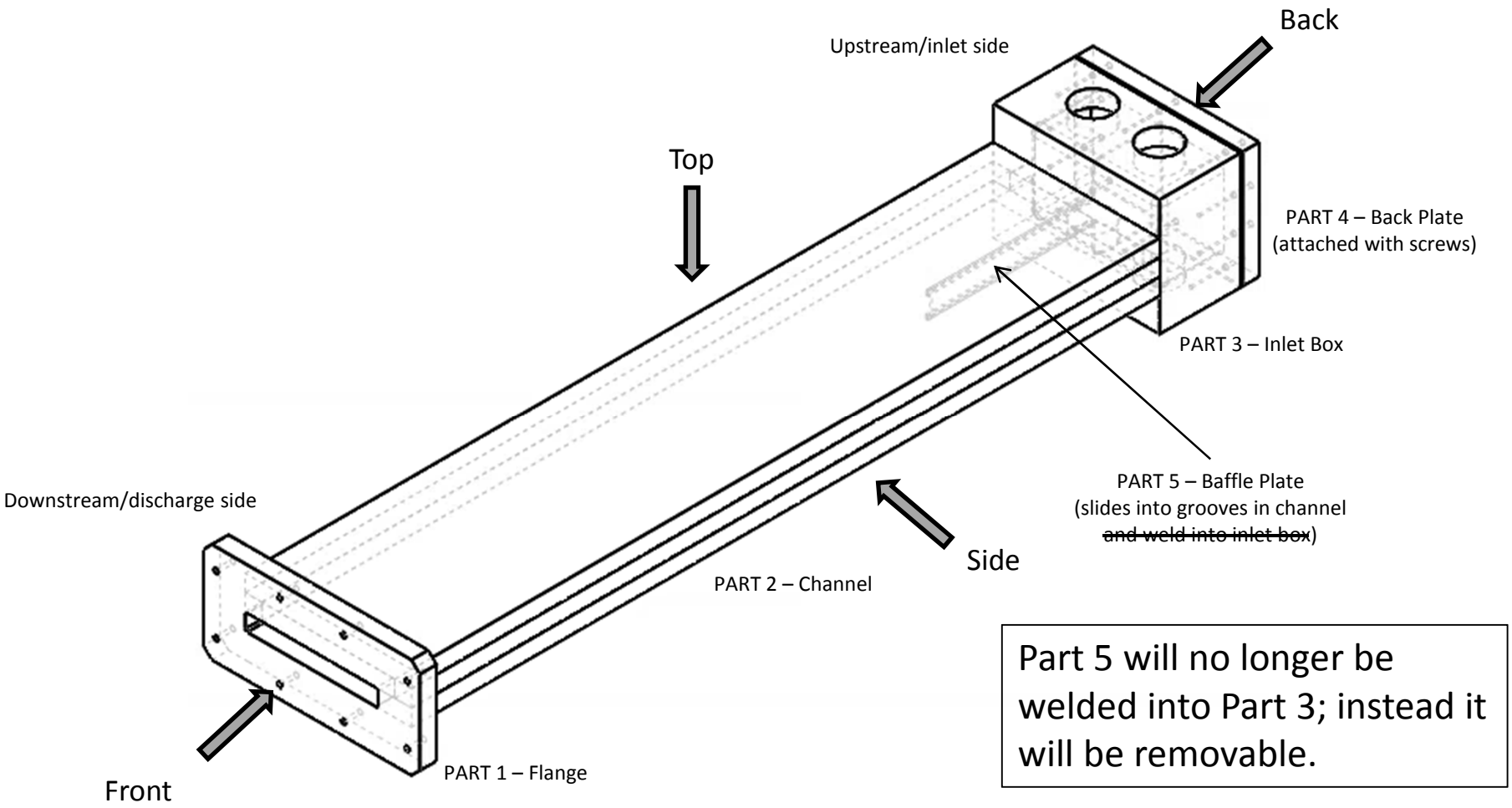

Part 5 will no longer be welded into Part 3; instead it will be removable.

ISOMETRIC ASSEMBLY DIAGRAM

Overall assembly view. Material for all parts is 6061 aluminum. For orientation, additional isometric views are provided on the parts drawings. Parts 1, 2, and 3 will be welded together. Part 5 will be inserted into grooves in Parts 2 and 3, ~~then welded inside to Part 3~~. Part 4 will be secured to Part 3 with #6-32 machine screws (provided by University of Maryland).

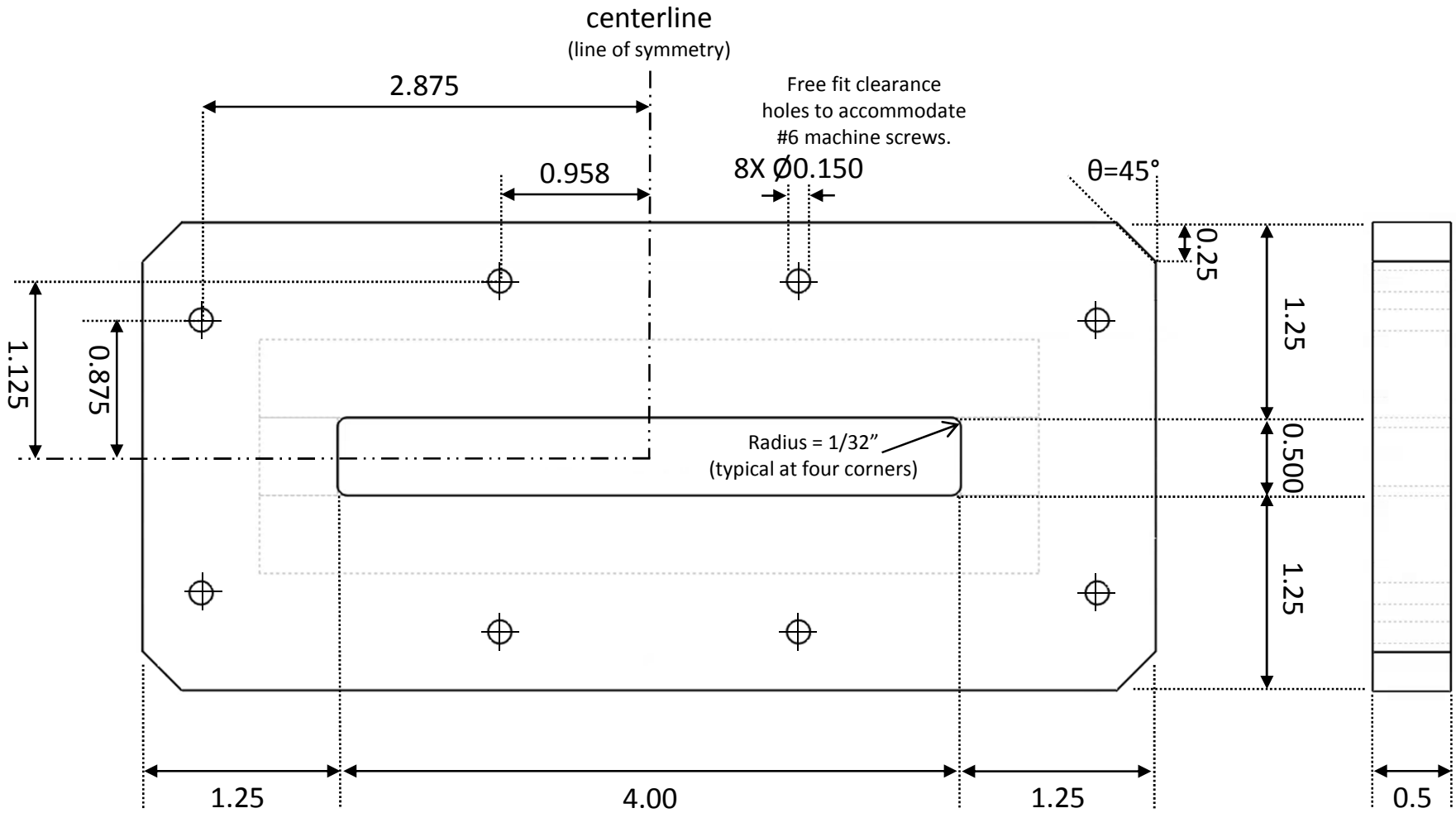

Isometric View

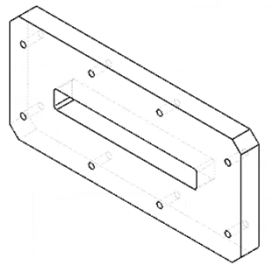

All dimensions are in inches.
Tolerances:
.X = ± 0.06"
.XX = ± 0.03"
.XXX = ± 0.01"
.XXXX = ± 0.003"

PART 1 – Flange (Front and Side View)

Shows flange and machine screw hole dimensions.

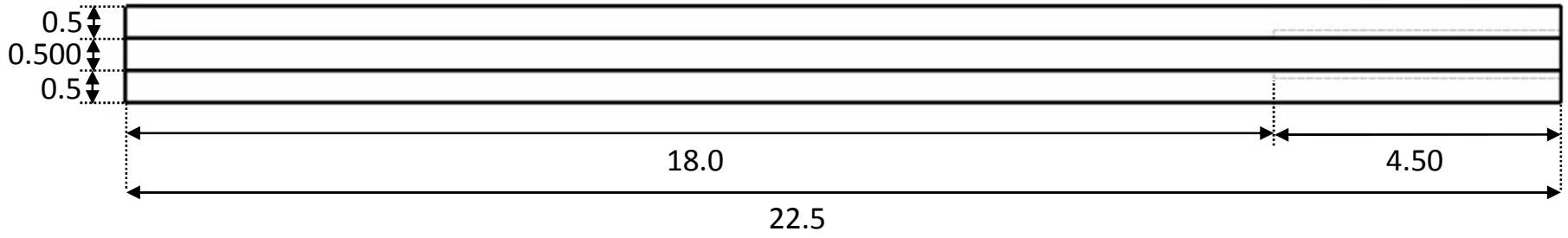

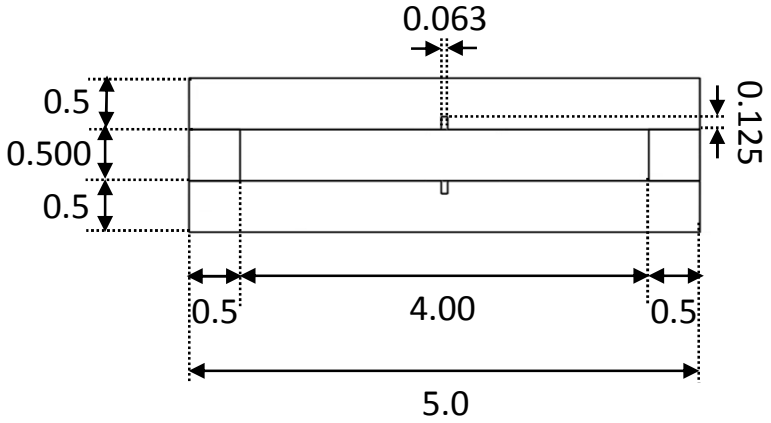

1/8”-deep, 1/16”-wide groove extends for 4.50” to allow for insertion of baffle plate.

Additional 1/32” radius at end of groove.

Isometric View

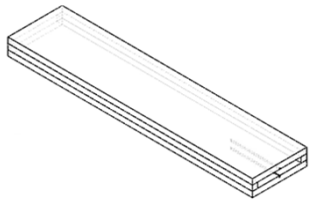

All dimensions are in inches.
Tolerances:
.X = ± 0.06”
.XX = ± 0.03”
.XXX = ± 0.01”
.XXXX = ± 0.003”

PART 2 – Channel (Side and Back View)

The four ½”-thickness bars are to be welded together. The critical dimension for our experiments is the height of 0.500”. The groove for the baffle plate must be in-line with the corresponding groove in the inlet box.

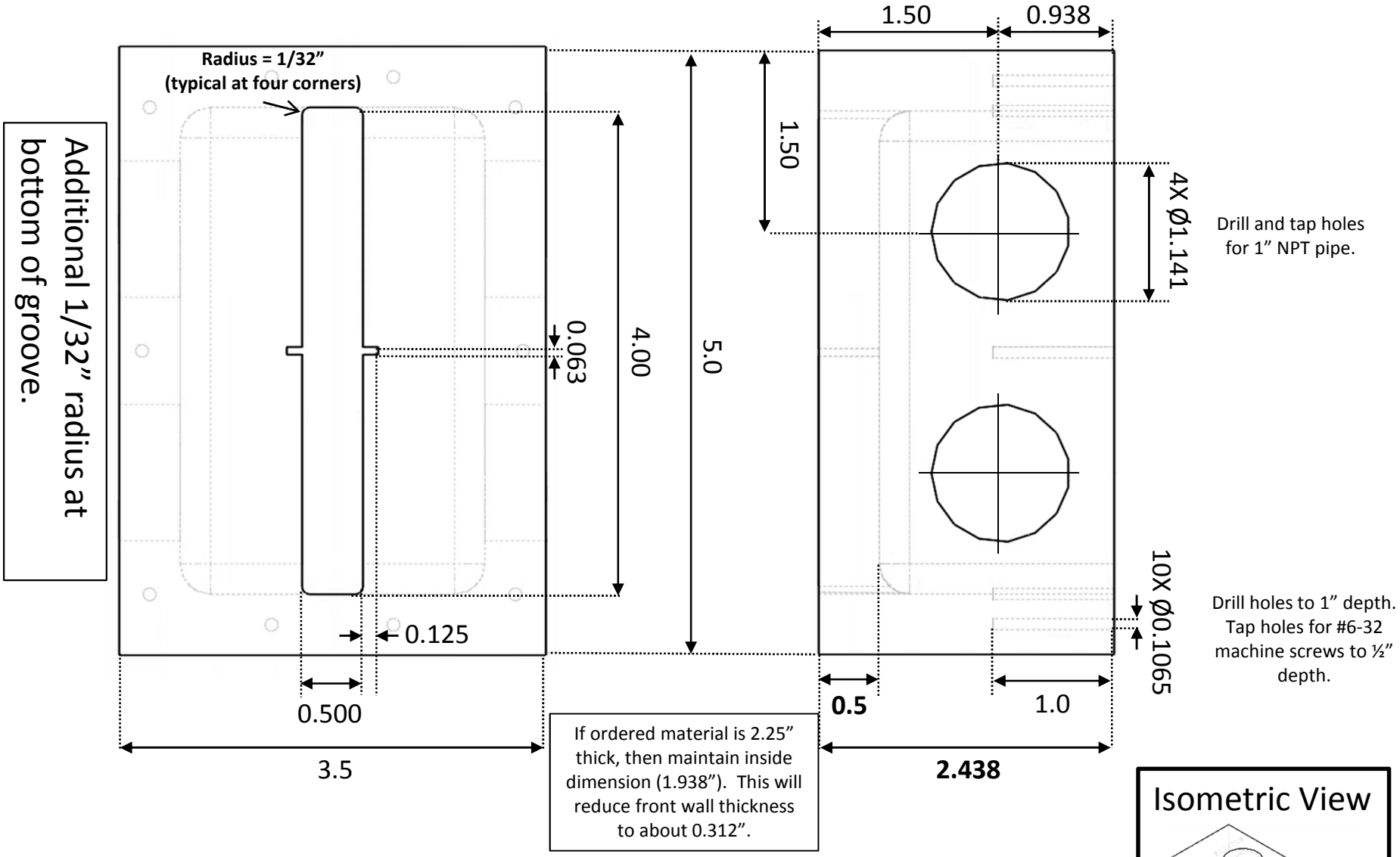

Isometric View

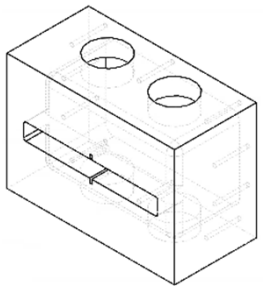

All dimensions are in inches.
Tolerances:
.X = ± 0.06"
.XX = ± 0.03"
.XXX = ± 0.01"
.XXXX = ± 0.003"

PART 3 – Inlet Box (Front and Top View)

Note that the 1/16" groove for the baffle plate must line up with the groove in the channel (Part 2).

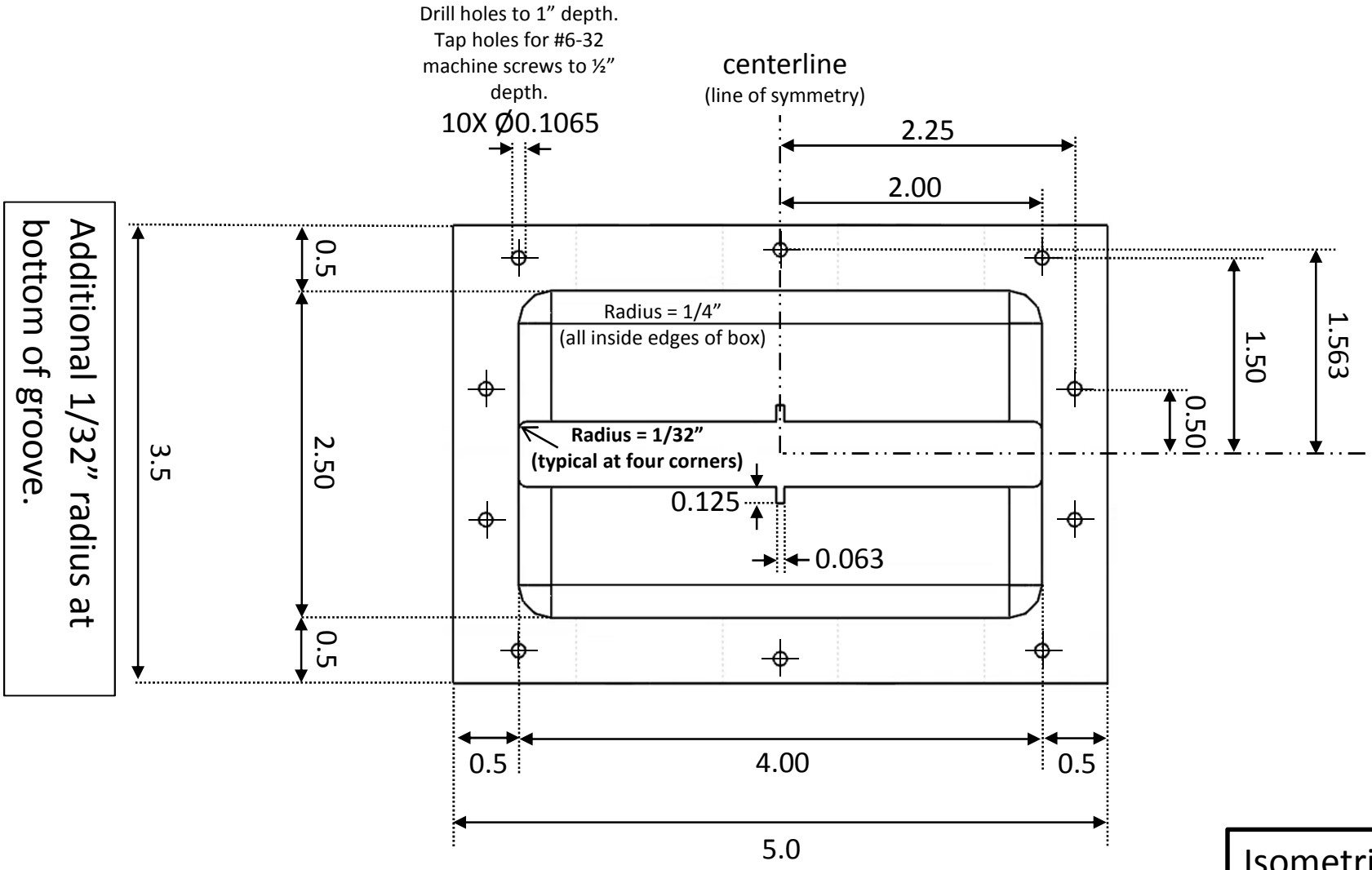

Isometric View

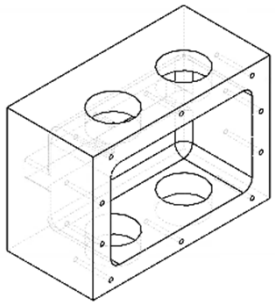

All dimensions are in inches.
Tolerances:
.X = ± 0.06”
.XX = ± 0.03”
.XXX = ± 0.01”
.XXXX = ± 0.003”

PART 3 – Inlet Box (Back View)

Dimensions and screw hole locations for inlet box.

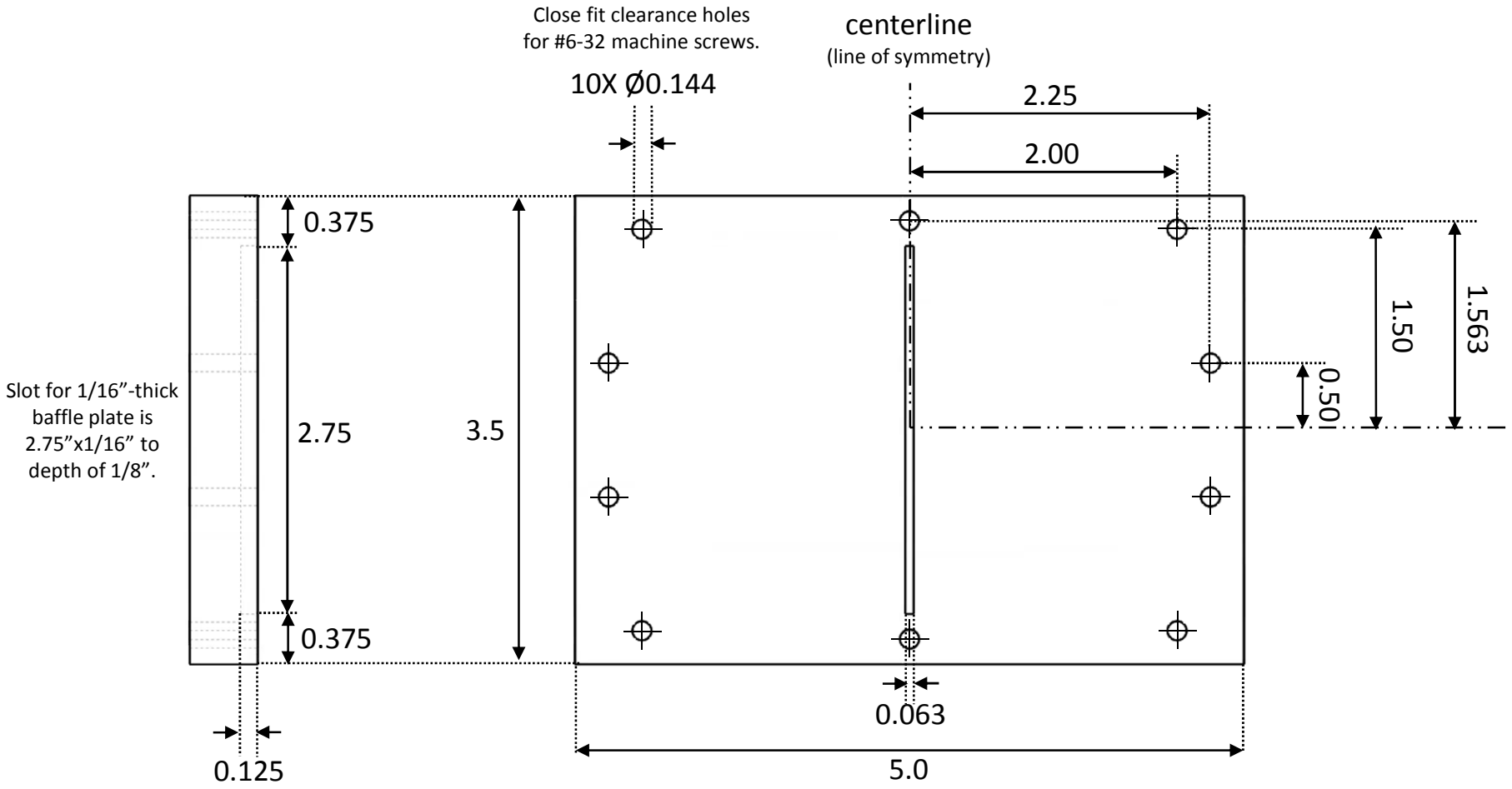

Additional 1/32” radius at ends of groove.

Isometric View

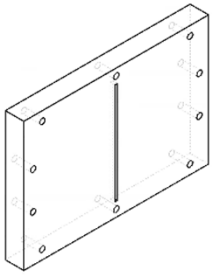

All dimensions are in inches.
Tolerances:
.X = ± 0.06”
.XX = ± 0.03”
.XXX = ± 0.01”
.XXXX = ± 0.003”

PART 4 – Back Plate (Side and Front View)

Dimensions and screw hole locations for back plate.

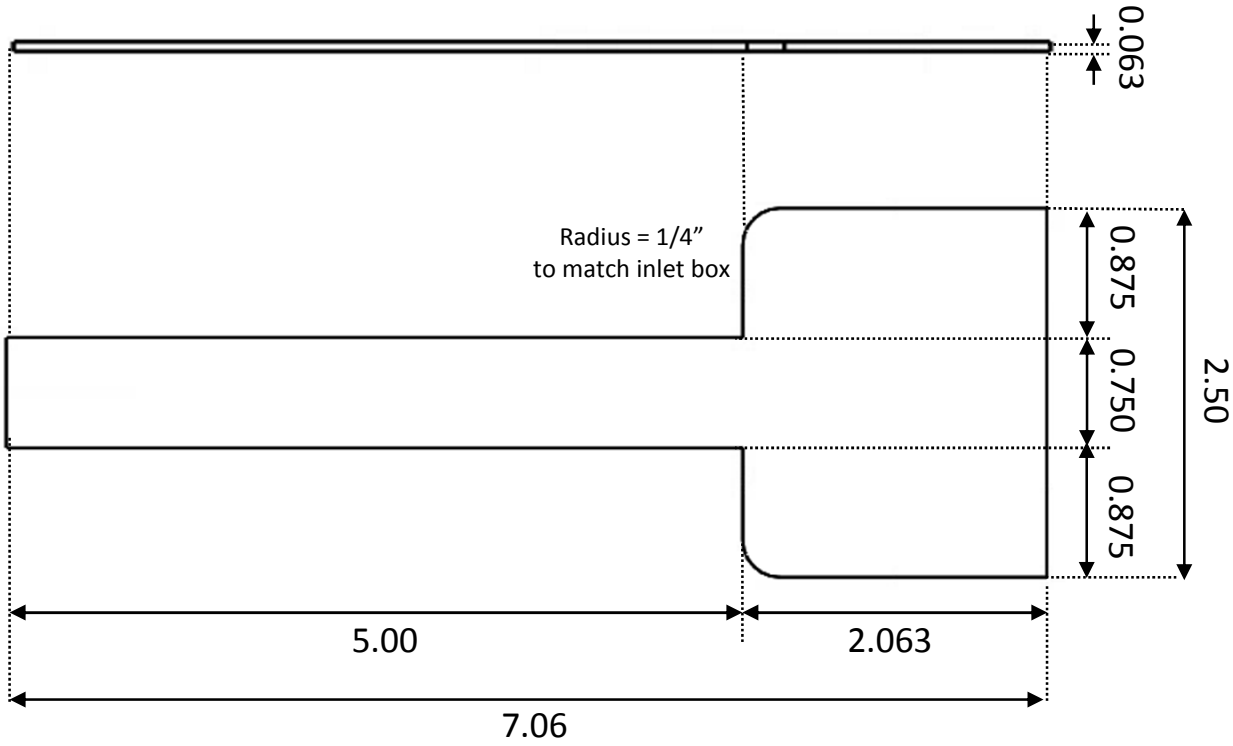

Part 5 will no longer be welded into Part 3; instead it will be removable.

Isometric View

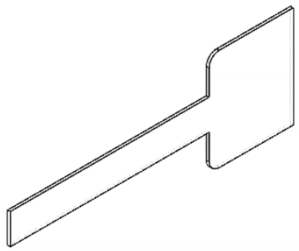

All dimensions are in inches.
Tolerances:
.X = ± 0.06"
.XX = ± 0.03"
.XXX = ± 0.01"
.XXXX = ± 0.003"

PART 5 – Baffle Plate (Top and Side View)

This part is intended to be slid into the grooves in the inlet box and channel ~~and welded in place~~.

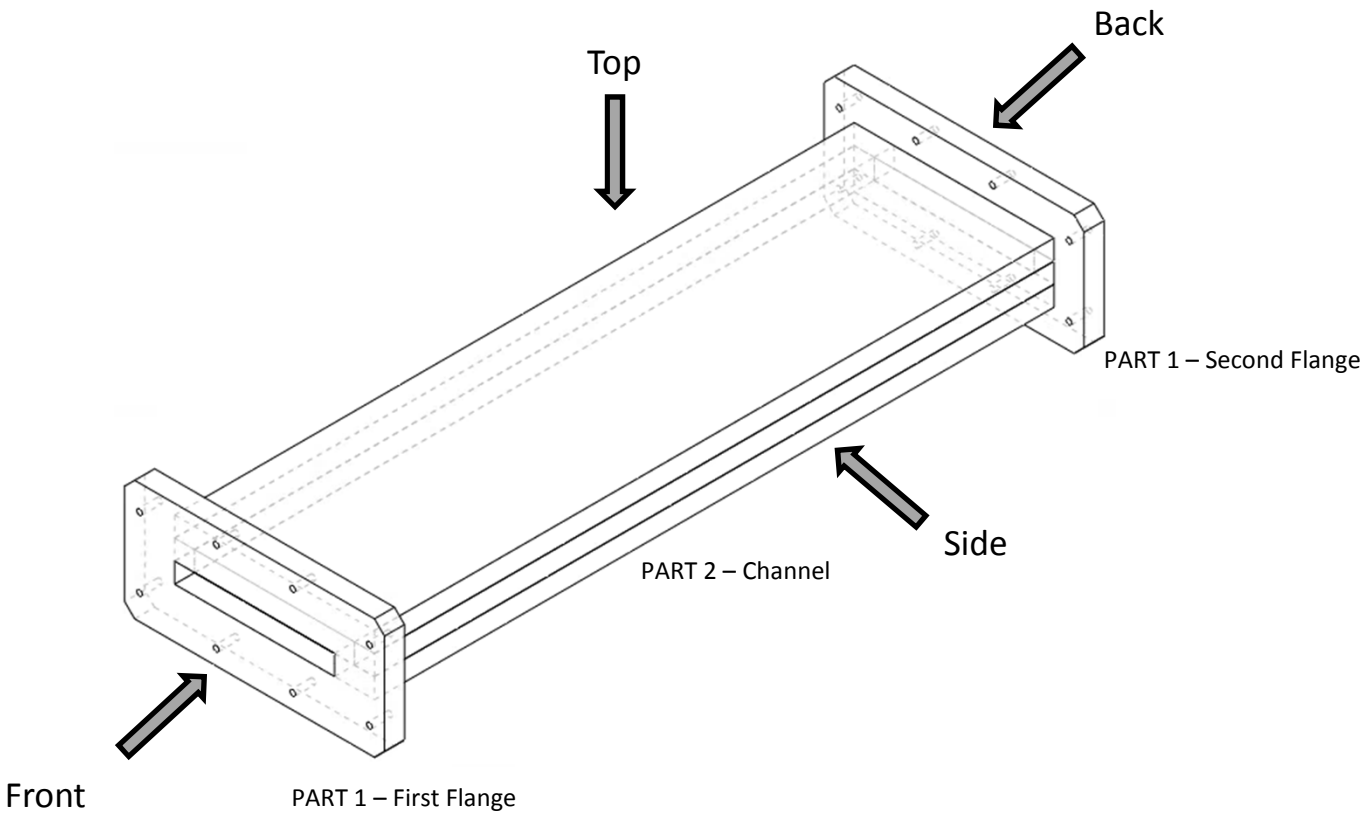

ISOMETRIC ASSEMBLY DIAGRAM

Overall assembly view. Material for all parts is 6061 aluminum. For orientation, additional isometric views are provided on the parts drawings. Part 1 needs to be built twice and welded to Part 2. Note that these parts are identical to Parts 1 and 2 in Assembly A, except that Part 2 is 17” and without the groove for the baffle plate.

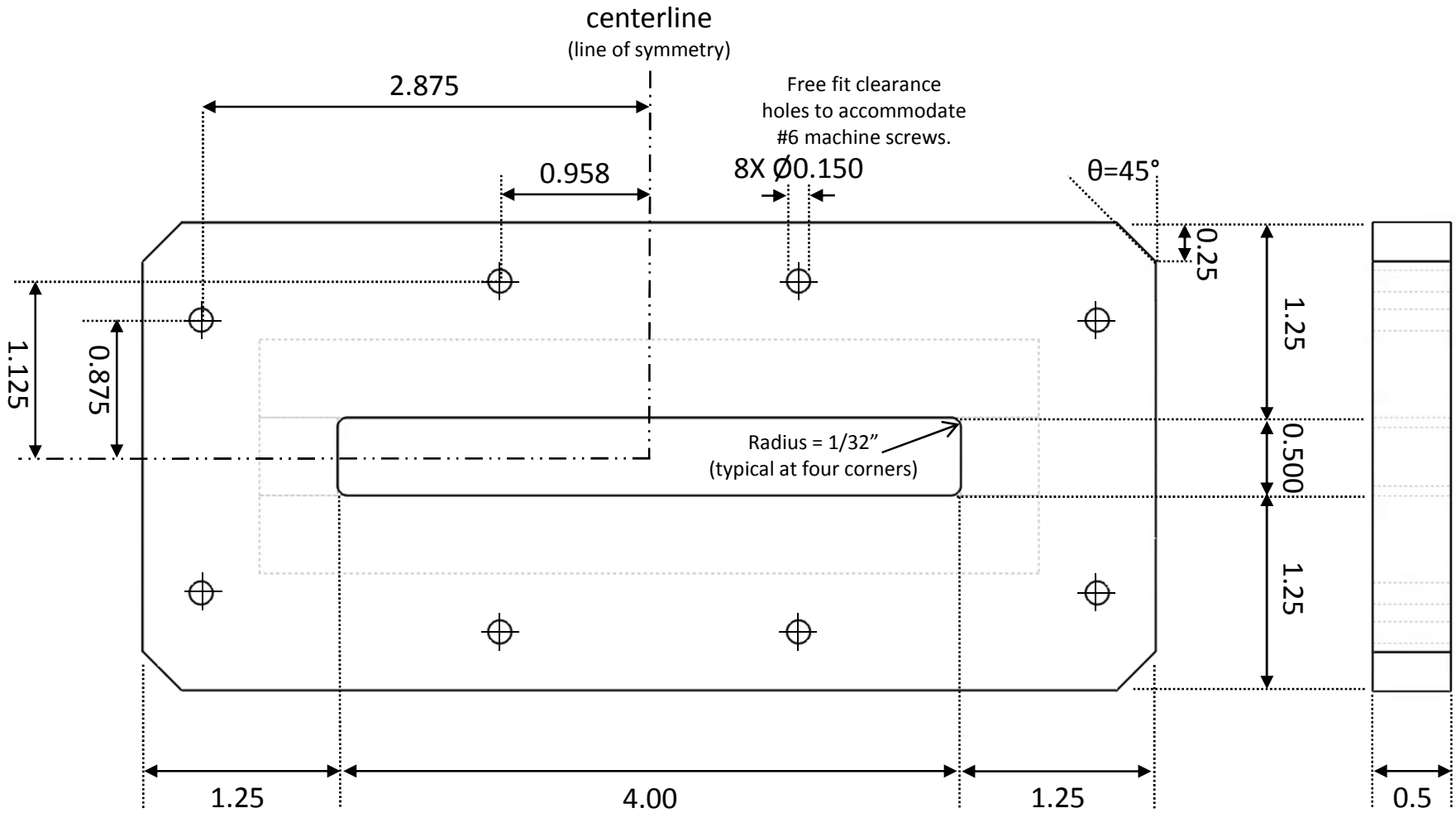

Isometric View

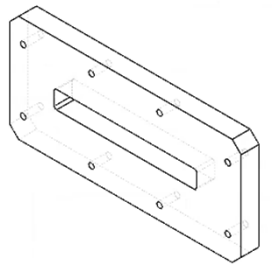

All dimensions are in inches.
Tolerances:
.X = ± 0.06"
.XX = ± 0.03"
.XXX = ± 0.01"
.XXXX = ± 0.003"

PART 1 – Flange (Front and Side View)

Shows flange and machine screw hole dimensions.

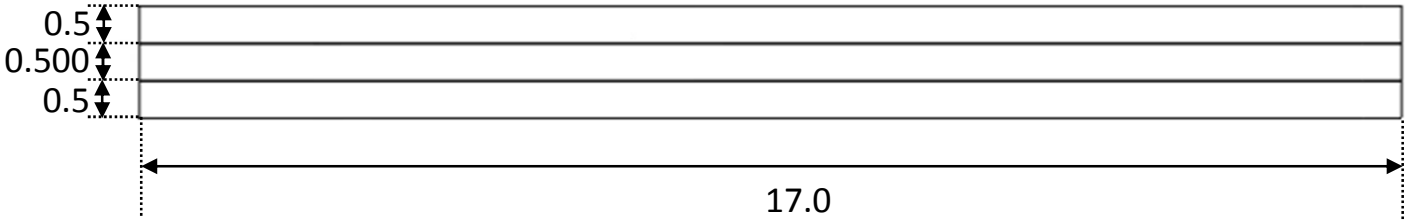

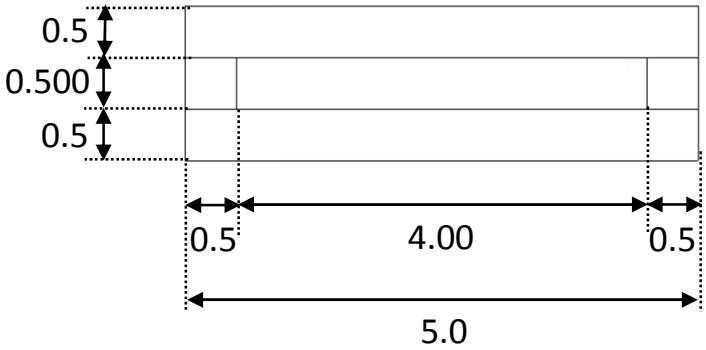

Isometric View

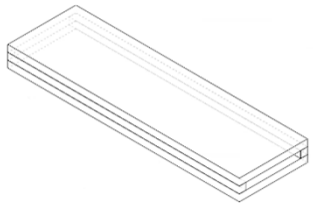

All dimensions are in inches.
Tolerances:
.X = ± 0.06”
.XX = ± 0.03”
.XXX = ± 0.01”
.XXXX = ± 0.003”

PART 2 – Channel (Side and Back View)

The four ½”-thickness bars are to be welded together. The critical dimension for our experiments is the height of 0.500”.

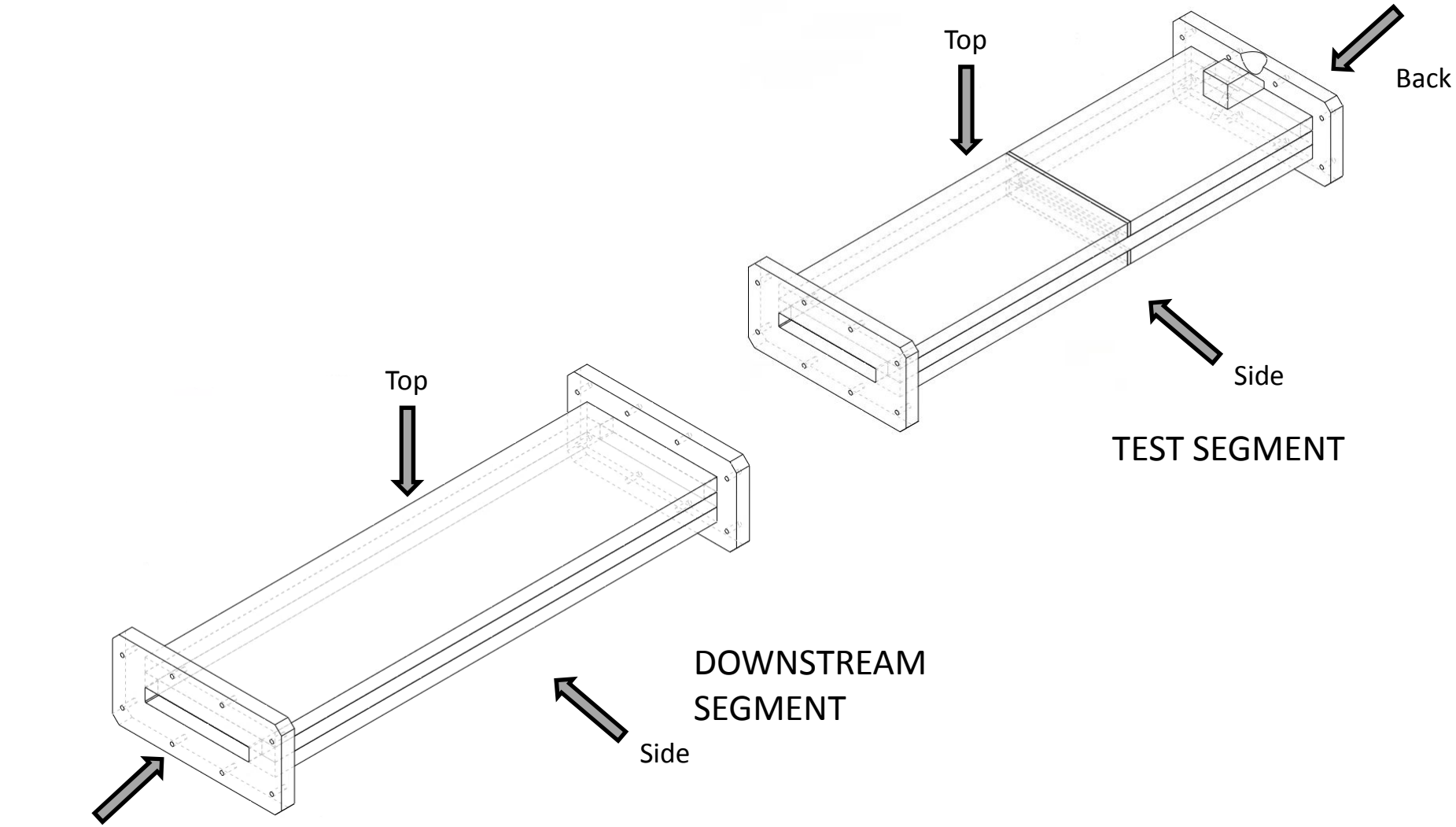

ISOMETRIC VIEW

Overall assembly view. We will need to take photographs of sub-mm size droplets inside the channel, so it is critical for the view through the top, bottom, and sides to be free from distortion. The two parts (labelled test segment and downstream segment) will be bolted together with #6 machine screws (provided by UMD).

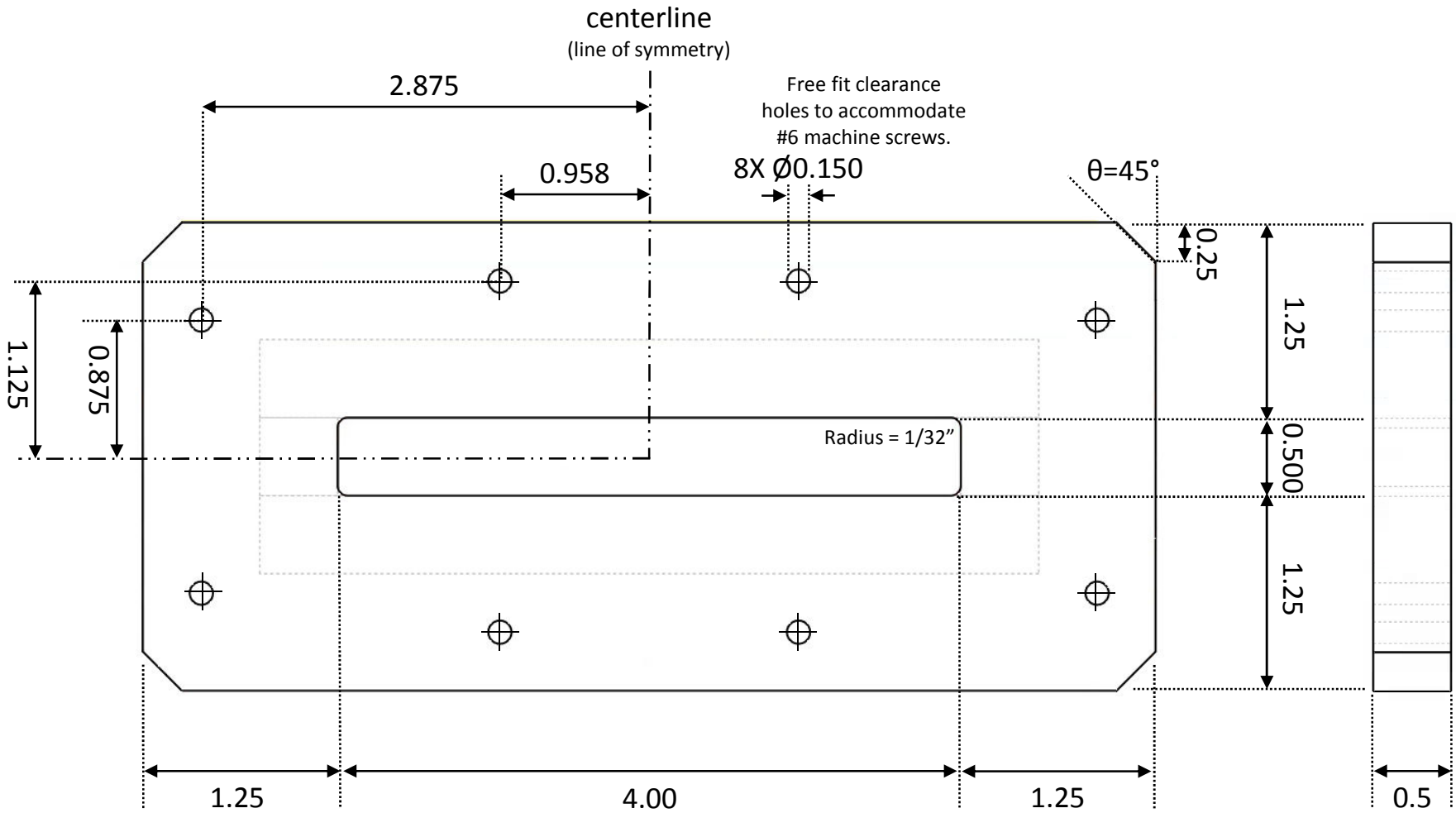

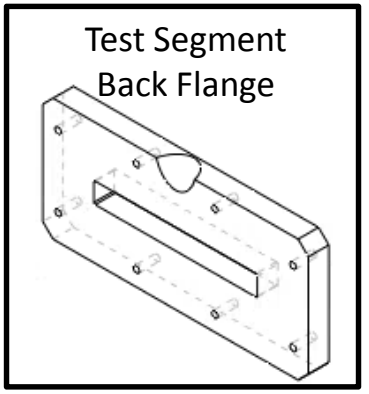

All dimensions are in inches.
Tolerances:
.X = ± 0.06”
.XX = ± 0.03”
.XXX = ± 0.015”

Flange (Front and Side View)

Shows flange and machine screw hole dimensions. Note that the back flange for test segment must also have a portion removed for the injection port (see isometric view to the right, and Section B for dimensions).

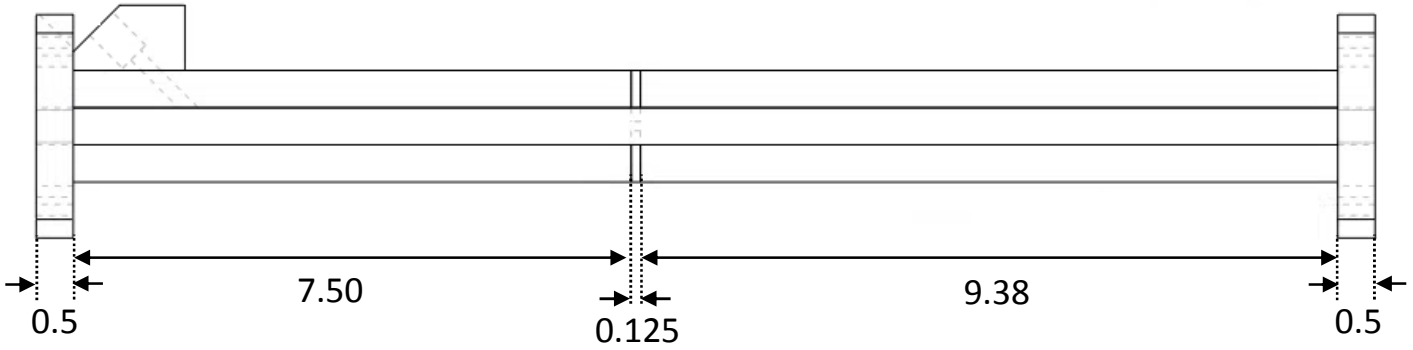

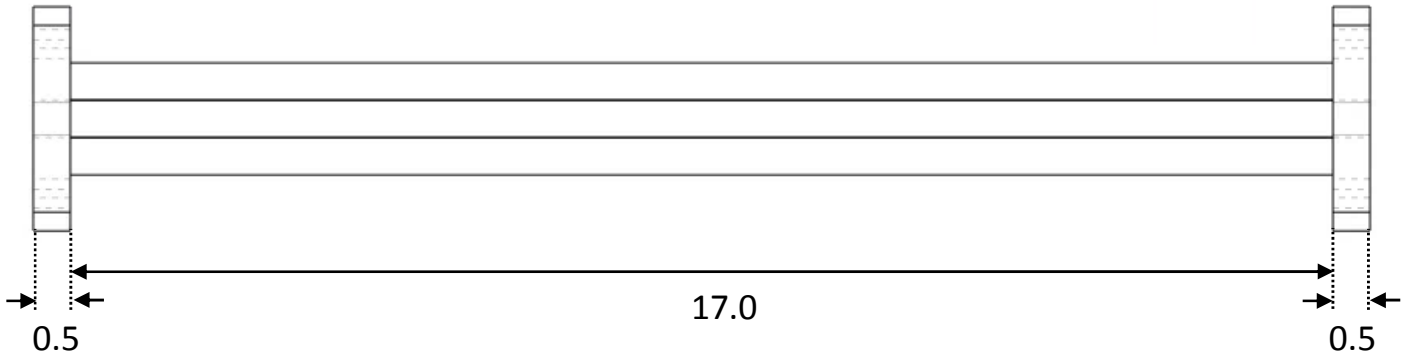

All dimensions are in inches.
Tolerances:
.X = ± 0.06”
.XX = ± 0.03”
.XXX = ± 0.015”

Side Elevation

The major lengths associated with this piece are shown. The heights are provided on the cross-sectional drawings.

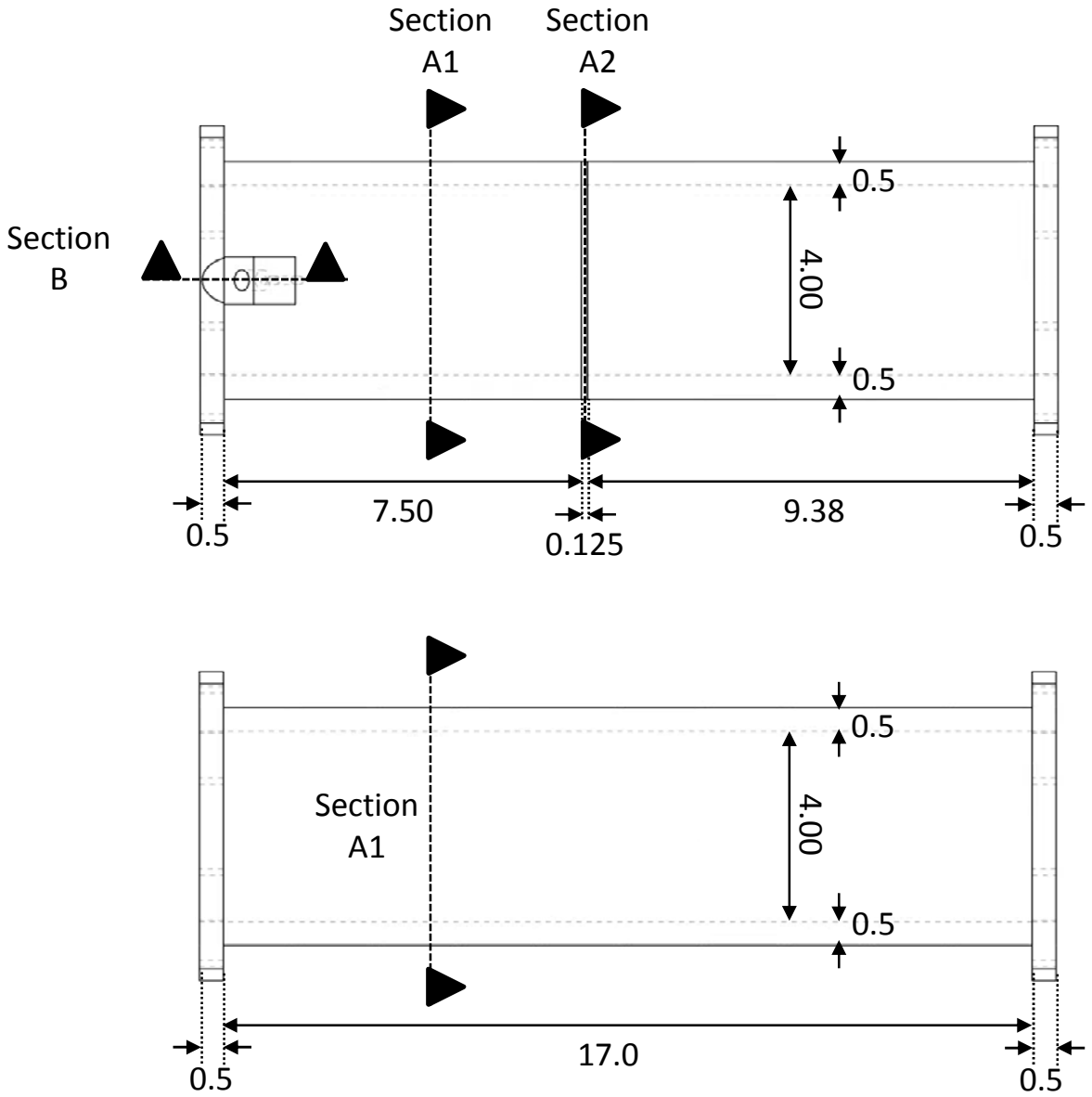

All dimensions are in inches.
Tolerances:
.X = ± 0.06”
.XX = ± 0.03”
.XXX = ± 0.015”

Top Elevation

The major lengths associated with this piece are shown. The locations of the critical sections are indicated with the dashed lines.

A1)

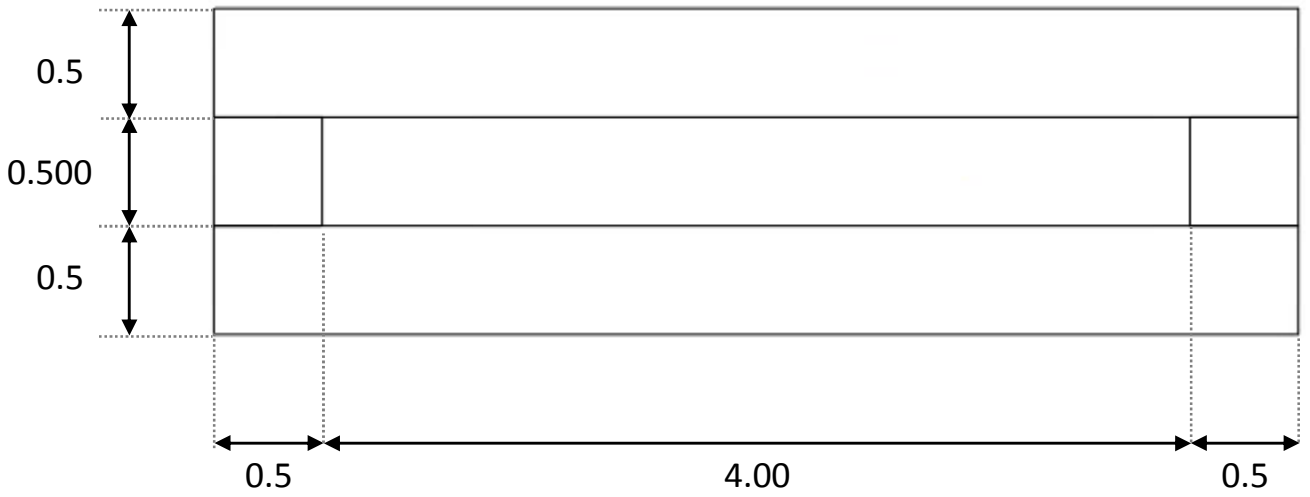

A2)

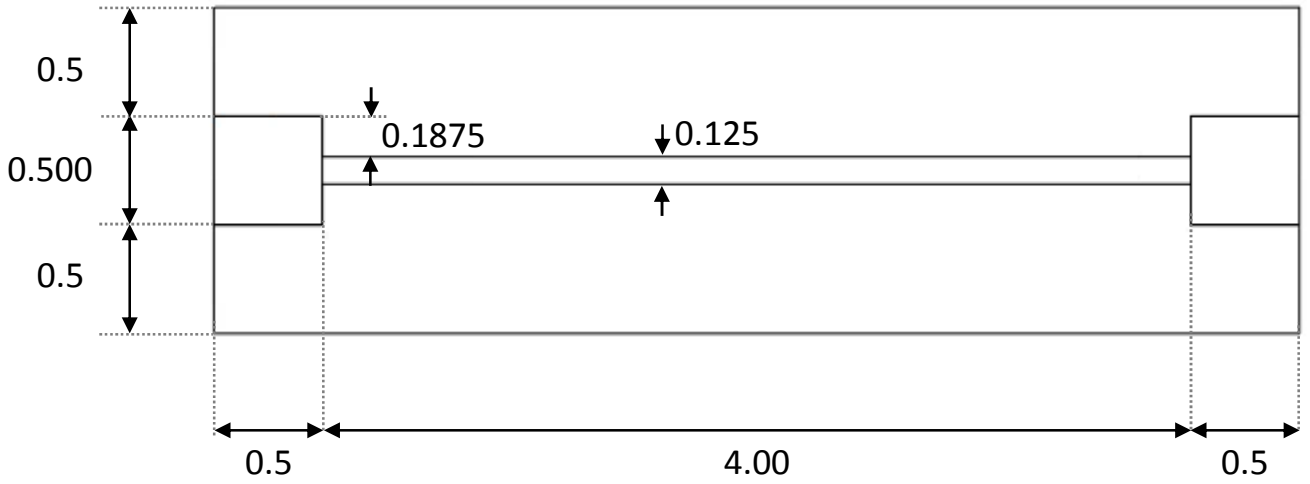

All dimensions are in inches.
Tolerances:
.X = ± 0.06”
.XX = ± 0.03”
.XXX = ± 0.015”

Section A – Open Channel and Orifice

A1) Section through Open Channel

A2) Section through Orifice Constriction

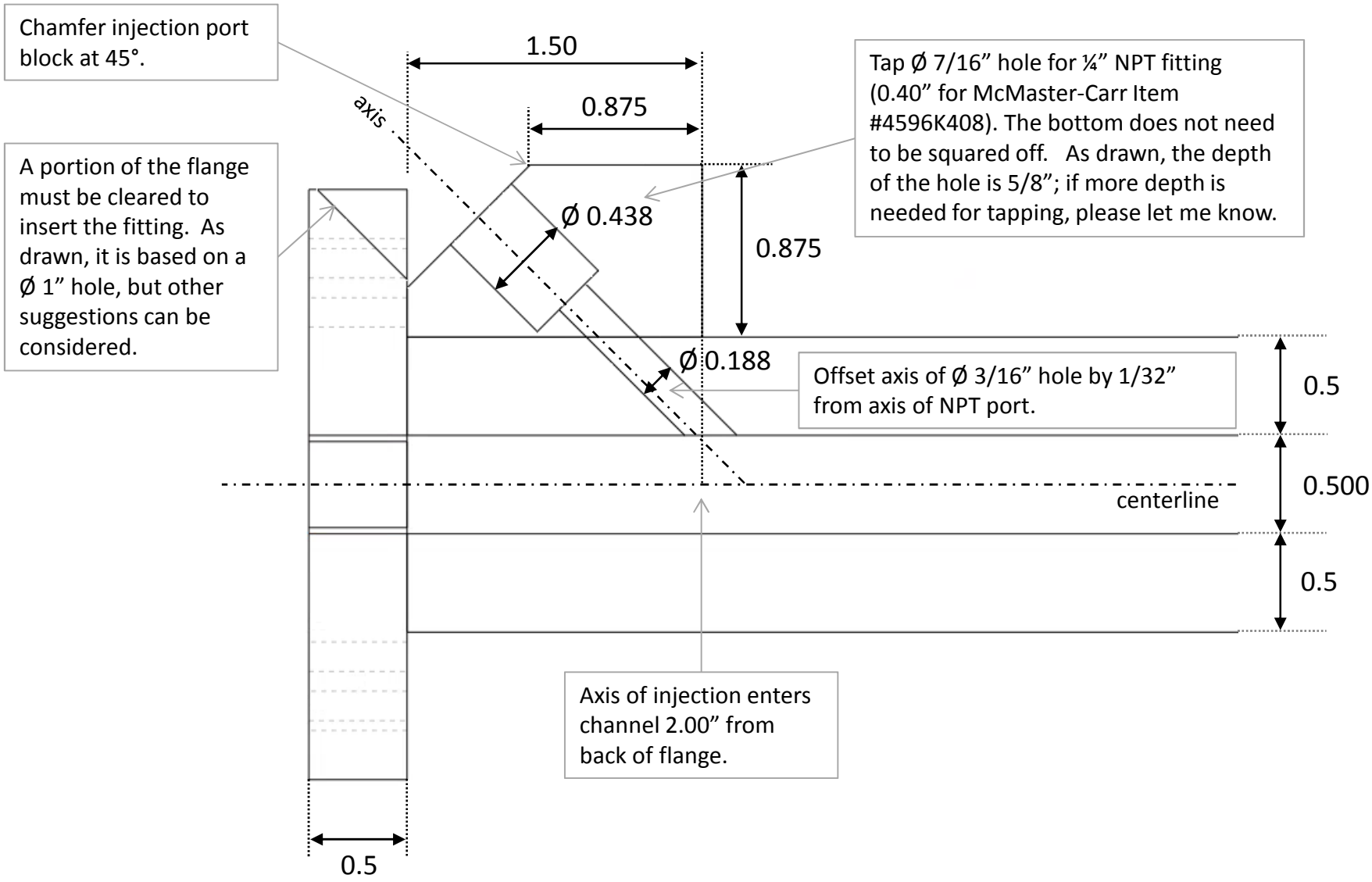

All dimensions are in inches.
Tolerances:
.X = ± 0.06"
.XX = ± 0.03"
.XXX = ± 0.015"

Section B – Injection Port

The dimensions of the injection port are shown. Some additional notes are provided, as there may be easier ways to construct this that do not interfere with the main function.

Appendix B: Computational Flow Field

This Appendix contains the results of the computational simulations of the flow fields through the slit for all flow conditions evaluated (see Table 2.2). The centre plane (x = 0) velocity magnitude, strain rate magnitude, shear rate, extensional rate, turbulence kinetic energy, and turbulence dissipation rate (where applicable) are presented in order of increasing channel Reynolds number Re_{ch}.

Table B.1. Summary of Figures in Appendix B.

Flow Field Property	**Continuous Phase and Channel Reynolds Number**		
	CO200FG Re_{ch} = 110–240	**CO70FG Re_{ch} = 240–600**	**Water Re_{ch} = 7,700–19,000**
Velocity Magnitude	B.1	B.5	B.9
Strain Rate Magnitude	B.2	B.6	B.10
Absolute Shear Rate	B.3	B.7	B.11
Extensional Rate	B.4	B.8	B.12
Turbulence Kinetic Energy	n/a	n/a	B.13
Turbulence Dissipation Rate	n/a	n/a	B.14

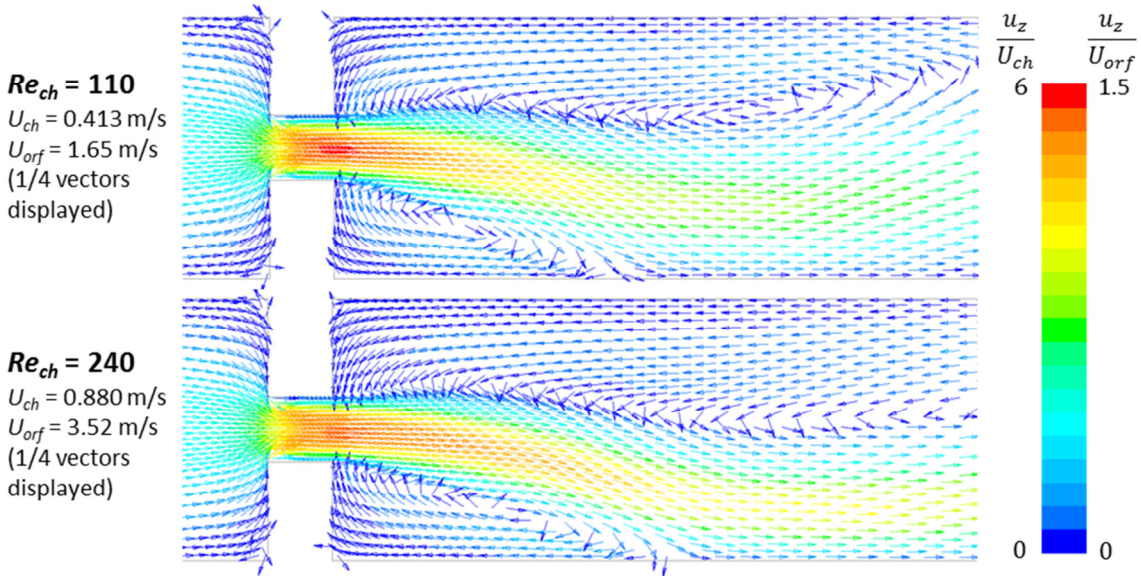

Figure B.1. Velocity vectors for laminar flows of CO200FG (μ_c = 0.0808 Pa-s) through the orifice. Vectors are coloured by velocity magnitude scaled with the superficial orifice or channel velocity.

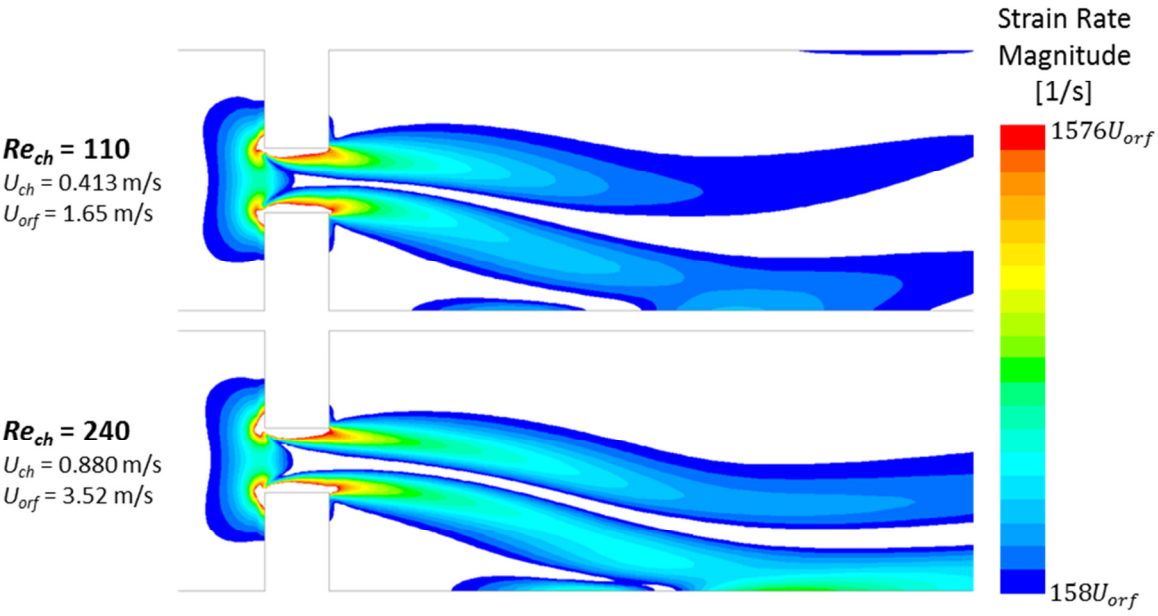

Figure B.2. Contours of strain rate magnitude for laminar flows of CO200FG (μ_c = 0.0808 Pa-s) through the slit orifice. Contours are coloured by strain rate magnitude (1/s) scaled with the superficial orifice velocity U_{orf} in units of m/s.

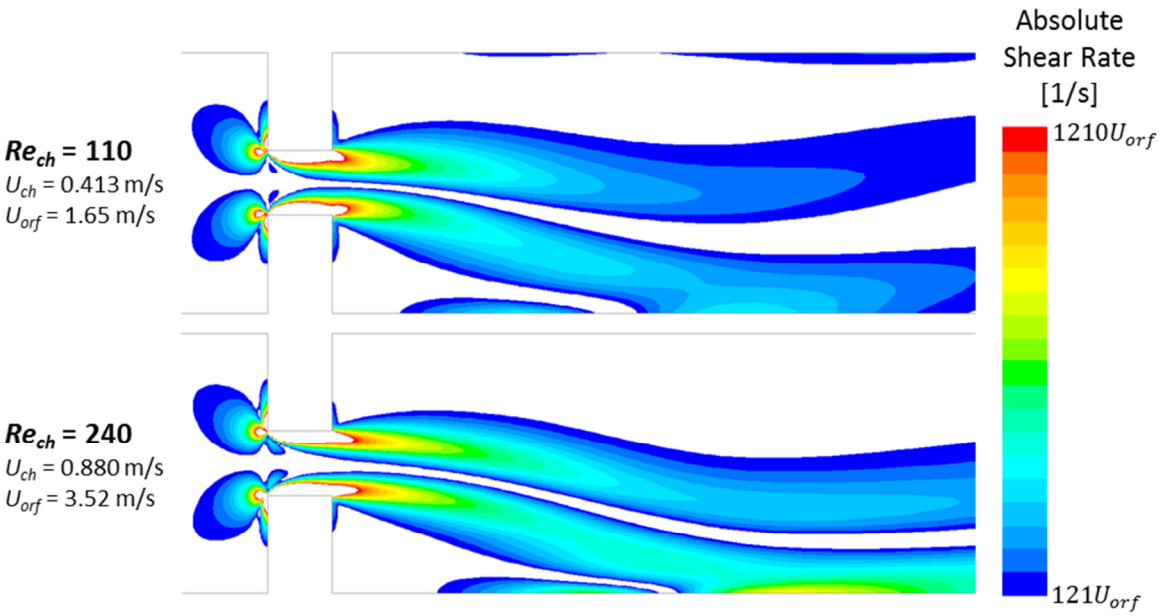

Figure B.3. Contours of absolute shear rate for laminar flows of CO200FG (μ_c = 0.0808 Pa-s) through the slit orifice. Contours are coloured by $du_z/dy+du_y/dz$ (1/s) scaled with the superficial orifice velocity U_{orf} in units of m/s.

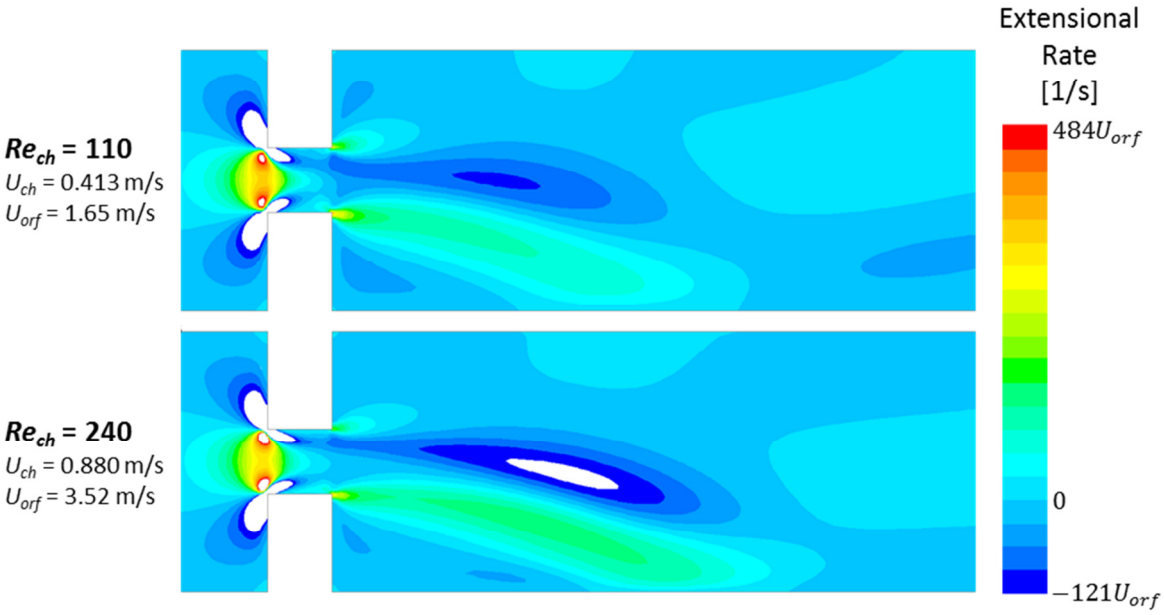

Figure B.4. Contours of extensional rate for laminar flows of CO200FG (μ_c = 0.0808 Pa-s) through the slit orifice. Contours are coloured by du_z/dz (1/s) scaled with the superficial orifice velocity U_{orf} in units of m/s.

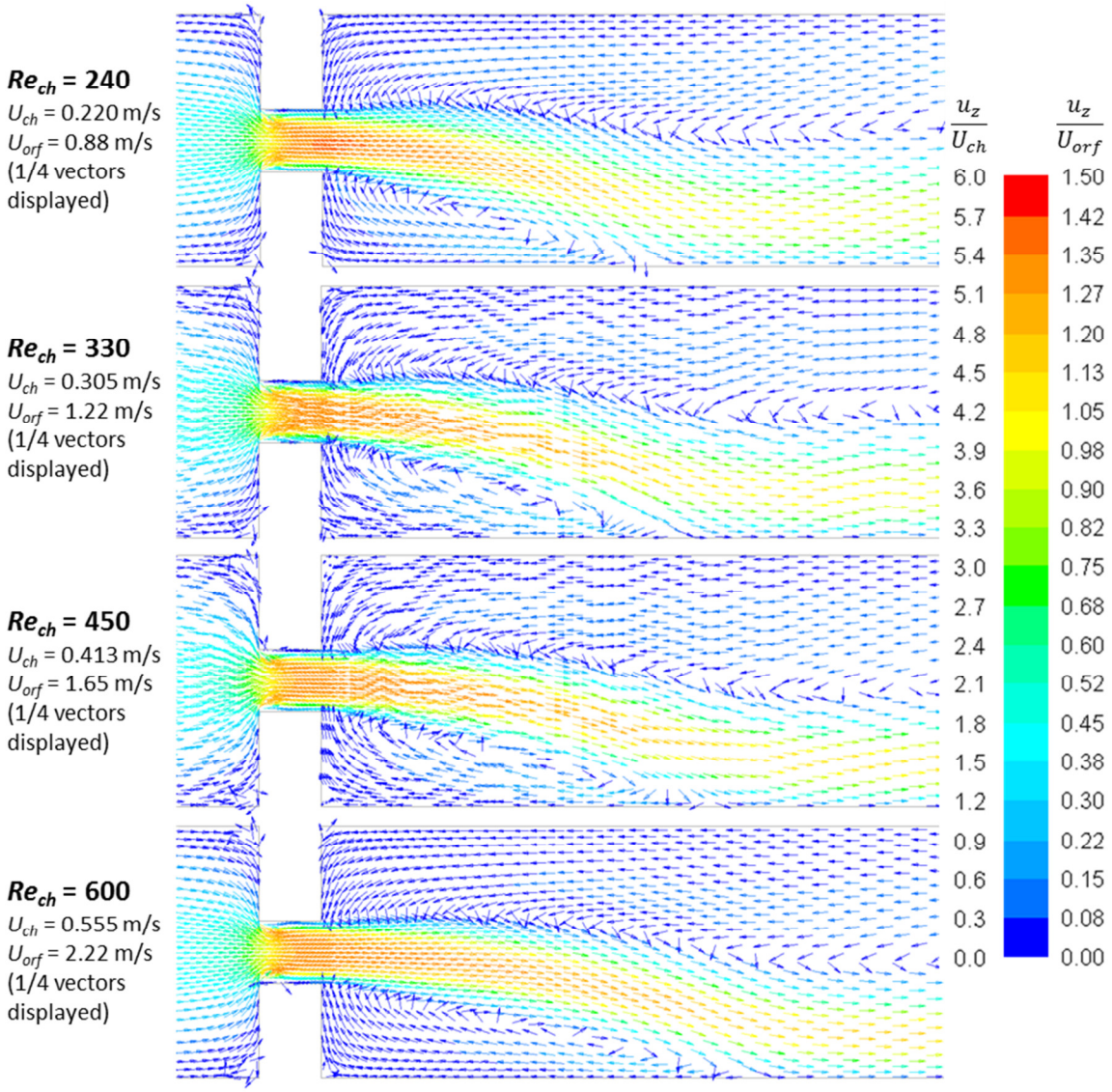

Figure B.5. Velocity vectors for laminar flows of CO70FG (μ_c = 0.0202 Pa-s) through the slit orifice. Vectors are coloured by velocity magnitude scaled with the superficial orifice or channel velocity.

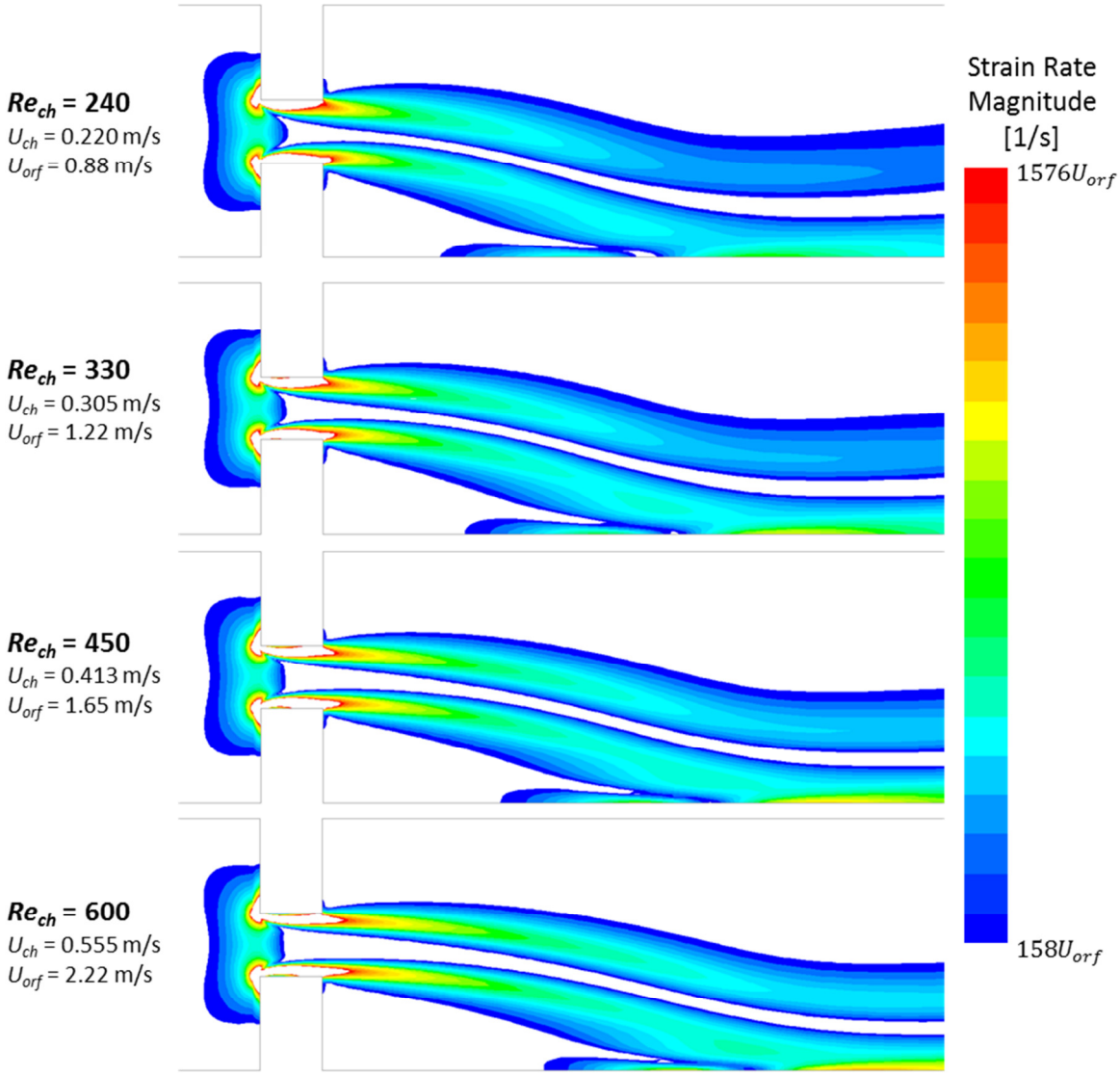

Figure B.6. Contours of strain rate magnitude for laminar flows of CO70FG (μ_c = 0.0202 Pa-s) through the slit orifice. Contours are coloured by strain rate magnitude (1/s) scaled with the superficial orifice velocity U_{orf} in units of m/s.

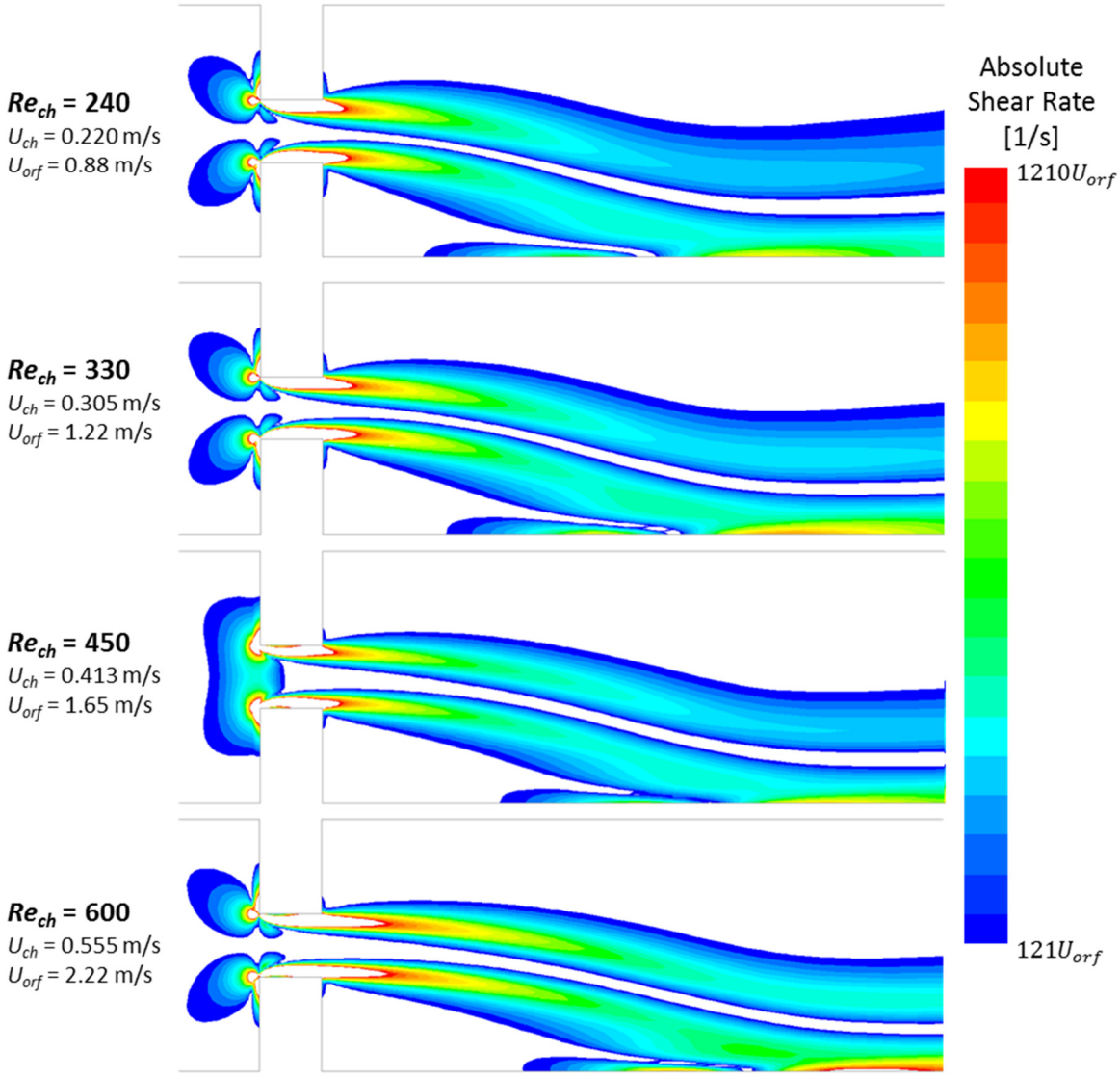

Figure B.7. Contours of absolute shear rate for laminar flows of CO70FG (μ_c = 0.0202 Pa-s) through the slit orifice. Contours are coloured by $du_z/dy+du_y/dz$ (1/s) scaled with the superficial orifice velocity U_{orf} in units of m/s.

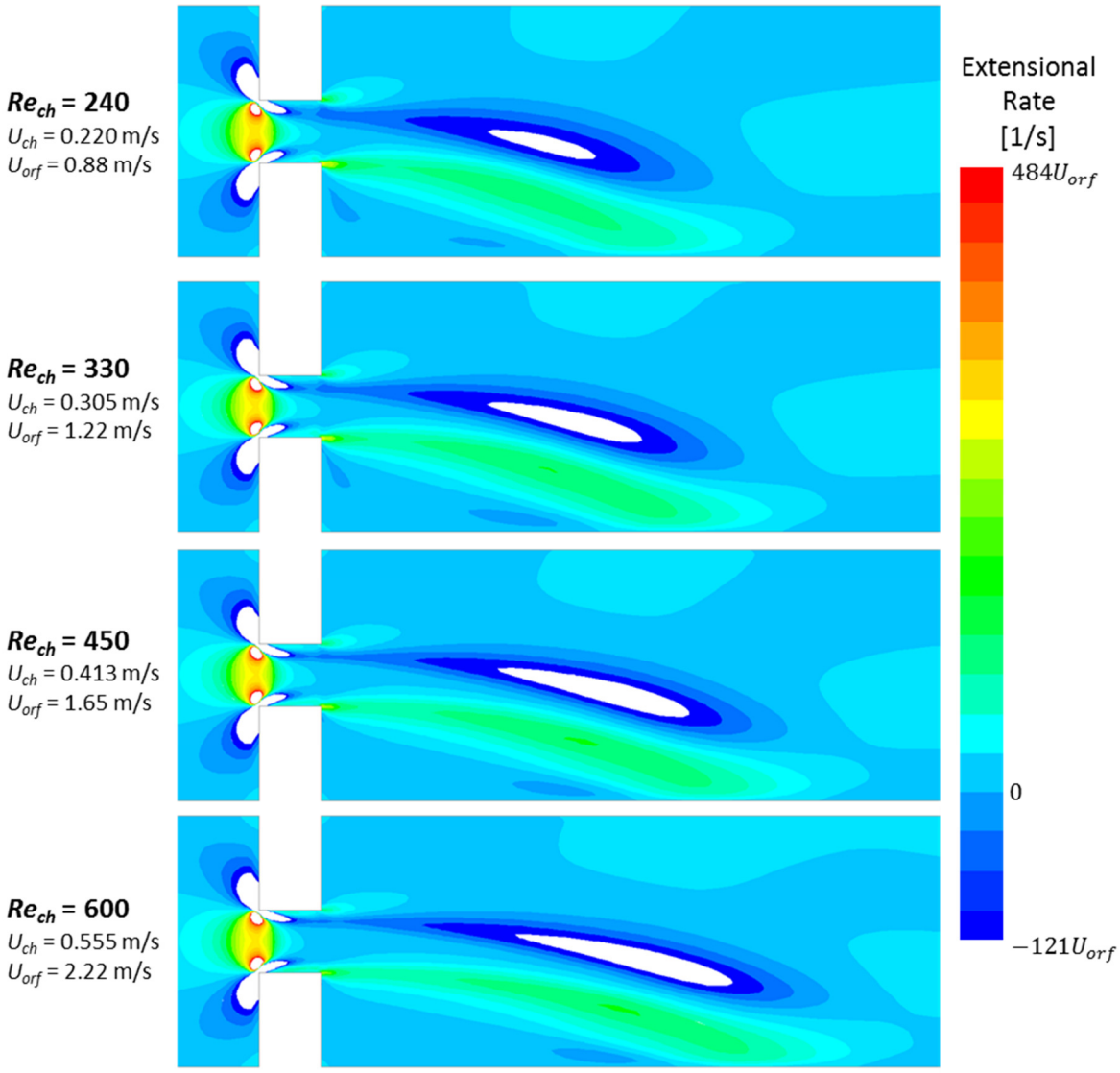

Figure B.8. Contours of extensional rate for laminar flows of CO70FG (μ_c = 0.0202 Pa-s) through the slit orifice. Contours are coloured by du_z/dz (1/s) scaled with the superficial orifice velocity U_{orf} in units of m/s.

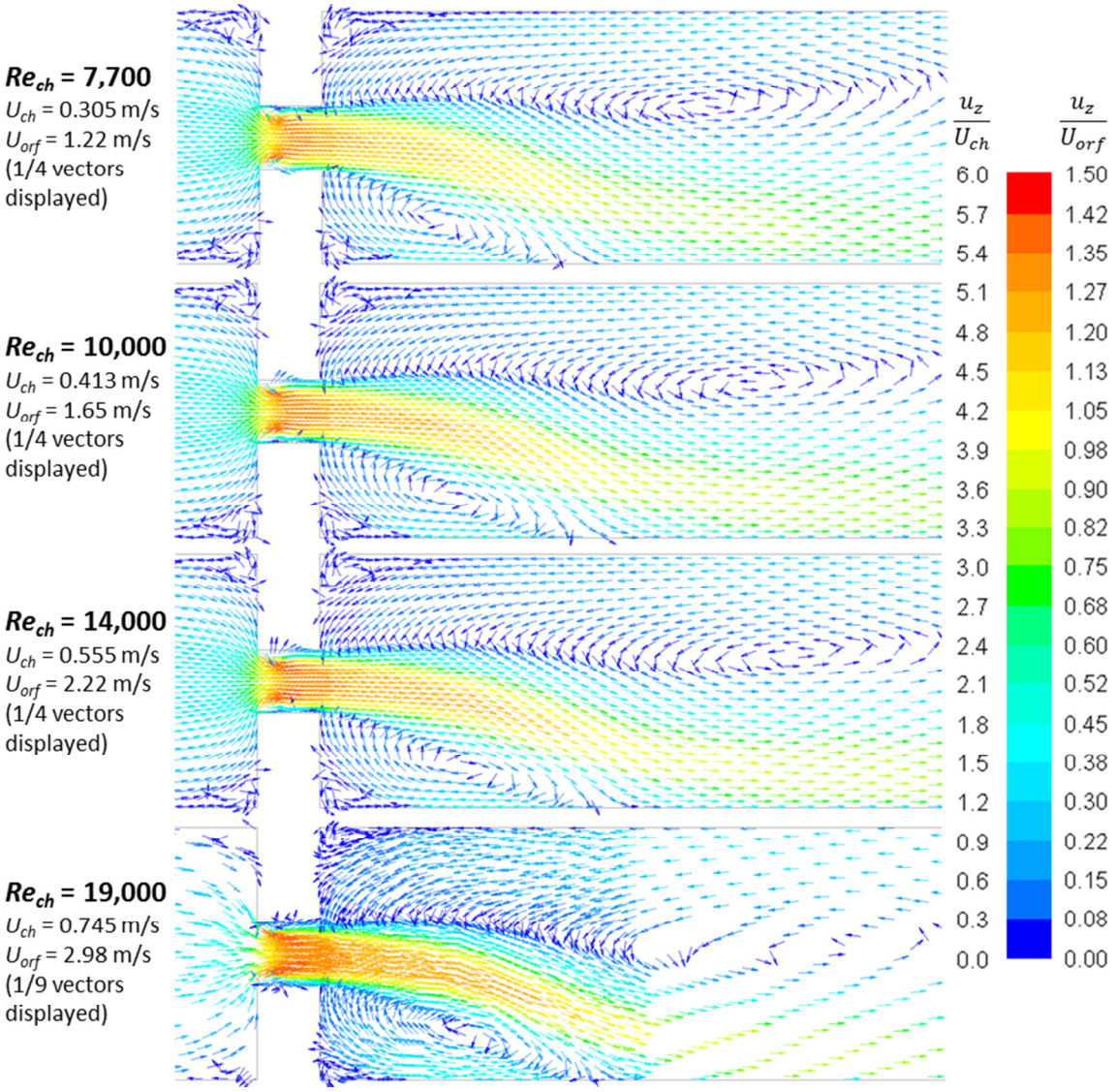

Figure B.9. Velocity vectors for turbulent flows of water through the slit orifice. Vectors are coloured by velocity magnitude scaled with the superficial orifice or channel velocity. Note that the Re_{ch} = 19,000 simulation has a more highly-refined grid in and immediately downstream of the orifice.

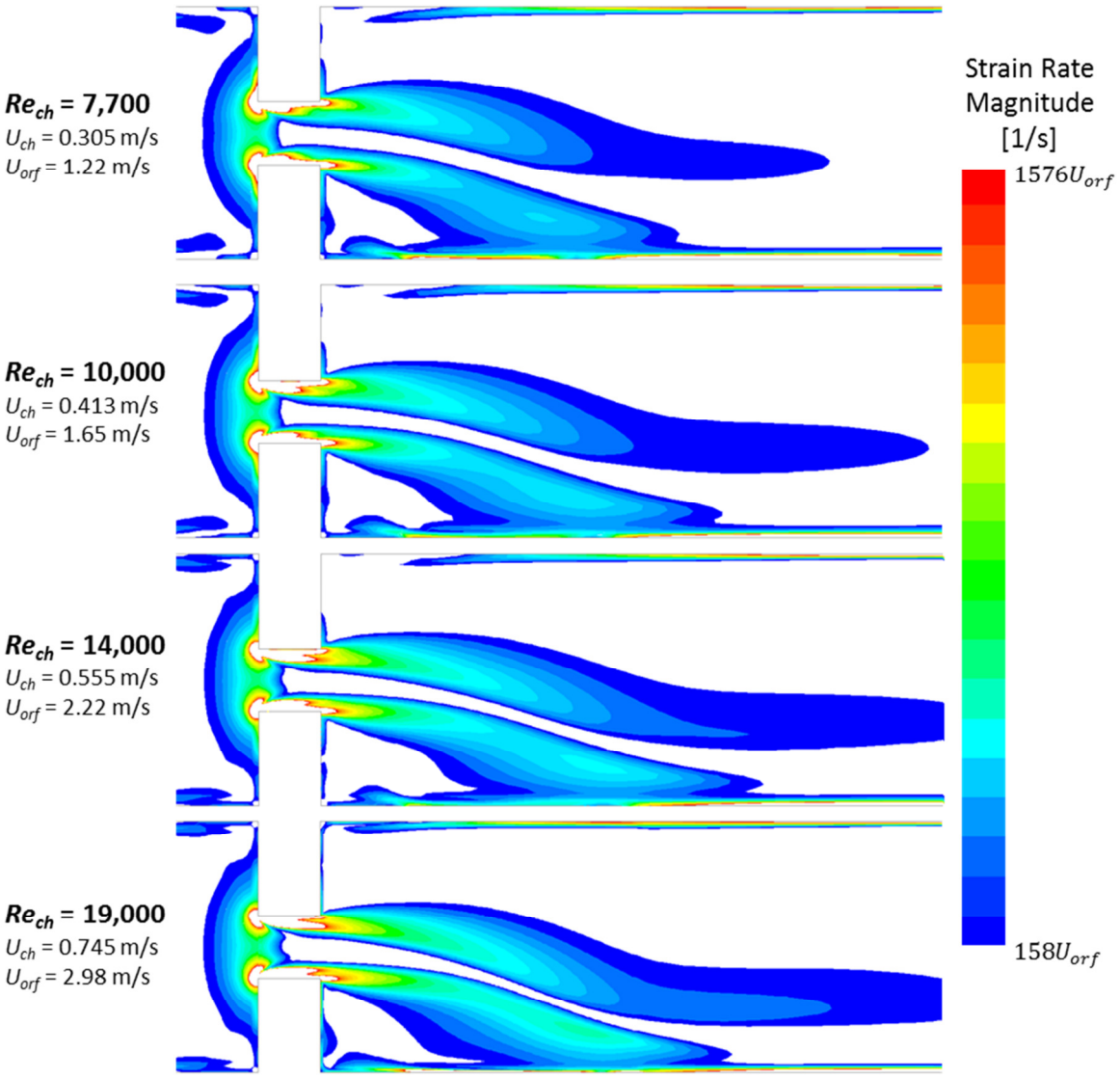

Figure B.10. Contours of strain rate magnitude for turbulent flows of water through the slit orifice. Contours are coloured by strain rate magnitude (1/s) scaled with the superficial orifice velocity U_{orf} in units of m/s.

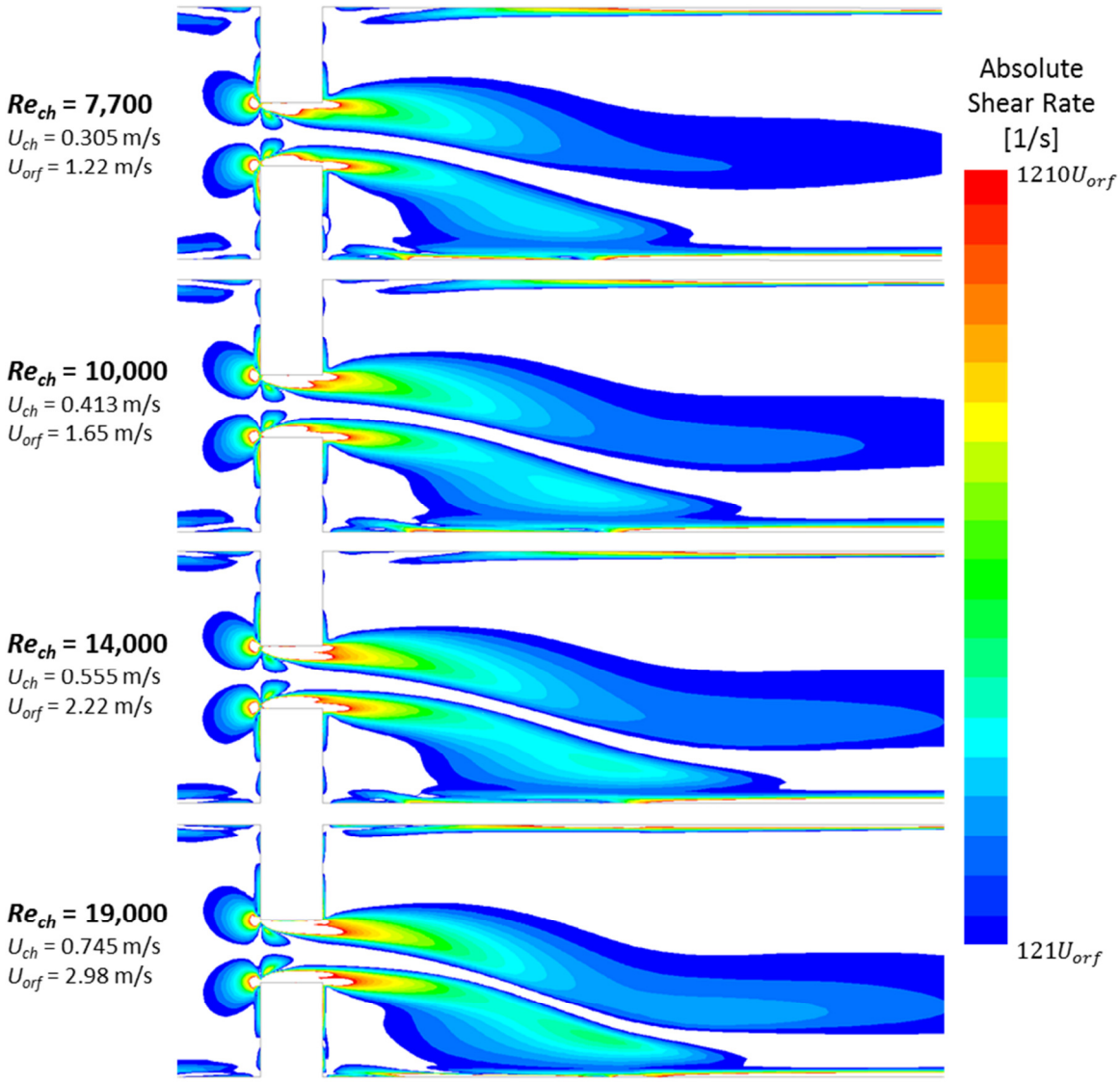

Figure B.11. Contours of absolute shear rate for turbulent flows of water through the slit orifice. Contours are coloured by $du_z/dy+du_y/dz$ (1/s) scaled with the superficial orifice velocity U_{orf} in units of m/s.

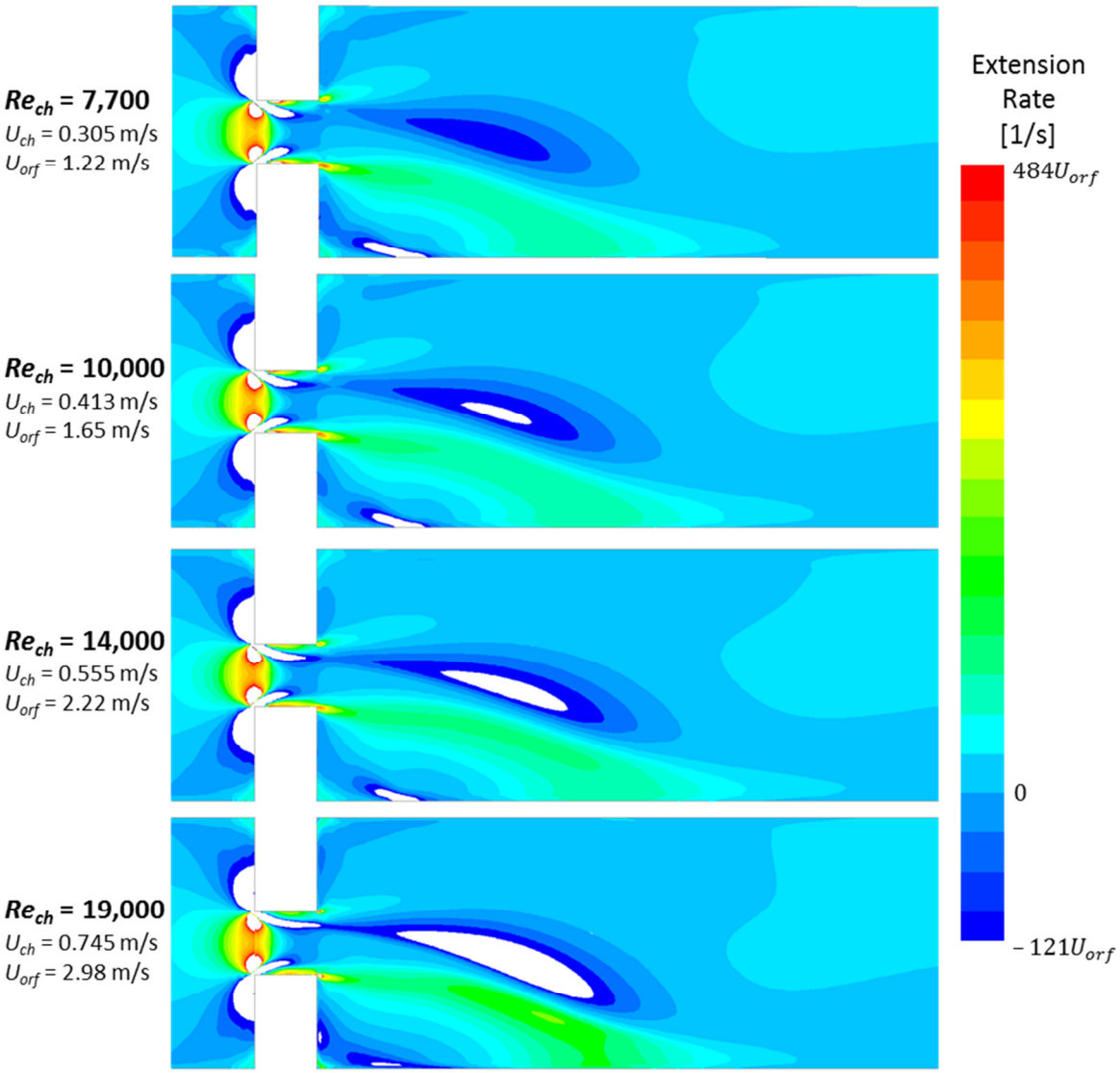

Figure B.12. Contours of extensional rate for turbulent flows of water through the slit orifice. Contours are coloured by du_z/dz (1/s) scaled with the superficial orifice velocity U_{orf} in units of m/s.

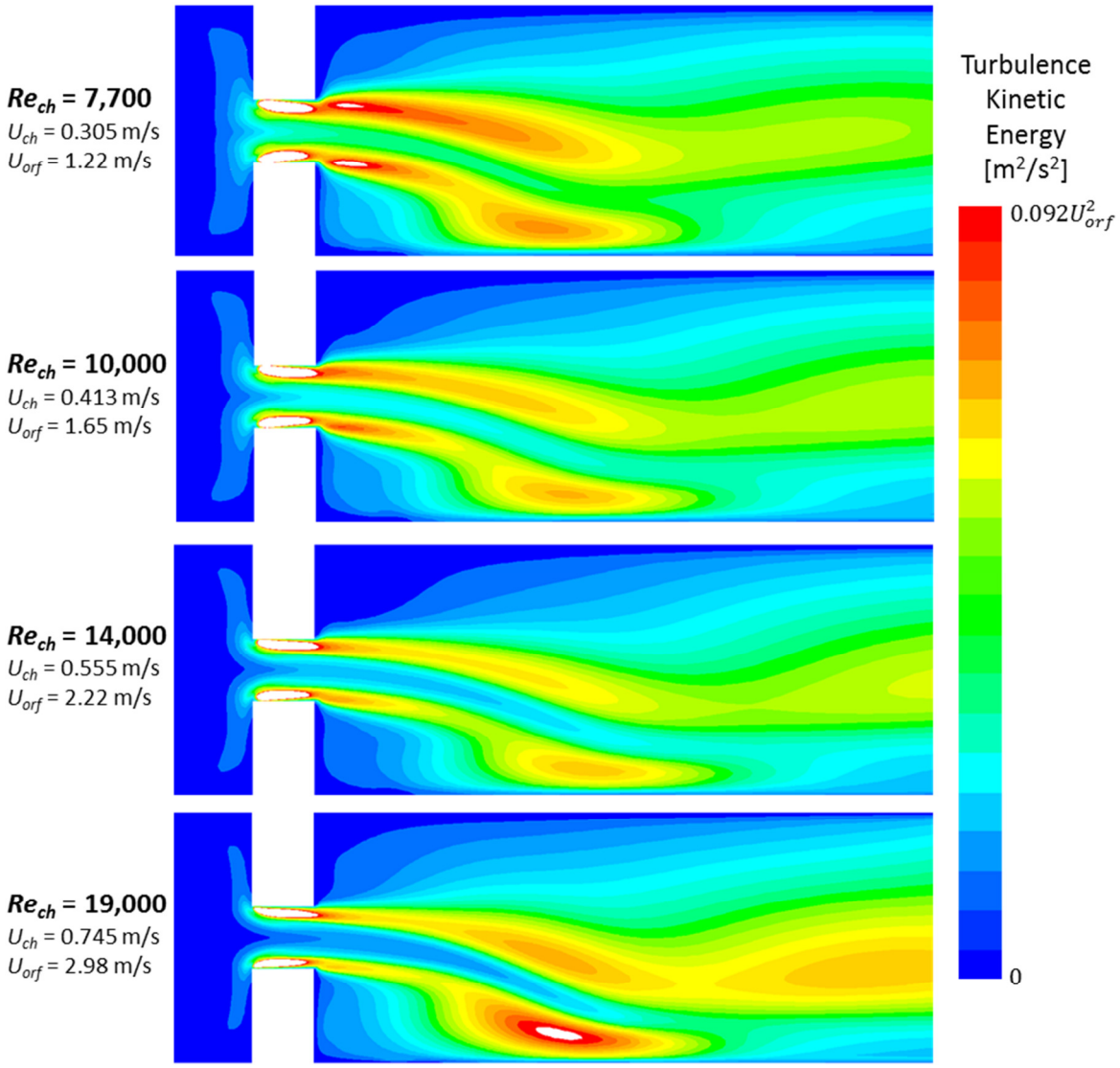

Figure B.13. Contours of turbulence kinetic energy for turbulent flows of water through the slit orifice. Contours are coloured by turbulence kinetic energy (m^2/s^2) scaled with the square of superficial orifice velocity in units of m/s.

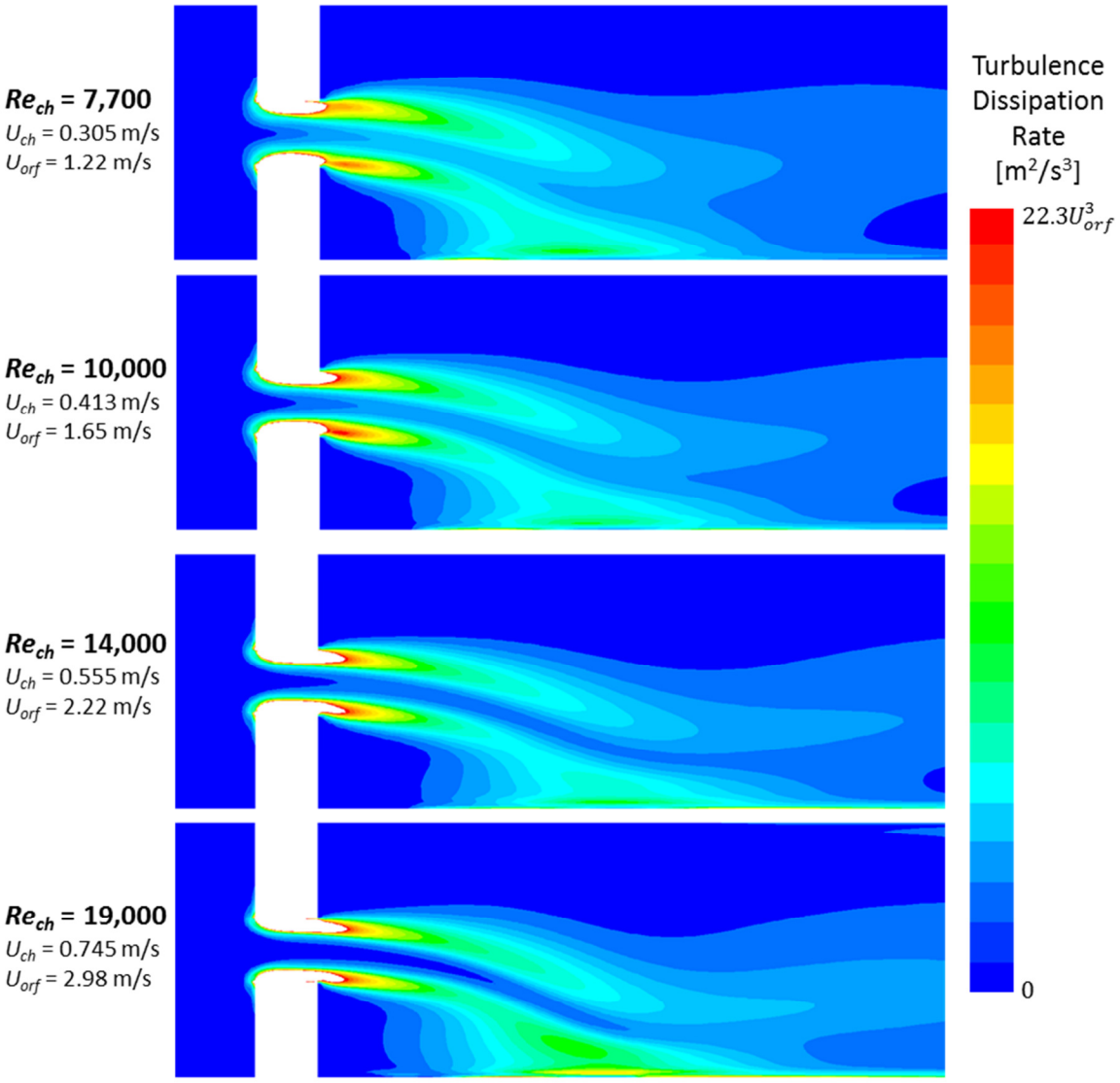

Figure B.14. Contours of turbulence dissipation rate for turbulent flows of water through the slit orifice. Contours are coloured by turbulence dissipation rate (m^2/s^3) scaled with the cube of superficial orifice velocity in units of m/s.

Appendix C: Drop Size and Trajectory Distribution

The droplet distributions for each investigated flow scenario are presented in this Appendix. A summary of the figures is listed in Table 1. The horizontal axis is the droplet diameter in micrometres. The vertical axis is the dimensionless incoming trajectory $y^*_{inc} = y_{inc}/\delta$, where y_{inc} is the cross-wise location of the droplet centroid as it approaches the orifice and δ (1.59 mm) is the half-width of the orifice. Both droplet diameter and incoming trajectory are evaluated about 0.5 H (6.35 mm) upstream of the orifice (see Section 2.3.3 for more details). 'O' markers denote droplets that remained intact, while 'X' markers indicate droplets that broke within the field of view.

Table C.1. Summary of Figures in Appendix C.

Figure Number	Continuous Phase	Dispersed Phase	Camera
C.1–C.4	Water (Turbulent)	CO70FG	Pulnix
C.5–C.7	Water (Turbulent)	Air	Pulnix
C.8–C.9	Water (Turbulent)	CO70FG	Phantom
C.10–C.11	Water (Turbulent)	Air	Phantom
C.12–C.15	CO70FG (Laminar)	Water	Point Grey
C.16–C.17	CO200FG (Laminar)	Water	Point Grey

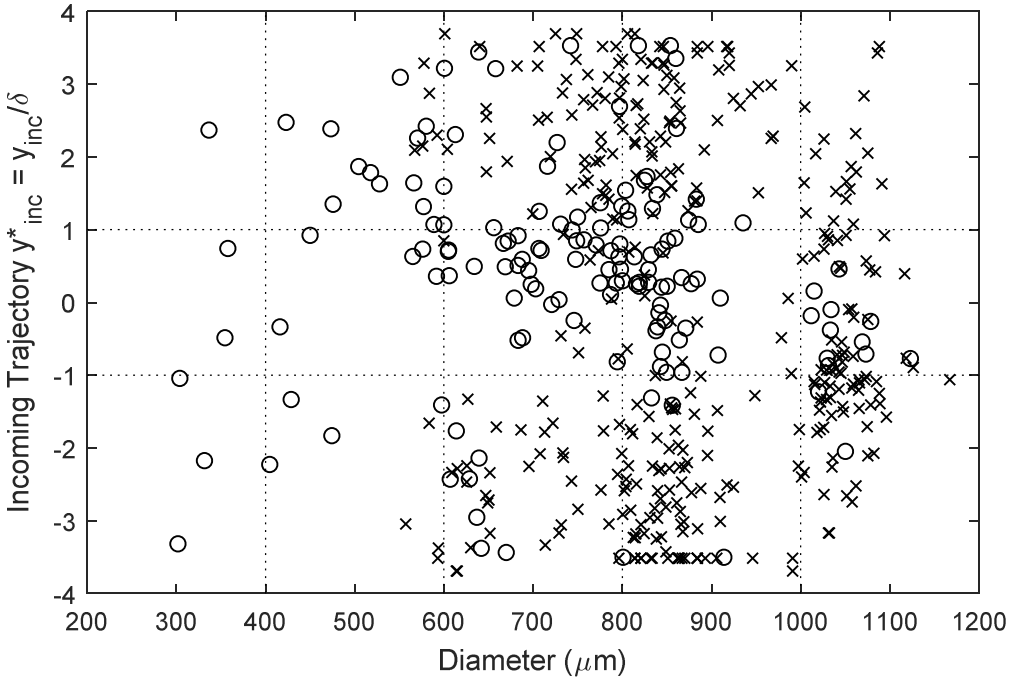

Figure C.1. Distribution of CO70FG droplets in water at Re_{ch} = 7,700 (Pulnix).

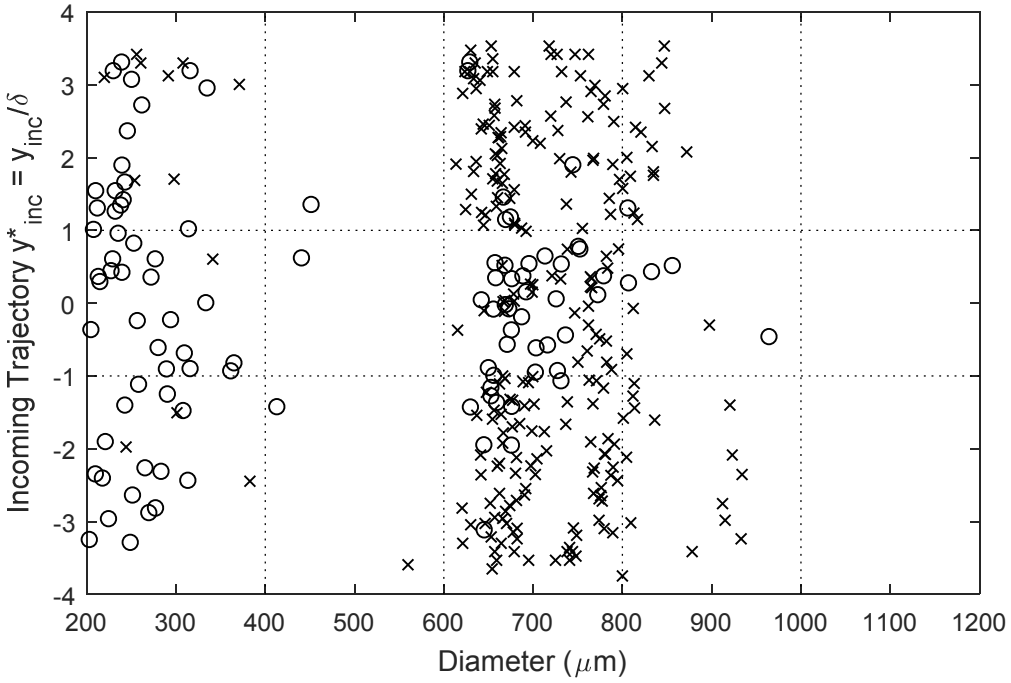

Figure C.2. Distribution of CO70FG droplets in water at Re_{ch} = 10,000 (Pulnix).

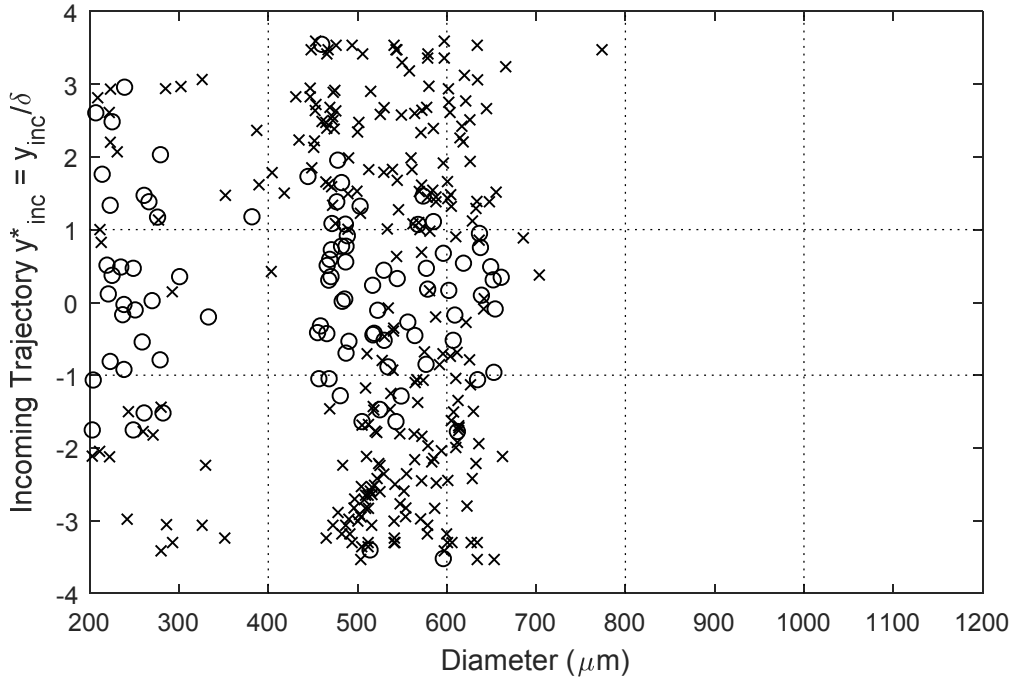

Figure C.3. Distribution of CO70FG droplets in water at Re_{ch} = 14,000 (Pulnix).

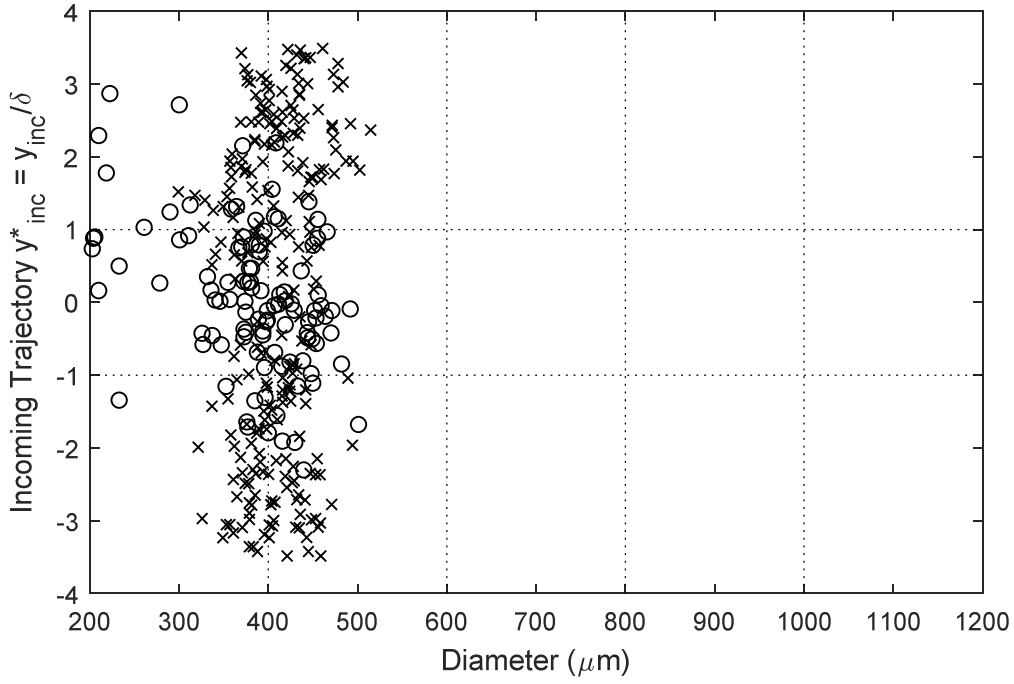

Figure C.4. Distribution of CO70FG droplets in water at Re_{ch} = 19,000 (Pulnix).

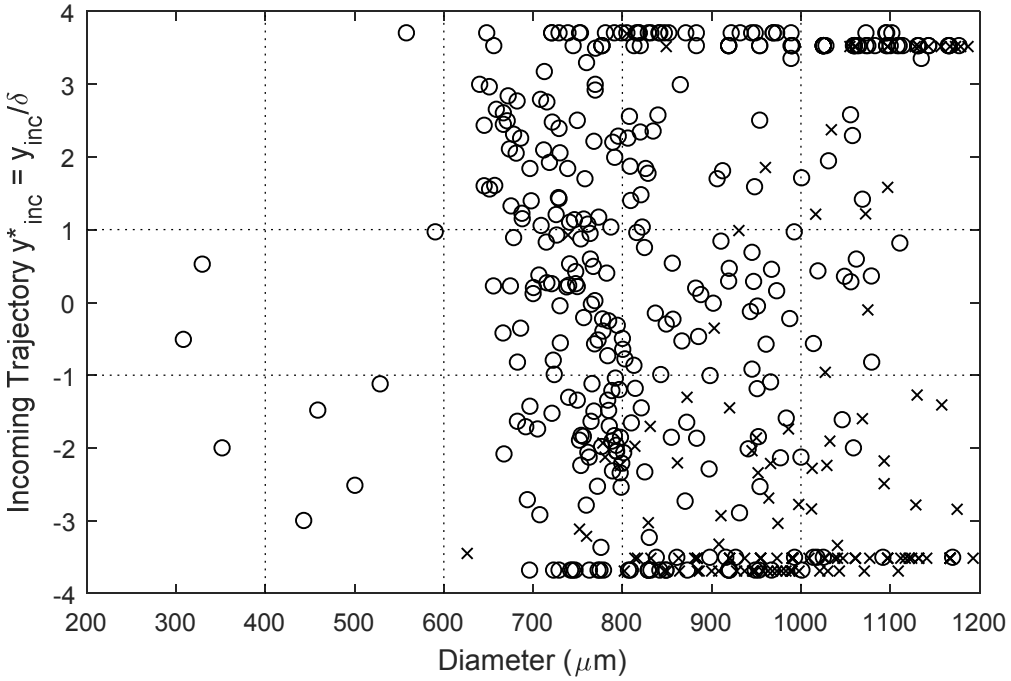

Figure C.5. Distribution of air bubbles in water at Re_{ch} = 7,700 (Pulnix).

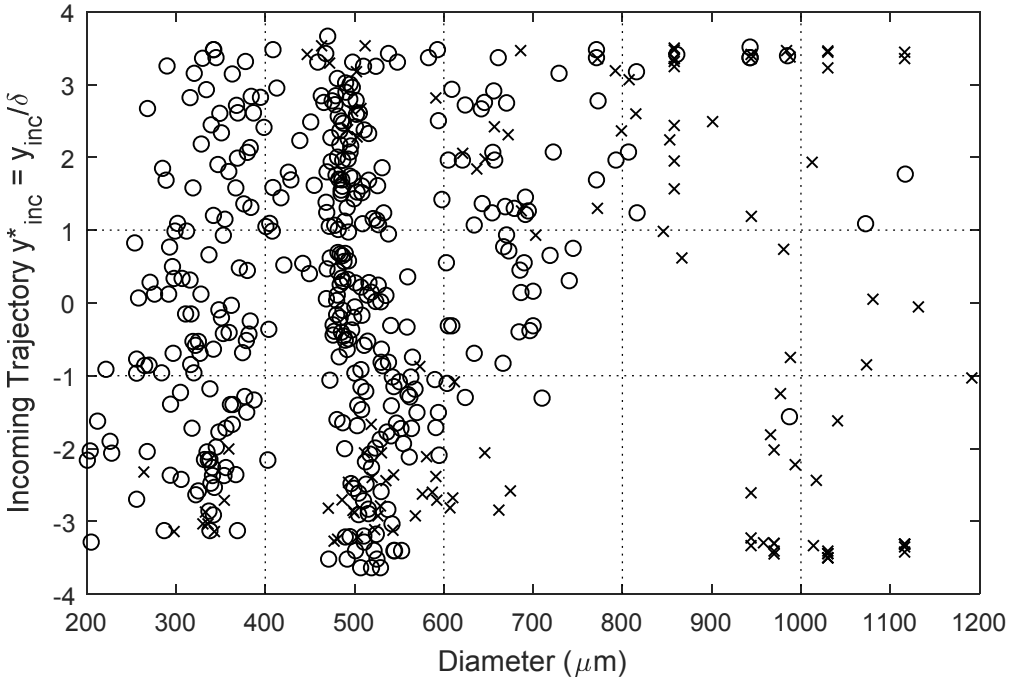

Figure C.6. Distribution of air bubbles in water at Re_{ch} = 10,000 (Pulnix).

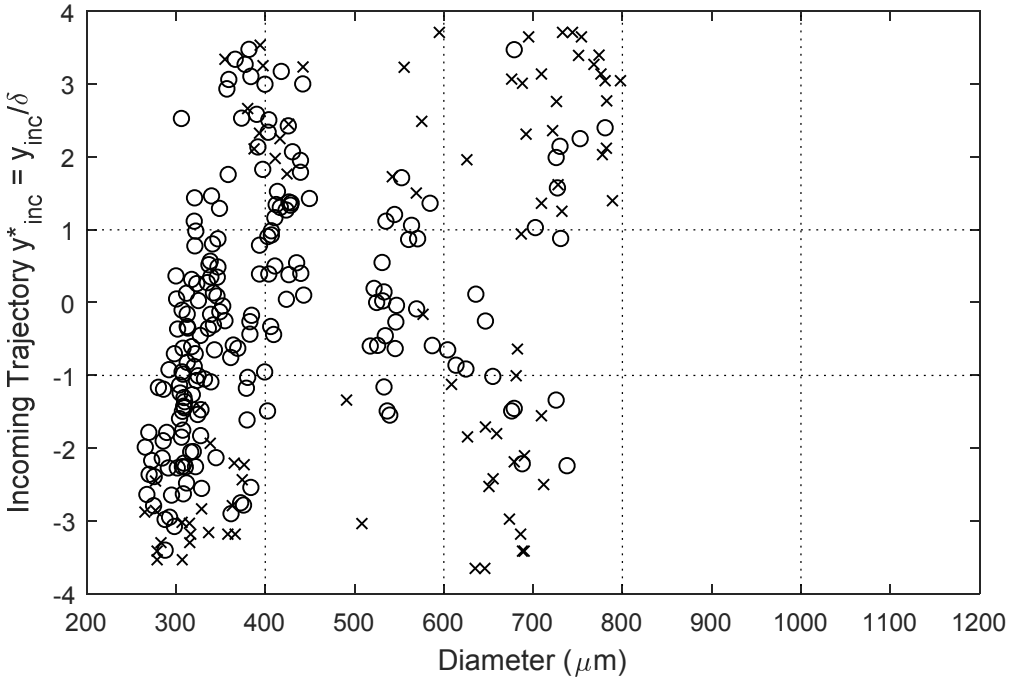

Figure C.7. Distribution of air bubbles in water at Re_{ch} = 14,000 (Pulnix).

This space has been intentionally left blank.

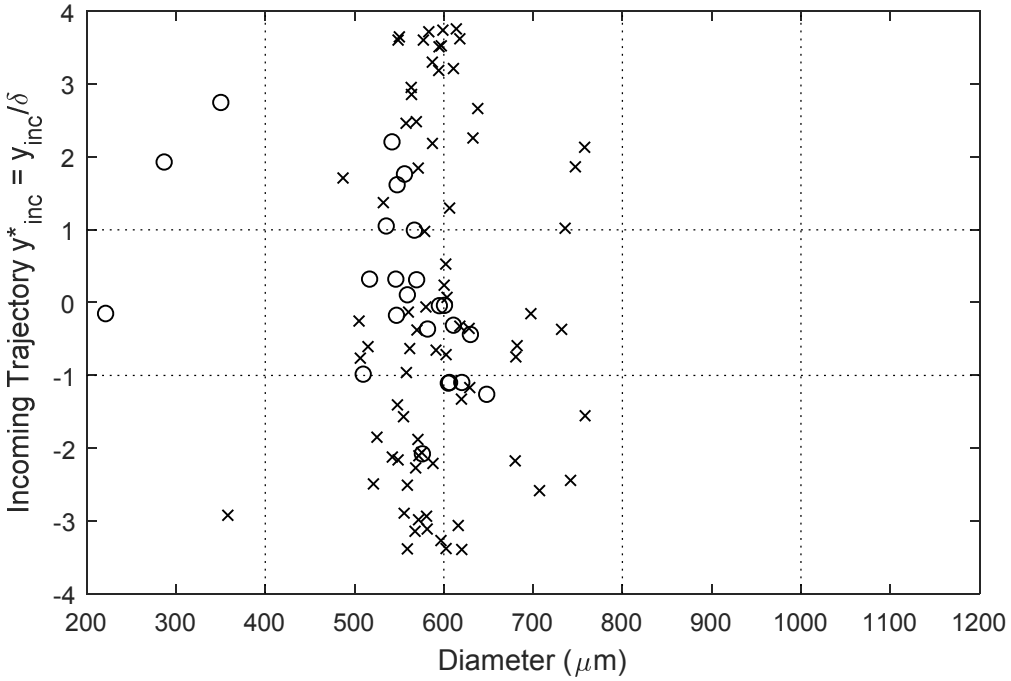

Figure C.8. Distribution of CO70FG droplets in water at Re_{ch} = 10,000 (Phantom).

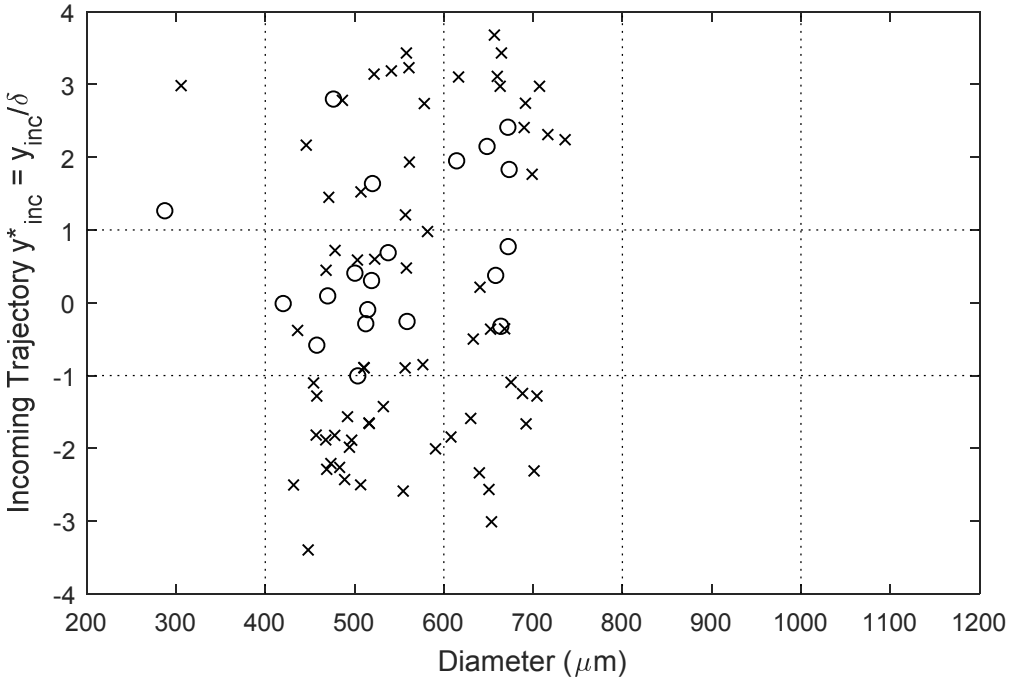

Figure C.9. Distribution of CO70FG droplets in water at Re_{ch} = 14,000 (Phantom).

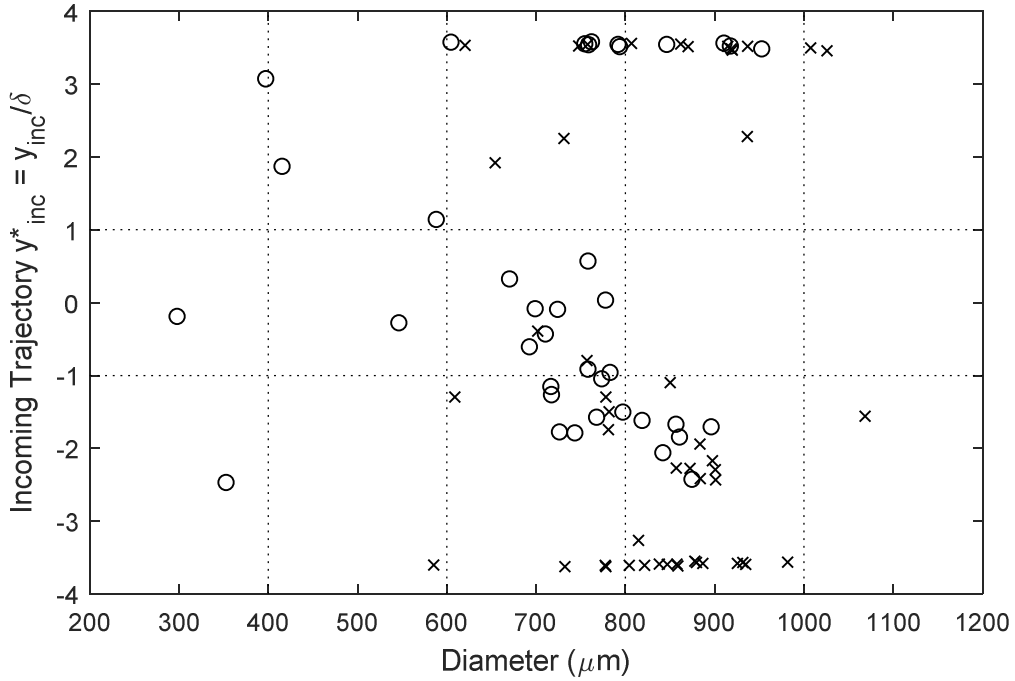

Figure C.10. Distribution of air bubbles in water at Re_{ch} = 10,000 (Phantom).

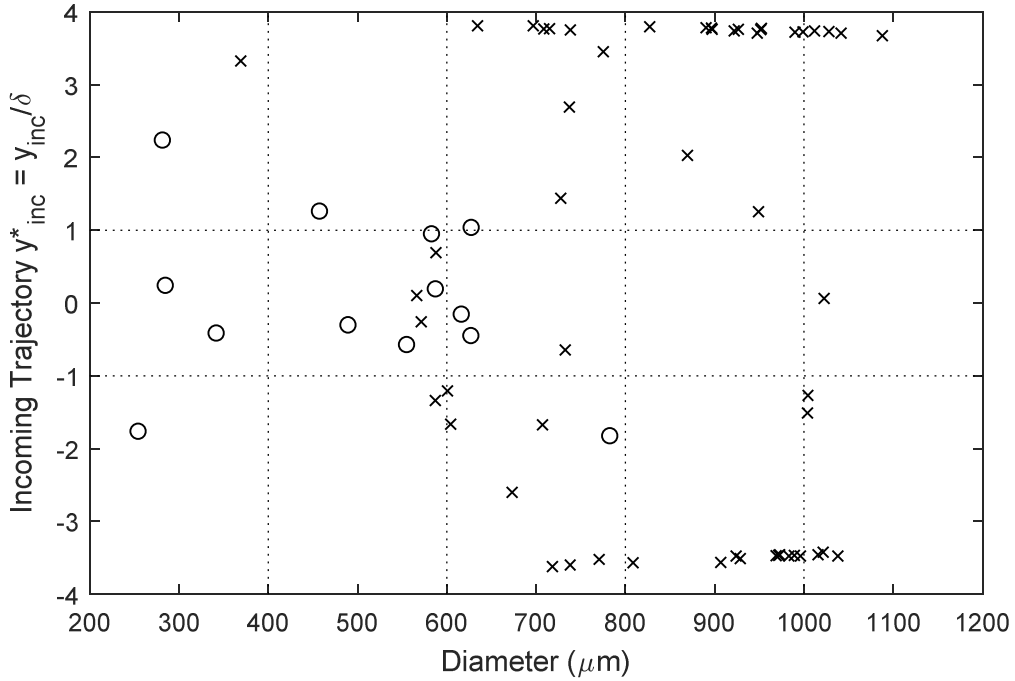

Figure C.11. Distribution of air bubbles in water at Re_{ch} = 14,000 (Phantom).

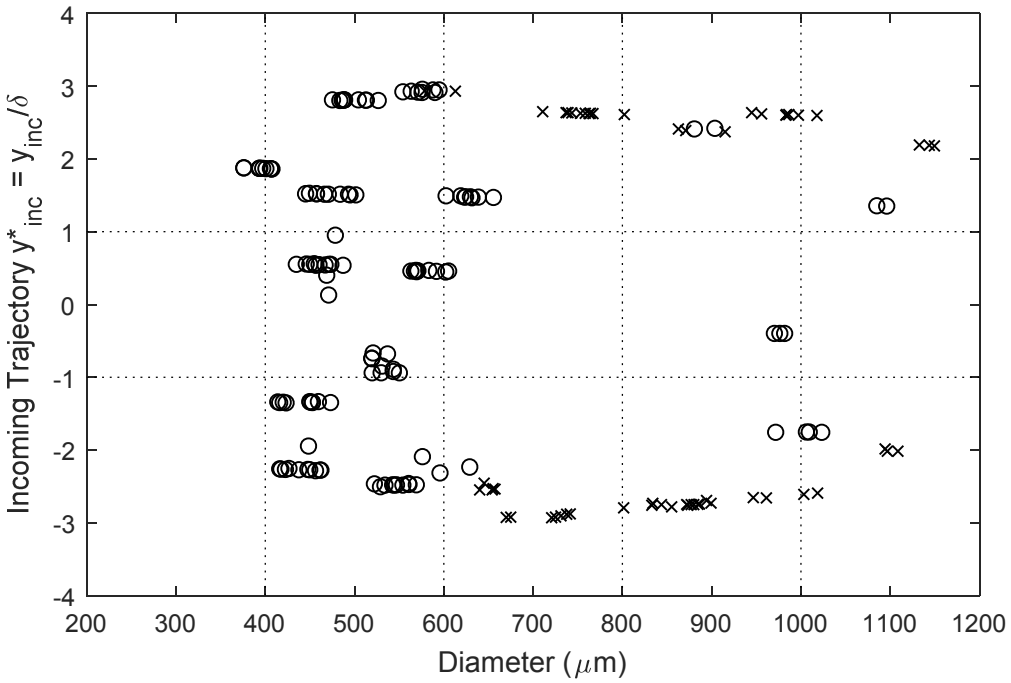

Figure C.12. Distribution of water droplets in CO70FG (μ_c = 0.0202 Pa-s) at Re_{ch} = 240 (Point Grey).

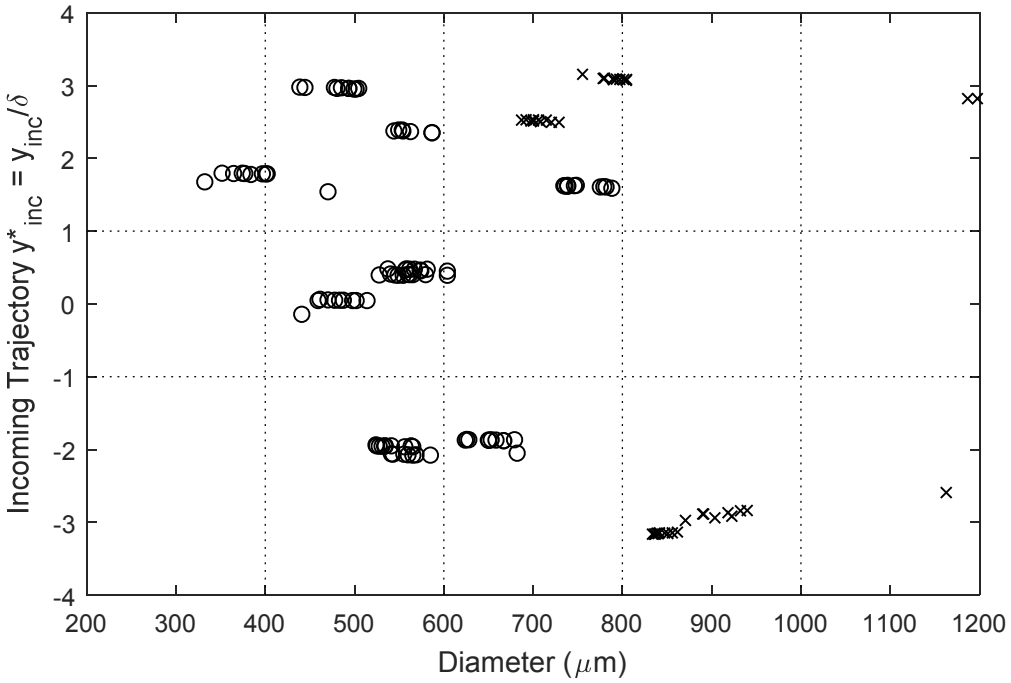

Figure C.13. Distribution of water droplets in CO70FG (μ_c = 0.0202 Pa-s) at Re_{ch} = 330 (Point Grey).

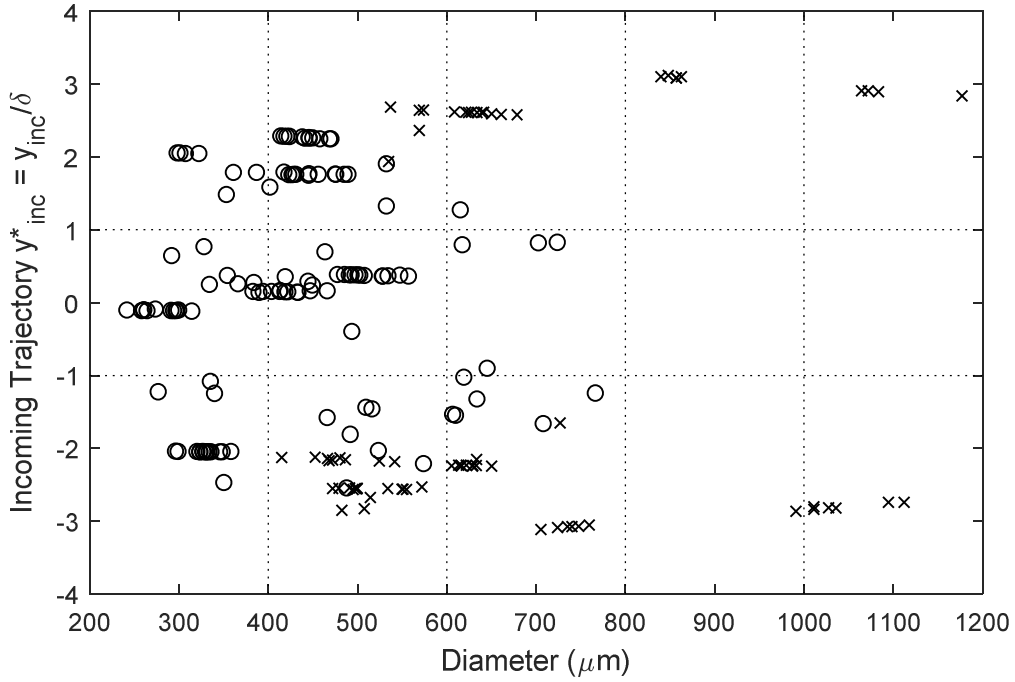

Figure C.14. Distribution of water droplets in CO70FG (μ_c = 0.0202 Pa-s) at Re_{ch} = 450 (Point Grey).

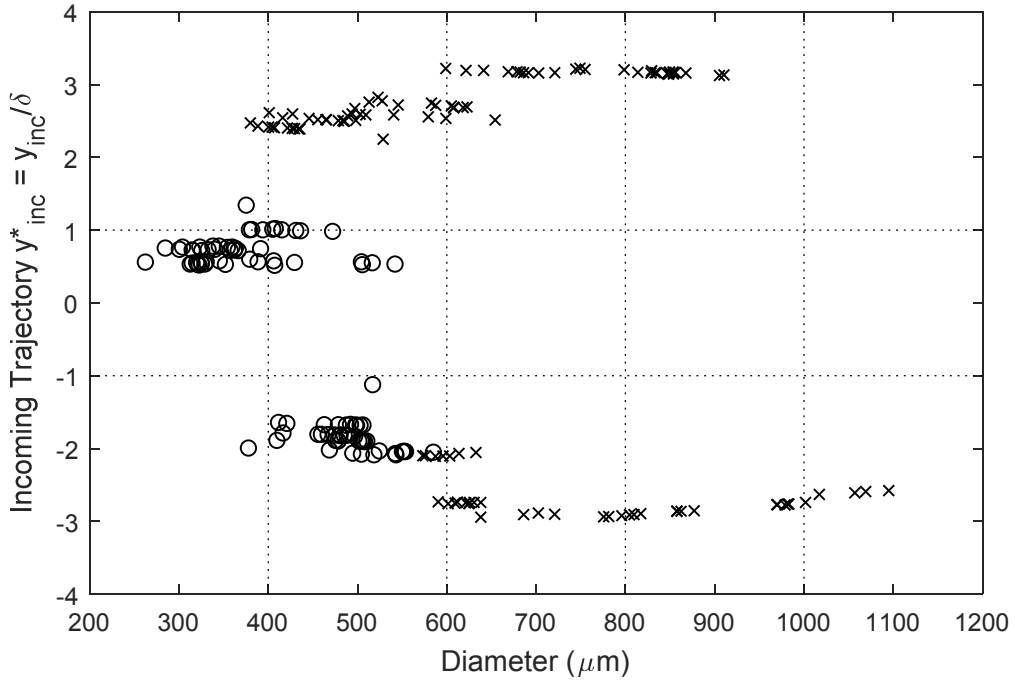

Figure C.15. Distribution of water droplets in CO70FG (μ_c = 0.0202 Pa-s) at Re_{ch} = 600 (Point Grey).

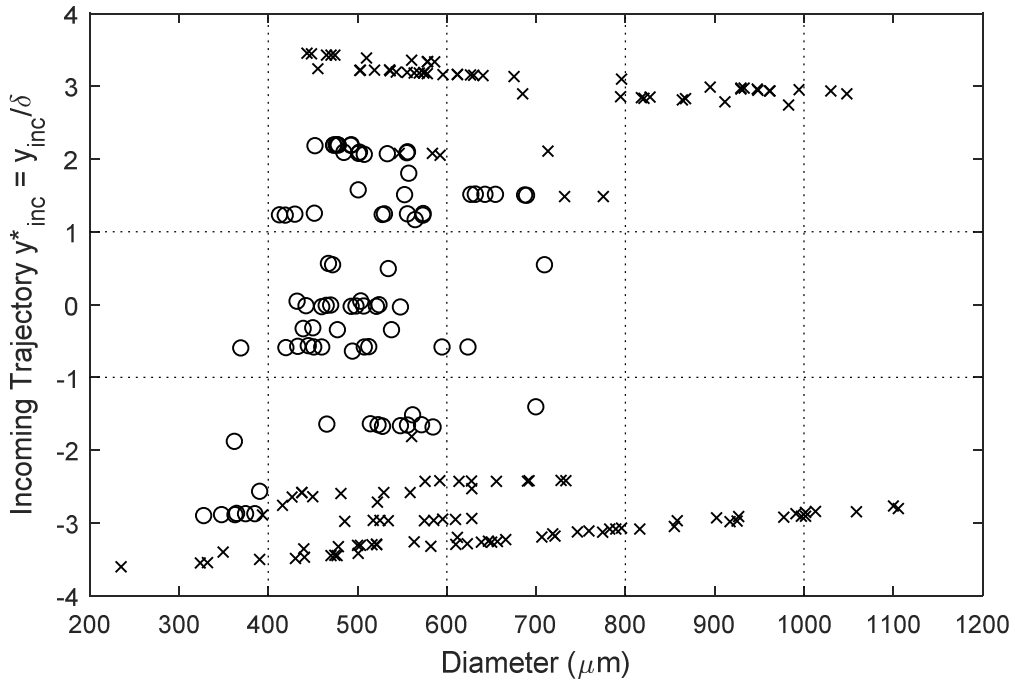

Figure C.16. Distribution of water droplets in CO200FG (μ_c = 0.0808 Pa-s) at Re_{ch} = 110 (Point Grey).

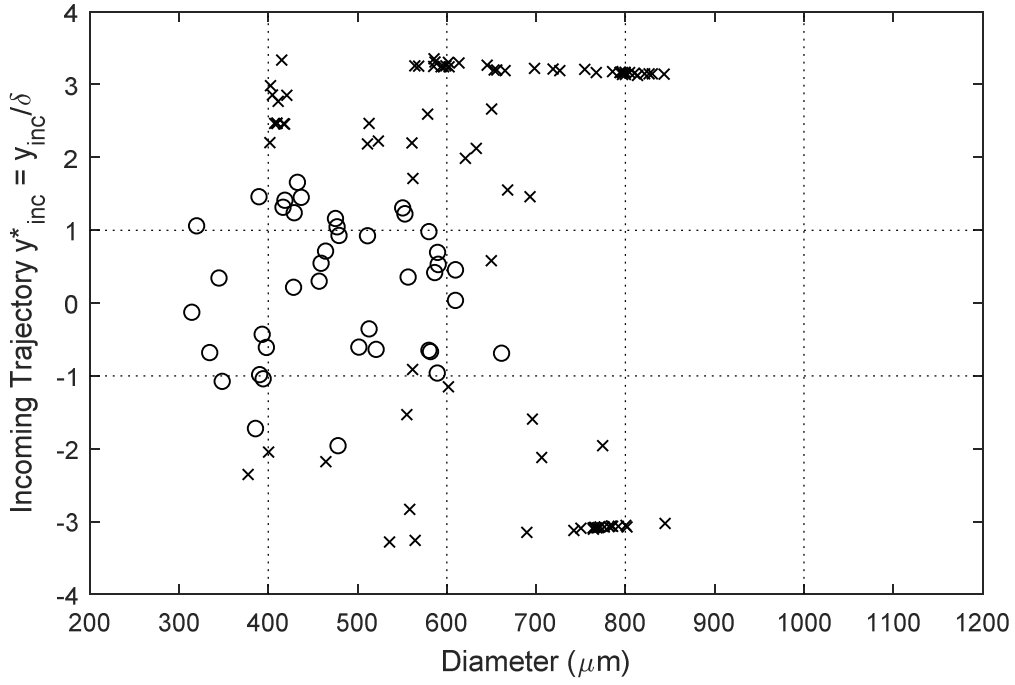

Figure C.17. Distribution of water droplets in CO200FG (μ_c = 0.0808 Pa-s) at Re_{ch} = 240 (Point Grey).

Appendix D: Droplet Trajectories

This Appendix contains all of the droplet and bubble trajectories assessed in the local Weber number analyses. Observations regarding these trajectories are discussed in more detail in Sections 4.2 and 5.2 for the turbulent and laminar experiments, respectively.

The trajectories for the turbulent flow experiments, shown in Figures D.1 to D.12, were imaged using the Phantom camera. The droplet trajectories through the orifice are shown in blue and red for channel Reynolds numbers of 10,000 and 14,000, respectively. Solid lines represent unbroken droplets, while dashed lines represent broken droplets. The circle marker denotes where the droplet breaks (or first breaks, in the case of multiple break-up events), travels out of the field of view, or moves out of the focus plane.

The trajectories for the laminar flow experiments were imaged using the Point Grey camera. Figures D.13 to D.26 show droplet trajectories categorized by incoming trajectory from $-3.5 \leq y^*_{inc} \leq 3.5$ in increments of 0.5. Trajectories for the 4 of 1026 imaged droplets with $|y^*_{inc}| > 3.5$ are not shown. Each dot represents an imaged centroid, with black and blue dots denoting images with CO70FG and CO200FG as the continuous phase, respectively. A red 'X' marker indicates the where break-up is first imaged. The range of diameters observed is presented under each trajectory plot.

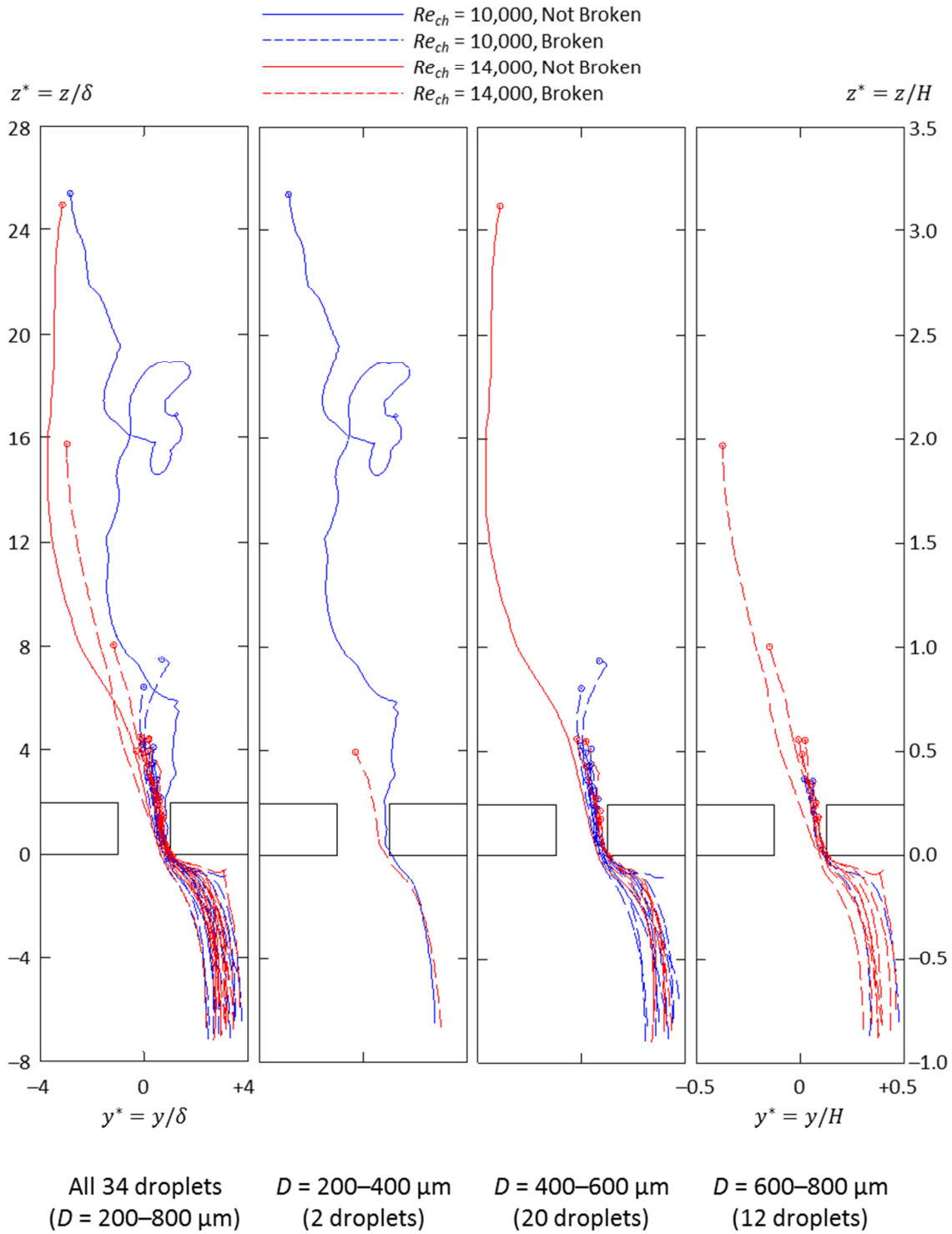

Figure D.1. Trajectories for CO70FG droplets in turbulent water flows with incoming trajectories $2.4 < y^*_{inc} < 4$.

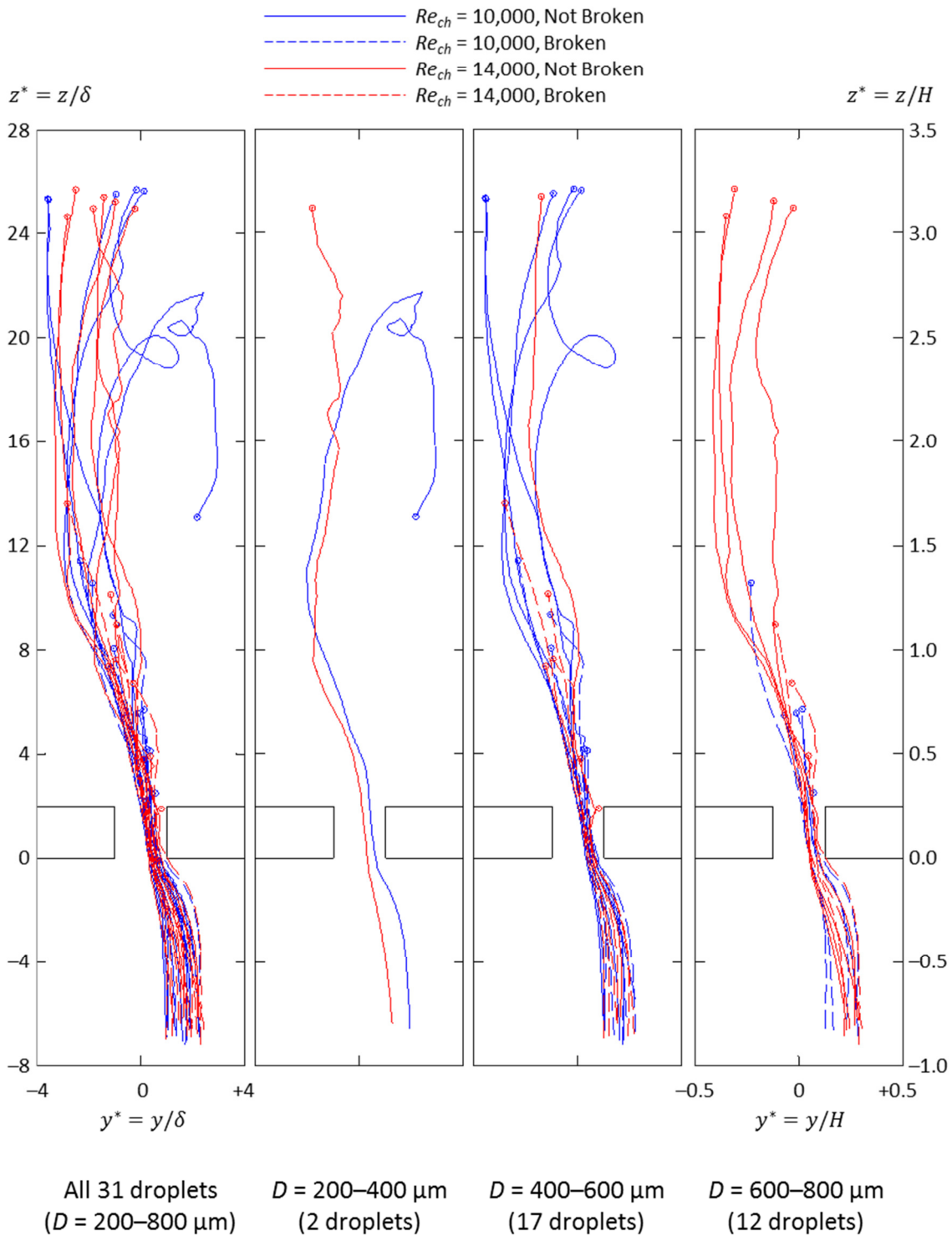

Figure D.2. Trajectories for CO70FG droplets in turbulent water flows with incoming trajectories $0.8 < y^*_{inc} < 2.4$.

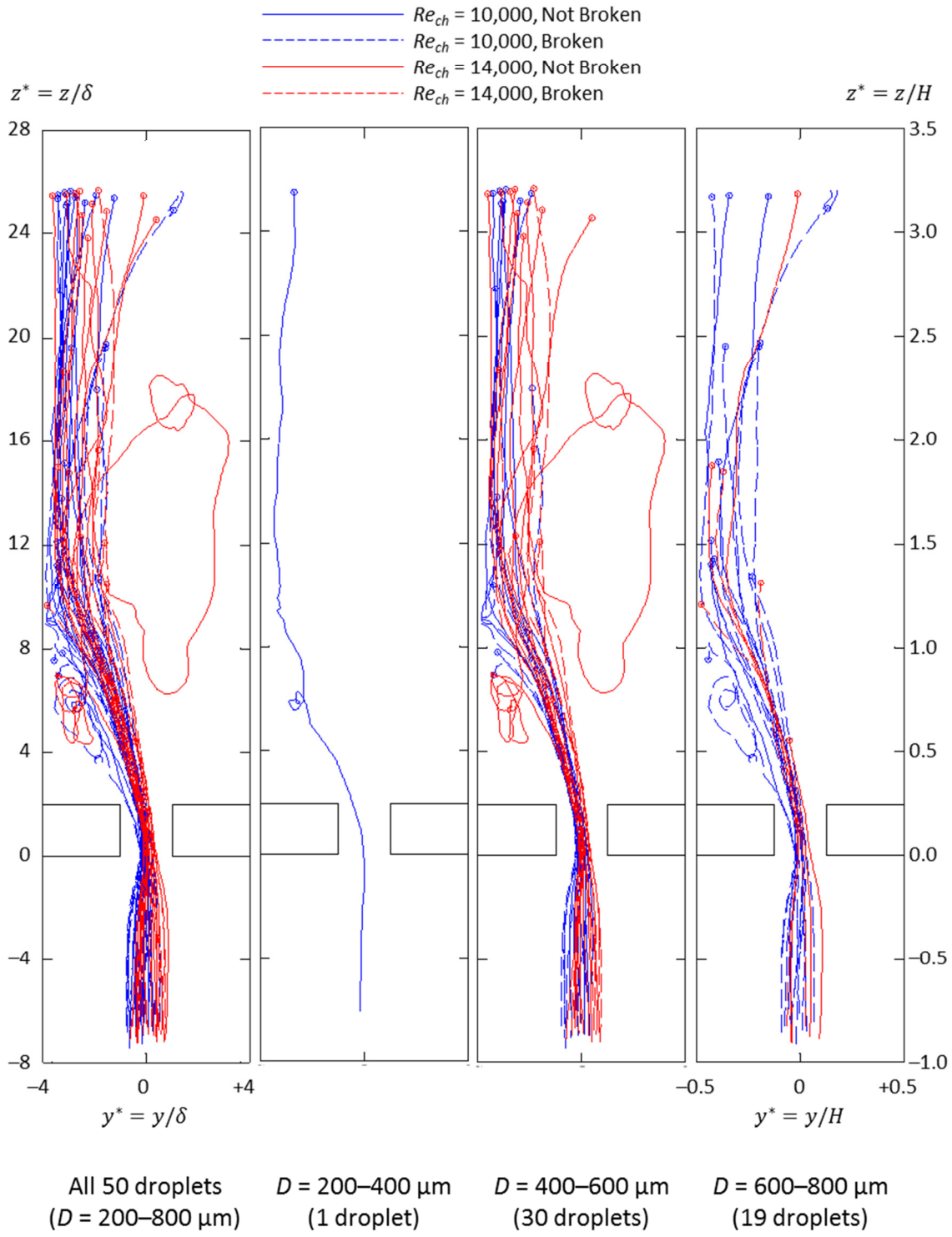

Figure D.3. Trajectories for CO70FG droplets in turbulent water flows with incoming trajectories $-0.8 < y^*_{inc} < 0.8$.

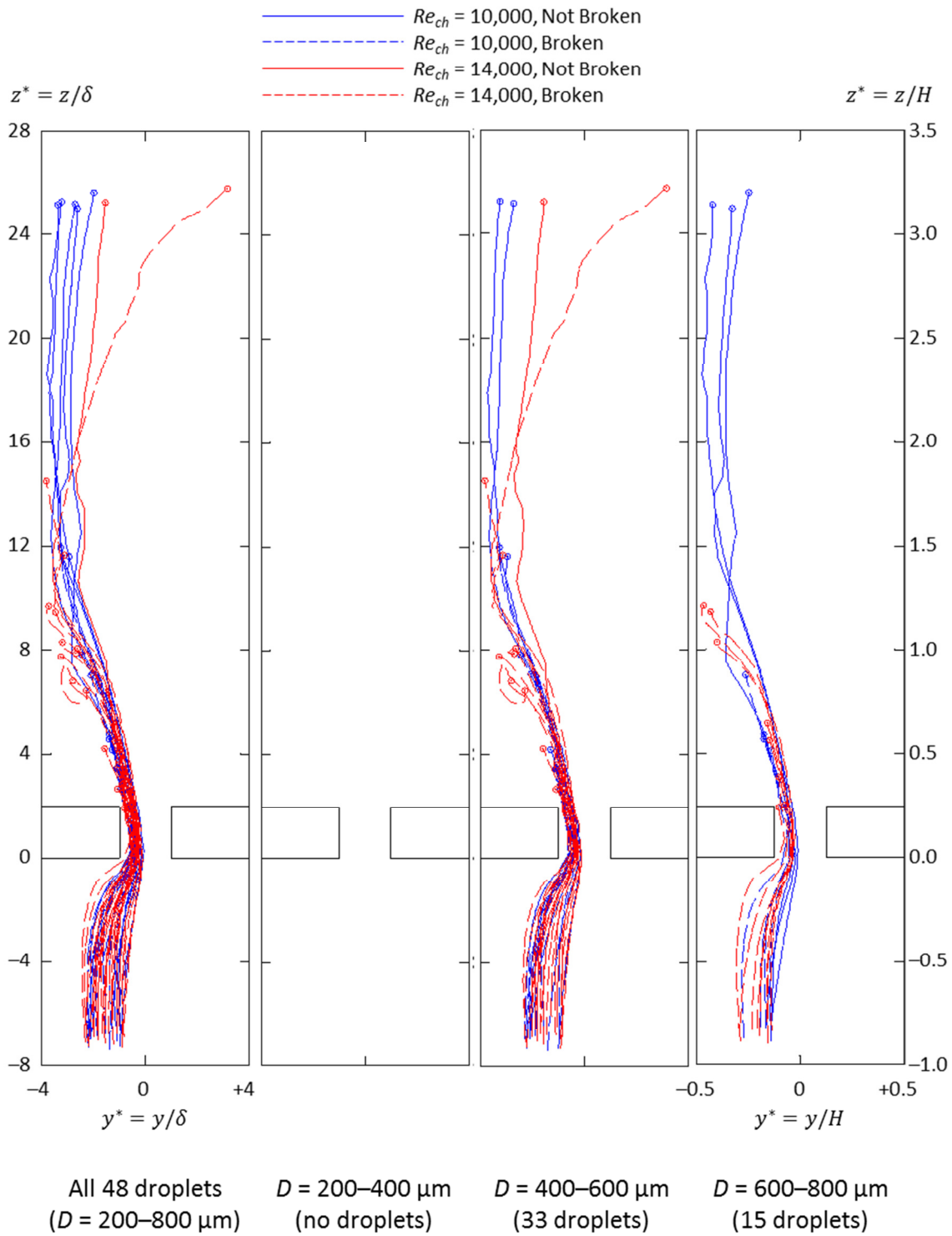

Figure D.4. Trajectories for CO70FG droplets in turbulent water flows with incoming trajectories $-2.4 < y^*_{inc} < -0.8$.

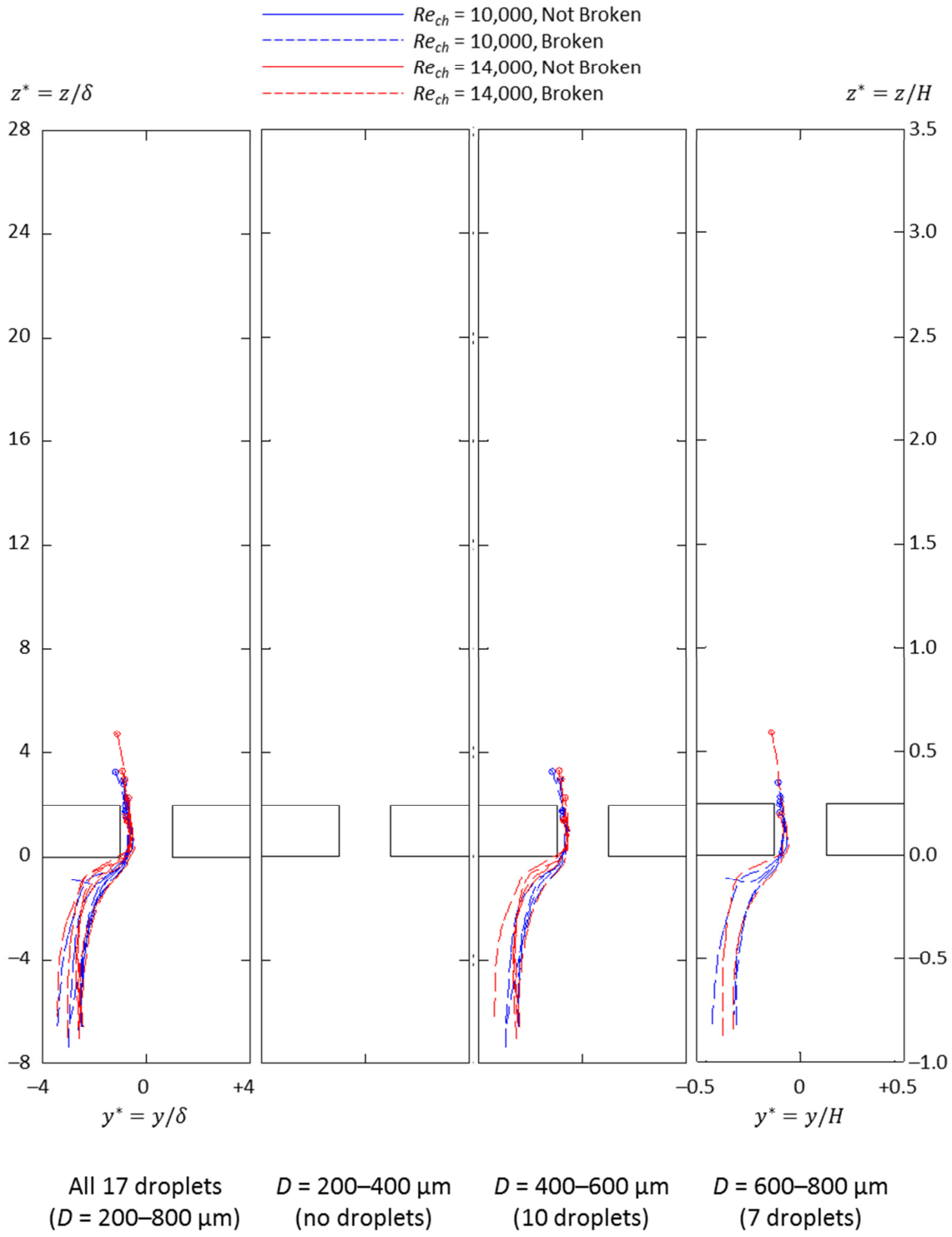

Figure D.5. Trajectories for CO70FG droplets in turbulent water flows with incoming trajectories $-4 < y^*_{inc} < -2.4$.

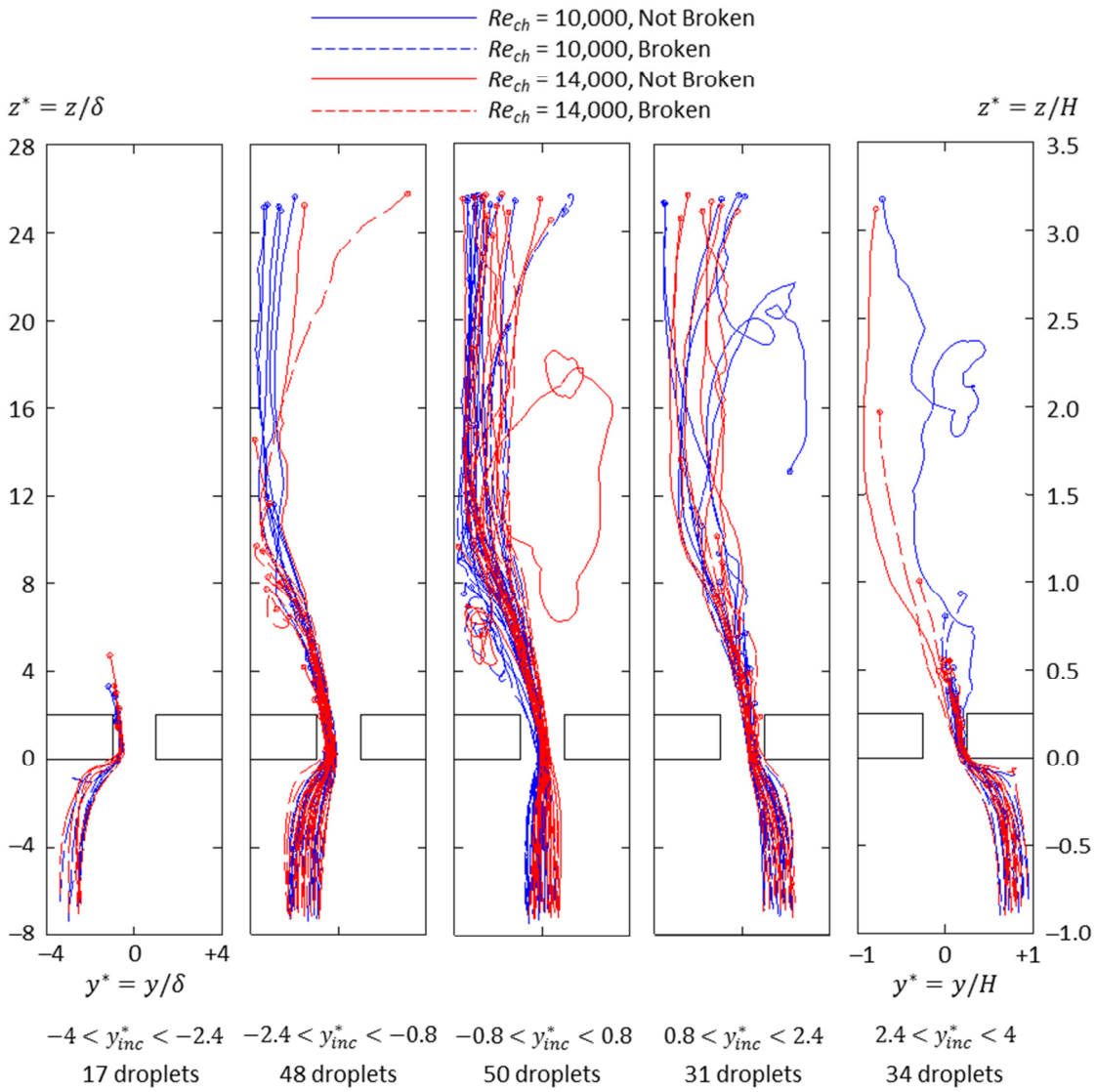

Figure D.6. Combined trajectories for all CO70FG droplets in turbulent water flows.

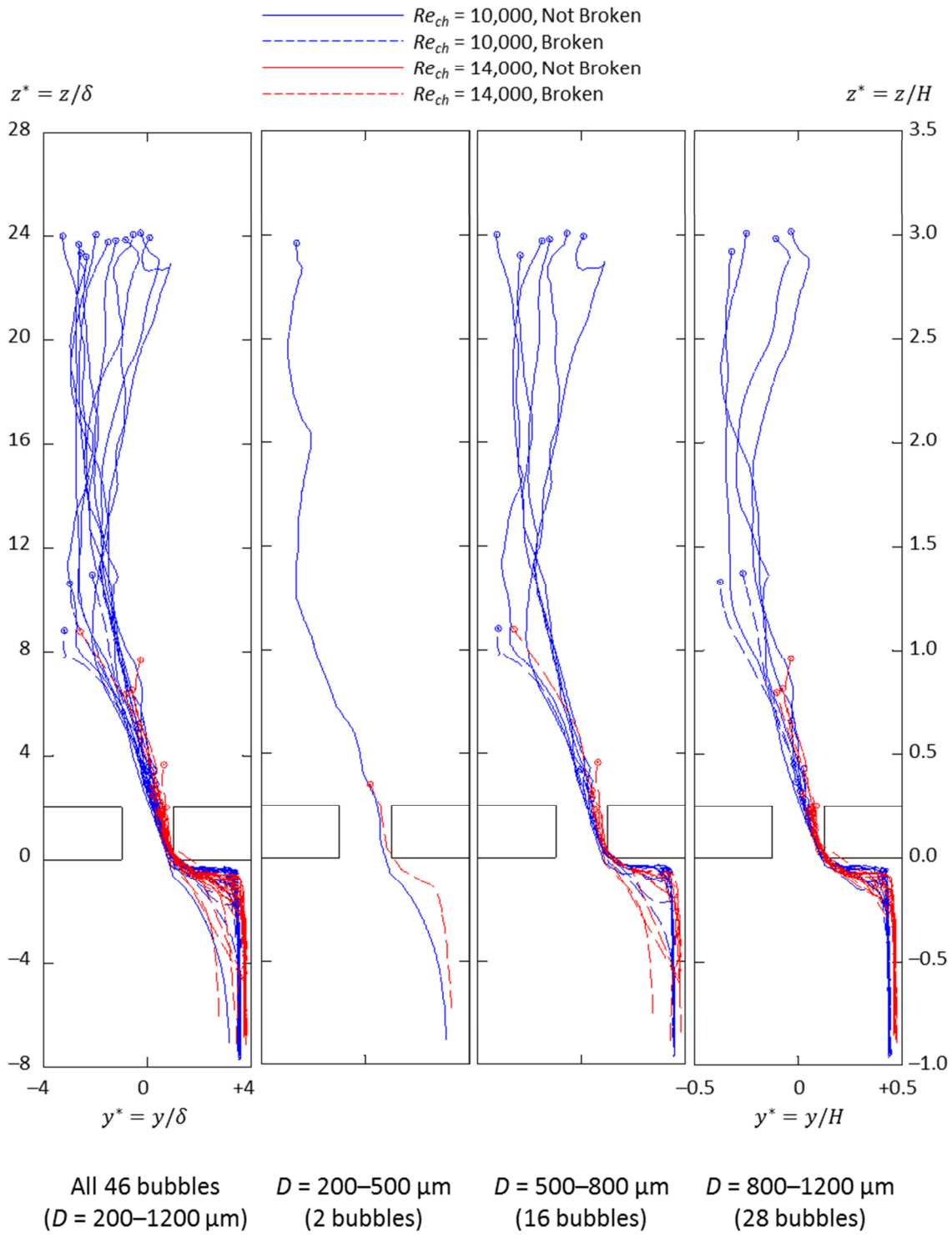

Figure D.7. Trajectories for air bubbles in turbulent water flows with incoming trajectories $2.4 < y^*_{inc} < 4$.

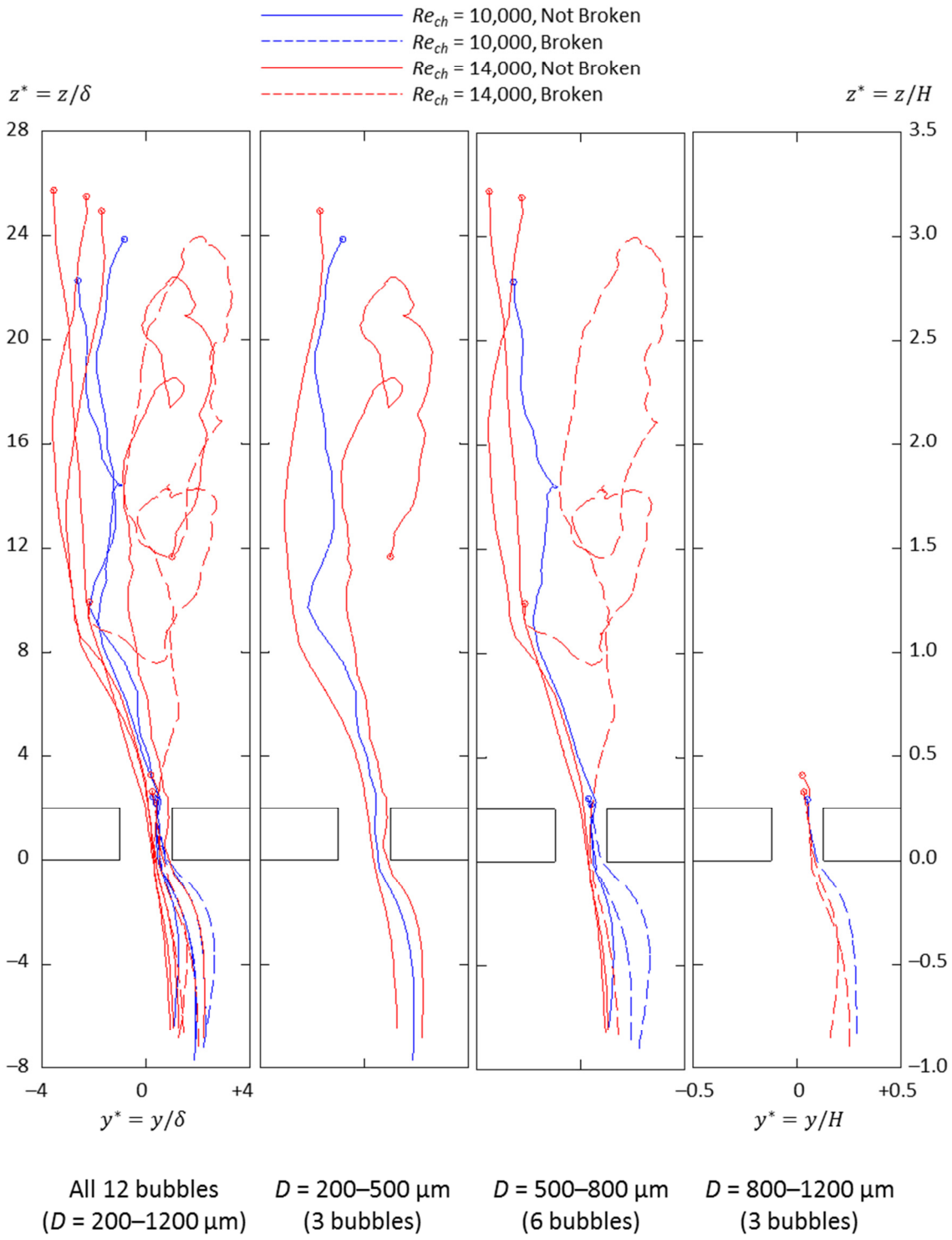

Figure D.8. Trajectories for air bubbles in turbulent water flows with incoming trajectories $0.8 < y^*_{inc} < 2.4$.

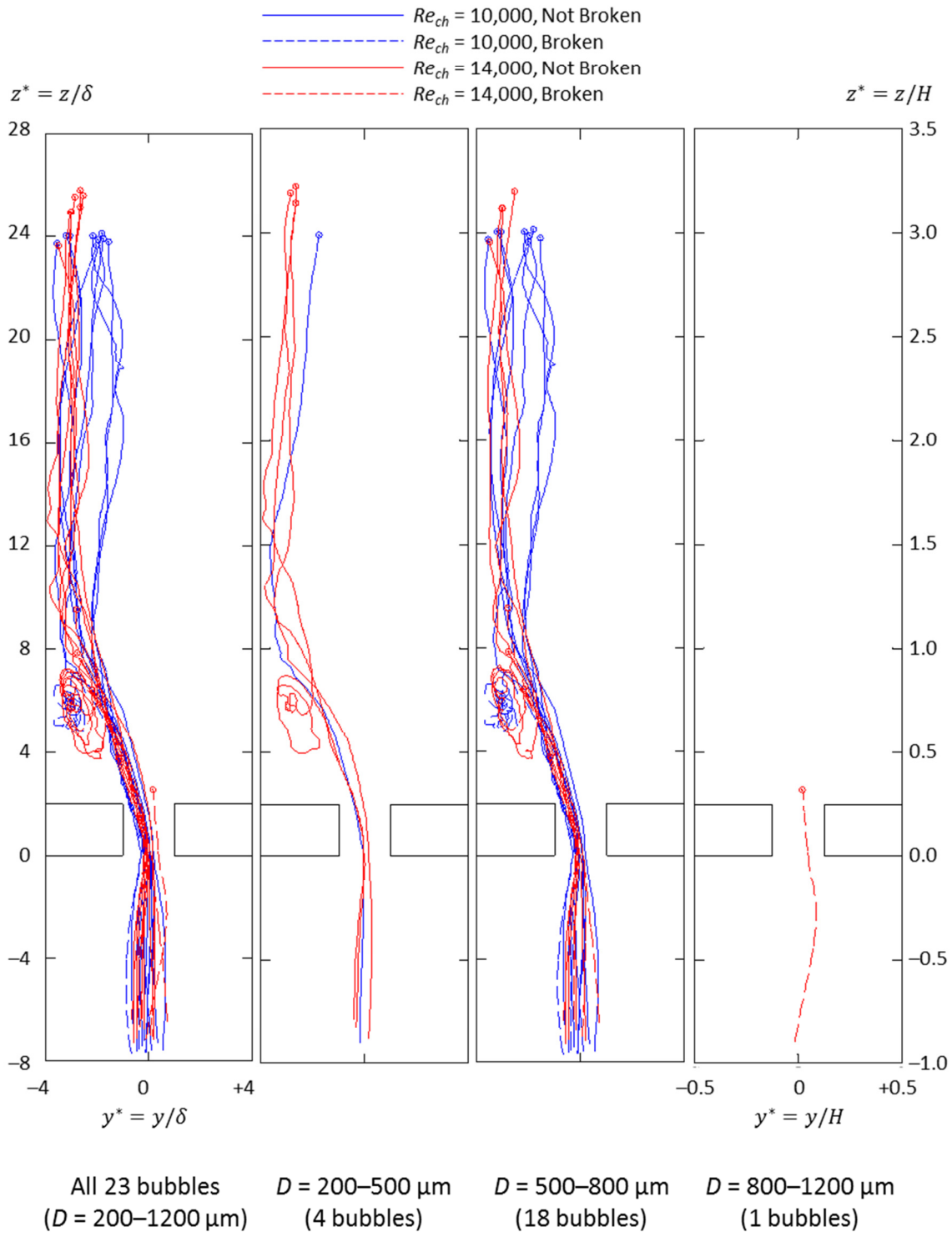

Figure D.9. Trajectories for air bubbles in turbulent water flows with incoming trajectories $-0.8 < y^*_{inc} < 0.8$.

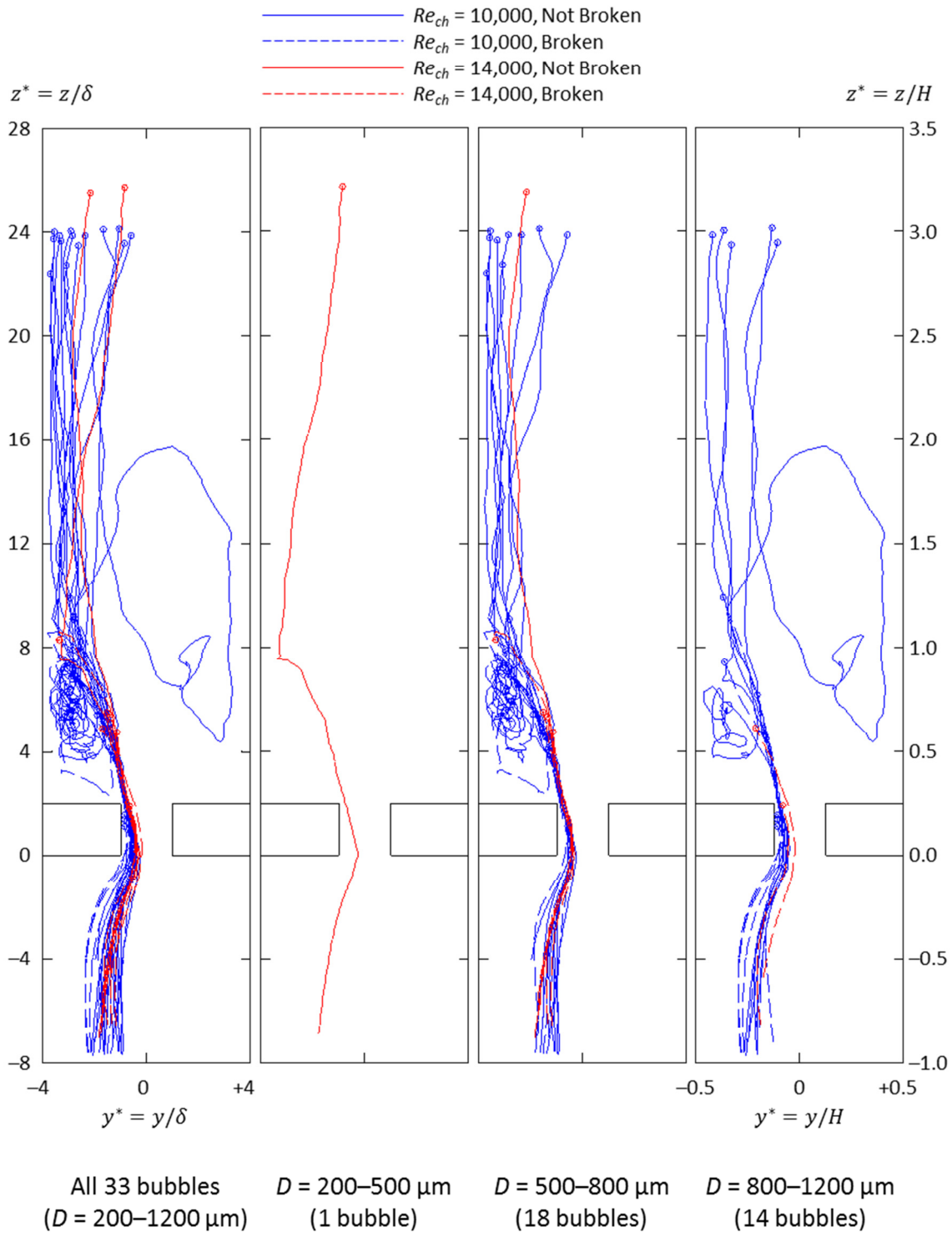

Figure D.10. Trajectories for air bubbles in turbulent water flows with incoming trajectories $-2.4 < y^*_{inc} < -0.8$.

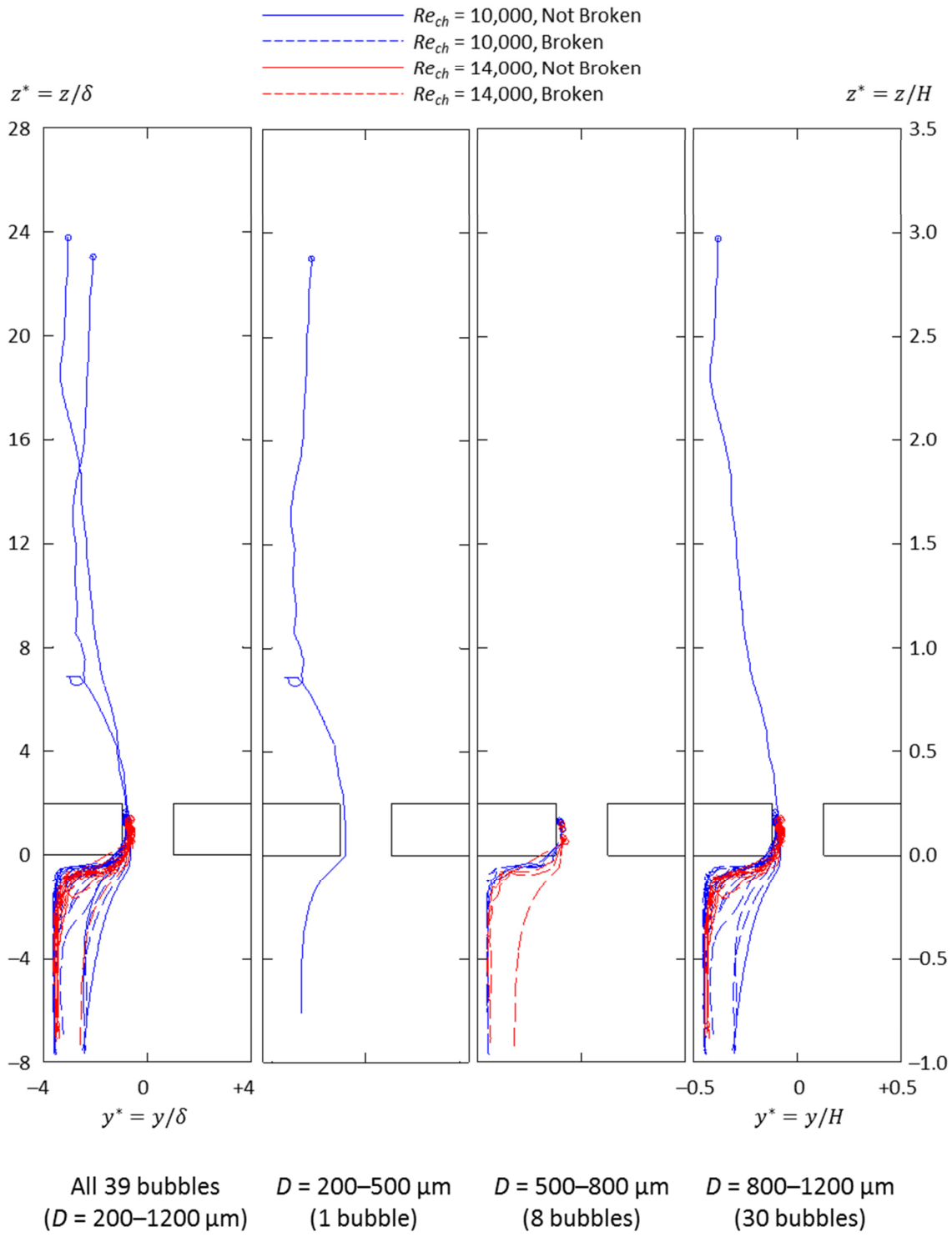

Figure D.11. Trajectories for air bubbles in turbulent water flows with incoming trajectories $-4 < y^*_{inc} < -2.4$.

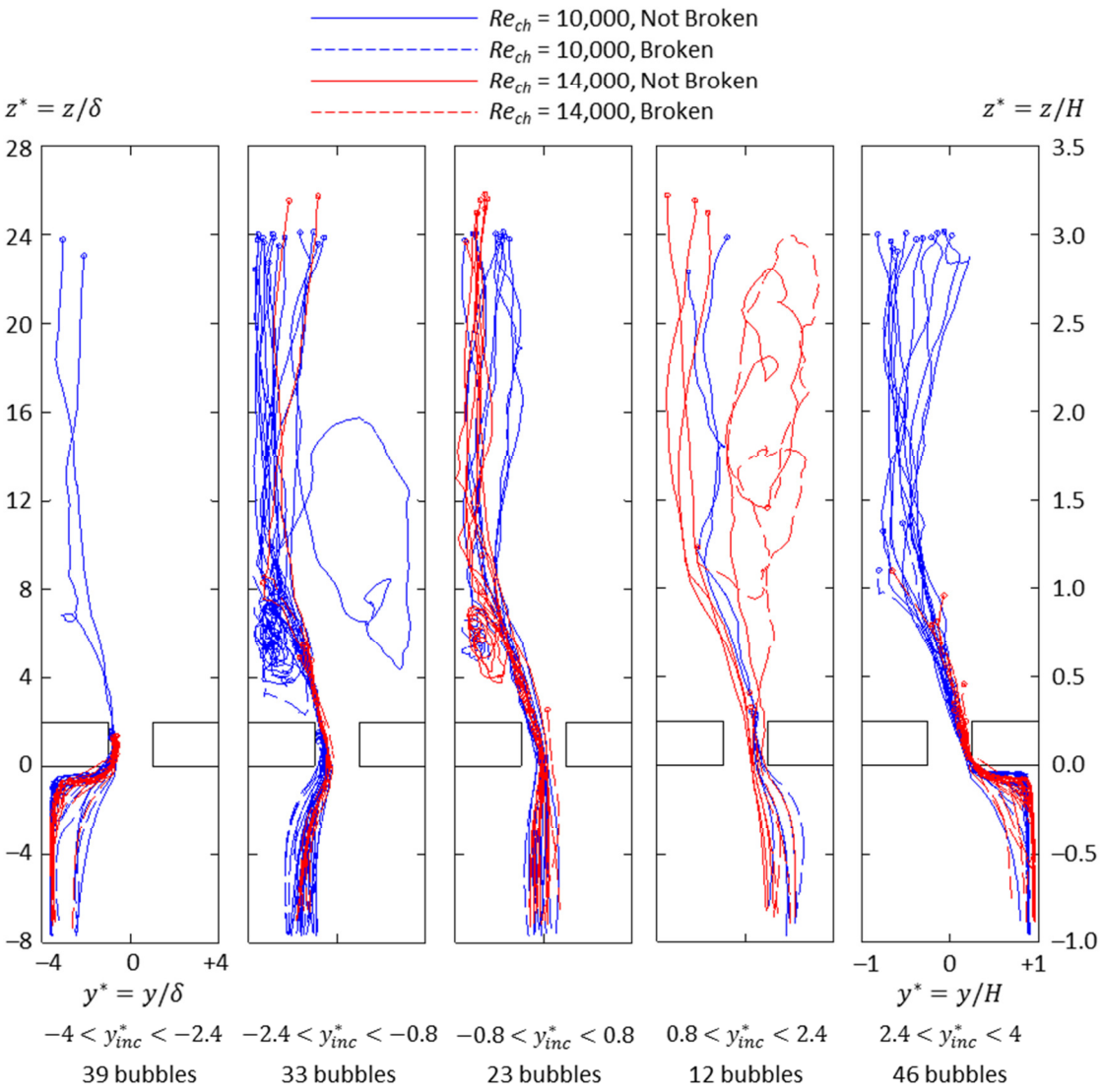

Figure D.12. Combined trajectories for all air bubbles in turbulent water flows.

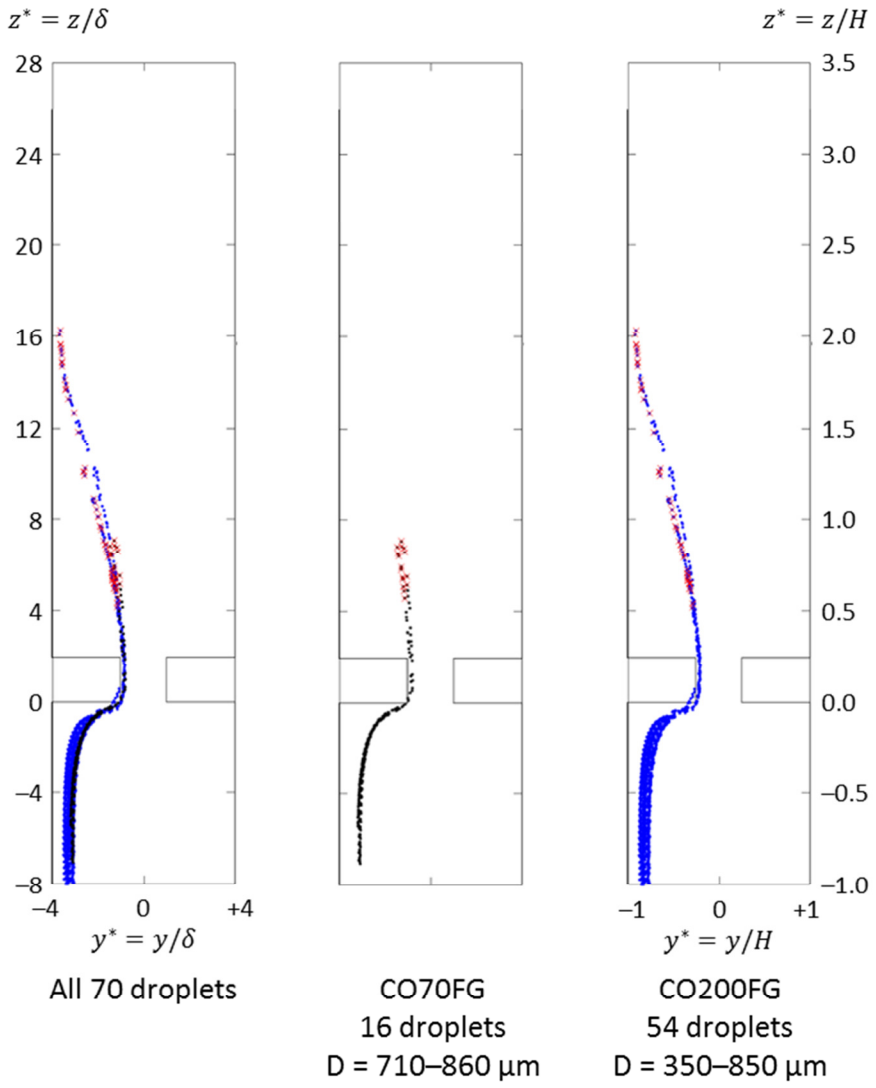

Figure D.13. Trajectories for water droplets in laminar Crystal Oil flows with incoming trajectories $-3.5 < y^*_{inc} < -3.0$.

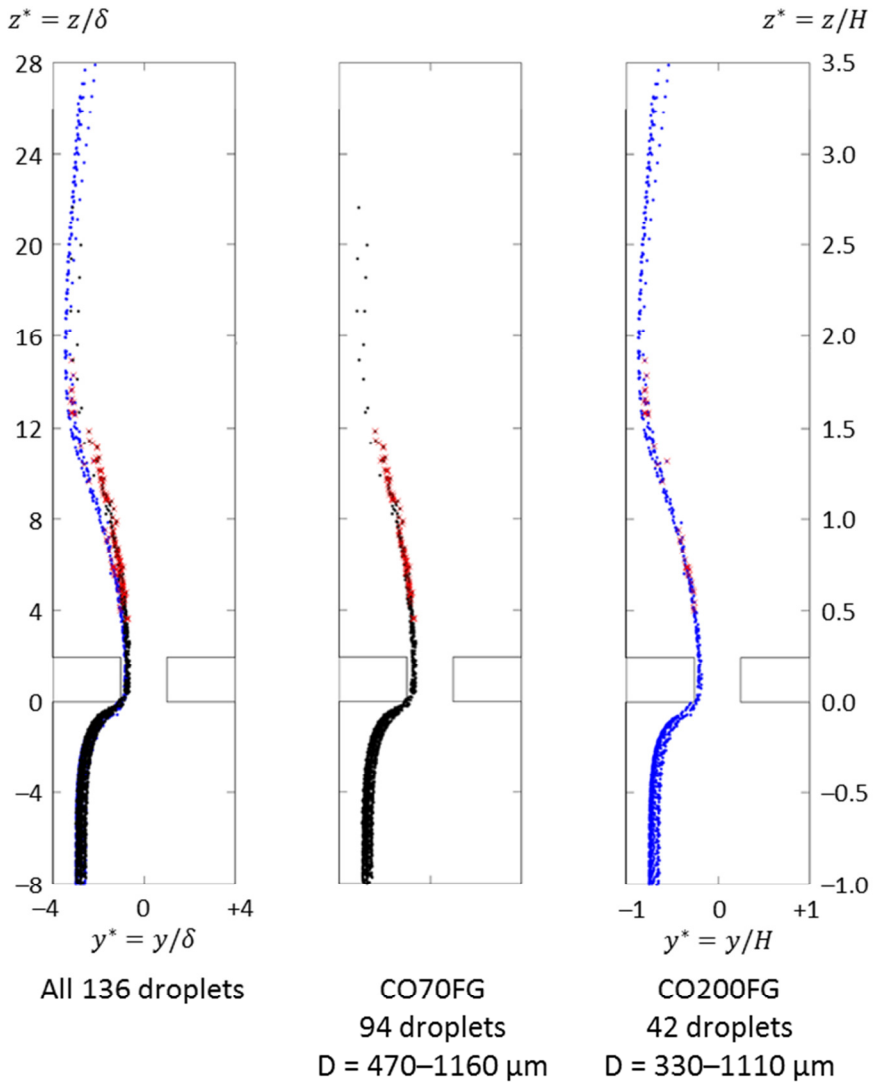

Figure D.14. Trajectories for water droplets in laminar Crystal Oil flows with incoming trajectories $-3.0 < y^*_{inc} < -2.5$.

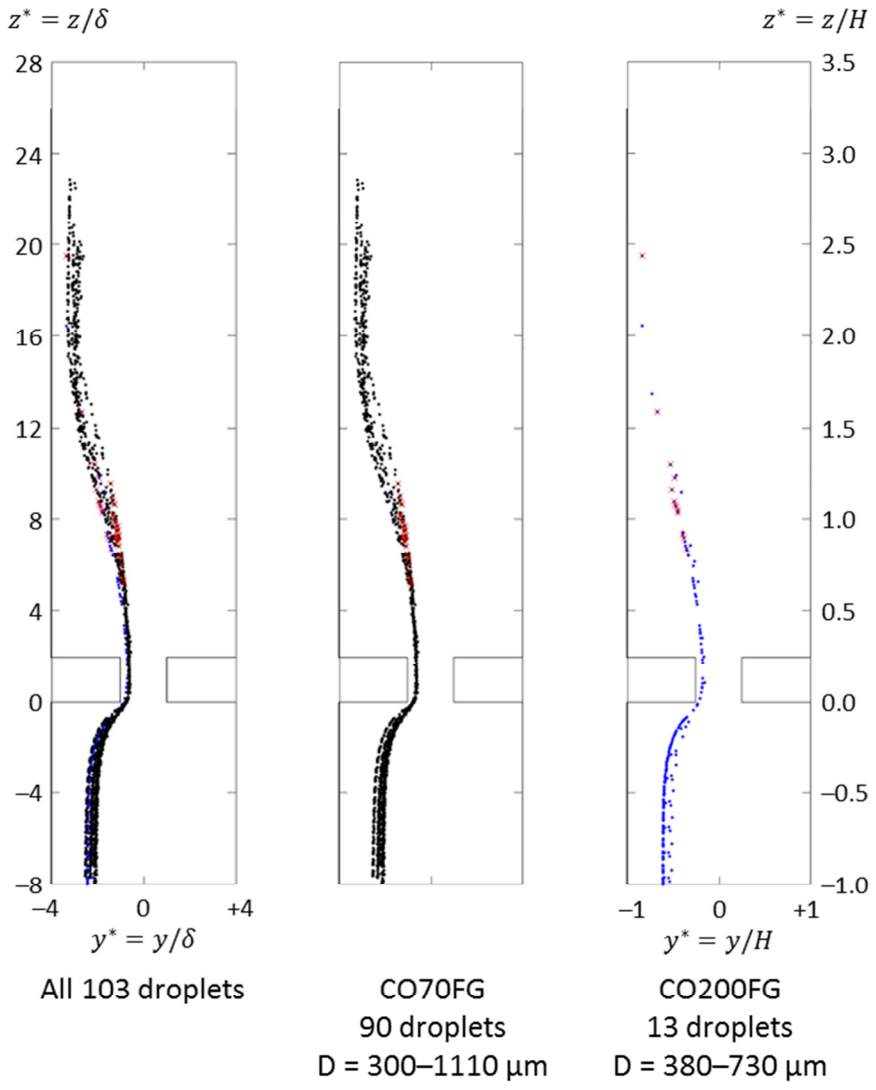

Figure D.15. Trajectories for water droplets in laminar Crystal Oil flows with incoming trajectories $-2.5 < y^*_{inc} < -2.0$.

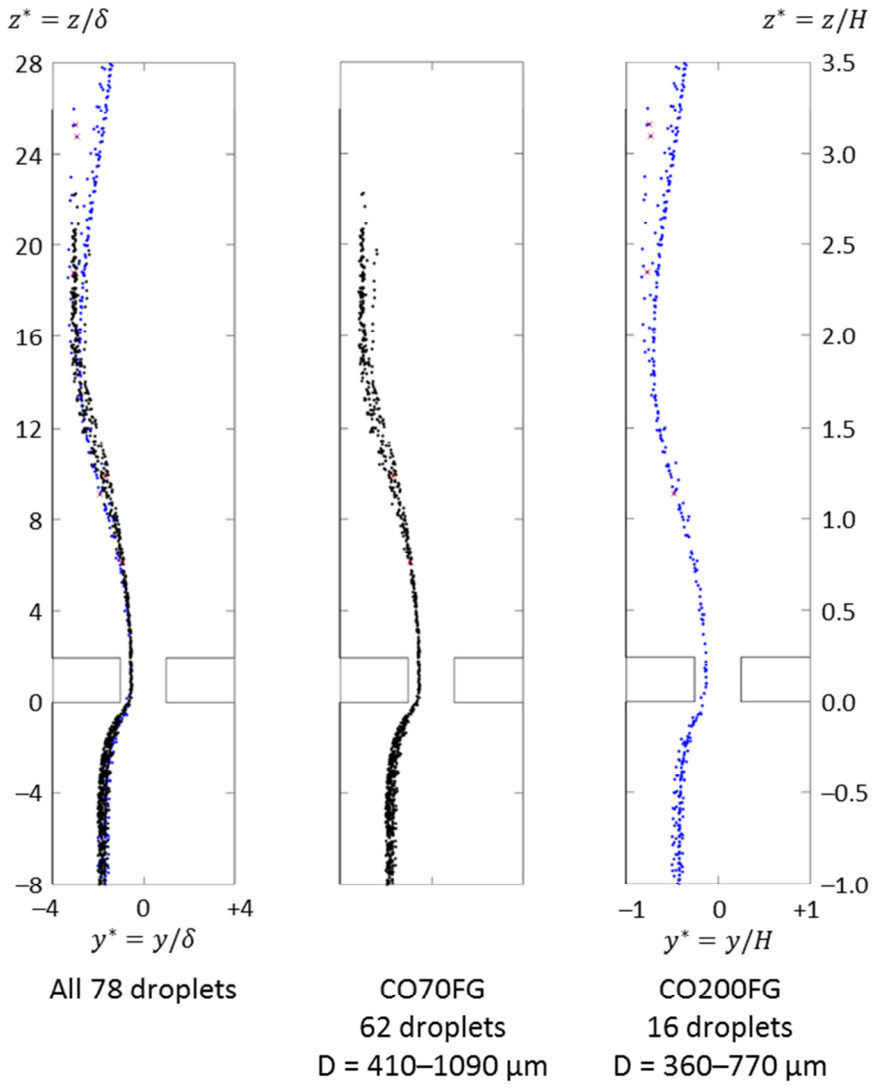

Figure D.16. Trajectories for water droplets in laminar Crystal Oil flows with incoming trajectories $-2.0 < y^*_{inc} < -1.5$.

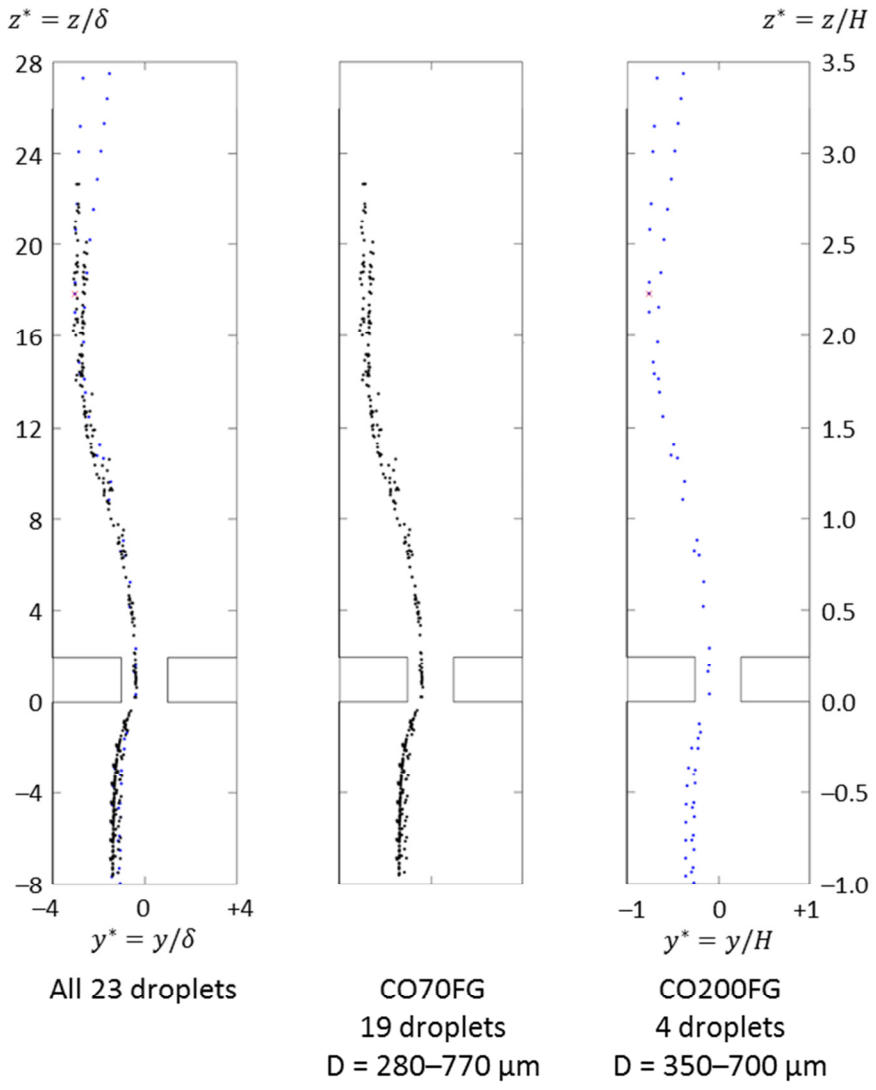

Figure D.17. Trajectories for water droplets in laminar Crystal Oil flows with incoming trajectories $-1.5 < y^*_{inc} < -1.0$.

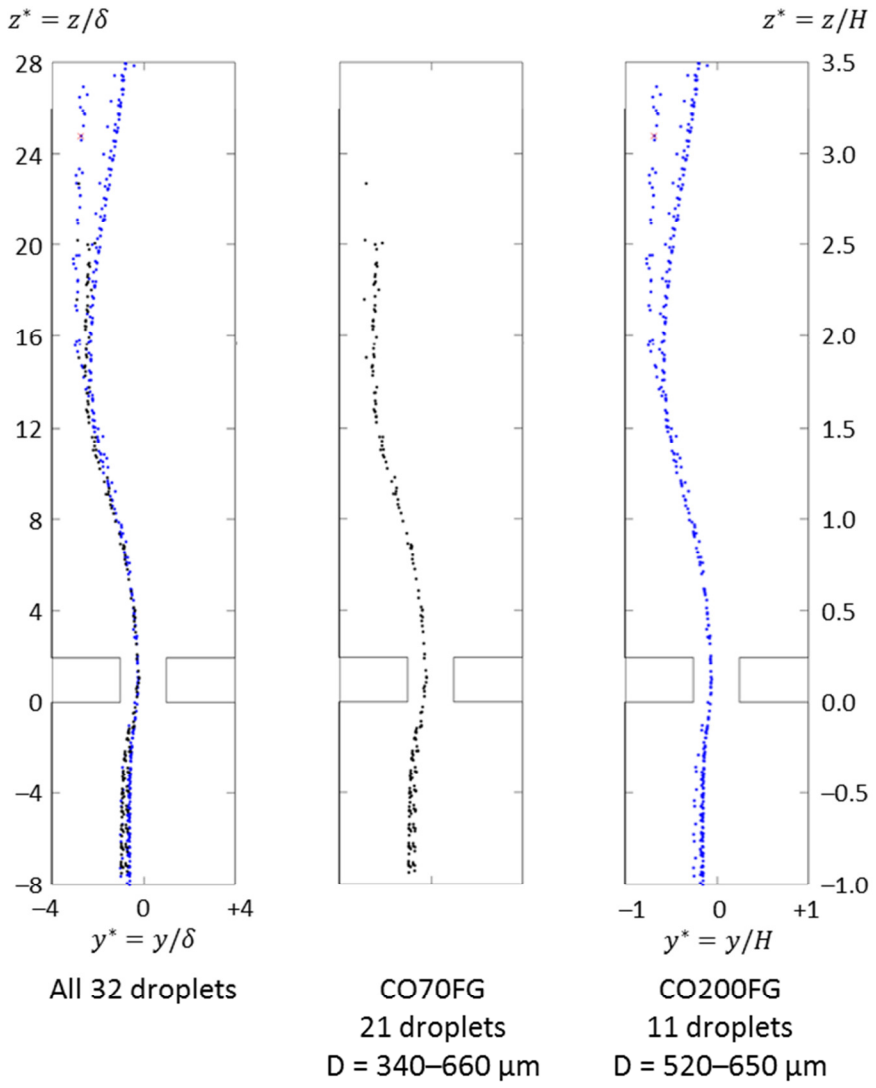

Figure D.18. Trajectories for water droplets in laminar Crystal Oil flows with incoming trajectories $-1.0 < y^*_{inc} < -0.5$.

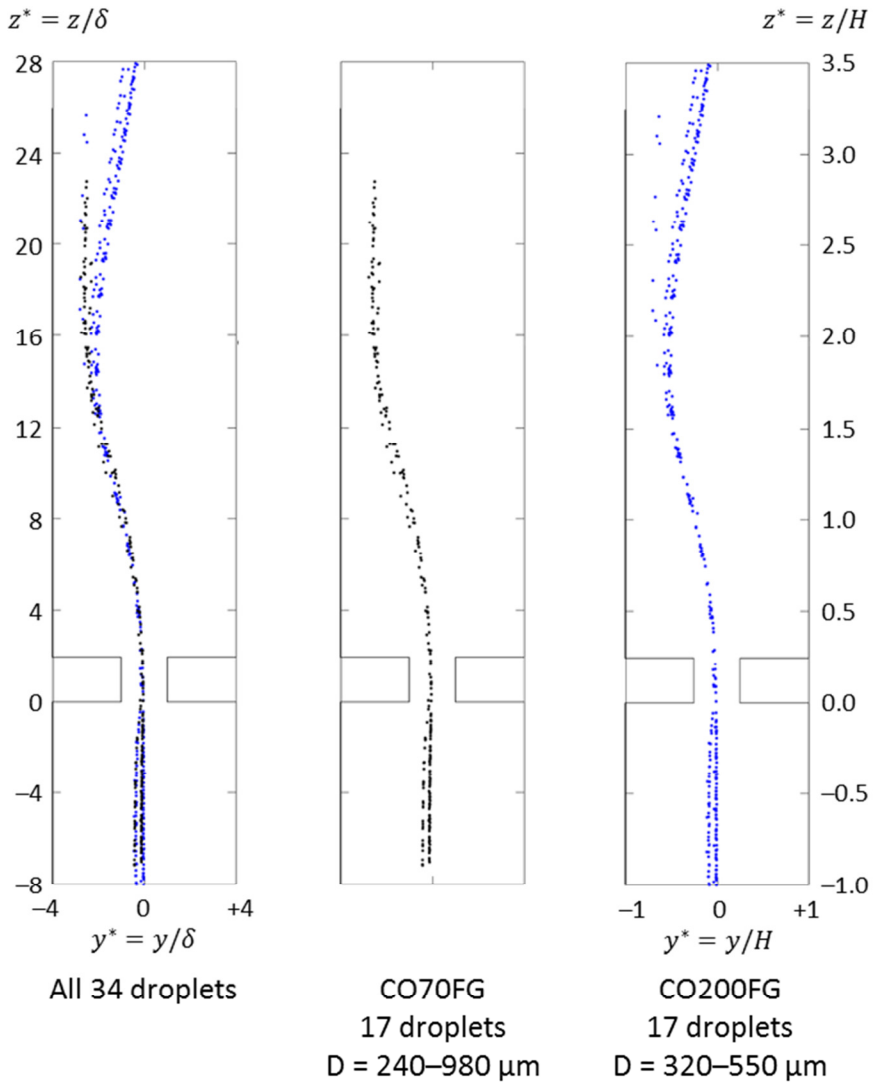

Figure D.19. Trajectories for water droplets in laminar Crystal Oil flows with incoming trajectories $-0.5 < y^*_{inc} < 0$.

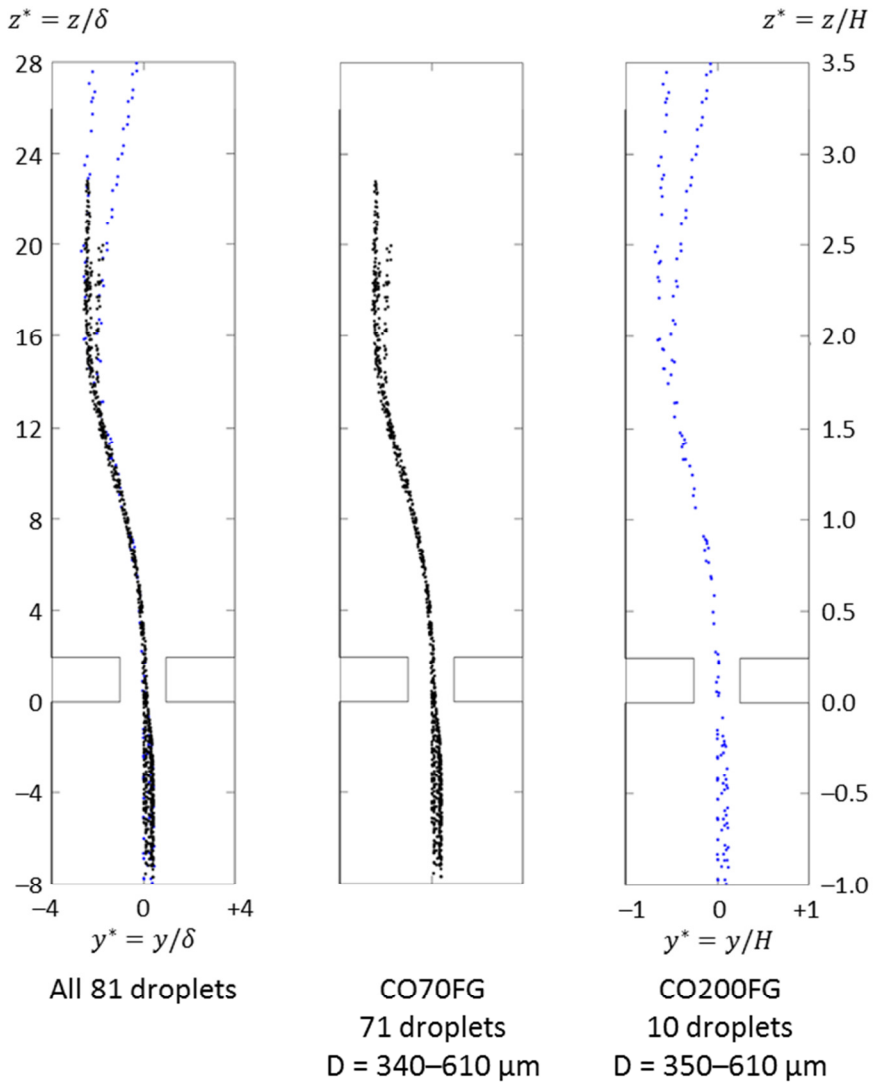

Figure D.20. Trajectories for water droplets in laminar Crystal Oil flows with incoming trajectories $0 < y^*_{inc} < 0.5$.

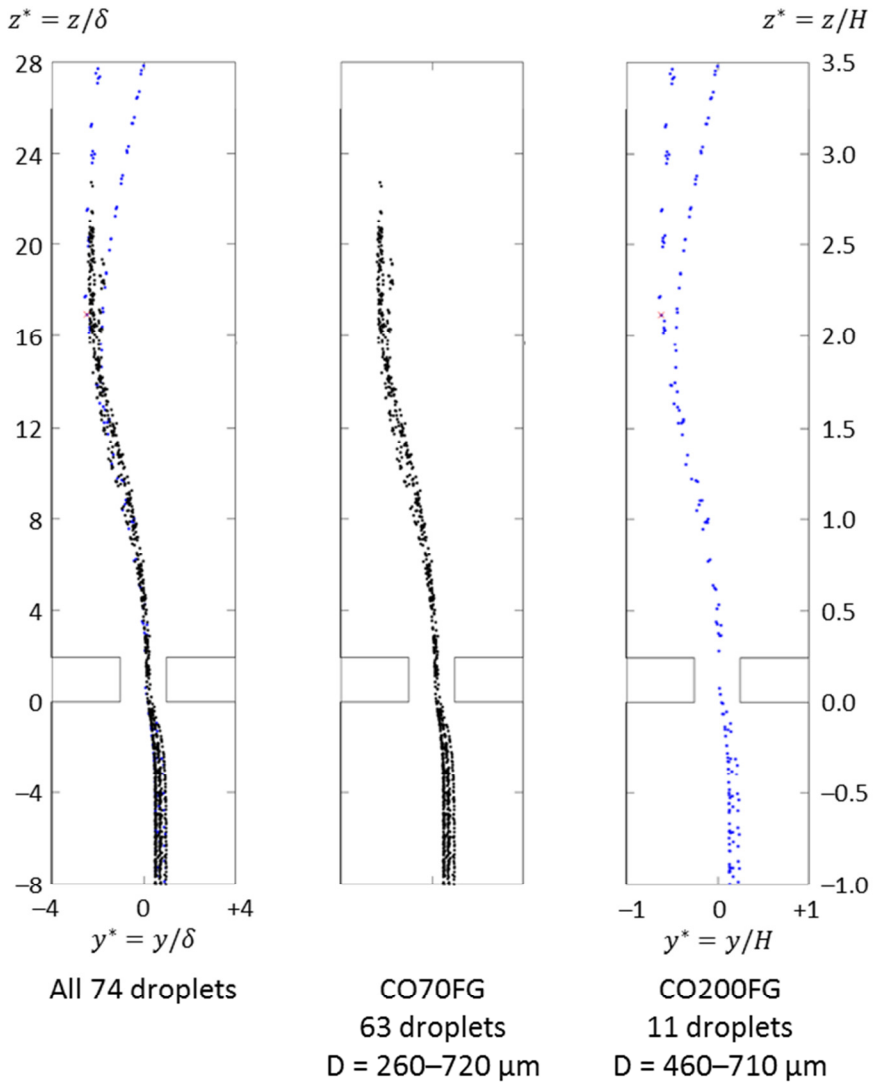

Figure D.21. Trajectories for water droplets in laminar Crystal Oil flows with incoming trajectories $0.5 < y^*_{inc} < 1.0$.

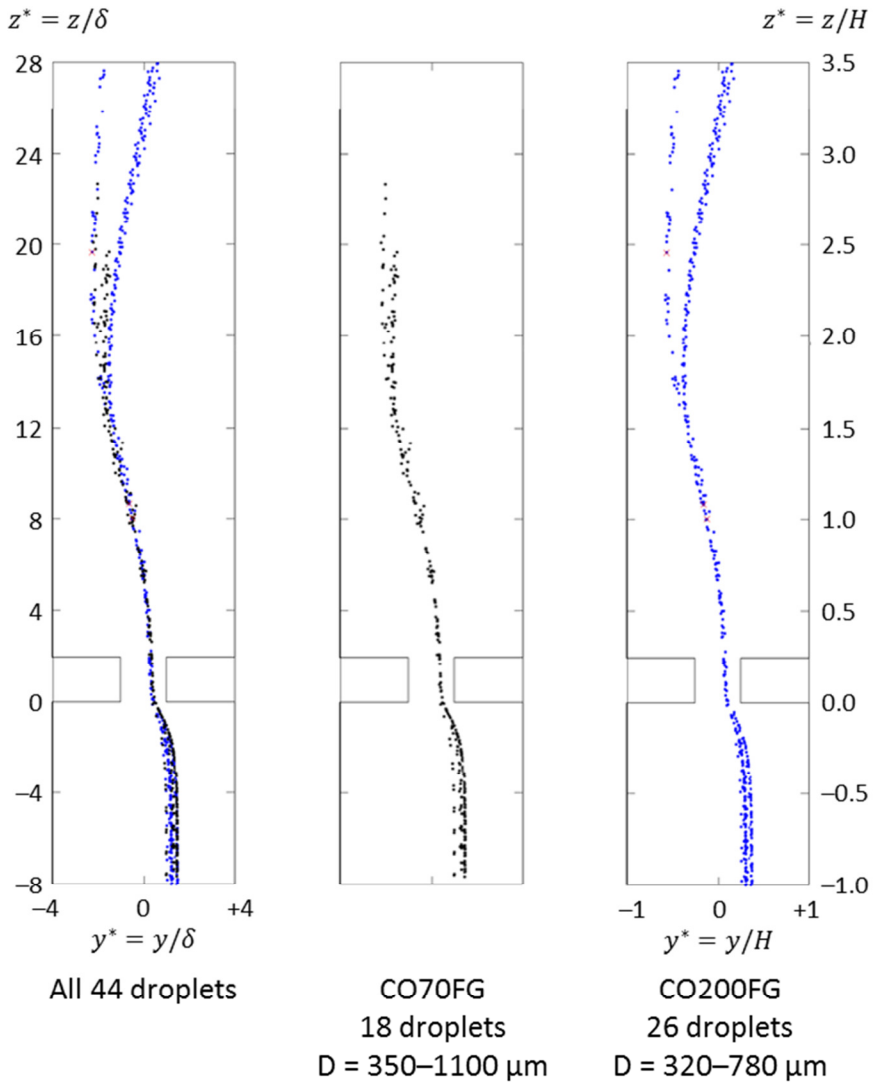

Figure D.22. Trajectories for water droplets in laminar Crystal Oil flows with incoming trajectories $1.0 < y^*_{inc} < 1.5$.

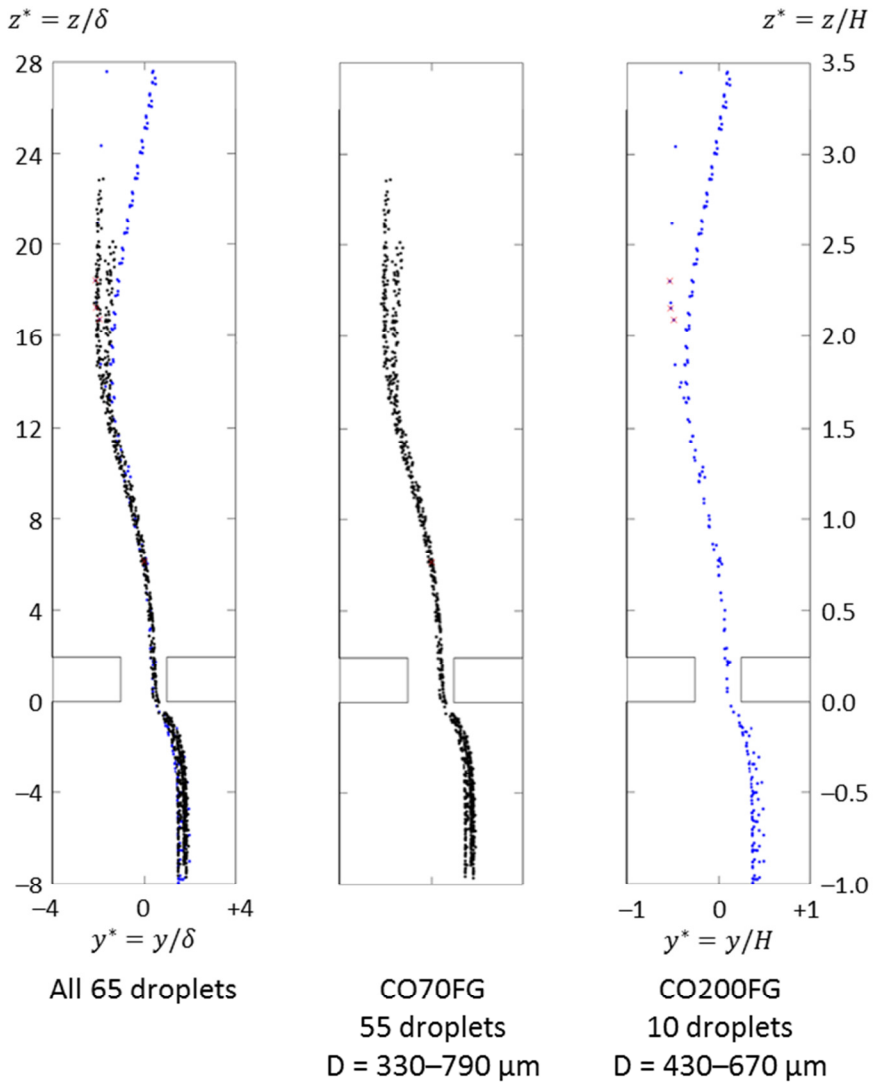

Figure D.23. Trajectories for water droplets in laminar Crystal Oil flows with incoming trajectories $1.5 < y^*_{inc} < 2.0$.

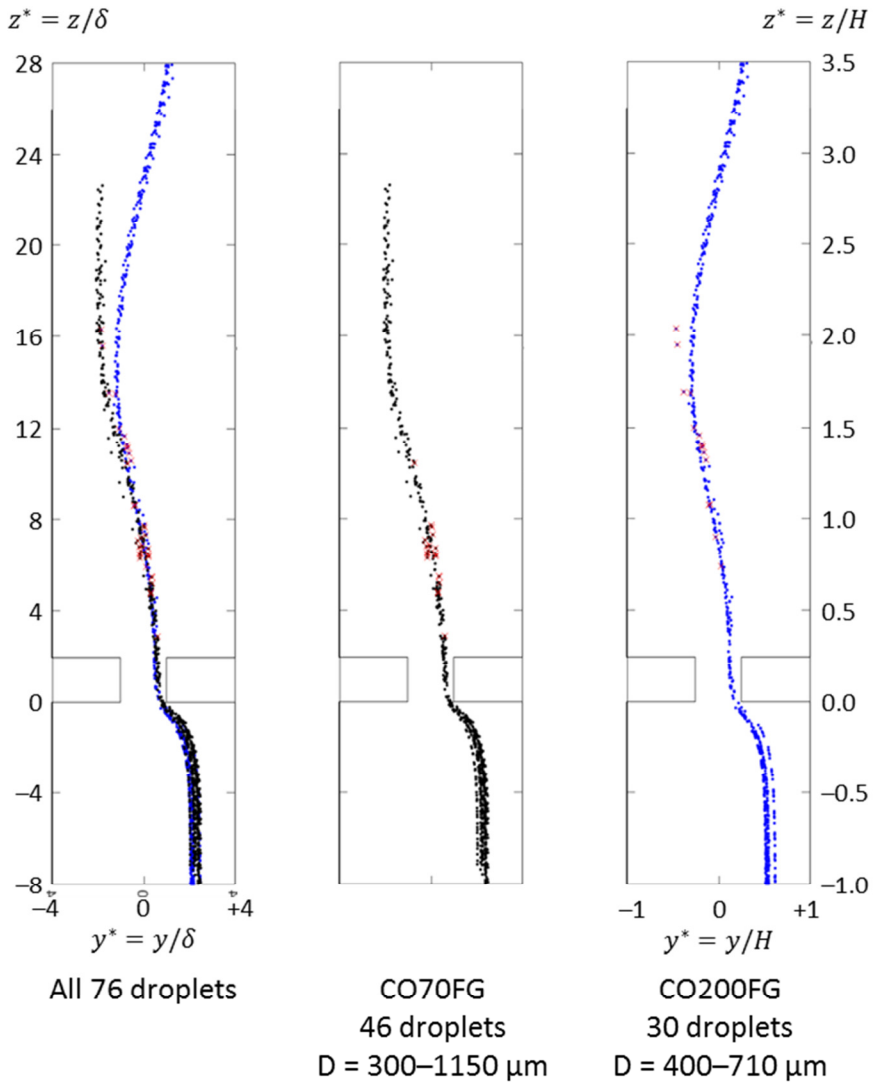

Figure D.24. Trajectories for water droplets in laminar Crystal Oil flows with incoming trajectories $2.0 < y^*_{inc} < 2.5$.

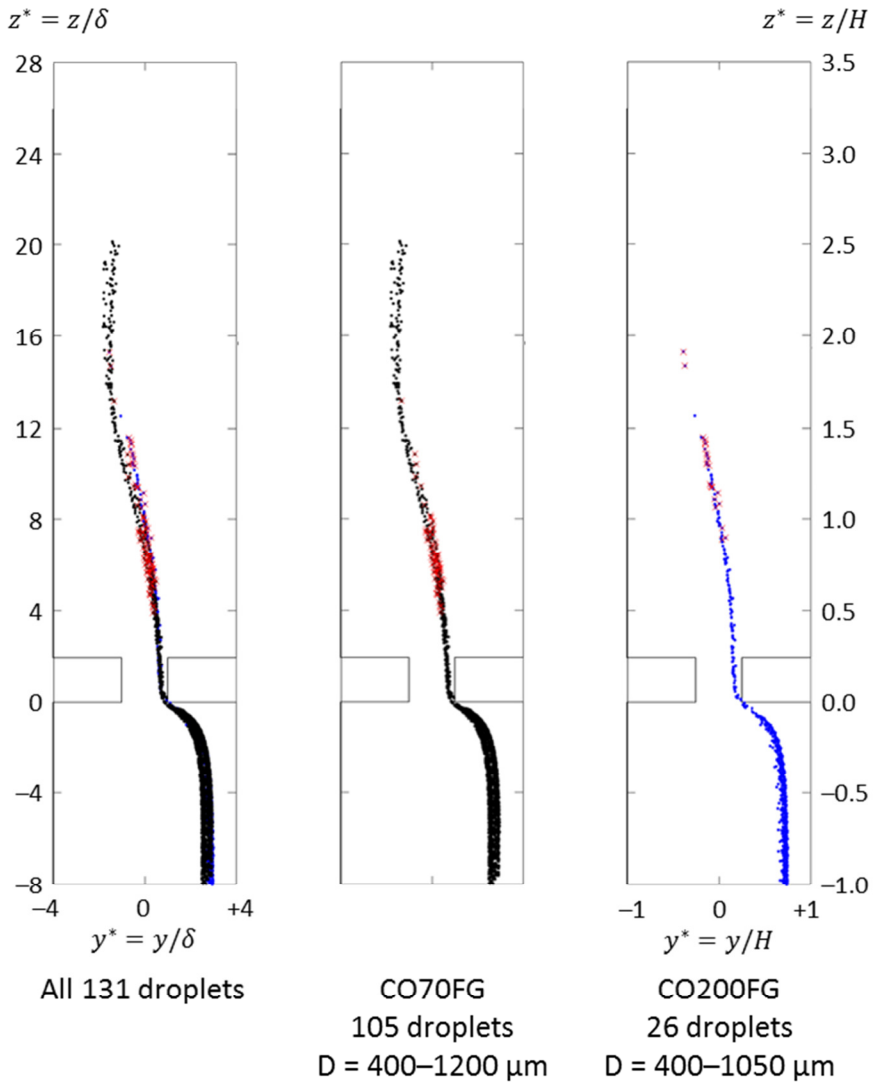

Figure D.25. Trajectories for water droplets in laminar Crystal Oil flows with incoming trajectories $2.5 < y^*_{inc} < 3.0$.

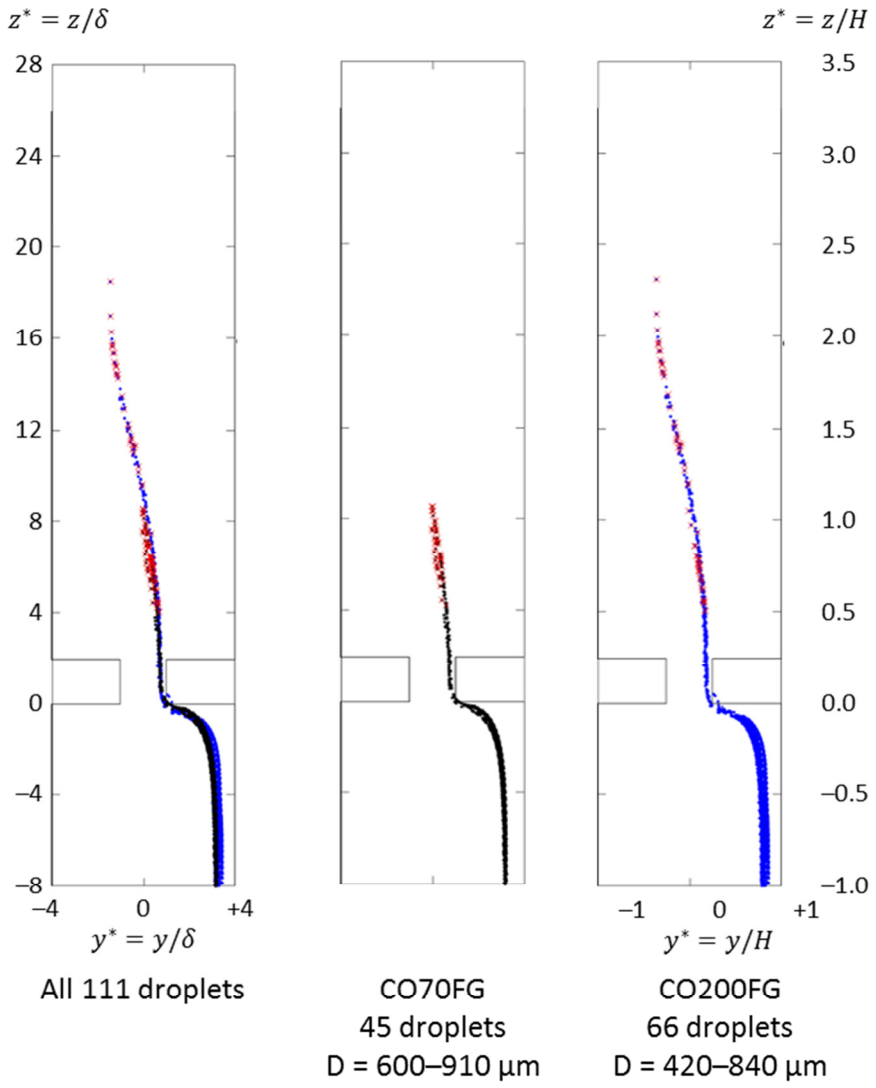

Figure D.26. Trajectories for water droplets in laminar Crystal Oil flows with incoming trajectories $3.0 < y^*_{inc} < 3.5$.

Appendix E: Droplet Terminal Velocity

The buoyancy-induced rise or fall of a droplet (or bubble) in a liquid medium is a more complicated than the corresponding rise or fall of a solid sphere because the no-slip condition applied at the interface generates an internal circulation that acts to slow the droplet's motion and change the droplet's shape. Clift *et al.* (1978) prepared the graphical correlation shown in Figure E.1(b) to relate the shape and terminal velocity Reynolds number to the Eötvös number (essentially a Bond number, relating gravitational to interfacial forces) and Morton number for a droplet or bubble at terminal velocity in an infinite stagnant liquid medium. These three dimensionless groups are presented in Equations E-1 to E-3, where U_t is the terminal velocity and g is the positive gravitational constant.

$$Re = \frac{\rho_c U_t D}{\mu_c} \tag{E-1}$$

$$Eo = \frac{g|\rho_c - \rho_d|D^2}{\sigma} \tag{E-2}$$

$$M = \frac{g\mu_c^4|\rho_c - \rho_d|}{\rho_c^2\sigma^3} \tag{E-3}$$

To allow for automated calculation of the terminal velocity for use in the fluid particle time scale, Figure E.1(b) was digitized. Because the ranges of Eötvös and Morton numbers for the current work were $10^{-3.1} \leq Eo \leq 10^{-0.5}$ and $10^{-11.4} \leq M \leq 10^{-3.2}$, each Morton number curve was extended to lower values of *Eo* and thus *Re*. The relationships between log(*Re*) and log(*Eo*) at fixed M are approximately linear for lower values of *Eo*, so the plots were extended on the assumption that this

linearity would continue. Figure E.1(a) shows the extended form of the plot. The extensions are based on a slope of 1.37, which is the average slope for all 11 curves at their lowest value of *Eo*.

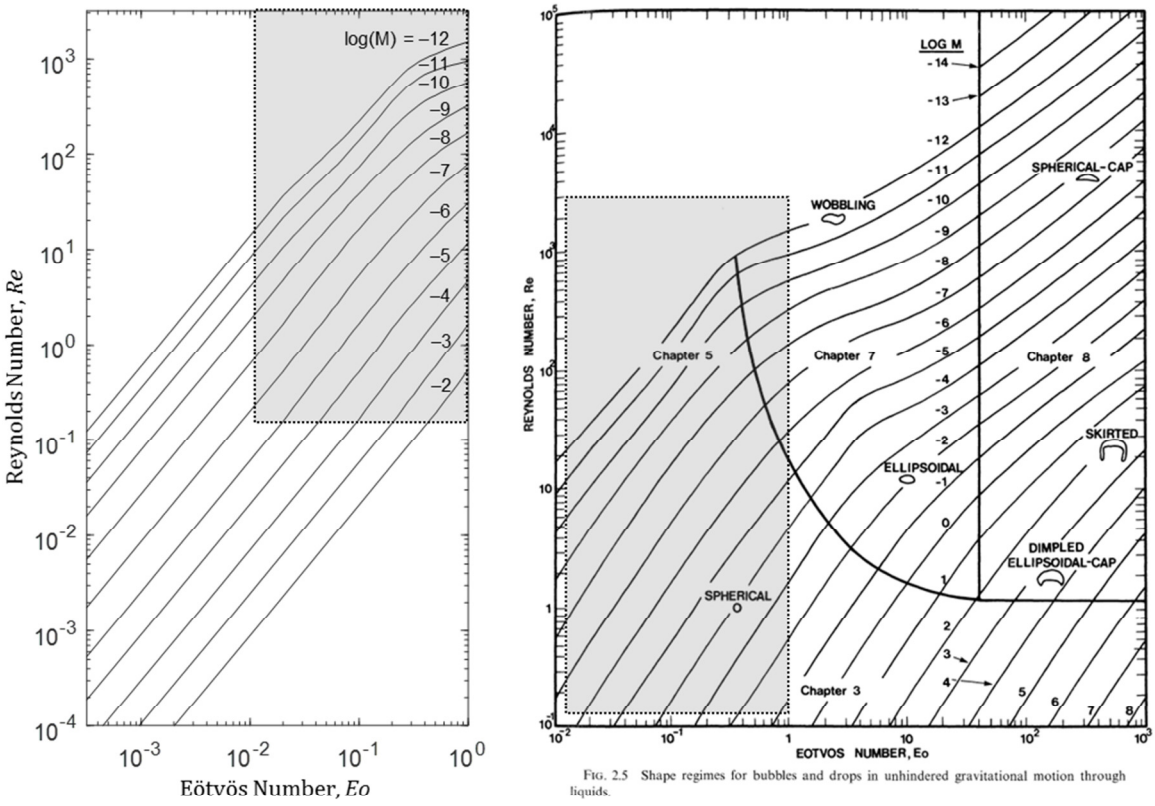

(a) Extended form of plot. (b) Original Plot from Clift *et al.* (1978).

Figure E.1. Relationship between Reynolds, Eötvös, and Morton numbers for the buoyancy-induced movement of an inviscid droplet or bubble in an infinite stagnant liquid medium. The grey box marks where the original plot was digitized for the purposes of the current work.

The values of log(Re) as a function of log(Eo) and log(M) are tabulated in Table E.1 for $10^{-1.7} \leq Eo \leq 1$; below this range, the relationship between log(Re) and log(Eo) is linear with a slope of 1.37.

Table E.1. Value of log(Re) as a function of log(Eo) and log(M).

log(Eo)	log(M)										
	-12	**-11**	**-10**	**-9**	**-8**	**-7**	**-6**	**-5**	**-4**	**-3**	**-2**
-1.70	1.556	1.329	1.021	0.673	0.216	-0.283	-0.806	-1.257	-1.739	-2.194	-2.638
-1.65	1.612	1.387	1.082	0.749	0.295	-0.208	-0.730	-1.189	-1.671	-2.125	-2.569
-1.60	1.668	1.445	1.148	0.817	0.373	-0.132	-0.649	-1.120	-1.602	-2.057	-2.501
-1.55	1.718	1.498	1.203	0.878	0.441	-0.069	-0.579	-1.052	-1.534	-1.988	-2.432
-1.50	1.774	1.556	1.264	0.946	0.517	0.007	-0.503	-0.983	-1.465	-1.920	-2.364
-1.45	1.834	1.615	1.324	1.016	0.592	0.080	-0.427	-0.915	-1.397	-1.851	-2.295
-1.40	1.890	1.673	1.385	1.085	0.663	0.153	-0.349	-0.846	-1.328	-1.783	-2.227
-1.35	1.940	1.723	1.440	1.143	0.731	0.216	-0.283	-0.783	-1.260	-1.714	-2.158
-1.30	2.001	1.779	1.501	1.208	0.802	0.290	-0.210	-0.710	-1.191	-1.646	-2.090
-1.25	2.056	1.839	1.564	1.274	0.875	0.368	-0.137	-0.632	-1.123	-1.577	-2.021
-1.20	2.109	1.890	1.617	1.334	0.941	0.431	-0.069	-0.568	-1.054	-1.509	-1.953
-1.15	2.165	1.953	1.680	1.395	1.014	0.509	0.004	-0.495	-0.986	-1.440	-1.884
-1.10	2.223	2.018	1.746	1.466	1.090	0.587	0.085	-0.420	-0.917	-1.372	-1.816
-1.05	2.288	2.084	1.809	1.526	1.155	0.661	0.158	-0.346	-0.849	-1.303	-1.747
-1.00	2.346	2.144	1.864	1.582	1.213	0.729	0.224	-0.283	-0.780	-1.235	-1.679
-0.95	2.412	2.210	1.932	1.640	1.279	0.799	0.297	-0.208	-0.697	-1.166	-1.610
-0.90	2.478	2.276	2.003	1.703	1.347	0.870	0.370	-0.132	-0.619	-1.097	-1.541
-0.85	2.538	2.339	2.064	1.758	1.403	0.931	0.433	-0.064	-0.548	-1.029	-1.473
-0.80	2.601	2.409	2.129	1.814	1.466	0.996	0.507	0.012	-0.475	-0.960	-1.404
-0.75	2.667	2.483	2.200	1.869	1.526	1.064	0.577	0.093	-0.397	-0.892	-1.336
-0.70	2.730	2.551	2.263	1.927	1.589	1.130	0.648	0.174	-0.319	-0.823	-1.267
-0.65	2.791	2.609	2.319	1.975	1.637	1.188	0.709	0.242	-0.253	-0.753	-1.199
-0.60	2.849	2.667	2.374	2.033	1.695	1.254	0.777	0.312	-0.177	-0.672	-1.130
-0.55	2.899	2.722	2.425	2.089	1.751	1.314	0.840	0.380	-0.104	-0.591	-1.062
-0.50	2.937	2.763	2.470	2.139	1.799	1.370	0.900	0.441	-0.041	-0.526	-0.993
-0.45	2.977	2.806	2.515	2.185	1.854	1.430	0.966	0.507	0.035	-0.445	-0.925
-0.40	3.005	2.841	2.556	2.233	1.905	1.491	1.032	0.572	0.108	-0.367	-0.856
-0.35	3.033	2.866	2.589	2.276	1.955	1.551	1.092	0.640	0.181	-0.293	-0.785
-0.30	3.053	2.886	2.614	2.311	1.996	1.602	1.148	0.698	0.249	-0.228	-0.720
-0.25	3.078	2.907	2.644	2.349	2.044	1.657	1.211	0.762	0.325	-0.150	-0.642
-0.20	3.103	2.924	2.669	2.387	2.084	1.713	1.274	0.825	0.396	-0.074	-0.566
-0.15	3.124	2.939	2.695	2.417	2.119	1.753	1.324	0.880	0.461	-0.008	-0.498
-0.10	3.144	2.952	2.715	2.450	2.155	1.801	1.380	0.946	0.532	0.065	-0.422
-0.05	3.162	2.967	2.735	2.483	2.190	1.849	1.430	1.006	0.603	0.141	-0.341
0.00	3.182	2.982	2.760	2.518	2.225	1.897	1.488	1.074	0.673	0.219	-0.258

References

Abbott DE, Kline SJ (1962). Experimental investigation of subsonic turbulent flow over single and double backward facing steps. *J. Basic Eng.* 84, 317–25.

Adamson AW (1976). *Physical Chemistry of Surfaces* (3rd ed). Wiley-Interscience, New York.

Andersson R, Andersson B (2006a). On the breakup of fluid particles in turbulent flows. *AIChE J.* 52, 2020–30.

Andersson R, Andersson B (2006b). Modeling the breakup of fluid particles in turbulent flows. *AIChE J.* 52, 2031–8.

ANSYS Fluent Theory Guide (Release 18.1). (2017). Accessed online at: https://support.ansys.com/portal/site/AnsysCustomerPortal/template.fss?file=%2Fprod_docu%2F18.1%2FANSYS+Fluent+Theory+Guide.pdf

Alopaeus V, Koskinen J, Keskinen KI, Majander J (2002). Simulation of the population balances for liquid-liquid systems in a nonideal stirred tank. Part 2—parameter fitting and the use of the multiblock method for dense dispersions. *Chem. Eng. Sci.* 57, 1815–25.

Batchelor GK (1959). *The theory of homogeneous turbulence*. Cambridge University Press, London.

Battaglia F, Tavener SJ, Kulkarni AK, Merkle CL (1997). Bifurcation of low Reynolds number flows in symmetric channels. *AIAA J.* 35, 99–105.

Bentley BJ, Leal LG (1986). An experimental investigation of drop deformation and breakup in steady, two-dimensional linear flows. *J. Fluid Mech.* 168, 241–83.

Berkman PD, Calabrese RV (1988). Dispersion of viscous liquids by turbulent flow in a static mixer. *AIChE J.* 34, 602–9.

Brady JF, Acrivos A (1982). The deformation and breakup of a slender drop in an extensional flow: inertial effects. *J. Fluid Mech.* 226, 443–51.

Calabrese RV (1975). The dispersion of discrete particles in a turbulent fluid field. Ph.D. dissertation, University of Massachusetts Amherst, USA

Calabrese RV, Chang TPK, Dang TP (1986a). Drop breakup in turbulent stirred-tank contactors. Part I. Effect of dispersed phase viscosity. *AIChE J.* 32, 657–66.

Calabrese RV, Middleman S (1979). The dispersion of discrete particles in a turbulent fluid field. *AIChE J.* 25, 1025–35.

Calabrese RV, Wang CY, Bryner NP (1986b). Drop breakup in turbulent stirred-tank contactors. Part III. Correlations for mean size and drop size distribution. *AIChE J.* 32, 677–81.

Chen HT, Middleman S (1967). Drop size distribution in agitated liquid-liquid systems. *AIChE J.* 13, 989–95.

Chen HC, Patel VC (1988). "Near-wall turbulence models for complex flows including separation. *AIAA Journal* 26, 641–48.

Cherdron W, Durst F, Whitelaw JH (1978). Asymmetric flows and instabilities in symmetric ducts with sudden expansions. *J. Fluid Mech.* 84, 13–31.

Clift R, Grace JR, Weber ME (1978). *Bubbles, drops, and particles*. Academic Press, New York.

Coulaloglou CA, Tavlarides LL (1977). Description of interaction processes in agitated liquid-liquid dispersions. *Chem. Eng. Sci.* 32, 1289–97.

Das PK (1996). Prediction of maximum stable diameter of viscous drops in a turbulent dispersion. *Chem. Eng. Technol.* 19, 39–42.

Drikakis D (1997). Bifurcation phenomena in incompressible sudden expansion flows. *Phys. Fluids* 9, 76–87.

Durst F, Melling A, Whitelaw JH (1974). Low Reynolds number flow over a plane symmetric sudden expansion. *J. Fluid Mech.* 64, 111–28.

Durst F, Pereira CF, Tropea C (1993). The plane symmetric sudden-expansion flow at low Reynolds number. *J. Fluid Mech.* 248, 567–81.

Eastwood C, Cartellier A, Lasheras JC (2004). The break-up of immiscible fluids in turbulent flows. *J. Fluid Mech.* 502, 309–33.

Escudier MP, Oliviera PJ, Poole RJ (2002). Turbulent flow through a plane sudden expansion of moderate aspect ratio. *Phys. Fluids*, 14, 3641–54.

Fearn RM, Mullin T, Cliffe KA (1990). Nonlinear flow phenomenon in a symmetric sudden expansion. *J. Fluid Mech.* 211, 595–608.

Galinat S, Masbernat O, Guiraud P, Dalmazzone C, Noik C (2005). Drop break-up in turbulent flow downstream of a restriction. *Chem. Eng. Sci.* 60, 6511–28.

Galinat S, Torres G, Masbernat O, Guiraud P, Risso F, Dalmazonne C, Noik C (2007). Breakup of a drop in a liquid-liquid pipe flow through an orifice. *AIChE J.* 53, 56–68.

Grace HP (1982). Dispersion phenomena in high viscosity immiscible fluid systems and application of static mixers as dispersion devices in such systems. *Chem. Eng. Commun.* 14, 225–77.

Ha J-W, Leal LG (2001). An experimental study of drop deformation and breakup in extensional flow at high capillary number. *Phys. Fluids* 13, 1568–76.

Hanks RW, Ruo H-C (1966). Laminar-turbulent transition in ducts of rectangular cross-section. *Ind. Eng. Chem. Fund.* 5, 558–61.

Hawa T, Rusak Z (2001). The dynamics of a laminar flow in a symmetric channel with a sudden expansion. *J. Fluid Mech.* 436, 283–320.

Hesketh RP, Etchells AW, Russell TWF (1987). Bubble size in horizontal pipelines. *AIChE J.* 33, 663–7.

Hesketh RP, Etchells AW, Russell TWF (1991). Experimental observations of bubble breakage in turbulent flow. *Ind. Eng. Chem. Res.* 30, 835–41.

Hinze JO (1955). Fundamentals of the hydrodynamic mechanism of splitting in dispersion processes. *AIChE J.* 1, 289–295.

Holmes TL (1973). Fluid mechanics of horizontal bubble flow. Ph.D. dissertation, University of Delaware, USA.

Jongen T (1992). Simulation and modeling of turbulent incompressible flows". PhD dissertation, École Polytechnique Fédérale de Lausanne, Switzerland.

Karabelas AJ. Droplet size spectra generated in a turbulent pipe flow of dilute liquid/liquid dispersions. *AIChE J.* 24, 170–80.

Khismatullin DB, Renardy Y, Cristini V (2003). Inertia-induced breakup of highly viscous drops subjected to simple sear. *Phys. Fluids* 15, 1351–4.

El Khoury GK, Petterson B, Andersson HI, Barri M (2010). Asymmetries in an obstructed turbulent channel flow. *Phys. Fluids* 22, 095103 (13 pages).

Ko DI (2013). Computational fluid dynamics simulations of an in-line slot and tooth rotor-stator mixer. M.S. thesis, University of Maryland College Park, USA.

Kolmogorov AN (1941). The local structure of turbulence in incompressible viscous fluid for very large Reynolds numbers. *Dokl. Akad. Nauk SSSR* 30, 301–5.

Kolmogorov AN (1949). On the disintegration of drops in a turbulent flow. *Dokl. Akad. Nauk SSSR* 66, 825–8.

Komrakova AE, Shardt O, Eskin D, Derkson JJ (2014). Lattice Boltzmann simulations of drop deformation and breakup in shear flow. *Int. J. Multiphase Flow* 59, 24–43.

Komrakova AE, Shardt O, Eskin D, Derkson JJ (2015). Effects of dispersed phase viscosity on drop deformation and breakup in inertial shear flow. *Chem. Eng. Sci.* 126, 150–9.

Kubie J, Gardner GC (1977). Drop sizes and drop dispersion in straight horizontal tubes and in helical coils. *Chem. Eng. Sci.* 32, 195–202.

Lamb H (1932). *Hydrodynamics*. Cambridge University Press, London.

Lasheras JC, Eastwood C, Martinez-Bazan C, Montanes JL (2002). A review of statistical models for the break-up of an immiscible fluid immersed into a fully developed turbulent flow. *Int. J. Multiphase Flow* 28, 247–78.

Launder BE, Spalding DB (1974). The numerical computation of turbulent flows. *Comput. Methods Appl. Mech. Eng.* 3, 269–89.

Leng DE, Calabrese RV (2004). Immiscible Liquid-Liquid Systems. In *Handbook of Industrial Mixing* (pp. 639–754). Wiley, New Jersey.

Levich VG (1962). *Physicochemical hydrodynamics*. Prentice-Hall, New Jersey.

Lumley JL (1957). Some problems connected with the motion of small particles in turbulent fluid. Ph.D. dissertation, The Johns Hopkins University, USA.

Maass S, Gabler A, Zaccone A, Paschedag R, Kraume M (2007). Experimental investigations and modelling of breakage phenomena in stirred liquid/liquid systems. *Chem. Eng. Res. Des.* 85, 703–9.

Maass S, Kraume M (2012). Determination of breakage rates using single drop experiments. *Chem. Eng. Sci.* 70, 146–64.

Marks CR (1998). Drop breakup and deformation in sudden onset strong flows. Ph.D. dissertation, University of Maryland College Park, USA.

Martinez-Bazan C, Montanes JL, Lasheras JC (1999a). On the breakup of an air bubble injected into a fully developed turbulent flow. Part 1. Breakup frequency. *J. Fluid Mech.* 401, 157–82.

Martinez-Bazan C, Montanes JL, Lasheras JC (1999b). On the breakup of an air bubble injected into a fully developed turbulent flow. Part 2. Size PDF of the resulting daughter bubbles. *J. Fluid Mech.* 401, 183–207.

McKinley GH, Renardy M (2011). Wolfgang von Ohnesorge. Phys. Fluids 23, 127101 (7 pages).

Miller CA, Scriven LE (1968). The oscillations of a fluid droplet immersed in another fluid. *J. Fluid Mech.* 32, 417–35.

Mizushima J, Okamoto H, Yamaguchi H (1996). Stability of flow in a channel with a suddenly expanded part. *Phys. Fluids* 8, 2933–42.

Mullin T, Shipton S, Tavener SJ (2003). Flow in a symmetric channel with an expanded section. *Fluid Dyn. Res.* 33, 433–52.

Percy JS, Sleicher CA (1983). Drop breakup in the flow of immiscible liquids through an orifice in a pipe. *AIChE J.* 29, 161–4.

Qian D, McLaughlin JB, Sankaranarayanan K, Sundaresan S, Kontomaris K (2006). Simulation of bubble breakup dynamics in homogeneous turbulence. *Chem. Eng. Comm.* 193, 1038–63.

Rallison JM (1984). The deformation of small viscous drops and bubbles in shear flows. *Ann. Rev. Fluid Mech.* 16, 45–66.

Ravelet F, Colin C, Risso F (2011). On the dynamics and breakup of a bubble rising in a turbulent flow. *Phys. Fluids* 23, 103301 (12 pages).

Renardy YY, Cristini V (2001a). Effect of inertia on drop breakup under shear. *Phys. Fluids* 13, 7–13.

Renardy YY, Cristini V (2001b). Scalings for fragments produced from drop breakup in shear flow with inertia. Phys. Fluids 13, 2161–4.

Rodriguez-Rodriguez J, Gordillo JM, Martinez-Bazan C (2006). Breakup time and morphology of drops and bubbles in a high-Reynolds-number flow. *J. Fluid Mech.* 548, 69–86.

Rueger PE (2013). Liquid-liquid dispersion in batch and in-line rotor stator mixers. Ph.D. Dissertation, University of Maryland, USA.

Rueger PE, Calabrese RV (2013). Dispersion of water into oil in a rotor-stator mixer. Part 1: Drop breakup in dilute systems. *Chem. Eng. Res. Des.* 91, 2122–33.

Rumscheidt FD and Mason SG (1961). Particle motions in sheared suspensions XII. Deformation and burst of fluid drops in shear and hyperbolic flow. *J. Coll. Sci.* 16, 238–61.

Rumscheidt FD and Mason SG (1962). Break-up of stationary liquid threads. *J. Coll. Sci.* 17, 260–9.

Shapira M, Degani D, Weihs D (1990). Stability and existence of multiple solutions for viscous flow in suddenly enlarged channels. *Comput. Fluids* 3, 239–58.

Sleicher CA (1962). Maximum stable drop size in turbulent flow. *AIChE J.* 8, 471–7.

Sobey IJ, Drazin PG (1986). Bifurcations of two-dimensional channel flows. *J. Fluid Mech.* 171, 263–87.

Solsvic J, Jakobsen HA (2015). Single drop breakup experiments in stirred liquid-liquid tanks. *Chem. Eng. Sci.* 131, 219–34.

Stegeman YW, van de Vosse FN, Meijer HEH (2002). On the applicability of the Grace curve in practical mixing operations. *Can. J. Chem. Eng.* 80, 1–6.

Stone, HA (1994). Dynamics of drop deformation and breakup in viscous fluids. *Ann. Rev. Fluid Mech.* 26, 65–102.

Stone HA, Bentley BJ, and Leal LG (1986). An experimental study of transient effects in the breakup of viscous drops. *J. Fluid Mech.* 173, 131–58.

Stone HA, Leal LG (1989a). Relaxation and breakup of an initially extended drop in an otherwise quiescent fluid. *J. Fluid Mech.* 198, 399–427.

Stone HA, Leal LG (1989b). The influence of initial deformation on drop breakup in subcritical time-dependent flows at low Reynolds numbers. *J. Fluid Mech.* 206, 223–63.

Taylor GI (1934). The formation of emulsions in definable fields of flow. *Proc. R. Soc. Lond. A*, vol. 146, pp. 501–23.

Tjahjadi M, Ottino JM (1991). Stretching and breakup of droplets in chaotic flows. *J. Fluid Mech.* 232, 191–219.

Vananroye A, Van Puyvelde P, Moldenaers P (2006). Effect of confinement on droplet breakup in sheared emulsions. *Langmuir* 22, 3972–4.

Wang CY, Calabrese RV (1986). Drop breakup in turbulent stirred-tank contactors. Part II. Relative influence of viscosity and interfacial tension. *AIChE J.* 32, 667–76.

Welty JR, Wicks CE, Wilson RE, Rorrer GL (2008). *Fundamentals of Momentum, Heat, and Mass Transfer* (5th ed). Wiley & Sons, New Jersey.

Wille R, Fernholz H (1965). Report on the first European Mechanics Colloquium, on the Coanda effect. *J. Fluid Mech.* 23, 801–19.

Wolfshtein M (1969). The velocity and temperature distribution in one-dimensional flow with turbulence augmentation and pressure gradient. *Int. J. Heat Mass Tran.* 12, 301–18.

Zaccone A, Gabler A, Maass S, Marchisio D, Kraume M (2007). Drop breakage in liquid-liquid dispersions: modelling of single drop breakage. *Chem. Eng. Sci.* 62, 6297–307.

Zhao X (2007). Drop breakup in dilute Newtonian emulsions in simple shear flow: New drop breakup mechanisms. *J. Rheol.* 51, 367–92.

De Zilwa SRN, Khezzar L, Whitelaw JH (2000). Flows through plane sudden-expansions. *Int. J. Numer. Meth. Fluids* 32, 313–29.

Archival Publications

Ko DI, Calabrese RV (***exp: 2018***). "Breakage of Single Droplets in an Inertial Laminar 2-D Orifice Flow." (***in preparation***)

Ko DI, Calabrese RV (***exp: 2018***). "Breakage of Single Droplets and Bubbles in a Turbulent 2-D Orifice Flow." (***in preparation***)

Ko DI, Kevala KR, Mishra VP, Calabrese RV (***exp: 2018***). Comparison of 3-D RANS Simulations and LDA for an In-line Slot and Tooth Rotor-Stator Mixer. (***in preparation***)

Minnick BA, Kim JW, Ko DI, Calabrese RV (***exp: 2018***). Flow and Power Characteristics of an Axial Discharge Rotor-Stator Mixer. *Chem. Eng. Res. Des.* (***accepted***)

Conference Presentations

Ko DI, Calabrese RV (2018). "Breakage of Single Droplets in a Laminar 2-D Orifice Flow." Mixing XXVI, Las Croabas, Puerto Rico. (***submitted***)

Ko DI, Calabrese RV (2017). "Breakage of Single Droplets in 2-D Turbulent Flows." 14th Annual Burgers Program Symposium, University of Maryland, MD, USA. (Poster, **Award**)

Ko DI, Calabrese RV (2017). "(577h) Breakage of Single Drops and Bubbles in a Turbulent 2-D Orifice Flow." AIChE Annual Meeting, Minneapolis, MN, USA.

Ko DI, Calabrese RV (2016). "Breakage of Single Droplets in 2-D Inertial Flows (A Progress Report)." Mixing XXV, Quebec City, QC, Canada.

Ko DI, Kim JW, Minnick BA, Jaimes Prada R, Calabrese RV (2015). "(376b) Computational Fluid Dynamics Simulation of a Pipeline Rotor-Stator Mixer." AIChE Annual Meeting, Salt Lake City, UT, USA.

Kim JW, Ko, DI, Kevala KR, Calabrese RV (2015). "(301f) IKA Prototype In-line Mixer: RANS Simulations & Comparison to PIV Data." AIChE Annual Meeting, Salt Lake City, UT, USA.